Numerical simulation of nanosecond repetitively pulsed discharges in air at atmospheric pressure : Application to plasma-assisted combustion

Fabien Tholin

To cite this version:

Fabien Tholin. Numerical simulation of nanosecond repetitively pulsed discharges in air at atmospheric pressure : Application to plasma-assisted combustion. Other. Ecole Centrale Paris, 2012. English. NNT : 2012ECAP0055 . tel-00879856

HAL Id: tel-00879856

https://theses.hal.science/tel-00879856

Submitted on 5 Nov 2013

École Centrale Paris

THÈSE

présentée par

Fabien THOLIN

pour l'obtention du

GRADE de DOCTEUR

Formation doctorale :	ED 287 Sciences pour l'ingénieur de l'Ecole Centrale Paris
Laboratoire d'accueil :	Laboratoire d'Énergétique Moléculaire et Macroscopique, Combustion (EM2C), UPR 288 du CNRS situé à l'ECP

Numerical simulation of nanosecond repetitively pulsed discharges in air at atmospheric pressure: Application to plasma-assisted combustion

Soutenue le 20 décembre 2012

Jury :

M.	Igor	Adamovich	Professeur à Ohio State University, NETL
M.	Jean-Pierre	Boeuf	Dir. de Recherche CNRS, LAPLACE
Mme	Anne	Bourdon	Dir. de Recherche CNRS, EM2C
M.	Sébastien	Célestin	Maître de Conf. à l'Univ. d'Orléans, LPC2E
Mme	Deanna	Lacoste	Ing. de Recherche CNRS, EM2C
M.	Christophe	Laux	Professeur à l'ECP, EM2C
M.	Jean-Hugues	Paillol	Professeur à l'Univ. de Pau, SIAME

École Centrale des Arts et Manufactures
Grand Établissement sous tutelle
du Ministère de l'Éducation Nationale
Grande Voie des Vignes
92295 Châtenay-Malabry Cedex
Tél : 33 (1) 41 13 10 00
Télex : 634 991 F EC PARIS

Laboratoire d'Énergétique Moléculaire et Macroscopique, Combustion (E.M2.C.)
UPR 288, CNRS et École Centrale Paris
Tél : 33 (1) 41 13 10 31
Fax : 33 (1) 47 02 80 35

2012 - xx

Remerciements

Je tiens à remercier tout d'abord ma directrice de thèse, Anne Bourdon, avec qui j'ai eu grand plaisir à travailler durant ces trois années de thèse au laboratoire EM2C. Je la remercie pour sa patience, sa pédagogie, sa disponibilité et son aide de tous les instants qui m'a vraiment permis d'avancer au cours de mon travail et de ne jamais rester bloqué. Je tiens aussi à remercier tous les autres chercheurs et personnels du laboratoire avec qui j'ai eu le plaisir d'interagir et d'échanger. Je pense entre autres à Deanna Lacoste, pour ses précieux conseils, sa bonne humeur et sa franchise, ainsi qu'à Christophe Laux et Nasser Darabiha, pour leur aide et le temps qu'ils ont pu m'accorder au cours de ces trois ans. Je remercie également l'équipe des mathématiques appliquées et notamment François Doisneau et Max Duarte, dont les conseils m'auront été très utiles dans mes travaux de développement. Je remercie naturellement les rapporteurs de ma thèse, Igor Adamovich, qui a pris la peine de venir depuis l'Ohio, et Jean-Pierre Boeuf, dont les remarques avisées m'auront permis de finaliser mon manuscrit et d'ouvrir de nouvelles perspectives dans mes travaux. Il en va de même pour les membres de mon jury : grâce à eux j'ai véritablement apprécié la phase de questions de ma soutenance de thèse. Parmi eux Sébastien Célestin, et Jean-Hugues Paillol, qui m'a beaucoup aidé sur les modèles de circuit et avec qui je me suis beaucoup entretenu. Je tiens également à remercier mes collègues de la communauté des plasmas froids, que j'ai pu rencontrer en master, en conférence ou en réunion et avec qui j'ai très vite sympathisé. Notamment Olivier Guaitella, Ilya et Daniil Marinov, ainsi que Jérôme Bredin, Lara Popelier, Julien Analoro, Virginie Martin, Claire Douat, Pierre Le Delliou et bien d'autres. Bien évidemment, je remercie l'ensemble des doctorants et stagiaires que j'ai fréquentés à EM2C et à l'École Centrale Paris au cours de ma thèse. Ils ont toujours assuré une très bonne ambiance entre les étudiants, parmi eux Adrien Lemal, Aurélien Guy, Vincent Leroy, Diana Tudorache, Sorour Refahi, Jean Lamouroux, Jean Caudal, Marie Zarrouati, Yufang Zang, Xu Da, Frédéric Boudy, et beaucoup d'autres... Je salue également les personnes avec qui j'ai partagé mon bureau (je perds au jeu tout en écrivant ces lignes): François Doisneau, Laurent Tranchant, Marien Simeni Simeni le bien nommé, Farah Kadouri, Julien Jarrige et Wenjie Tao. Enfin, je me dois de remercier tout particulièrement mes collègues et amis de l'axe plasma froid : David Pai, Florent Sainct, Diane Rusterholtz-Duval, François

Pechereau et Jaroslav Jánský, avec qui j’ai eu le plaisir d’échanger si souvent ! Et enfin bien sûr, Zdeněk Bonaventura ! qui m’a offert une aide extrêmement précieuse tout au long de mon séjour à EM2C, formé sur le code et apporté énormément de connaissances en programmation et méthodes numériques. Je le remercie également de m’avoir donné un accès au calculateur Anila, basé à l’Université Masaryk de Brno. Ainsi, ma thèse est affectueusement dédicacée aux calculateurs Anila, Igloo, et feu Madness, en compagnie desquels j’ai passé tant de nuits et de week-ends. Je remercie encore mes parents, ma famille et mes proches, qui m’ont toujours soutenu pendant ces trois années ainsi que toutes les personnes présentes à ma soutenance.

This work has been supported by a grant from the French Ministry of Research delivered by École Centrale Paris. It has also been partly supported by the PREPA (Grant n° ANR-09-BLAN-0043) and the PLASMAFLAME (Grant n° ANR-11-BS09-0025) projects.

Abstract

In this Ph.D. thesis, we have carried out numerical simulations to study nanosecond repetitively pulsed discharges (NRPD) in a point-to-point geometry at atmospheric pressure in air and in H_2-air mixtures.

Experimentally, three discharge regimes have been observed for NRPD in air at atmospheric pressure for the temperature range $T_g = 300$ to 1000 K: corona, glow and spark. To study these regimes, first, we have considered a discharge occurring during one of the nanosecond voltage pulses. We have shown that a key parameter for the transition between the discharge regimes is the ratio between the connection-time of positive and negative discharges initiated at point electrodes and the pulse duration.

In a second step, we have studied the dynamics of charged species during the interpulse at $T_{\mathrm{g}} = 300$ and 1000 K and we have shown that the discharge characteristics during a given voltage pulse remain rather close whatever the preionization level (in the range 10^9-10^{11} cm^{-3}) left by previous discharges. Then, we have simulated several consecutive nanosecond voltage pulses at $T_{\mathrm{g}} = 1000$ K at a repetition frequency of 10 kHz. We have shown that in a few voltage pulses, the discharge reaches a stable quasi-periodic glow regime observed in the experiments.

We have studied the nanosecond spark discharge regime. We have shown that the fraction of the discharge energy going to fast heating is in the range 20%-30%. Due to this fast heating, we have observed the propagation of a cylindrical shockwave followed by the formation of a hot channel in the path of the discharge that expands radially on short timescales ($t < 1$ μs), as observed in experiments. Then we have taken into account an external circuit model to limit the current and then, we have simulated several consecutive pulses to study the transition from multipulse nanosecond glow to spark discharges.

Finally the results of this Ph.D. have been used to find conditions to obtain a stable glow regime in air at 300 K and atmospheric pressure. Second we have studied on short time-scales ($t \leq 100\mu$s) the ignition by a nanosecond spark discharge of a lean H_2-air mixture at 1000 K and atmospheric pressure with an equivalence ratio of $\Phi = 0.3$. We have compared the relative importance for ignition of the fast-heating of the discharge and of the production of atomic oxygen. We have shown that the ignition with atomic oxygen seems to be slightly more efficient and has a completely different dynamics.

Résumé

Dans cette thèse, nous avons étudié des décharges nanosecondes répétitives pulsées dans une géométrie pointe-pointe à la pression atmosphérique dans l'air et dans des mélanges hydrogène-air. Expérimentalement, trois régimes de décharges ont été observés dans l'air à pression atmosphérique entre 300 et 1000 K : couronne, diffus et arc. Pour étudier ces différents régimes, nous avons tout d'abord simulé une décharge ayant lieu pendant un des pulses de tension nanosecondes. Nous avons montré qu'un paramètre clé pour la transition entre les régimes est le rapport entre le temps de connexion entre les décharges positives et négatives initiées aux pointes et la durée du pulse de tension.
Dans une seconde étape, nous avons étudié la dynamique des espèces chargées entre les pulses de tension à 300 et 1000 K et nous avons montré que les caractéristiques de la décharge pendant un pulse de tension dépendaient très peu du niveau de préionisation (dans la gamme 10^9-10^{11} cm^{-3}) laissé par les décharges précédentes. Nous avons ensuite simulé plusieurs pulses de tensions consécutifs à T_g=1000 K à une fréquence de 10 kHz. Nous avons montré que, en quelques pulses de tension, la décharge atteint un régime diffus "stable", observé dans les expériences.
Nous avons ensuite étudié le régime de décharge de type arc nanoseconde. Nous avons montré que la fraction d'énergie de la décharge allant dans le chauffage rapide de l'air est de 20-30 %. A cause de ce chauffage rapide, nous avons observé la propagation d'une onde de choc cylindrique suivie par la formation d'un canal chaud, sur le passage initial de la décharge, qui se dilate radialement sur des temps courts ($t \leqslant 1$ μs), comme observé dans les expériences. Ensuite nous avons pris en compte un modèle de circuit externe pour limiter le courant et ainsi nous avons simulé plusieurs pulses consécutifs pour étudier la transition entre les régimes diffus et d'arc nanoseconde.
Pour finir, les résultats de cette thèse ont été utilisés pour trouver des conditions d'obtention d'un régime diffus stable à 300 K et à la pression atmosphérique.
Puis nous avons étudié l'allumage sur des temps courts ($t \leqslant 100$ μs) d'un mélange pauvre H_2-air par une décharge de type arc nanoseconde à 1000 K et à pression atmosphérique avec une richesse de 0.3. Nous avons comparé les importances relatives pour l'allumage du chauffage rapide et de la production d'oxygène atomique.
Nous avons montré que l'allumage par l'oxygène atomique semble être légère-

ment plus efficace et a une dynamique complètement différente de celle initiée par le chauffage rapide.

Contents

Introduction

Atmospheric pressure air plasmas

Low temperature plasma discharges operating at atmospheric pressure have received increasing attention in recent years, both in academic research groups and in industry for their ability to produce active species in well-controlled environments and at very low energy cost. These discharges are found in a growing list of successful practical applications such as ozone generation, polymer processing, excitation of laser and excimer lamps, pollution control, biological decontamination, medical treatment, aerodynamic flow control, and thin film coating [*Pilla et al.*, 2006; *Massines et al.*, 2003; *Fridman et al.*, 2005].

Among these applications, plasma assisted combustion and ignition [*Starikovskiy and Aleksandrov*, 2013] may be one of the most promising to significantly reduce pollutant emission and fuel consumption since combustion represents 80% of the energy production in the world. Particularly, non-thermal plasma discharges have proven their ability to ignite very lean mixtures which provide lower nitrogen oxide emissions, lower maximum temperatures and higher engine efficiency through higher compression ratios.

In the last few years, atmospheric pressure plasma microjets have also received considerable interest because of the possibility of propagating non-thermal plasmas in air. This property opens up new possibilities including, among others, localized surface treatment, decontamination and biomedical applications [*Laroussi et al.*, 2012; *Lu et al.*, 2012].

One of the main problems in plasma discharge experiments and applications comes from the fact that, at atmospheric pressure, the cold nonequilibrium plasma discharge is a transient event. A simple way to generate cold plasmas is to use electrodes at high-voltage separated by a gaseous gap. However, at atmospheric pressure, the originally cold plasma rapidly becomes a high-conducting junction that evolves into a thermal plasma where heavy species tend to be in equilibrium with the electrons at a few tens of thousands degrees Kelvin. This is the so-called arc discharge. There are several ways to prevent this equilibrium of temperature between heavy species and electrons. Two main solutions are Dielectric Barrier Discharges (DBD) and Nanosecond Repetitively Pulsed (NRP) discharges.

Dielectric barrier discharges have been studied since the invention of the ozonizer

by Siemens in 1857. DBDs at atmospheric pressure produced by applied voltage at low frequency in gaseous gaps on the order of a few millimeters are mainly constituted of unstably triggered nonequilibrium transient plasma filaments. The dielectric barrier prevents the formation of an arc because charges deposited by the plasma filament on the dielectric material are trapped. These charges are deposited such that the electric field becomes too low to produce more current and the process stops in a few tens of nanoseconds.
Another solution is to use nanosecond repetitively pulsed (NRP) discharges. Indeed, the application of high-voltage pulses generates a high electric field that allows an efficient electron impact ionization. In NRP, the idea is to turn off the electric field before substantial ionization occurs, to avoid an extremely fast increase of the gas temperature. Finally, the use of repetitive voltage pulses results in the accumulation of active species interesting for applications.
In *Pai et al.* [2010b] and *Rusterholtz* [2012], a detailed experimental study of the NRP discharges in air has been carried out in the temperature range of 300 to 1000 K at atmospheric pressure. It is interesting to note that the cumulative effect of repeated pulsing achieves steady-state behaviour. Thus, even though they are transient, the nanosecond repetitively pulsed (NRP) discharges have a visual resemblance with dc discharge regimes. For an air temperature in the range 300 to 1000 K, as the applied voltage increases, three different discharge regimes are observed. At low voltage, a corona regime is observed, with light emitted only near the point electrodes. For higher voltages, a glow regime is observed. This regime has an emission which fills the gap in a diffuse manner. Finally, for even higher voltages, a regime reminiscent of a spark discharge is observed with an intense emission. The measurements show that the glow regime has low levels of emission, gas heating and electrical conduction current, indicating that it is non-thermal. In contrast to the non-thermal glow regime, the thermal nanosecond spark regime emits strongly, heats the gas by several thousand degrees Kelvin and has tens of amperes of conduction current. Further details on the experimental results may be found in *Pai* [2008]; *Rusterholtz* [2012].

Depending on the application, the constraints on the NRPD can differ significantly. For plasma assisted combustion, the discharge should be designed to produce as much as reactive species as possible and some heat released in the discharge can be in this case a positive effect for combustion enhancement. On the other hand, for biomedical applications it is important to have a cold discharge without any heating, and to control accurately the active species that are produced to obtain the expected effect. In other applications, such as biodecontamination, the UV light emission from the discharge is a key issue and one should control the production of electron excited molecules able to emit at the desired wavelength. The shape, the volume and the spatial extension of the plasma generated are also important parameters for applications. In plasma assisted ignition, large, diffuse plasma volumes for volumetric ignition, or multi-filament discharge structures for multi-point ignition of mixtures may be needed [*Starikovskiy and Aleksandrov*, 2013].

The optimization of the production of active chemical species by a NRP discharge, its heating, its structure and its radiation is a current challenge for many applications. However these discharges are rather complex and a better understanding is necessary to be able to control them in a more efficient way.

Scope of the thesis

At the laboratory EM2C, since several years a very detailed experimental study on a NRPD discharges in air at atmospheric pressure in a preheated air flow (300 to 1000 K) has been carried out [*Rusterholtz*, 2012; *Pai et al.*, 2010a]. In parallel, we have started to develop the simulations of these discharges. In a previous Ph.D. work we have simulated the dynamics of the discharge during one voltage pulse between two-point electrodes [*Celestin*, 2008]. In this thesis, we want to go on the investigation of nanosecond repetitively pulsed discharges in air at atmospheric pressure in a point-to-point geometry from a numerical point of view, to compare the results with the experimental studies carried out at EM2C, and to address some key issues concerning the use of NRPD for applications.
In the first part of this thesis the goal is to improve our current understanding of the physics of NRPD in a point-to-point configuration:

- In Chapter 1, we will introduce briefly the numerical methods employed to simulate the nanosecond repetitively pulsed discharges in air at atmospheric pressure.

- In Chapter 2, the goal is to better understand the different regimes of nanosecond pulsed discharges in air at atmospheric pressure highlighted experimentally by *Pai et al.* [2010b] and *Rusterholtz* [2012]. For this purpose we perform single pulse simulations and we carry out a parametric study on the influence of the applied voltage, the gap size, the radius of the electrodes and the air temperature. Finally, we will present a comparison between simulations and experiments.

- In Chapter 3, we propose to study the influence of the repetition frequency of NRPD. More precisely, we focus on the effect of the evolution of the preionization level pulse after pulse and on the influence of an external flow.

- In Chapter 4, we put emphasis on the spark regime of NRPD and we study the heating of the ambient air due to the discharge energy deposition. We model a nanosecond spark discharge, its fast-heating, and the resulting compressible flow dynamics.

- In Chapter 5, we propose to take into account the influence of the external circuit model and we simulate a multipulse spark discharge.

In the second part of the thesis, we study two applications of NRPD at atmospheric pressure:

- First, in Chapter 6, we propose a strategy to obtain a glow discharge in atmospheric pressure air at 300 K. Then we carry out a parametric study and address the problems of the glow-to-spark transition and the branching of the discharge at 300 K.

- Then, in Chapter 7, we build a model to study the plasma assisted ignition of a lean pre-mixed hydrogen-air mixture. The goal is to study the relative importance for ignition between the fast-heating and the atomic oxygen production.

Part I

Physics of nanosecond repetitively pulsed discharges in air at atmospheric pressure

Chapter 1

Numerical models for nanosecond discharges at atmospheric pressure

1.1 Introduction

In this chapter, we present the model used to simulate streamer discharges in air at atmospheric pressure in Section 1.2. In Section 1.3, we briefly describe the chosen numerical method and then we discuss the different strategies to mesh the different point-to-point geometries studied in this work. In Section 1.4, we present the transport properties and reaction rates for charged species in air at atmospheric pressure at 300 and 1000 K and we discuss briefly the scaling of the photoionization source term in Section 1.5. Finally, in Section 1.6, we describe the model used to compute the optical emissions of the discharge and in Section 1.7, we present the calculation of the energy of the discharge.

1.2 Streamer equations

The most common and effective model to study the dynamics of streamers in air at atmospheric pressure is based on the following drift-diffusion equations for electrons, positive and negative ions coupled with Poisson's equation:

$$\begin{aligned}
&\partial_{\mathrm{t}}\mathrm{n_e} + \vec{\nabla}\cdot(\mathrm{n_e}\vec{\mathrm{v}}_{\mathrm{e}} - \mathrm{D_e}\vec{\nabla}\mathrm{n_e}) &&= \mathrm{S_e} + \mathrm{S_{ph}}\\
&\partial_{\mathrm{t}}\mathrm{n_n} + \vec{\nabla}\cdot(\mathrm{n_n}\vec{\mathrm{v}}_{\mathrm{n}} - \mathrm{D_n}\vec{\nabla}\mathrm{n_n}) &&= \mathrm{S_n}\\
&\partial_{\mathrm{t}}\mathrm{n_p} + \vec{\nabla}\cdot(\mathrm{n_p}\vec{\mathrm{v}}_{\mathrm{p}} - \mathrm{D_p}\vec{\nabla}\mathrm{n_p}) &&= \mathrm{S_p} + \mathrm{S_{ph}}\\
&\nabla^2\mathrm{V} = -\frac{\mathrm{q_e}}{\epsilon_0}(\mathrm{n_p} - \mathrm{n_n} - \mathrm{n_e})
\end{aligned} \tag{1.1}$$

with

$$\vec{\mathrm{E}} = -\vec{\nabla}V \tag{1.2}$$

and

$$\vec{\mathrm{v}}_i = \mu_i \vec{\mathrm{E}} \tag{1.3}$$

where subscripts "e", "p" and "n" refer to electrons, positive and negative ions, respectively. n_i is the number density of species i, D_i and μ_i are the diffusion coefficient and the mobility of specie i respectively. $\mathrm{q_e}$ is the absolute value of electron charge, and ϵ_0 is the permittivity of free space. E is the absolute value of the electric field and V is the electric potential. $\mathrm{S_{ph}}$ is the photoionization source term and the S_i terms stand for the source terms of specie i due to chemical reactions and are given by:

$$\left\{\begin{array}{ll} \mathrm{S_e} = (\partial_\mathrm{t}\mathrm{n_e})_\mathrm{chem} & = (\nu_\alpha - \nu_\eta - \beta_\mathrm{ep}\,\mathrm{n_p})\,\mathrm{n_e} + \nu_\mathrm{det}\,\mathrm{n_n} \\ \mathrm{S_n} = (\partial_\mathrm{t}\mathrm{n_n})_\mathrm{chem} & = -(\nu_\mathrm{det} + \beta_\mathrm{np}\,\mathrm{n_p})\,\mathrm{n_n} + \nu_\eta\,\mathrm{n_e} \\ \mathrm{S_p} = (\partial_\mathrm{t}\mathrm{n_p})_\mathrm{chem} & = -(\beta_\mathrm{ep}\,\mathrm{n_e} + \beta_\mathrm{np}\,\mathrm{n_n})\,\mathrm{n_p} + \nu_\alpha \mathrm{n_e} \end{array}\right. \tag{1.4}$$

where ν_α, ν_det and ν_η stand for the ionization, detachment and attachment frequencies respectively. β_ep is the recombination rate coefficient between positive ions and electrons and β_np is the recombination rate coefficient between positive and negative ions.

In this fluid model for streamer simulations, magnetic field effects on the streamer propagation are neglected as discussed in *Celestin* [2008] and we simply solve Poisson's equation to derive the electric field. To close the continuity equations, we have used the classical drift-diffusion approximation, valid for highly collisional plasmas and we have assumed that all transport coefficients and chemical source terms are functions of the local reduced electric field E/N, where E is the electric field magnitude and N is the air neutral density. In this work, we have chosen to use a simple fluid model with only continuity equations coupled to Poisson's equations. This model has been widely studied in the literature and has proven its efficiency for the simulation of streamer discharges at atmospheric pressure [*Kulikovsky*, 1997].

1.3 Studied geometry and numerical model for streamer equations

In this work, we study axi-symmetric streamers propagating between two aligned point electrodes as shown on Figure 1.1 and thus cylindrical coordinates (x, r), are used with the $x-$axis as axis of the discharge.

The charged species transport equations (Equations (1.1)) are solved using a modified Scharfetter-Gummel algorithm [*Kulikovsky*, 1995] with the parameter of this scheme, $\epsilon_{ISG} = 10^{-2}$. It is important to note that the modified Scharfetter-Gummel scheme was developed in 1D. We have adapted it to 2D by splitting the numerical treatment into two one-dimensional problems in the $\vec{\mathrm{x}}$ and $\vec{\mathrm{r}}$ directions, respectively. A directional first order Lie-Trotter splitting

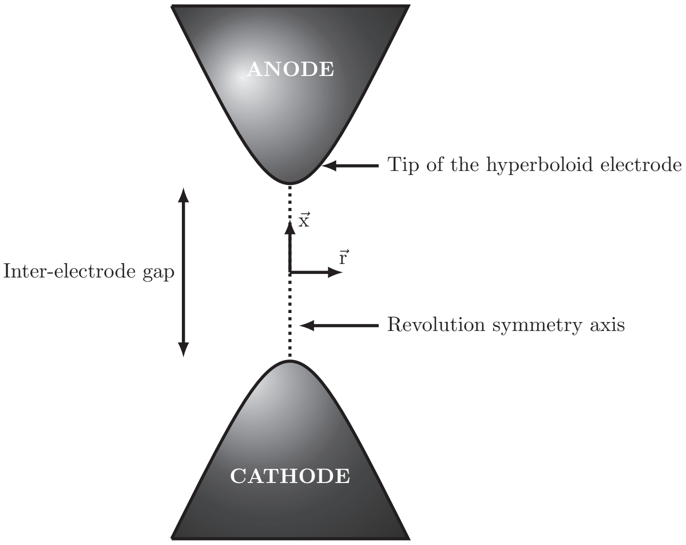

Figure 1.1: *Geometry of the 2D axisymmetric point-to-point configuration*

method is used with an alternation of the order between $\vec{x}$ and $\vec{r}$ in two successive time steps to improve accuracy.

In this work, as in *Celestin et al.* [2009] we have taken into account simplified boundary conditions: near the anode and cathode surfaces, gradients of electron density are assumed to be zero. The ghost fluid method has been used to take into account the exact shapes of the electrodes in the resolution of Poisson's equation on a rectilinear grid [*Celestin et al.*, 2009].

The finite difference form of the Poisson's equation is solved using the SuperLU solver [*Demmel et al.*, 1999] (`http://crd.lbl.gov/~xiaoye/SuperLU/`) with Dirichlet boundary conditions on electrodes and Neumann boundary conditions on the other axial and radial boundaries of the computational domain.

For the time integration during the voltage pulse, we have used a simple first-order Euler time integration for fluxes (Equations (1.1)) and the photoionization source term, and for other source terms, an explicit fourth order Runge Kutta method [*Ferziger and Peric*, 2002].

To define the time step of the simulations, we follow the approach discussed in *Vitello et al.* [1994]. The time scales of relevance for selection of the time step, which would provide model stability and accuracy, are the Courant δt_c, effective ionization δt_I and dielectric relaxation δt_D time scales. The explicit expressions for the time scales can be found in *Vitello et al.* [1994]. The model time step is calculated as δt=min$(A_c\delta t_c, A_I\delta t_I, A_D\delta t_D)$ with A_c=0.5, A_I=0.05 and A_D=0.5. In practical streamer calculations, during the ignition phase, the time step is almost always defined by the minimum value of the ionization time scale corresponding to the maximum field and maximum ionization frequency ν_{imax} in the streamer head (δt_I=1/ν_{imax}). We note that in our modeling we adopt a small A_I value, which is a factor of two less than that used in *Vitello* *et al.* [1994].

The dielectric relaxation timestep δt_D may also be the most limiting timestep when the electron density becomes significant as shown by Equation (1.5).

$$\delta t_D = \frac{\epsilon_0}{\mathrm{q}_e \sum_i |\mathrm{n_i}\mu_i|} \tag{1.5}$$

In this work, we have carried out simulations in a point-to-point geometry with hyperboloid electrodes with a radius of curvature R_p in the range 25-300 μm and for gap sizes in the range 2.5-10 mm.

For all discharge simulations, we have used computational domains with a radius of $r_\mathrm{max} = 1.0$ cm and a length x_max depending on the gap, discretized on a fixed rectilinear grid with $n_\mathrm{x} \times n_\mathrm{r}$ cells. Table 1.1 summarizes the values of x_max, n_x and n_r for the different gaps studied in this work (except for some cases in Chapter 3, in these cases the related information is given explicitly in the text). The grid is Cartesian, with an axial cell size of 2.5 μm at the electrode tips. In the axial direction, between both electrodes, the mesh size is expanded following a geometric progression until it reaches 5 μm and then is kept constant. Beyond these regions, the grid expands axially following a geometric progression up to the boundaries. In the radial direction, a cell size of 2.5 μm is used from the symmetry axis and up to $r = 750\,\mu$m and then the mesh size is expanded following a geometric progression. In all the simulations presented in this work (except for some cases in Chapter 3 and in these cases the locations of both electrodes is given in the text), the tip of the cathode is located at $x_\mathrm{C} = 0.75$ cm, and the position of the tip of the anode x_A for the different gaps is given in Table 1.1.

gap (mm)	2.5	5	10
n_x	1160	1660	2660
n_r	460	460	460
x_max (mm)	17.5	20	25
r_max (mm)	10	10	10
x_C (mm)	7.5	7.5	7.5
x_A (mm)	10	12.5	17.5

Table 1.1: *Characteristics of the simulation domains used for the different gaps.*

1.4 Transport properties and reaction rates for charged species in air at atmospheric pressure at 300 and 1000 K

In this work, we study the discharge dynamics at atmospheric pressure between two point electrodes in ambient air at $T_{\mathrm{g}} = 300\,\mathrm{K}$ and in preheated air at $T_{\mathrm{g}} = 1000\,\mathrm{K}$. At $T_{\mathrm{g}} = 300\,\mathrm{K}$, all transport parameters and reaction rates for air are taken from *Morrow and Lowke* [1997] and diffusion coefficients for ions are derived from mobilities using Einstein relation:

$$\frac{\mathrm{D}_i}{\mu_i} = \frac{\mathrm{k_B T}_i}{\mathrm{q}_i} \tag{1.6}$$

where T_i is the temperature of specie i and $\mathrm{k_B}$ the Boltzmann constant.

Tanaka [2004] studied the influence of temperature on $\mathrm{E_{br}}$, the breakdown field of air at atmospheric pressure and showed that up to 2000 K, the reduced electric field $\mathrm{E_{br}/N}$ remains constant. Then, as in *Celestin et al.* [2009] and *Bourdon et al.* [2010], to take into account the fact that the discharge occurs at atmospheric pressure at $T_{\mathrm{g}} = 1000$ K, we have only scaled the value of the total air density: $\mathrm{N_{1000}} = 0.3 \times \mathrm{N_{300}}$ where $\mathrm{N_{300}} = 2.45 \times 10^{19}\,\mathrm{cm^{-3}}$ is the density of air at 300 K. The decrease of the total density by a factor of 3.3 as the temperature increases from 300 to 1000 K, increases by the same factor the local reduced electric field E/N and then has a direct impact on transport parameters and reaction rates for air.

Figures 1.2 and 1.3 show the electron diffusion coefficient $\mathrm{D_e}$ and the electron mobility μ_{e} at 300 and 1000 K. Two sets of coefficients are compared : The values given by *Morrow and Lowke* [1997], used in this work, and the results from the Bolsig+ code [*Hagelaar and Pitchford*, 2005], and a rather good agreement is obtained. The values are scaled with the air density and both at 300 and 1000 K the diffusion coefficient for electrons is increasing with the electric-field while the mobility decreases due to higher collision frequency with neutrals. However, the absolute value of the drift velocity of electrons $|\mathrm{v_e}|$ increases rapidly with the electric-field, and it may be as high as 10^8 cm s^{-1} at 1000 K (1% of the speed of light) for the high electric-field values obtained in streamer discharges ($>$ 100 kV cm^{-1}). The drift velocity is then higher in this range of electric-field than the thermal velocity of electrons, defined by:

$$V_{\mathrm{th}} = \sqrt{\frac{8\mathrm{k_B T_e}}{\pi \mathrm{m_e}}} \tag{1.7}$$

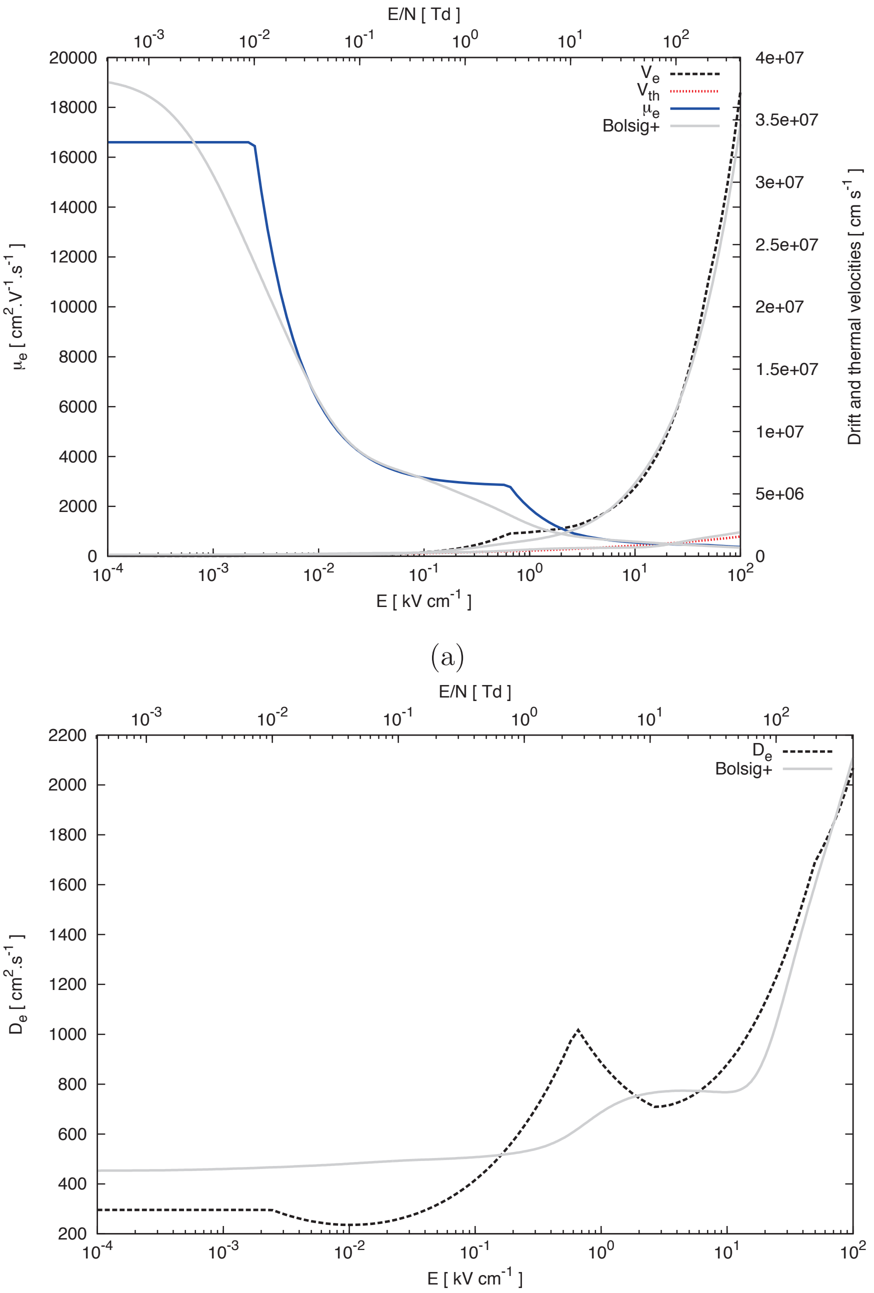

(a)

(b)

Figure 1.2: *Transport parameters of electrons in air at 300 K and atmospheric pressure as a function of the electric-field: (a) electron mobility (μ_e), drift velocity (V_e), and thermal velocity (V_{th}); (b) diffusion coefficient (D_e). Comparison between the values given by Morrow and Lowke [1997] and the results from the Bolsig+ two-term Boltzmann solver [Hagelaar and Pitchford, 2005].*

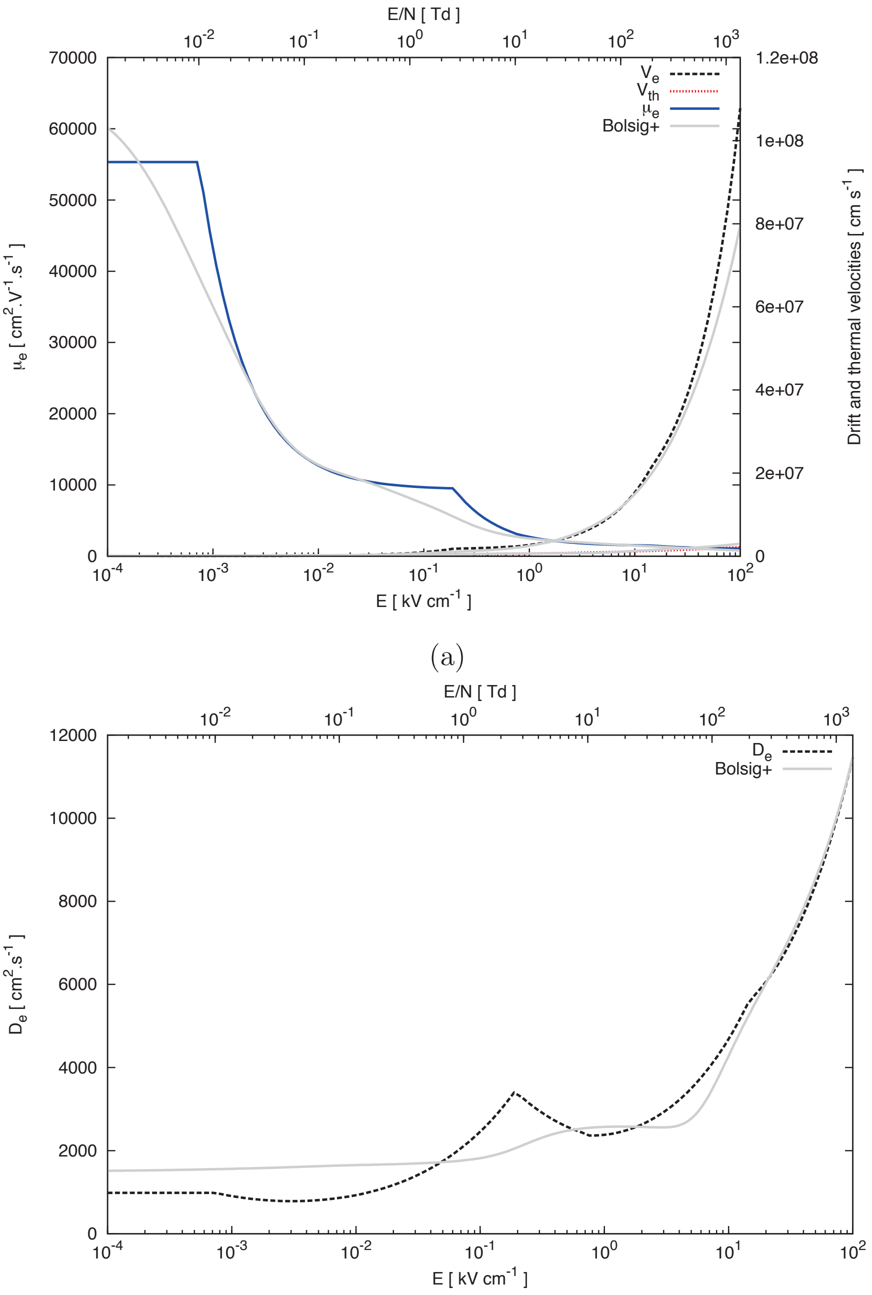

(a)

(b)

Figure 1.3: *Transport parameters of electrons in air at 1000 K and atmospheric pressure as a function of the electric-field: (a) electron mobility (μ_e), drift velocity (V_e), and thermal velocity (V_{th}); (b) diffusion coefficient (D_e). Comparison between the values given by Morrow and Lowke [1997] and the results from the Bolsig+ two-term Boltzmann solver [Hagelaar and Pitchford, 2005].*

Tanaka [2004] has taken into account the change of the air composition with temperature and has accurately computed the ionization and attachment coefficients in air at atmospheric pressure up to 3500 K. For our study we have compared at 1000 K, the cross-sections of ionization (σ_α) and attachment (σ_η) derived from *Morrow and Lowke* [1997] with the results from *Tanaka* [2004]. Cross-sections σ_α and σ_η are related to the the frequencies of ionization (ν_α) and attachment (ν_η) through Equations (1.8).

$$\begin{aligned} \nu_\alpha &= \mathrm{N_g}\sigma_\alpha \mathrm{V_e} \\ \nu_\eta &= \mathrm{N_g}\sigma_\eta \mathrm{V_e} \end{aligned} \tag{1.8}$$

Where $\mathrm{N_g}$ is the neutral species concentration, and $\mathrm{V_e}$ the norm of the electron velocity (drift velocity and thermal velocity). We have obtained a rather good agreement even if our set of coefficients slightly overestimate ionization compared to the coefficients derived by Tanaka in the electric field range 2-12 kV/cm. Figure 1.4 shows the comparison of the ionisation and attachment frequencies up to 100 kV/cm between the values given by *Morrow and Lowke* [1997] and the results from Bolsig+ [*Hagelaar and Pitchford*, 2005] at 300 K (a) and 1000 K (b).

As expected, the breakdown field, (defined as the electric field for which attachment and ionization coefficients are equal) is $\mathrm{E_{br}} \simeq 10$ kV cm^{-1} at 1000 K and $\mathrm{E_{br}} \simeq 30$ kV cm^{-1} at 300 K.

We observe a rather good agreement on the ionization frequency even if our set of coefficients slightly underestimate the attachment frequency compared to Bolsig+ for electric-field values higher than $\simeq$60 kV/cm at 300 K and $\simeq$20 kV/cm at 1000 K. However in this range, the ionization frequency is much higher than the attachment frequency and this difference may not have a significant influence.

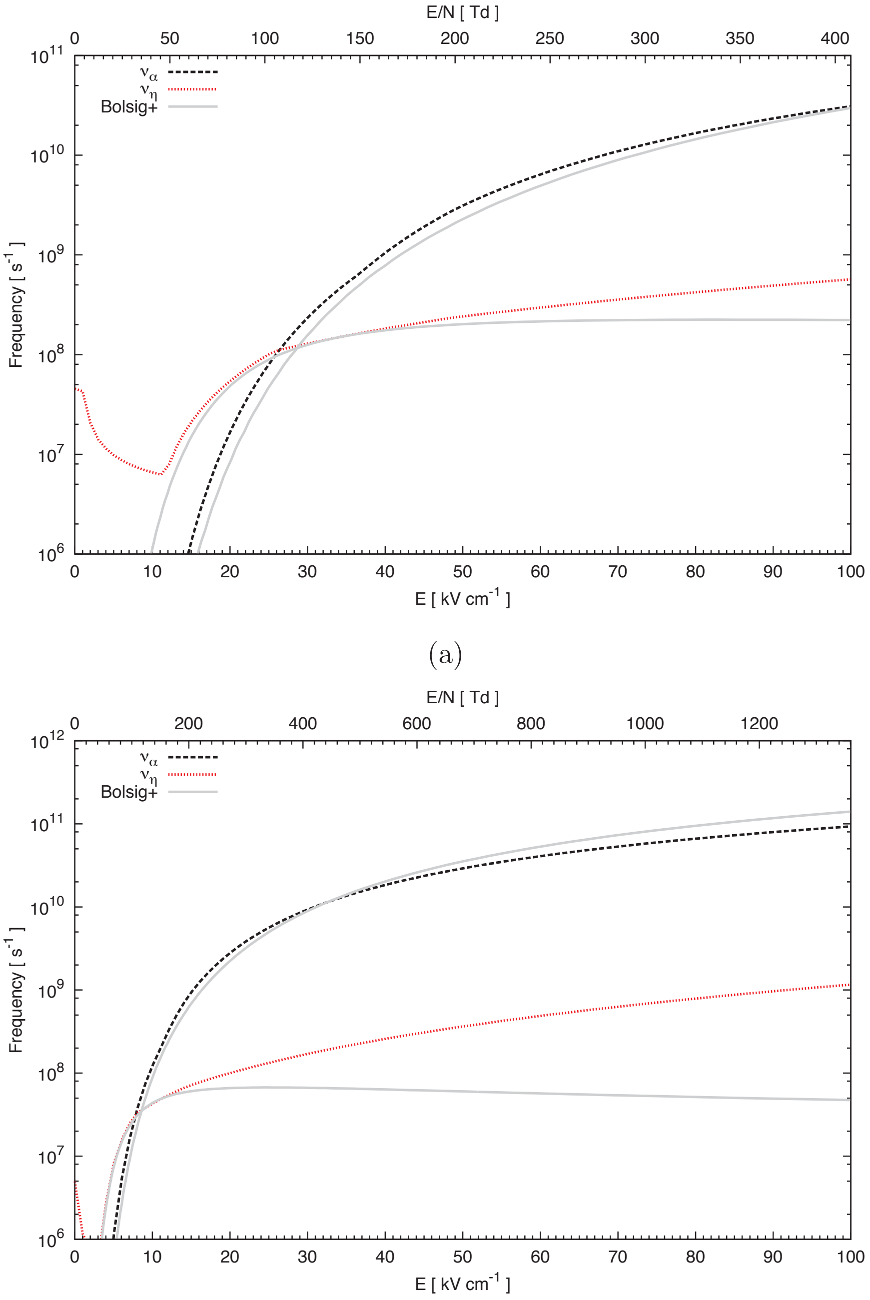

(a)

(b)

Figure 1.4: *Ionization frequency ν_α and attachment frequency ν_η in atmospheric pressure air at 300 K (a) and 1000 K (b). Comparison between the values given by Morrow and Lowke [1997] and the results from the Bolsig+ two-term Boltzmann solver [Hagelaar and Pitchford, 2005].*

1.5 Photoionization source term at 300 and 1000 K

The photoionization source term S_{ph} in Equations (1.1) is an important non-local process in air at atmospheric pressure and 300 K, for the ignition and the propagation of streamers when the preionization background is very low ($\leqslant 10^4$ cm^{-3}). Conversely, when the preionization background is high enough, its influence is almost negligible. Then the relative importance of photoionization versus preionization will be discussed in detail in Chapter 3 for discharges at 300 K.

In this work, the S_{ph} source term is computed thanks to the three-group SP_3 model proposed in *Bourdon et al.* [2007] with boundary conditions given in *Liu et al.* [2007] for discharges in air at atmospheric pressure and 300 K. As we study discharges at 300 and 1000 K, in this section, we discuss the scaling of the photoionization source term at 1000 K.

The three-group SP_3 model proposed in *Bourdon et al.* [2007] is based on the work of Zheleznyak et al [*Zheleznyak et al.*, 1982]. In this model, the photons emitted in the range 98-102.5 nm by the radiative de-excitation of the three highly excited levels of nitrogen $N_2(b^1\Pi_u)$, $N_2(b'^1\Sigma_u^+)$ and $N_2(c_4'^1\Pi_u)$ are able to photo-ionize the molecular oxygen in air [*Liu and Pasko*, 2004]. The source term for energetic photons γ_α able to photo-ionize the gas can then be written as the radiative decay of the excited nitrogen specie $N_2^*(k)$ on the electronic level k:

$$\frac{d[\gamma_\alpha]}{dt} = [N_2^*(k)]\, A_{N_2^*(k)} \tag{1.9}$$

where $A_{N_2^*(k)}$ is the Einstein coefficient of the excited specie $N_2^*(k)$. The evolution of the concentration $[N_2^*(k)]$ is given by:

$$\frac{d[N_2^*(k)]}{dt} = -\frac{[N_2^*(k)]}{\tau_{N_2^*(k)}} + \nu_k^*\, n_e + \sum_{m>k} [N_2^*(m)] A_{N_2^*(m)} \tag{1.10}$$

where $[N_2^*(m)]$ is the concentration of electron excited nitrogen on the level m, and ν_k^* is the excitation frequency through electron impact of level k. In the model, it as assumed that the excitation frequency is proportional to the ionization frequency: ν_α. $\tau_{N_2^*(k)}$ is the lifetime of the excited level $N_2^*(k)$. It depends on the radiative de-excitation of $N_2^*(k)$ and its quenching by N_2 and O_2 at the rates α_1 and α_2 respectively (cm^3 s^{-1}). $\tau_{N_2^*(k)}$ is given by

$$\tau_{N_2^*(k)} = \frac{1}{A_{N_2^*(k)} + \alpha_1[N_2] + \alpha_2[O_2]} = \frac{1}{A_{N_2^*(k)}} \left(\frac{p_q}{p + p_q}\right) \tag{1.11}$$

$$\tag{1.12}$$

$$\text{with :} \quad p_q = \frac{A_{N_2^*(k)} k_B T_g N}{\alpha_1[N_2] + \alpha_2[O_2]} \tag{1.13}$$

Where p is in our case the atmospheric pressure, and p_q is the quenching pressure. Then $\tau_{N_2^*(k)}$ is in the range 0.03-0.3 ns at atmospheric pressure [*Liu and Pasko*, 2004]. In the Zhelezniak model [*Zheleznyak et al.*, 1982], it is assumed that the production of $N_2^*(k)$ thanks to the cascading from the higher excited levels is negligible and that a steady state is obtained very fast (the time derivative of density on the left hand side of Equation (1.10) is assumed to be zero). Then the density of $N_2^*(k)$ is given by:

$$[N_2^*(k)] = \tau_{N_2^*(k)} \nu_k^* \, n_e \tag{1.14}$$

Combining Equations (1.9), (1.11) and (1.14), the production rate of ionizing photons can be written as:

$$\frac{d\gamma_\alpha}{dt} = \nu_k^* n_e \left(\frac{p_q}{p + p_q} \right) \tag{1.15}$$

Liu and Pasko [2006] have discussed similarity laws for streamers at different pressures. In our work, we study discharges at the same pressure but at different air densities. As discussed in *Liu and Pasko* [2006] in accordance with similarity laws, the streamer timescales, the streamer spatial scales and the streamer electron density scale with the air density as $\sim 1/N$, $\sim 1/N$ and $\sim N^2$. Using scaling laws, in Equation (1.15), n_e and ν_k^* scale in N^2 and N. It is important to note that the Zhelezniak model [*Zheleznyak et al.*, 1982] has been written for room temperature conditions in particular in the writing of the fraction $(p_q/p + p_q)$. Then in the scaling of the photoionization at 1000 K, we have checked two hypotheses: either p is constant and p_q is scaled, or p is scaled and p_q is constant. We have compared results in both cases and they are very close. In the 3-group SP_3 model, three absorption coefficients for the three effective wavelengths of photoionization in air are considered. These absorption coefficients are proportional to the molecular oxygen concentration $[O_2]$ and they scale in $1/N$. Finally, the photoionization source term S_{ph} in Equation (1.1) and the corresponding photo-electron concentration scale in $1/N^3$ in terms of maximum value but the photoionization radiation spreads on distances inversely proportional to the density N.

However, as will be discussed in chapters 2 and 3, as in this work we study repetitive discharges, at 1000 K a significant amount of seed charges may be present at the beginning of a given voltage pulse due to previous pulses. Then we have observed that the photoionization source term has a small influence on the discharge dynamics studied in this work at 1000 K.

1.6 Optical emission of streamer discharges in air

Streamers are fast transient phenomena with highly non-homogeneous electric-field distributions and large variations of densities of charged and excited species. Usually in the simulation of discharges, we solve Equations (1.1) and we present results as 2D evolutions of the electron density and of the absolute value of the electric field. However, to compare with experiments, it is interesting to compute the optical emission of the discharge.

The emission of a streamer discharge in air at atmospheric pressure in the visible spectrum is usually considered to be dominated by the emission from the first and the second positive bands of nitrogen, and the first negative bands of the nitrogen ion N_2^+:

$$N_2(B^3\Pi_g) \rightarrow N_2(A^3\Sigma_u^+) + h\nu \tag{1.16}$$

$$N_2(C^3\Pi_u) \rightarrow N_2(B^3\Pi_g) + h\nu \tag{1.17}$$

$$N_2^+(B^2\Sigma_u^+) \rightarrow N_2^+(X^2\Sigma_g^+) + h\nu \tag{1.18}$$

The evolution of the concentrations $[N_2(B^3\Pi_g)]$, $[N_2(C^3\Pi_u)]$ and $[N_2^+(B^2\Sigma_u^+)]$ is given by a system of three ODEs of the form of Equation (1.10). We have included these ODE in the discharge code and these equations are solved explicitly with a fourth order Runge-Kutta time integration scheme. It is important to note that Equation (1.10) for excited states is solved simultaneously with the streamer equations. This gives a full time-dependent solution of optical emissions in the modelling of the streamer processes. All coefficients for the three band systems are taken from *Liu and Pasko* [2004] and *Bonaventura et al.* [2011].

The experimentally detected intensities of light for the three bands are directly proportional to the radiative deexcitation rates of the excited states [*Kozlov et al.*, 2001]:

$$I_k = T_k A_k n_k, \tag{1.19}$$

where k is one of the three excited species $N_2^*(k)$, $A_{N_2^*(k)}$ is the Einstein coefficient of the excited specie $N_2^*(k)$ and T_k is a transmission coefficient, which depends on the characteristics of the optical system and the sensitivity of the detector. In this work, we assume that the transmission coefficients T_k for the three studied bands are equal to 1. The number of photons emitted per second from a volume element $\delta V^i = 2\pi r^i \delta z^i \delta r^i$, where r^i is radial distance and δz^i and δr^i are the axial and radial sizes of cell i, is

$$N^i_{ph,k} = A_k n_k \delta V^i. \tag{1.20}$$

If the discharge is observed along a line of sight, the measured optical emission intensity of each band at a given time is given by:

$$\Psi_k = 10^{-6} \int_{\mathcal{L}} I_k \, dl, \tag{1.21}$$

where I_k is in $cm^{-3}s^{-1}$, l is in cm and the intensity Ψ_k is in Rayleighs, and the integration is performed along the optical path $\mathcal{L}$. In this paper, as in *Pasko* *et al.* [1997] and *Liu and Pasko* [2004], the effects of radiative transfer between the source of the emission and the observer are not taken into account. In Equation (1.21), the intensity, I_k, is an axially symmetric function of cylindrical radius $f(r)$. Then to calculate the intensity Ψ_k for a horizontal line of sight (namely a line perpendicular to the discharge axis), it is necessary to perform the integration in Equation (1.21) taking into account the radial profile of I_k; this is the classical direct Abel's transformation. The emission of each band can then be time integrated on the duration of the camera gates used in experiments for fast-camera imaging of discharges in ambient air (typically 1-2 ns).

1.7 Energy of the discharge

In Chapter 3.3, we will study the influence of the preionization level on the energy released in the discharge. The Poynting's theorem is given by:
The Poynting's theorem is given by:

$$\partial_t(u) + \vec{\nabla} \cdot (\vec{\Pi}) = -\vec{j_c} \cdot \vec{E} \tag{1.22}$$

with

$$u = \frac{1}{2}\epsilon_0 E^2 + \frac{1}{2}\frac{B^2}{\mu_0} \qquad\qquad \vec{\Pi} = \frac{\vec{E} \times \vec{B}}{\mu_0} \tag{1.23}$$

where $\vec{E}$ is the electric field, $\vec{B}$ is the magnetic field, $\vec{\Pi}$ is the Poynting vector, u is the electromagnetic energy density and $\vec{j_c}$ is the current density. According to this theorem, the total volumic power of the plasma discharge going to the matter is $\vec{j_c}.\vec{E}$.
Then, by integrating over time the right hand side term of Equation (1.22) we can compute the total energy density $e_\mathrm{J}(t)$ given by the plasma discharge to the matter:

$$e_\mathrm{J}(t) = \int_0^t \vec{j_c} \cdot \vec{E}\mathrm{d}t \tag{1.24}$$

By integrating Equation (1.24) over the volume of the simulation domain V one can obtain the total energy E_J of the discharge as a function of time:

$$E_\mathrm{J}(t) = \iiint_V e_\mathrm{J}(t)\mathrm{d}\tau \tag{1.25}$$

Chapter 2

Discharge dynamics during one nanosecond voltage pulse

Some results of this chapter has been published in *Tholin and Bourdon* [2011]; *Tholin et al.* [2011].

2.1 Introduction

As mentioned in the introduction, in the experimental study of nanosecond repetitively pulsed discharges in air between two point electrodes in the temperature range of 300 to 1000 K at atmospheric pressure [*Pai et al.*, 2010a], three different discharge regimes have been observed: corona, glow and spark regimes. It is interesting to note that corona and spark discharge regimes were easily obtained under almost all experimental conditions, whereas the glow regime often existed only over a limited range of the conditions. For a 10 ns voltage pulse with a repetition frequency of 30 kHz, a 5 mm gap between point electrodes with a radius of curvature of about 200 μm, *Pai et al.* [2010a] have been able to generate the NRP glow discharge from 750 to 1000 K. Very recently, for a frequency of 1 kHz, a 5 mm gap between point electrodes with a radius of curvature of about 50 μm, a glow regime has been observed at 300 K [*Tholin et al.*, 2011]. *Pai et al.* [2010a] have studied the influence of different parameters (applied voltage, pulse repetition frequency, gas temperature, interelectrode gap distance and radius of curvature of electrodes) on the different discharge regimes.
As a first step to compare with experiments, in *Celestin et al.* [2009] and *Bourdon et al.* [2010], a single discharge in air occurring during one of the nanosecond voltage pulses at 1000 K between two hyperboloid electrodes with a radius of curvature $R_\mathrm{p} \simeq 300\,\mu\mathrm{m}$ and separated by 5 mm has been simulated. It was shown that the early stages of the development of the discharge consist of positive and negative streamers propagating from the anode and the cathode, respectively. After the interaction of both discharges, the positive streamer

propagates very rapidly towards the cathode in the volume pre-ionized by the negative streamer. In *Celestin et al.* [2009] and *Bourdon et al.* [2010], simulations have been carried out assuming a constant applied voltage. To be closer to experiments [*Pai et al.*, 2010a], in this chapter, we have modeled the steep voltage rise in 5 ns and then the voltage plateau in the range 5 to 15 kV using a sigmoid function. In the experiments, the duration of the voltage plateau is of about 10 ns followed by a steep decrease in 5 ns. In the following sections, we propose to simulate the discharge dynamics until the end of the voltage plateau and to discuss the different discharge structures obtained before the voltage decrease. The objective of this chapter is to identify in the simulations, the three discharge regimes observed in the experiments and then to compare the conditions of existence of these different regimes in the simulations and in the experiments at $T_{\mathrm{g}} = 300$ and 1000 K.

As in *Celestin et al.* [2009] and *Bourdon et al.* [2010], in this chapter, we simulate a single discharge in air occurring during one of the nanosecond voltage pulses using the 2D discharge model presented in Section 1.2.

As many discharges have occurred before the simulated one, as in *Celestin et al.* [2009] and *Bourdon et al.* [2010], we have estimated a uniform density of seed positive ions and electrons of 10^{-9} cm^{-3} for $\mathrm{T_g}$=300 and 1000 K at the end of a given interpulse after many voltage pulses. Furthermore, we have neglected the influence of photoionization. In Chapter 3, we will study in detail the dynamics of charged species during the interpulses and validate a posteriori these hypotheses for NRPD in the frequency range 1-10 kHz.

In Section 2.2, we propose to study the discharge dynamics at 1000 K and in Sections 2.3 to 2.6, we carry out a detailed parametric study in varying the applied voltage, the size of the interelectrode gap and the radius of curvature of hyperboloid electrodes. Then in Section 2.7 we study the discharge dynamics at 300 K and finally, in Section 2.8, we compare experimental and numerical images of the discharge dynamics at 300 K.

2.2 Discharge dynamics at T_{g} =1000 K

In this section, as a reference test-case for the parametric study, we first simulate the discharge dynamics at T_{g} = 1000 K for an applied voltage of 5 kV, a 5 mm gap and point electrodes with a radius of curvature of $R_{\mathrm{p}} = 50\,\mu$m. Figure 2.1 shows the time sequence of the distributions of the absolute value of the electric field and of the electron density at t =10, 12 and 14 ns. The dynamics of the discharge is essentially the same as the one obtained with a constant applied voltage and electrodes with $R_{\mathrm{p}} = 300\,\mu m$ in *Bourdon et al.* [2010] with a positive streamer and a negative streamer propagating from the anode and cathode, respectively. After the interaction of both streamers, the positive streamer propagates very rapidly towards the cathode in the volume pre-ionized by the negative discharge. On Figure 2.1, we note that the magni-

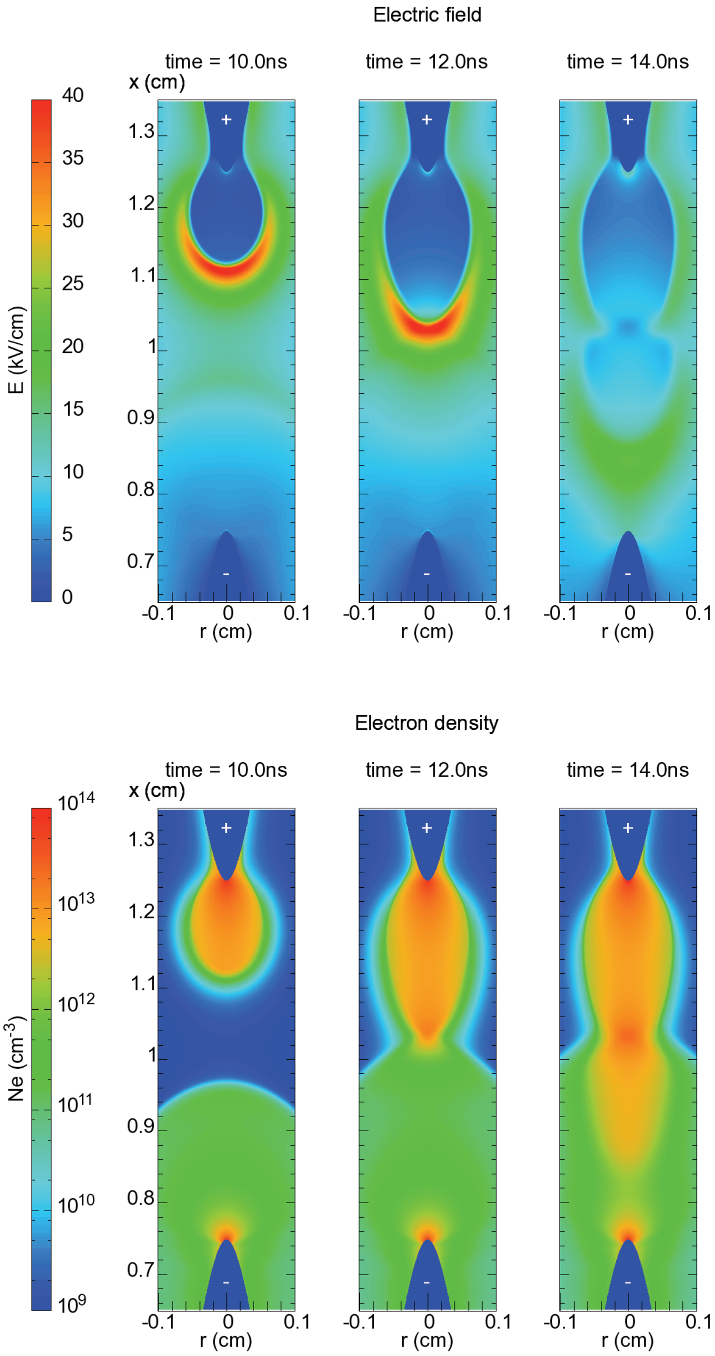

Figure 2.1: *Dynamics of the discharge at* $T_\mathrm{g} = 1000$ *K for an applied voltage of 5 kV, a 5 mm gap and point electrodes with* $R_\mathrm{p} = 50\,\mu m$*. Cross-sectional views of the magnitude of the electric field and the electron density at* $t = 10$*, 12 and 14 ns.*

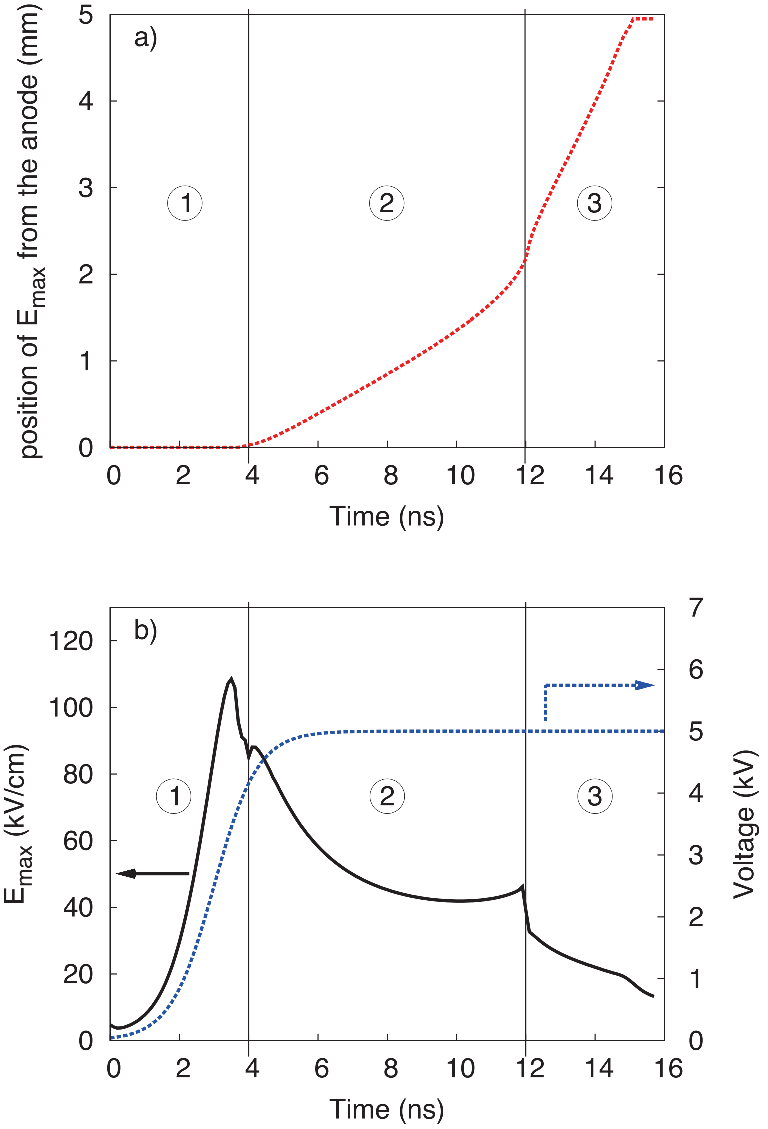

Figure 2.2: *Time evolutions of the position of the maximum electric field* $E_{\max}$ *along the axis of symmetry (a) and of the value of* $E_{\max}$ *and the applied voltage (b) for the same conditions as Figure 2.1.*

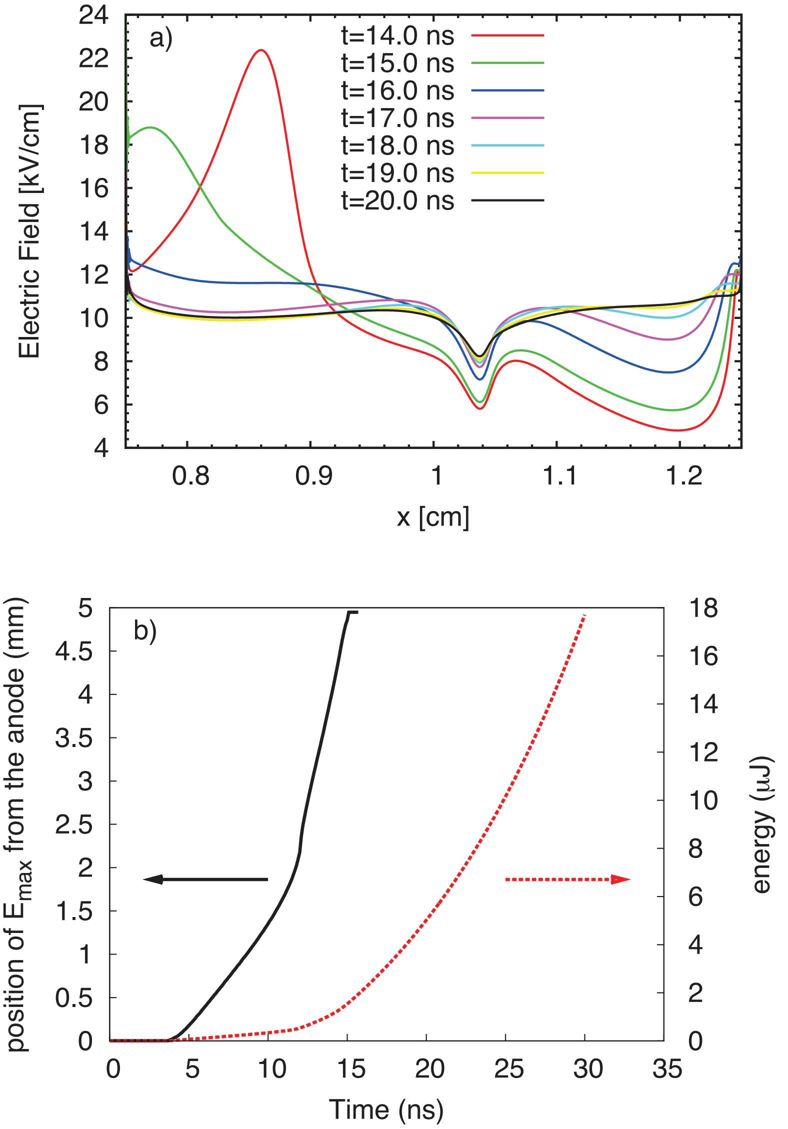

Figure 2.3: *Time evolutions of the value of the electric field along the axis of symmetry after the connection of both discharges (a) and of the energy* e_{J} *given by Eq. (1.25) and the position of* $E_{\max}$ *(b) for the same conditions as Figure 2.1. The tip of the cathode is located at* $x_{\mathrm{C}} = 0.75$ *cm, and the tip of the anode is at* $x_{\mathrm{A}} = 12.5$ *mm.*

tude of the electric field in the negative front is less than in the positive one. Then, the position of E_{max}, the maximum of the magnitude of the electric field on the symmetry axis, corresponds to the position of the positive discharge front. For the conditions of Figure 2.1, Figure 2.2 (a) shows the time evolution of the position of E_{max} and Figure 2.2 (b) shows the time evolutions of E_{max} and of the applied voltage. As mentioned in Section 2.1, the applied voltage increases and then is constant for $t > 5$ ns. In this chapter, the value of the voltage plateau is referred to as the applied voltage.

On Figure 2.2, three phases are observed. During the first phase, the peak electric field is first increasing due to the increase of the applied voltage and starts to decrease at t =3 ns due to the space charge formation close to the anode tip. At around t =4 ns, before the maximum of the applied voltage, the positive discharge starts to propagate. The second phase corresponds to the propagation of the positive discharge from t =4 to 12 ns. Figure 2.2 shows that the velocity of the positive discharge is almost constant during its propagation and is about 275 km s^{-1}. After the start of the propagation, the peak electric field in the positive discharge front decreases as the discharge escapes from the high Laplacian field region close to the point and stabilizes around 40 kV cm^{-1} in the gap. We have checked that this value corresponds to the peak electric field in the head of a stationary positive streamer propagating in a weak field in air at P_{atm} and T_{g}=1000 K. At P_{atm} and T_{g}=300 K, the peak electric field in the head of a stationary positive streamer propagating in a weak field in air is about 120 kV cm^{-1} [*Kulikovsky*, 1998]. As expected from similarity relations [*Liu and Pasko*, 2006], the peak electric field in the head of a stationary positive streamer propagating in a weak field in air at P_{atm} is N_{300}/N_{1000} times less at T_{g}=1000 K than at T_{g}=300 K.

Just before t =12 ns, Figure 2.2 (b) shows that the maximum electric field in the positive discharge front increases slightly due to the influence of the negative discharge. At t =12 ns, the two discharges are impacting each other almost at the middle of the gap, and then the positive discharge propagates very rapidly towards the cathode in the volume pre-ionized by the negative discharge (phase 3). After the connection, as shown by Figure 2.2 (a), the positive discharge propagates with a constant velocity about three times faster than before connection ($\sim$900 km s^{-1}). We note that the maximum electric field is linearly decreasing during this third phase until the discharge reaches the cathode at t =15 ns. Figure 2.3 (a) shows the time evolution of the axial electric field on the symmetry axis after the connection of both discharges from t =14 to 20 ns. We note that the electric field becomes rapidly rather uniform in the inter-electrode gap and converges towards the average electric field in the gap $E_{\mathrm{gap}} \simeq 10$ kV cm^{-1} for 5 kV applied on a 5 mm gap, which is the breakdown field for P_{atm} and T_{g}=1000 K. Figure 2.3 (b) shows the energy e_{J} derived from the time integrated Joule heating term (Eq. (1.24)) as a function of time. We note that this energy remains very low during the discharge propagation in the gap and starts to increase exponentially for $t > 15$ ns in the conduction phase, after the arrival of the positive streamer at the cathode.

As already mentioned, experimentally, three different discharge regimes (corona, glow and spark) have been observed as the voltage increases with a fixed duration of the voltage pulse [*Pai et al.*, 2009, 2010a]. In the following sections, we will study the influence of the applied voltage on the discharge dynamics. In this section, we first study the influence of the pulse duration on the discharge structure.

For an applied voltage of 5 kV, Figure 2.1 shows that up to t =12 ns, the two discharges are separated and then the emission of the discharge is located in two spots close to the point electrodes [*Bourdon et al.*, 2010]. Then with a voltage pulse duration less than 12 ns, Figure 2.1 shows that for an applied voltage of 5 kV a corona regime is obtained. After the connection of both discharges, the emission of the discharge fills the gap and then for a voltage pulse duration of about 12 ns, a discharge in the glow regime is observed. In the following, the time necessary to have the connection between the discharges will be called the connection time. It represents the minimal duration of the pulse to have the corona to glow transition in given voltage and geometry conditions. For $t > 12$ ns, Figure 2.1 shows that a high electron density plasma channel is formed between the two electrodes with an average field which is equal to the breakdown field at T_{g}=1000 K (Figure 2.3 (a)). As shown by Figure 2.3 (b), for voltage pulse durations longer than 12 ns, the conductivity of the plasma channel increases and then the discharge may start heating the gas, leading to the glow to spark transition. Then, from the simulation results, it seems that one key parameter for the transition between these three discharge regimes is the ratio between the connection time of the discharge and the pulse duration. If this ratio is less than 1, the pulse duration is too short for the discharges to connect and then it corresponds to the corona regime. If this ratio is around 1, the plasma discharge has just the time to fill the interelectrode gap and then this corresponds to the glow regime. Finally, if this ratio is larger than 1, the discharge may heat the gas and then the glow-to-spark transition may occur.

Then, to study more in detail the conditions to obtain the different discharge regimes, in the following sections we propose to study the influence of the geometry, gas temperature and applied voltage on the connection time.

2.3 Influence of the applied voltage on the discharge dynamics at T_{g}=1000K

In experiments, it is generally easier to vary the value of the applied voltage than any geometrical parameter. Therefore *Pai et al.* [2010a] have studied in detail the voltage conditions to obtain the glow regime at T_{g}=1000 K. These authors have put forward that two conditions have to be fulfilled: the first one is to apply a sufficiently high voltage to ensure the ignition of the discharge at the point electrodes and the second one is to have an electric field equal at least

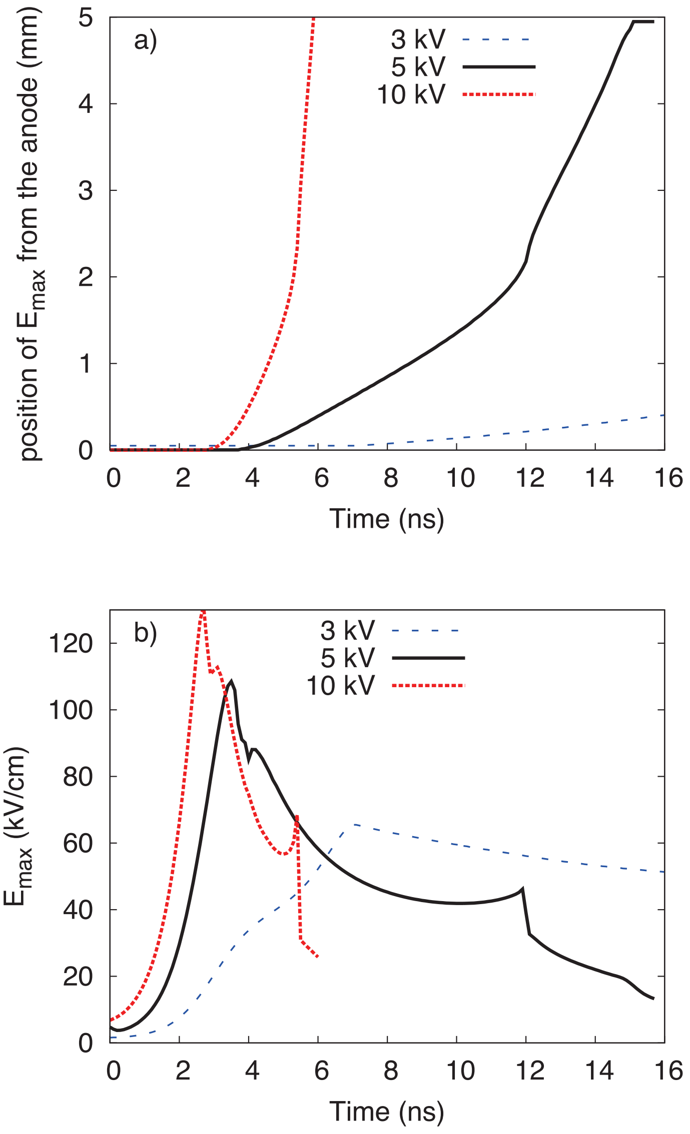

Figure 2.4: *Influence of the applied voltage on the time evolutions of the position of the maximum electric field* $E_{\max}$ *(a) and the value of* $E_{\max}$ *(b) along the axis of symmetry for* $T_g = 1000$ *K,* R_p*=50* μ*m and a 5 mm gap.*

to the breakdown field in the gap to maintain a discharge during the conduction phase. In our simulations, we also found that there is a minimal voltage to be applied for a given pulse duration to have the ignition and propagation of both discharges until the connection. At T_{g}=1000 K, with R_{p}=50 μm, a 5 mm gap and a voltage pulse duration of about 10 ns, as shown on Figures 2.1 and 2.2, this minimal voltage is about 5 kV, which is very close to experimental results. Figure 2.4 shows the time evolutions of the position of the positive discharge front, and of the value of the peak electric field in the positive discharge front E_{max} for three different values of the applied voltage: 3, 5 and 10 kV. In the point-to-point geometry studied in this work, after the voltage rise, the minimal external Laplacian field $E_{\mathrm{L,min}}$ is obtained in the middle of the gap by symmetry. As the applied voltage increases from 3 to 10 kV, we have noted that $E_{\mathrm{L,min}}$ increases from 2.2 to 4.8 kV cm^{-1}. For 3 kV, Figure 2.4 shows that the positive streamer starts to propagate at about 8 ns instead of 4 ns for the 5 kV case, with a velocity almost ten times less than for the 5 kV case. On Figure 2.4 (b), we note that for 3 kV the peak electric field increases slowly and is only of about 60 kV cm^{-1} at t =8 ns, the moment when the discharge starts propagating in comparison to about 90 kV cm^{-1} at t =4 ns for the 5 kV case. For $t > 8$ ns for 3 kV, the peak electric field slowly decreases towards 40 kV cm^{-1}. It is interesting to note that the slowly propagating discharge obtained for 3 kV corresponds to an average field in the gap of $E_{\mathrm{gap}} \simeq 6$ kV cm^{-1}, less than the breakdown field. Finally, as observed in the experiments, our simulation results show that for an applied voltage of 3 kV and a voltage pulse duration of about 10 ns, the obtained discharge is in the corona regime. For an applied voltage of 5 kV, we have shown in the previous section that after the connection, the electric field in the gap rapidly converges towards the value of the breakdown field which is the average field in the gap in these conditions (Figure 2.3 (a)). For voltages higher than 5 kV, as for example for 10 kV, Figure 2.4 shows that the ignition time is only slightly decreased as the voltage increases. Indeed, as the rise time is the same for all applied voltages, higher voltage values are obtained earlier for higher applied voltages which results in a small reduction of the ignition time as the applied voltage increases. Conversely, Figure 2.4 shows that the increase of voltage by a factor 2 between 5 and 10 kV, decreases the connection time from 12 to 5 ns, that is to say by more than a factor 2. The average velocity of the positive discharge before connection is about 910 km s^{-1} for the 10 kV case, that is to say about 3.3 times higher than for 5 kV and then the time of arrival of the positive discharge at the cathode is only of about 6 ns at 10 kV instead of about 15 ns at 5 kV. After connection, the velocity of the discharge is 5.5 times faster for 10 kV than for 5 kV and the ratio between the velocity before and after connection is around 3.3 at 5 kV and 5.3 for 10 kV.

On Figure 2.4 (b), we note that for 10 kV the peak electric field is of about 110 kV cm^{-1} at the moment when the discharge starts propagating in comparison to about 90 kV cm^{-1} for the 5 kV case. Then for 10 kV, the peak electric field rapidly decreases and as the propagation is very fast, the electric field in the positive streamer head is about 60 kV cm^{-1} at the connection time. For 10 kV applied on a 5 mm gap, the average electric field in the gap is $E_{gap} \simeq 20$ kV cm^{-1} which is higher than the breakdown field at T_g=1000 K. Then for an applied voltage of 10 kV and a pulse duration of about 10 ns, after the fast propagation of the discharge in the gap in less than 6 ns, the discharge may heat the gas and then the glow to spark transition may occur.

2.4 Influence of the gap on the discharge dynamics at T_g=1000 K

First it is interesting to note that from an electrostatic point of view, as the point-to-point geometry is symmetric, in the simulations, the electric field in the middle of the gap depends strongly on the gap distance whereas the electric field near the tip is primarily determined by the radius of curvature of the tip R_p. If the gap is widened, the Laplacian electric field near the electrode tips of fixed radius of curvature R_p decreases less than it does in the middle of the gap.

Figure 2.5 shows the time evolutions of the position of the positive discharge front, and of the value of E_{max} for two different values of the gap: 2.5 and 5 mm. As the gap increases from 2.5 to 5 mm for the same applied voltage, we have noted that the minimal value of the Laplacian field in the middle of the gap $E_{L,min}$ decreases from 8 to 3.8 kV cm^{-1}. As expected, Figure 2.5 shows that as the gap increases, the time necessary for the connection also increases. We note that the connection time increases by a factor 2 as the gap increases from 2.5 to 5 mm. Conversely, it is interesting to note that the ignition time is the same for both gaps and then the discharge velocities are very different. For the 2.5 mm gap, the velocity is 450 km s^{-1} before connection, which is 1.6 times faster than with the 5 mm gap. After connection, the velocity is 3.5 times faster with the 2.5 mm gap in comparison to the 5 mm gap, and for the 2.5 mm gap, the velocity of the discharge increases by a factor 7 between before and after the connection.

It is interesting to note on Figure 2.5 (b) that the peak electric field in the positive streamer head is almost the same for both gaps and decreases after connection to the average electric field in the gap E_{gap}=20 kV cm^{-1} for 2.5 mm and 10 kV cm^{-1} for 5 mm. Then, decreasing the gap from 5 to 2.5 mm decreases the connection time by a factor 2 and increases the average electric field in the gap to values higher than the breakdown field at T_g=1000 K. Then for R_p=50 μm, an applied voltage of 5 kV with a pulse duration of 10 ns, the glow regime may be obtained for a gap of 5 mm and a spark regime for 2.5 mm. These results are in good agreement with experiments [*Pai et al.*, 2010a].

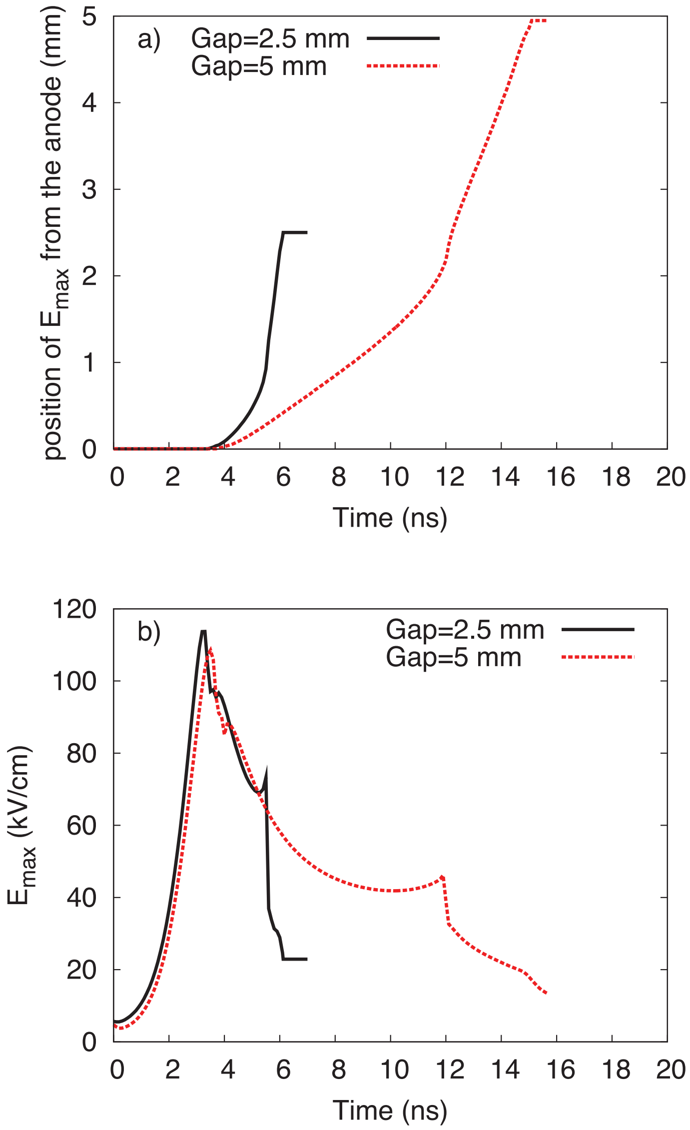

Figure 2.5: *Influence of the gap on the time evolutions of the position of the maximum electric field* $E_{\max}$ *(a) and the value of* $E_{\max}$ *(b) along the axis of symmetry for* $T_g =$ *1000 K,* R_p*=50* μ*m and an applied voltage of 5 kV.*

2.5 Influence of the radius of curvature of the point electrodes on the discharge dynamics at $T_{\rm g}$=1000K

Figure 2.6 shows the time evolutions of the position of the positive discharge front, and of the value of $E_{\rm max}$ for four different values of $R_{\rm p} = 25, 50, 100$ and 300 μm for $T_{\rm g}$=1000 K, an applied voltage of 5 kV and a 5 mm gap. For the same applied voltage, as the radius of curvature of electrodes increases from 25 to 300 μm, we have noted that the minimal value of the Laplacian field in the middle of the gap $E_{\rm L,min}$ increases from 3.2 to 5.2 kV cm^{-1} and the peak value of the electric field at the point electrodes decreases. As the ignition of the discharge depends on the value of the Laplacian electric field close to the point electrodes, Figure 2.6 shows that as the radius of curvature increases, the ignition time of the discharge increases. Then, Figure 2.6 shows that as $R_{\rm p}$ increases from 25 μm to 300 μm, the average discharge velocity decreases from 275 km s^{-1} to 190 km s^{-1} before connection and from 900 to 665 km s^{-1} after connection. It is interesting to note that the connection time increases only by a factor 1.2 as the radius of curvature of the point electrodes increases by a factor 6 from $R_{\rm p}$ = 50 to 300 μm. Figure 2.6(b) shows that, just before connection, for all studied values of $R_{\rm p}$, the maximum electric field in the positive discharge front reaches a value of about 40 kV cm^{-1}. As mentioned in the previous section, this value corresponds to the peak electric field in the head of a stationary positive streamer propagating in a weak field in air at $T_{\rm g}$=1000 K. Then it is interesting to note that, for a positive streamer starting its propagation with a higher peak electric field as for $R_{\rm p} = 50\,\mu$m, Figure 2.6 shows that the peak electric field decreases during the streamer propagation to reach the value of about 40 kV cm^{-1}. Conversely for $R_{\rm p} = 300\,\mu$m, the peak electric field in the streamer head is lower than 40 kV cm^{-1} as it starts propagating and then the peak electric field increases during the discharge propagation to reach this value.

To study more in detail the influence of $R_{\rm p}$ on the discharge structure, Figure 2.7 shows the distributions of the absolute value of the electric field and of the electron density at t =11.5 ns for $R_{\rm p}$ = 50 and 300 μm. As already observed on Figure 2.6, the velocity of the discharge decreases as the radius of curvature increases. Furthermore, Figure 2.7 shows that the radial expansion of the positive streamer close to the point increases as $R_{\rm p}$ decreases, due to the increase of the radial component of the Laplacian field close to the point as $R_{\rm p}$ decreases. Figure 2.7 shows that the radius of the positive streamer is varying during its propagation for $R_{\rm p} = 50\,\mu$m whereas it remains constant for $R_{\rm p} = 300\,\mu$m. Finally, after connection, Figure 2.6 shows that for all values of $R_{\rm p}$ the electric field converges towards the average electric field in the gap $E_{\rm gap}$ =10 kV cm^{-1}.

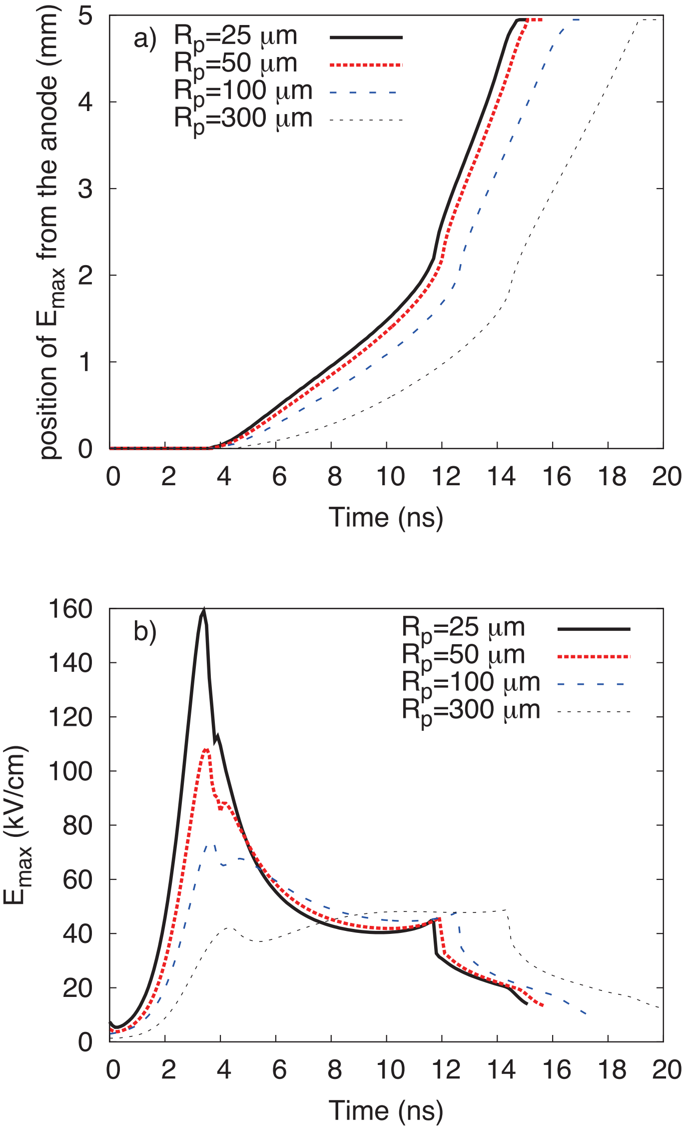

Figure 2.6: *Influence of the radius of curvature of point electrodes* R_{p} *on the time evolutions of the position of the maximum electric field* $E_{\max}$ *(a) and the value of* $E_{\max}$ *(b) along the axis of symmetry for* $T_{\mathrm{g}} = 1000$ *K, an applied voltage of 5 kV and a 5 mm gap.*

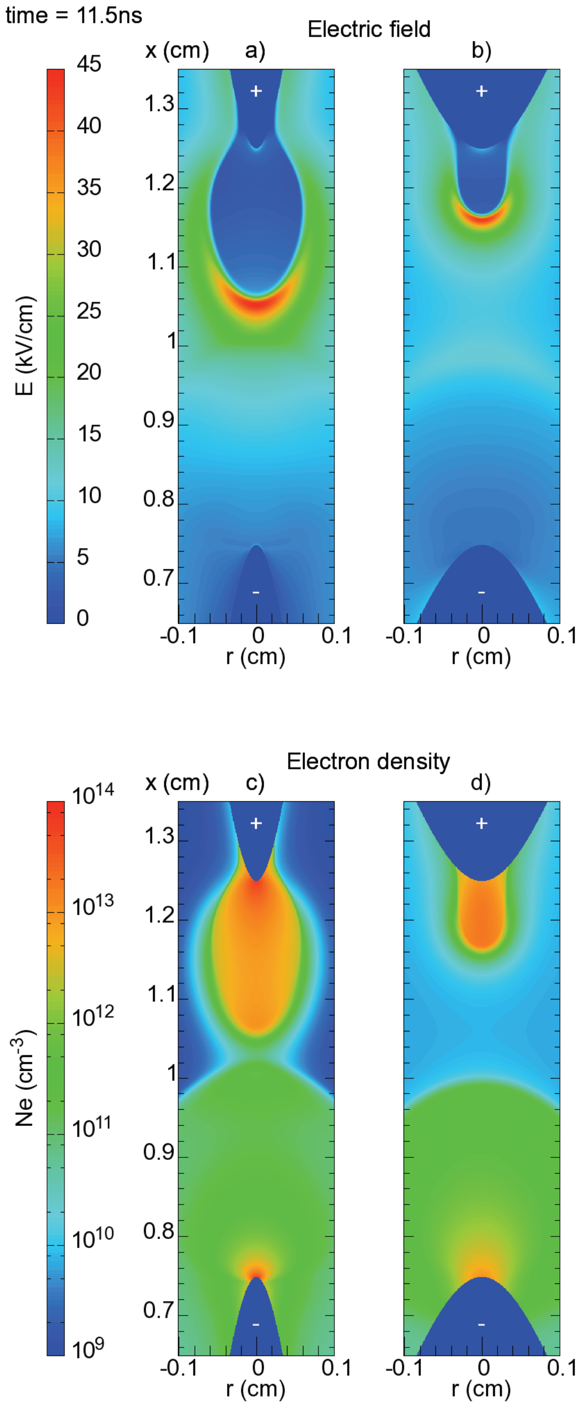

Figure 2.7: *Influence of the radius of curvature of point electrodes* R_p *on cross-sectional views of the magnitude of the electric field (left) and the electron density (right) for* R_p*=50* μ*m ((a) and (c)) and* R_p*=300* μ*m ((b) and (d)) at* t *=11.5 ns for* $T_\mathrm{g} = 1000$ *K, an applied voltage of 5 kV and a 5 mm gap.*

2.6 Summary of the results of the parametric study carried out at T_g=1000 K

Table 2.1 summarizes the results obtained in the preceding sections on ignition and connection times, discharge velocity before and after connection and values of E_{gap} and $E_{L,min}$. We note that at T_g=1000 K, the ignition time of the positive discharge depends mostly of the applied voltage and is almost independent of the gap and the radius of curvature of electrodes. As expected, the ignition time increases as the the applied voltage decreases. We also note that the connection time increases as the applied voltage decreases and the gap increases and is even almost proportional to these quantities in the range of conditions studied in this work. Conversely, the radius of curvature of electrodes has a smaller effect on the connection time and slightly decreases as the radius of curvature of electrodes decreases. For all the studied conditions, we have found that the peak electric field in the positive streamer head converges during its propagation towards 40 kV cm^{-1}, which corresponds to the peak electric field in the head of a stationary positive streamer propagating in a weak field in air at P_{atm} and T_g=1000 K.
In agreement with experiments, in our simulations we have observed that there is a minimal voltage to be applied for a given pulse duration to have the ignition of the discharges and a stable propagation of both discharges until the connection. At T_g=1000 K, with R_p=50 μm, a 5 mm gap and a voltage pulse duration of about 10 ns, this minimal voltage is about 5 kV, which is very close to experimental results.

R_p (μm)	50	50	50	50	25	100	300
Applied Voltage (kV)	5	5	10	3	5	5	5
Gap (mm)	2.5	5	5	5	5	5	5
Ignition time (ns)	4	4	3	8	4	4	5
Connection time (ns)	6	12	5	-	12	13	14.5
Velocity before connection (km s^{-1})	450	275	913	37.5	275	235	190
Velocity increase after connection	7	3.3	5.3	-	3.3	3.3	3.5
E_{gap} (kV cm^{-1})	20	10	20	6	10	10	10
$E_{L,min}$ (kV cm^{-1})	8	3.8	4.8	2.2	3.2	4.2	5.2

Table 2.1: *Discharge characteristics at T_g =1000 K for different applied voltages, gaps and values of R_p*

In *Pai et al.* [2010a], they have also considered that to have a glow regime at T_g=1000 K, the electric field in the gap during the conduction phase has to be at least equal to the breakdown field, which is 10 kV cm^{-1} for P_{atm} and T_g=1000 K. For all the conditions studied in this work, we have found that after the connection of positive and negative discharges, the electric field becomes

rather uniform in the gap and converges towards E_{gap} the average electric field for the given applied voltage and gap size.
In our simulations, we have noted that if E_{gap} is less than the breakdown field, the ignition time of the positive discharge increases significantly and the velocity of the discharge decreases. Then, for a voltage pulse duration of about 10 ns used in the experiments [*Pai et al.*, 2010a], we have noted that for conditions with an average electric field in the gap less than the breakdown field, the discharge remains in the corona regime. In our simulations, if E_{gap} is equal or higher than the breakdown field, we have noted that the conductivity of the plasma channel obtained after the positive streamer arrival at the cathode increases rapidly and then the discharge may start heating the gas, leading to the glow to spark transition. For these conditions, to obtain the glow regime, it is important that the connection time of the discharge be almost equal to the duration of the voltage pulse. In this case, the discharge has just the time to fill the interelectrode gap and no heating is observed. If the voltage pulse duration is longer than the connection time of the discharge, the discharge may heat the gas and then the glow-to-spark transition may occur.

2.7 Discharge dynamics at $T_{\mathrm{g}} = 300$ K

In this section, we simulate the discharge dynamics at $T_{\mathrm{g}} = 300$ K for the same geometry as in Figure 2.1. As the gas density increases by a factor N_{300}/N_{1000} of about 3 between $T_{\mathrm{g}} = 300$ K and 1000 K, we have checked that the minimal applied voltage to have the ignition of the discharges and a stable propagation of both discharges until the connection for a voltage pulse duration of about 10 ns is 15 kV at 300 K, that is to say 3 times the minimal voltage at 1000 K. For an applied voltage of 15 kV, Figure 2.8 shows the time sequences of the distributions of the absolute value of the electric field and the electron density at t =6.7, 7.7 and 8.7 ns for an interelectrode gap of 5 mm, an applied voltage of 15 kV and point electrodes with $R_{\mathrm{p}} = 50\,\mu$m. It is interesting to note that the discharge structure at T_{g} =300 K is very close to the one obtained in Figure 2.1 at T_{g} =1000 K for an applied voltage of 5 kV with almost similar radial expansions of positive and negative streamers and their connection almost in the middle of the gap. However, due to the different gas densities, we note that the electric field and the electron density in the streamer heads are almost 3 times and one order of magnitude, respectively, higher for $T_{\mathrm{g}} = 300$ K than for $T_{\mathrm{g}} = 1000$ K. These results are in agreement with scaling laws of streamer properties with change of gas density N with the peak electric scaled as $\sim N$ and the electron density scaled as $\sim N^2$ [*Liu and Pasko*, 2006]. For the conditions of Figure 2.8, Figure 2.9 shows the time evolutions of the axial position of the positive discharge front and of E_{max}. As for T_{g} =1000 K, three phases are observed in the discharge dynamics. During the first phase, the peak electric field is first increasing due to the increase of the applied voltage and at about

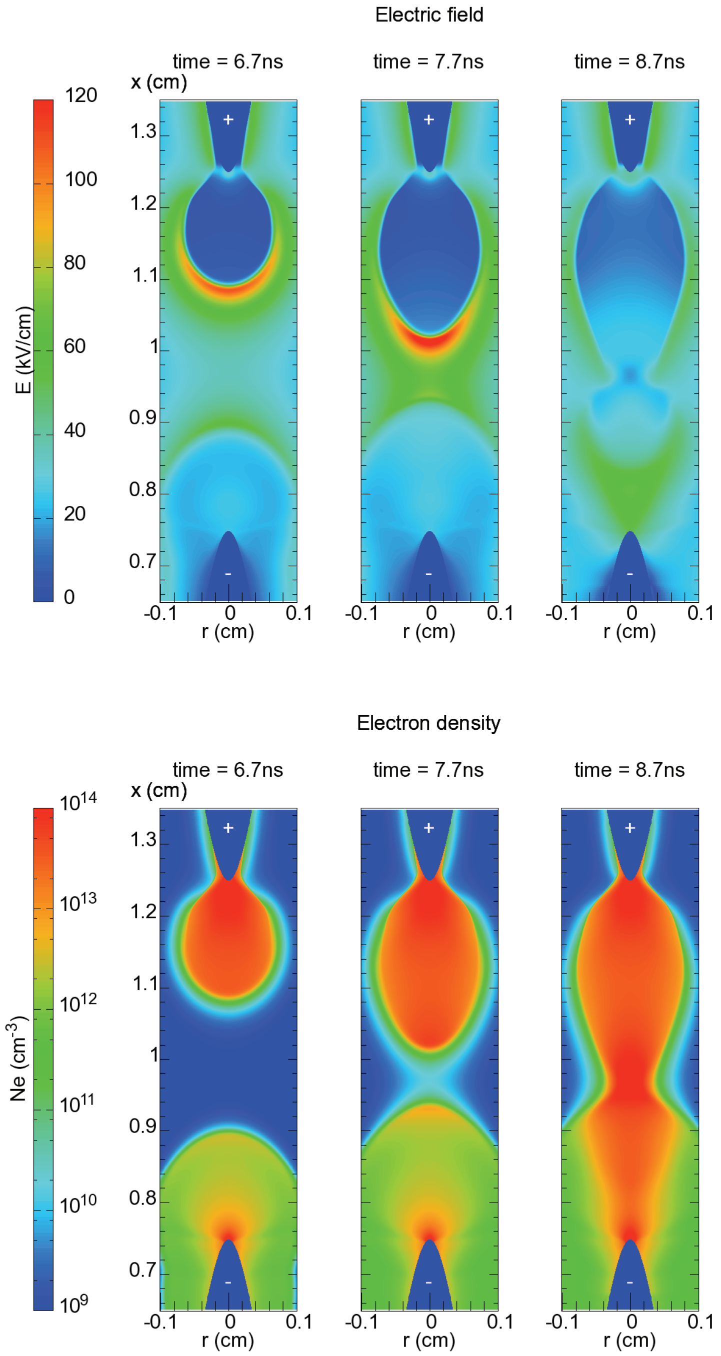

Figure 2.8: *Dynamics of the discharge at* $T_\mathrm{g} = 300$ *K for an applied voltage of 15 kV, a 5 mm gap and point electrodes with* $R_\mathrm{p} = 50\,\mu m$. *Cross-sectional views of the magnitude of the electric field and the electron density at t =6.7, 7.7 and 8.7 ns.*

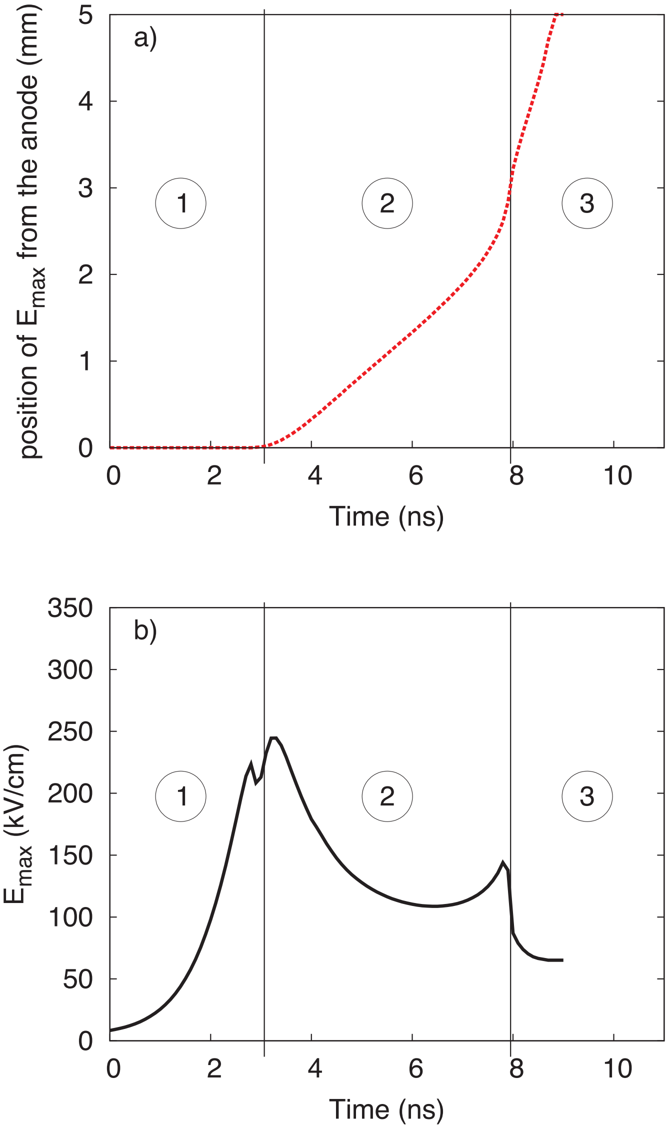

Figure 2.9: *Position of the maximum electric field* $E_{\max}$ *(a) and value of* $E_{\max}$ *(b) along the axis of symmetry as a function of time for the same conditions as Figure 2.8*

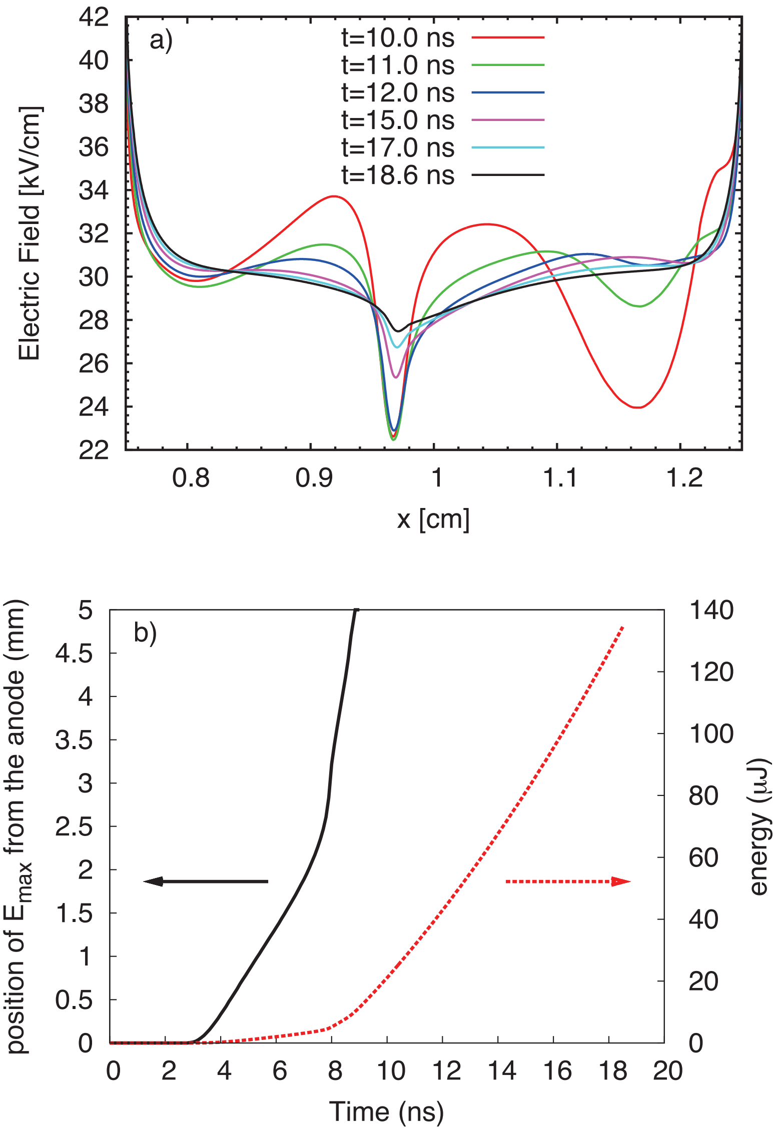

Figure 2.10: *Time evolutions of the value of the electric field along the axis of symmetry after the arrival of the positive streamer at the cathode (a) and of the energy* e_{J} *given by Eq. (1.24) and the position of* $E_{\max}$ *(b) for the same conditions as Figure 2.8. The tip of the cathode is located at* $x_{\mathrm{C}} = 0.75$ *cm, and the tip of the anode is at* $x_{\mathrm{A}} = 12.5$ *mm.*

t =3 ns, before the maximum of the applied voltage, the positive discharge starts to propagate. The second phase corresponds to the propagation of the positive discharge from t =3 to 8 ns. Figure 2.9 shows that the velocity of the positive discharge is almost constant during its propagation and is about 500 km s^{-1}. After the start of the propagation, the peak electric field in the positive discharge front decreases as the discharge escapes from the high Laplacian field region close to the point and stabilizes around 120 kV cm^{-1} in the gap, which corresponds to the peak electric field in the head of a stationary positive streamer propagating in a weak field in air at P_{atm} and T_{g}=300 K [*Kulikovsky*, 1998]. Just before t =8 ns, Figure 2.9 (b) shows that the maximum electric field in the positive discharge front increases slightly due to the influence of the negative discharge. At t =8 ns, the two discharges are impacting each other almost at the middle of the gap, and then the positive discharge propagates very rapidly towards the cathode in the volume pre-ionized by the negative discharge (phase 3). During this phase, the positive discharge propagates with a constant velocity about 4.5 times faster than before connection and the positive discharge finally reaches the cathode at t =9 ns.

Figure 2.10 (a) shows the time evolution of the axial electric field after the positive streamer arrival at the cathode from t =10 to 18.6 ns. We note that the electric field becomes rapidly rather uniform in the inter-electrode gap and converges towards the average electric field in the gap $E_{\mathrm{gap}} \simeq 30$ kV cm^{-1} for 15 kV and a 5 mm gap, which is the breakdown field for P_{atm} and T_{g}=300 K. Figure 2.10 (b) shows the energy e_{J} derived from the time integrated Joule heating term (Eq. (1.24)) as a function of time. We note that this energy remains very low during the discharge propagation in the gap and starts to increase exponentially for $t > 8$ ns in the conduction phase. At 15 ns $e_{\mathrm{J}} = 80\,\mu J$ for 15 kV and T_{g}=300 K and is only $1.6\,\mu J$ for 5 kV and T_{g}=1000 K (Figure 2.3), i.e. 50 times less. Using similarity relations *Tardiveau et al.* [2001], the Joule heating term scales as $\sim N^3$ and then for similar conditions the ratio between the Joule heating at 300 and 1000 K should be around $(N_{300}/N_{1000})^3 = 36$. As mentioned in section 1.4, for the conditions studied in this work at T_{g}=300 and 1000 K, similarity conditions are not fulfilled. If we consider a voltage pulse duration of 15 ns, Figure 2.10 (b) and Figure 2.3 (b) show that the heating of the gas may be more significant at T_{g}=300 K than at 1000 K and then the glow to spark transition may occur more easily at T_{g}=300 K than as 1000 K if the pulse duration is slightly longer than the connection time.

Then as mentioned in section 2.2 for T_{g} =1000 K, Figures 2.8 to 2.10 show that three different discharge regimes can be obtained depending on the ratio between the connection time of the discharge and the pulse duration. For an applied voltage of 15 kV, Figure 2.8 shows that with a voltage pulse duration less than 8 ns, a corona regime is obtained. After the connection of both discharges, the emission of the discharge fills the gap and then for a voltage pulse duration of about 8 ns, a discharge in the glow regime is observed. For voltage pulse durations longer than 8 ns, the conductivity of the plasma channel increases and then the discharge may start heating the gas, leading to the glow to spark transition.

For many applications as biomedical, surface treatment and decontamination, the challenge is to produce a large plasma volume at atmospheric pressure at low power with a low gas temperature and a high chemical reactivity. Therefore, in Chapter 5, we will study in detail the conditions to obtain a glow discharge in air in large interelectrode gaps at 300K with a NRP discharge.

2.8 Numerical and experimental images of the discharge dynamics at $T_{\mathrm{g}} = 300$ K

In this section, we present experimental and simulated images of the dynamics of formation of the NRP discharge in air at atmospheric pressure and at $T_{\mathrm{g}} = 300$ K. In the experimental set-up, two steel point electrodes are used in a vertical pin-pin configuration with an interelectrode gap of 5 mm. NRP discharges are produced using short-duration (10 ns) high voltage pulses at a repetition frequency of 1-30 kHz in an atmospheric pressure air flow. In *Pai et al.* [2009] positive polarity pulses were applied to the anode and the cathode was grounded. In this work, positive (+9 kV) and negative (−9 kV) pulsed voltages are applied to the anode and cathode, respectively, to avoid perturbations of the Laplacian electric potential from grounded objects around the experiment (i.e., the distribution of the Laplacian electric field at both electrode tips is symmetric). In the experiments the electrodes can be assumed to be hyperboloids with a radius of curvature of about 50 μm. For this work, images of discharges have been taken for an NRP frequency of 1 kHz in air flowing at 10 m s^{-1}, at 300 K and at atmospheric pressure. An ICCD Pimax camera 512 × 512 is used with 50 accumulations. Images are taken every nanosecond with an integration time of 2 ns.

In parallel to experiments, we have carried out discharge simulations at $T_{\mathrm{g}} =$ 300 K and atmospheric pressure using the 2D discharge model presented in Section 1.2 with the model for optical emissions presented in Section 1.6. Hyperboloid electrodes with a radius of curvature of 100 μm are considered. An electric potential difference of 15 kV is applied to electrodes with a voltage rise time of 5 ns to be close to the experimental conditions. As in previous sections, we have simulated a single discharge and then, to take into account the numerous preceding discharges, we have estimated a density of seed charges on the order of 10^9 cm^{-3}. For air discharges at atmospheric pressure the emission of the second positive (2P) system of N_2 is known to be the most intense. Then, to compare with experimental images, we have computed line-of-sight integrated 2P emission time integrated over 2 ns.

Figure 2.11 shows calculated 2P emissions ((a), (c), (e), (g)) and experimental ((b), (d), (f), (h)) images of the discharge at different times of the discharge formation. The time t_0 of the first images ((a) and (b)) is adjusted to have the

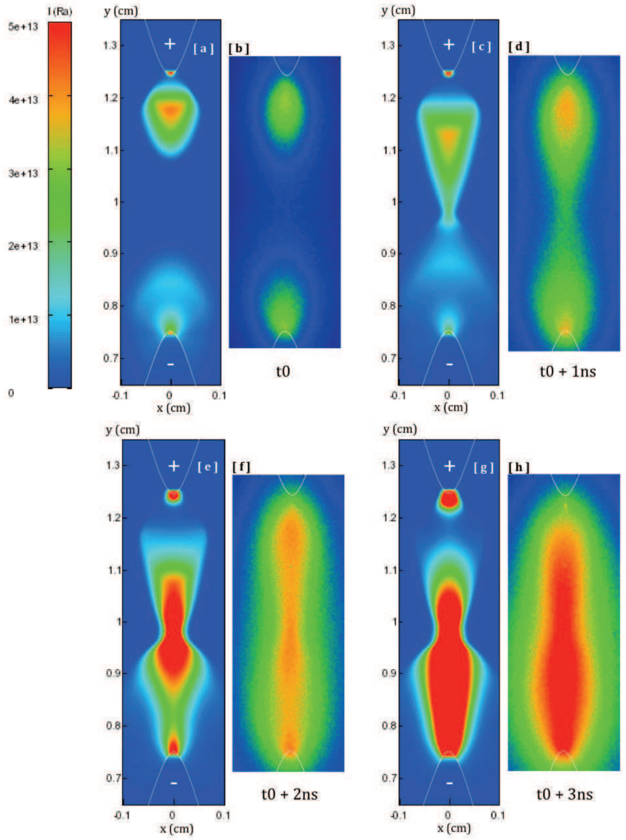

Figure 2.11: *Spatial distributions of calculated ((a), (c), (e), (g)) line-of-sight 2P emission time integrated over 2 ns and experimentally measured ((b), (d), (f), (h)) optical emission. A linear intensity scale is used for experimental and simulation results. The maximum value of the calculated intensity is* $5{\times}10^{13}$ *Rayleigh.*

best experimental/simulation agreement. Successive experimental and simulated images are obtained at a time interval of 1 ns. We note that rather good agreement is obtained between simulations and experiments during the entire duration of the discharge formation. At $t = \mathrm{t}_0$, corona discharges are observed on both electrodes with more intense emission on the anode side. At $t = \mathrm{t}_0+1$ ns, we observe the connection of both the positive and negative discharges. As both discharges have different radial extends, it is interesting that the connection area is a bottleneck that we observe on images up to $t = \mathrm{t}_0+3$ ns. After the connection, as observed in previous sections, the positive discharge rapidly propagates towards the cathode and then at $t = \mathrm{t}_0+2$ ns, Figures 2.11 (e)-(f) show an intense emission in the bottleneck region due to contribution of the two discharges, which then extends to the cathode at $t = \mathrm{t}_0+3$ ns (Figures 2.11(g)-(h)). We note that at $t = \mathrm{t}_0+3$ ns, the radial extension of the optical emission is larger on the cathode side than on the anode side.
The excellent agreement obtained between experiment and simulation on Figure 2.11 validates the dynamics of formation of the air discharge at atmospheric pressure and T_g = 300 K between two point electrodes at the early stages of its development.

2.9 Conclusion

In this chapter, we have studied the dynamics of an air discharge in a point-to-point geometry at atmospheric pressure during one voltage pulse at T_g = 300 and 1000 K. From the simulation results, it seems that one key parameter for the transition between the three discharge regimes observed in the experiments is the ratio between the connection time of the discharge and the pulse duration. If this ratio is less than 1, the pulse duration is too short for the discharges to connect and then it corresponds to the corona regime. If this ratio is around 1, the plasma discharge has just the time to fill the interelectrode gap, no heating is observed and then, this corresponds to the glow regime. Finally, if this ratio is larger than 1, the applied voltage is maintained during the conduction phase and if the electric field in the gap is higher than the breakdown field, the discharge may heat the gas and then the glow-to-spark transition may occur. We have shown that after the propagation of two streamers in the gap and their connection, the average electric field in the conducting channel between electrodes converges towards the average electric field in the gap. At T_g = 1000 K, we have found that in agreement with experimental results [*Pai et al.*, 2010a] for a 10 ns duration voltage pulse, a glow regime may be obtained if the average electric field in the gap is at least equal to the breakdown field. We have verified this criterion for gaps less or equal to 5 mm, for electrodes with radius of curvature in the range 25 to 300 μm at T_g = 1000 K for applied voltages up to 10 kV.
As for T_g=1000 K, for T_g=300 K we have observed that the conductivity of

the plasma channel obtained after the positive streamer arrival at the cathode increases rapidly. Then if the voltage pulse duration is longer than the connection time of the discharge, the discharge may start heating the gas, leading to the glow to spark transition. Between the two reference cases considered at T_{g}=300 and at 1000 K, with in both cases R_{p}=50 μm, a 5 mm gap and an applied voltage of 15 kV and 5 kV respectively, we note that for a same duration of pulse of 15 ns, the energy of the discharge is 50 times higher at T_{g}=300 than at 1000 K. Using similarity relations, this ratio should be around 36. Then comparing the two reference cases, the heating of the gas appears to be more significant at 300 K than at 1000 K and then the glow to spark transition may occur more easily at 300 K than as 1000 K if the pulse duration is slightly longer than the connection time.

Finally, we have compared experimental and simulated images of the dynamics of a NRP discharge in air at atmospheric pressure and at $T_{\mathrm{g}} = 300$ K. The excellent agreement obtained validates the dynamics of formation of the air discharge between two point electrodes at the early stages of its development.

Chapter 3

Simulation of several voltage pulses in the NRPD glow regime

3.1 Introduction

In Chapter 2, we have simulated a single discharge in air occurring during one of the nanosecond voltage pulses. As many discharges have occurred before the simulated one, we have carried out simulations assuming an uniform density of seed positive ions and electrons of 10^9 cm^{-3} in the interelectrode gap at the beginning of the studied voltage pulse for $T_g = 300$ and 1000 K and we have neglected the influence of photoionization.

In this chapter, we propose to model more accurately the dynamics of charged species during the interpulse at $T_g = 300$ and 1000 K for repetitive pulses in the frequency range of 1 to 100 kHz. Based on these results, in Section 3.3, we will carry out a detailed study on the influence of the preionization level and photoionization on the discharge dynamics during a single voltage pulse at $T_g = 300$ and 1000 K. Then in Section 3.4, we will simulate several consecutive pulses of a glow discharge at $T_g = 1000$ K at 10 kHz and we will study the dynamics of formation of a stable quasi-periodic glow regime observed in the experiments [*Pai*, 2008]. Finally, in Section 3.5 , we will discuss the influence of a laminar air flow at 10 m s^{-1} aligned with the axis of electrodes on the discharge dynamics. It is important to note that in this chapter, we will consider only discharges in the glow regime and then no heating of air by the discharge will be considered. The air heating by the discharge leading to the nanosecond spark regime will be studied in Chapter 4.

3.2 Modeling of the air plasma during the interpulse

In experiments, after the voltage pulse, the voltage decreases to zero, with very often some additional small bumps of voltage. In the simulations, we have assumed that the voltage decreases monotonously to zero at the end of the voltage pulse and that in the interpulse there is no applied voltage. To model the air plasma during the interpulse, it is then important to take into account the chemistry and the diffusion of charged species during the interpulse.

3.2.1 Chemistry of charged species during the interpulse

During the interpulse, the densities of charged species will evolve following a zero-field chemistry described by:

$$\left\{\begin{array}{ll} \partial_{\mathrm{t}}\mathrm{n_e} & = \nu_{\mathrm{det}}\,\mathrm{n_n} - (\nu_\eta + \mathrm{k}_{\beta,\mathrm{ep}}\,\mathrm{n_p})\,\mathrm{n_e} \\ \partial_{\mathrm{t}}\mathrm{n_n} & = \nu_\eta\,\mathrm{n_e} - (\nu_{\mathrm{det}} + \mathrm{k}_{\beta,\mathrm{np}}\,\mathrm{n_p})\,\mathrm{n_n} \\ \partial_{\mathrm{t}}\mathrm{n_p} & = -(\mathrm{k}_{\beta,\mathrm{ep}}\,\mathrm{n_e} + \mathrm{k}_{\beta,\mathrm{np}}\,\mathrm{n_n})\,\mathrm{n_p} \end{array}\right. \tag{3.1}$$

where $\mathrm{n_e}$, $\mathrm{n_n}$ and $\mathrm{n_p}$ stand for the densities of electrons, negative ions and positive ions respectively. ν_{det} is the detachment frequency, ν_η is the attachment frequency, $\mathrm{k}_{\beta,\mathrm{ep}}$ the recombination rate coefficient between positive ions and electrons and $\mathrm{k}_{\beta,\mathrm{np}}$ is the recombination rate coefficient between positive and negative ions.

The fastest process occurring as soon as the applied voltage decreases to zero is the attachment of the electrons on the neutral gas molecules. Two-body attachment processes are negligible at low electric field, and then electrons are rapidly converted into negative ions due to the low-field three body attachment reaction:

$$e + \mathrm{O_2} + \mathrm{O_2} \rightarrow \mathrm{O_2^-} + \mathrm{O_2} \tag{3.2}$$

Assuming that in the interpulse, the electron temperature is equal to the air temperature ($T_{\mathrm{e}} = T_{\mathrm{g}}$), the three body attachment rate coefficient (k_{45}) given by *Kossyi et al.* [1992] becomes:

$$\eta = 1.4 \times 10^{-29}(0.2N)^2 \frac{300}{T_{\mathrm{g}}} e^{\frac{-600}{T_{\mathrm{g}}}}\ s^{-1} \tag{3.3}$$

At 300 K, *Popov* [2010] has recently shown that $\mathrm{O_2^-}$ ions could be rapidly transformed into ions with a larger electron bound energy. However, in this work we have assumed that negative ions are $\mathrm{O_2^-}$ ions.

The evolution of charged species during an interpulse depends also on the electron detachment reaction:

$$\mathrm{O_2^-} + \mathrm{O_2} \rightarrow e + \mathrm{O_2} + \mathrm{O_2} \tag{3.4}$$

In *Benilov and Naidis* [2003], the detachment rate coefficient k_{det} proposed by *Mnatsakanyan and Naidis* [1991] is used. This rate coefficient is given as a function of the air temperature and the electric field:

$$k_{\mathrm{det}} = 2 \times 10^{-10}(0.2N) e^{\frac{-0.52}{T_{\mathrm{eff}}}} \frac{1 - e^{-4\theta}}{1 - e^{\theta}}\ s^{-1} \tag{3.5}$$

$$\text{with :} \begin{cases} \theta & = 0.13 \left(\dfrac{11360}{T_\mathrm{g}} - \dfrac{1}{T_\mathrm{eff}} \right) \\ T_\mathrm{eff} & = \dfrac{T_\mathrm{g}}{11360} + 5.2 \times 10^{-6} \left(\dfrac{E}{N} 10^{17} \right)^2 \end{cases}$$

where E/N is in Td and T_eff is an effective temperature that takes into account the air temperature and the applied reduced electric-field. In the limit of zero electric field, this rate coefficient becomes:

$$k_\mathrm{det} = 1.6 \times 10^{-10} N e^{\frac{-0.52}{T_\mathrm{eff}}} \ s^{-1} \tag{3.6}$$

with $T_\mathrm{eff} = T_g/11360$. It is important to note that Equation (3.5) has to be carefully implemented in Fortran codes to guarantee that it reduces to Equation (3.6) at zero electric field.

As expected, the detachment rate coefficient is five orders of magnitude smaller at 300 K (11 s^{-1}) than at 1000 K (3.55×10^6 s^{-1}). On the other hand, the attachment rate coefficient is one order of magnitude higher at 300 K (4.55×10^7 s^{-1}) than at 1000 K (6.148×10^6 s^{-1}).

For the electron-ion and ion-ion recombination, we have to consider different reactions, depending on the nature of positive ions. At 300K, positive ions are certainly O_4^+ ions [*Pancheshnyi*, 2005] and then the electron-ion recombination reaction is:

$$e + \mathrm{O}_4^+ \rightarrow \mathrm{O}_2 + \mathrm{O}_2 \tag{3.7}$$

with the rate coefficient (k_{30}) given by *Kossyi et al.* [1992]

$$k_{30} = 1.4 \times 10^{-6} \times \left(\frac{300}{T_\mathrm{e}} \right)^{1/2} cm^3 s^{-1} \tag{3.8}$$

For the ion-ion recombination, two-body and three-body processes have to be considered. The two-body recombination reaction with O_2^- and O_4^+ ions is:

$$\mathrm{O}_2^- + \mathrm{O}_4^+ \rightarrow \mathrm{O}_2 + \mathrm{O}_2 + \mathrm{O}_2 \tag{3.9}$$

with a rate coefficient of $\simeq 10^{-7}$ cm^3 s^{-1} [*Kossyi et al.*, 1992] (reaction II in section 2.7) and the three-body recombination reaction is:

$$\mathrm{O}_2^- + \mathrm{O}_4^+ + M \rightarrow \mathrm{O}_2 + \mathrm{O}_2 + \mathrm{O}_2 + M \tag{3.10}$$

with a reaction rate coefficient [*Kossyi et al.*, 1992] (reaction V in section 2.7):

$$k_V \times N \simeq 2 \times 10^{-25} N \times \left(\frac{300}{T_\mathrm{g}} \right)^{2.5} cm^3 s^{-1} \tag{3.11}$$

At 300 K, we have $k_V \times N \simeq 5 \times 10^{-6}$ cm^3 s^{-1} and then the three-body recombination is more efficient than the two-body recombination process.

At 1000 K [*Riousset et al.*, 2010; *Naidis*, 1999], positive ions are certainly O_2^+ ions and then the electron-ion recombination reaction is:

$$e + O_2^+ \rightarrow O + O \tag{3.12}$$

with the rate coefficient (k_{40}) given by *Kossyi et al.* [1992]

$$k_{40} = 2 \times 10^{-7} \times \left(\frac{300}{T_\mathrm{e}}\right) cm^3 s^{-1} \tag{3.13}$$

For the ion-ion recombination, at 1000 K, two-body recombination reactions are more efficient than three-body processes. For two-body processes with O_2^- and O_2^+ ions, two reactions are given in *Kossyi et al.* [1992]:

$$O_2^- + O_2^+ \rightarrow O_2 + O_2 \tag{3.14}$$

with a rate coefficient given by *Kossyi et al.* [1992] (reaction I in section 2.7):

$$k_I \simeq 2 \times 10^{-7} \times \left(\frac{300}{T_\mathrm{g}}\right)^{0.5} cm^3 s^{-1} \tag{3.15}$$

and:

$$O_2^- + O_2^+ \rightarrow O_2 + O + O \tag{3.16}$$

with a rate coefficient given by *Kossyi et al.* [1992] (reaction II in section 2.7):

$$k_I \simeq 1 \times 10^{-7}\, cm^3 s^{-1} \tag{3.17}$$

Then we note that at 300 and 1000 K at atmospheric pressure, the electron-ion and ion-ion recombination processes are rather slow processes, with rate coefficients in the range $10^{-7} - 5 \times 10^{-6}$ cm^3 s^{-1}. At repetition frequencies in the range 1-100 kHz, charged species produced by a pulsed discharge will only partially recombine during the interpulse and some seed charges will be present at the beginning of the next voltage pulse.

According to Equations (3.1) if we neglect recombination processes in comparison to attachment and detachment processes during the interpulse, the steady state is characterized by:

$$k_\mathrm{det}\, \mathrm{n_n} = \eta\, \mathrm{n_e} \tag{3.18}$$

Then the ratio between the detachment and the attachment rate coefficients allows to estimate the ratio of the electron density over the negative ion density in the quasi steady-state of an interpulse. So one gets that there are approximately 10^7 times more negative ions than electrons at 300 K but only 1.7 times more negative ions than electrons at 1000 K at the end of an interpulse.

These results are confirmed by 0D simulations of the time-evolution of charged species densities in zero electric-field in taking into account all terms in Equations (3.1). As already mentioned in Chapter1, to solve the chemistry part in the discharge phase during the voltage pulse, we use an explicit fourth order Runge Kutta method. For the chemistry during the interpulses, we solve the system of ODEs (Equations (3.1)) with the implicit Runge-Kutta method RADAU5 of order 5 developed by *Hairer and Wanner* [2010]. As initial condition for densities of charged species, we have considered conditions close to those of the plasma channel of a nanosecond pulsed discharge before the voltage decrease at the end of the pulse ($\mathrm{n_p} = 1.1 \times 10^{14}$ cm^{-3}, $\mathrm{n_e} = 10^{14}$ cm^{-3} and $\mathrm{n_n} = 10^{13}$ cm^{-3}). Figure 3.1 (a) shows the evolution of the charged species densities during an interpulse of 10 μs (100 kHz repetition frequency) at $\mathrm{T_g}$=300 K. Two distinct phases can be identified: First, due to the low-field three body attachment, the electron density decreases rapidly to a very low value around 10^4 cm^{-3} in less than 400 ns. At the end of this attachment phase, the densities of positive and negative ions are almost equal and the ratio between the densities of negative ions and electrons is very close to the one given by Equation (3.18). In a second phase, the charged species slowly recombine at a constant rate until the end of the interpulse and the final preionization at t=10 μs is $n_p \simeq n_n \simeq 10^{10}\,\mathrm{cm^{-3}}$.

Figure 3.1 (b) shows the time evolutions of densities of charged species at $\mathrm{T_g}$=1000 K obtained with the same initial condition as in Figure 3.1 (a). As at 300 K, at $\mathrm{T_g}$=1000 K electrons are attaching very fast to form negative ions during the first phase that lasts 2 μs. It is interesting to note that at the end of the attachment phase, the electron density is about one half of the negative ion density and one third of the positive ion density. This is due to to the quite high detachment rate relatively to the three body attachment at 1000 K. Then the recombination phase of negative ions and electrons with positive ions has a much slower dynamics and the final preionization at t=10 μs is $4\times10^{11}\,\mathrm{cm^{-3}}$. It is interesting to note that these results are barely affected by the initial condition of the 0D simulations. At 300K, as mentioned in *Wormeester et al.* [2010], after the rapid attachment phase, we have $n_p \simeq n_n$ and then the time evolution of the densities of charges species is given by:

$$\frac{\mathrm{dn_p}}{\mathrm{d}t} \simeq -\beta\,\mathrm{n_p}^2 \tag{3.19}$$

where $\beta = \beta_{\mathrm{np}}$. The solution for $\mathrm{n_p}$ is:

$$\mathrm{n_p(t)} = \frac{1}{\beta t + \frac{1}{\mathrm{n_{p0}}}} \simeq \frac{1}{\beta t}\ \ (\text{for}\ \ \mathrm{t} > \frac{1}{\beta \mathrm{n_{p0}}}) \tag{3.20}$$

where $\mathrm{n_{p0}}$ is the positive ion density obtained at the end of the pulse. Then, for $\mathrm{t} > 1/(\beta \mathrm{n_{p0}})$, the value of the ion density during the interpulse is independent of the initial density of charged species in the discharge channel. In our case for air at atmospheric pressure at 300 K, the lowest value of β is $\beta \simeq 10^{-7}\mathrm{cm^3s^{-1}}$

and n_{p0} in the discharge channel is $n_{p0} \simeq 10^{14}$ cm^{-3}. Then the highest value of $1/(\beta n_{p0})$ is about 0.1 μs which corresponds to a frequency of 10 MHz. At 1000K, even if the density of electrons is not negligible after the first rapid attachment phase, we have also assumed that $n_p(t) \simeq 1/(\beta t)$ for $t > 1/(\beta n_{p0})$. At 1000 K, the lowest value of β is $\beta \simeq 10^{-7}$cm^{3}s^{-1} and n_{p0} in the discharge channel is $n_{p0} \simeq 10^{13}$ cm^{-3}. Then the highest value of $1/\beta n_{p0}$ is about 1 μs which corresponds to a frequency of 1 MHz. In this work, we have studied repetitive discharges with frequencies in the range 1-100 kHz, then the final value of seed charges at the end of the interpulse is independent on charged species densities at the end of the previous voltage pulse.

Based on Figures 3.1 and Equation (3.20), as a conclusion of this section, we have shown that in the frequency range 10-100 kHz, at 300 and 1000 K the highest preionization level at the end of an interpulse is between 10^{10} and 4×10^{11} cm^{-3}. The preionization level of 10^9 cm^{-3} taken into account in Chapter 2 corresponds to repetition frequencies in the range 1-10 kHz. We have shown that at 300 and 1000 K for repetitive discharges with frequencies in the range 1-100 kHz, the final value of seed charges at the end of the interpulse is independent on charged species densities at the end of the previous voltage pulse.

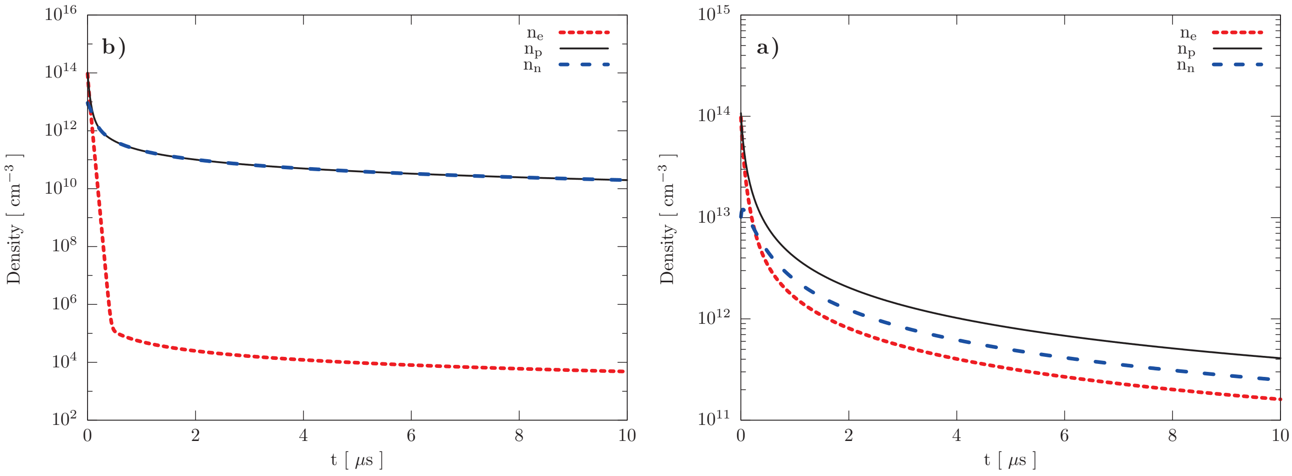

(a) (b)

Figure 3.1: *Evolution of electron, positive and negative ion densities as a function of time during the interpulse of a nanosecond repetitively pulsed discharge at 100 kHz in air at 300 K (a) and at 1000 K (b)*

3.2.2 Diffusion during the interpulse

The diffusion coefficient of electrons in zero applied electric field in ambient air is around ten thousands times higher than the one of ions. However, this difference of diffusion velocities generates a small space charge able to slow down the electrons and to accelerate the ions such that they finally diffuse at the same speed preserving the quasi-neutrality of the plasma: this is the so-called ambipolar diffusion. In this work, ambipolar diffusion has been studied in the case of the interpulse of a NRPD considering positive ions, electrons and negative ions. Basically, the motion of the charged species in the presence of an electric field is described by drift-diffusion equations. In the case of the ambipolar diffusion in zero applied electric-field, the only electric field is the ambipolar electric field $\mathbf{E}_{\mathrm{amb}}$ generated by the charged species moving at different velocities. The ambipolar motion can then be described by the set of drift-diffusion equations:

$$\begin{cases} \mathbf{F}_{\mathrm{e}} = -D_{\mathrm{e}}\nabla n_{\mathrm{e}} - n_{\mathrm{e}}\mu_{\mathrm{e}}\mathbf{E}_{\mathrm{amb}} \\ \mathbf{F}_{\mathrm{p}} = -D_{\mathrm{p}}\nabla n_{\mathrm{p}} + n_{\mathrm{p}}\mu_{\mathrm{p}}\mathbf{E}_{\mathrm{amb}} \\ \mathbf{F}_{\mathrm{n}} = -D_{\mathrm{n}}\nabla n_{\mathrm{n}} - n_{\mathrm{n}}\mu_{\mathrm{n}}\mathbf{E}_{\mathrm{amb}} \end{cases} \tag{3.21}$$

The ambipolar constraint that ensures the quasi-neutrality of the plasma can be written as in *Ramshaw and Chang* [1993]:

$$\sum_i \mathrm{q}_i\mathbf{F}_i = 0 \quad \Rightarrow \mathbf{F}_{\mathrm{e}} + \mathbf{F}_{\mathrm{n}} = \mathbf{F}_{\mathrm{p}} \tag{3.22}$$

where $\mathbf{F}_i$ and q_i are respectively the flux and the charge of specie i. Combining Equations (3.21) and (3.22), one gets the expression of $\mathbf{E}_{\mathrm{amb}}$:

$$\mathbf{E}_{\mathrm{amb}} = \frac{D_{\mathrm{p}}\nabla n_{\mathrm{p}} - D_{\mathrm{e}}\nabla n_{\mathrm{e}} - D_{\mathrm{n}}\nabla n_{\mathrm{n}}}{n_{\mathrm{e}}\mu_{\mathrm{e}} + n_{\mathrm{p}}\mu_{\mathrm{p}} + n_{\mathrm{n}}\mu_{\mathrm{n}}} \tag{3.23}$$

Equations (3.21) and (3.23) preserve the quasi-neutrality of the plasma. Usually in discharge codes, drift-diffusion fluxes are computed for all species except one and the density of the last specie is deduced for the neutrality of the plasma. If we neglect the diffusion and the mobility of ions compared to the one of electrons, and the gradient of the electronic temperature, Equation (3.23) reduces to the expression of the ambipolar field of a multicomponent, multi-temperature plasma obtained by *Ramshaw and Chang* [1993]:

$$\mathbf{E}_{\mathrm{amb}} = \frac{\nabla p_{\mathrm{e}}}{n_{\mathrm{e}}\mathrm{m}_{\mathrm{e}}\mathrm{q}_{\mathrm{e}}} \tag{3.24}$$

Different numerical schemes may be used to solve the system of Equations (3.21) and (3.23). We have considered a test-case with a Gaussian neutral plasma with a half-width of 250 μm. The peak positive ion density is $\mathrm{n}_{\mathrm{p}} = 1.1 \times 10^{14}$ cm^{-3}, the peak electron density is $\mathrm{n}_{\mathrm{e}} = 10^{14}$ cm^{-3}, and the peak negative ion density is $\mathrm{n}_{\mathrm{p}} = 10^{13}$ cm^{-3}. These density profiles are representative of the plasma channel of a pulsed nanosecond glow discharge at atmospheric pressure. We have studied the diffusion of this Gaussian distribution during 100 μs which is the duration of the interpulse of a NRPD at a 10 kHz repetition frequency. In this test-case, we solve Equations (3.21) and (3.23) for the three charged species. Figure 3.2 shows the 2D distributions of the initial electron density and the corresponding absolute value of the ambipolar electric-field. As expected, the initial ambipolar field is very small compared to the electric-field values during the discharge, with a maximum around 7 V cm^{-1}. Non-intuitively, the maximum of the ambipolar electric-field is located at some distance from the maximum of the density and from the maximum of density gradients.

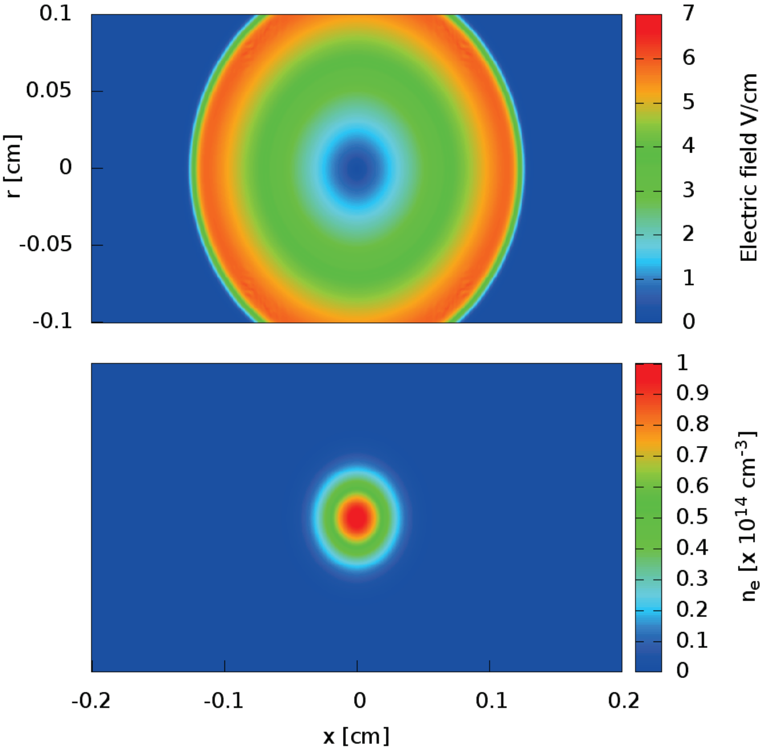

Figure 3.2: *Initial electron density and ambipolar electric-field generated by a Gaussian plasma in a zero applied electric-field*

Figure 3.3 shows the profiles of the densities of electrons and positive ions and of the absolute value of the ambipolar electric-field on the symmetry axis at t=1 μs and 100 μs. In this case, a second order centered scheme has been used to compute the drift-diffusion fluxes. As expected, Figure 3.3 shows that charged species diffuse in time. We have checked that the ambipolar constraint is well respected and that the space charge variation is very close to zero with very small oscillations on the order 10^{-20} C cm^{-3}. The quasi-neutrality of the plasma is then maintained during the transport.

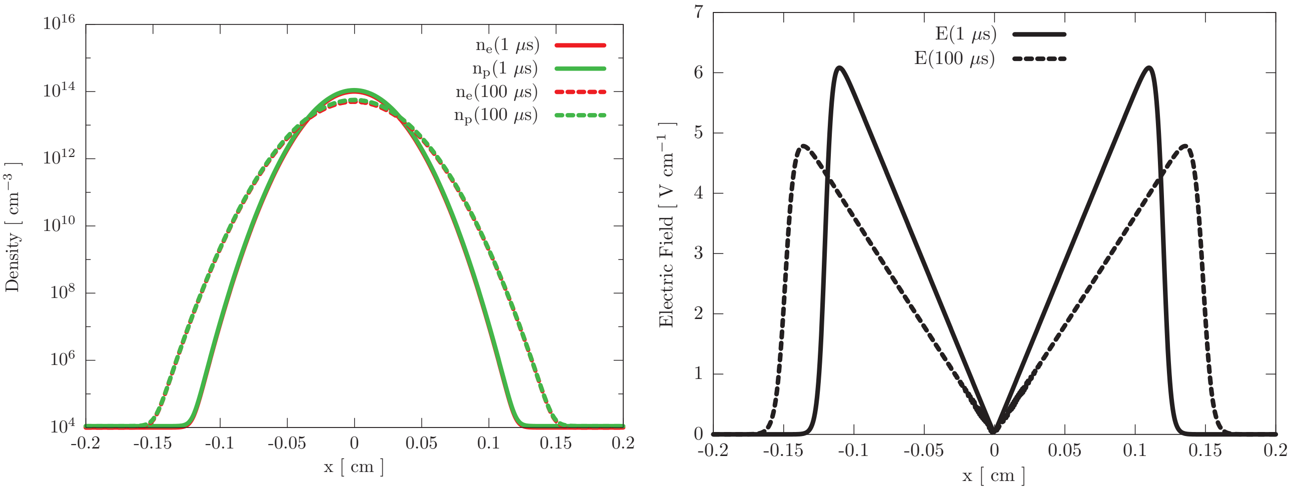

(a) (b)

Figure 3.3: *(a): Electron and positive ion densities and (b): absolute value of the ambipolar electric-field on the symmetry axis at t=1 μs and 100 μs. Drift-diffusion fluxes are computed using a second order centered scheme.*

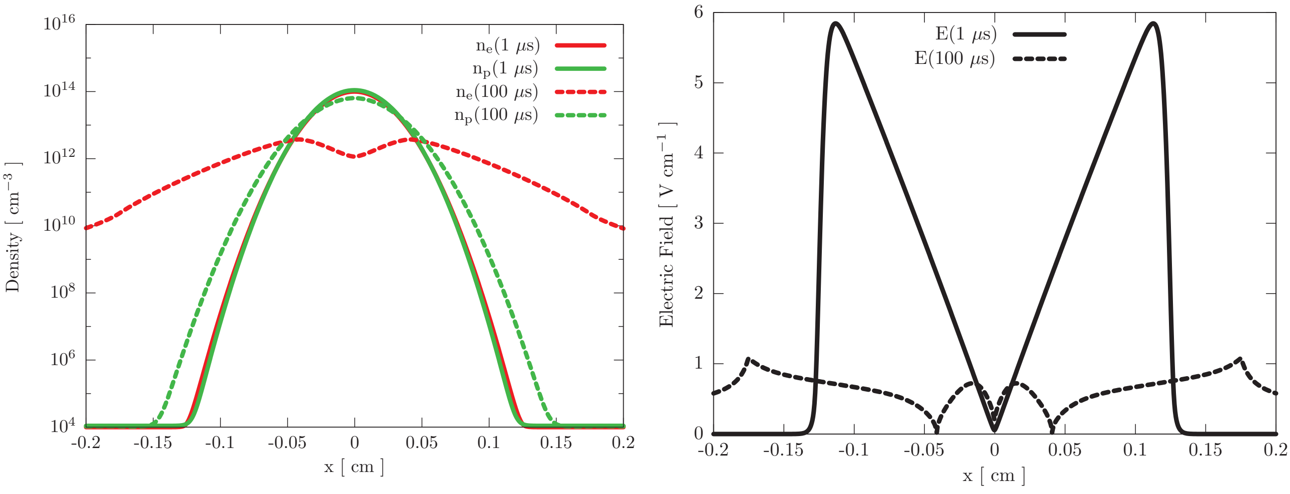

(a) (b)

Figure 3.4: *(a): Electron and positive ion densities and (b): absolute value of the ambipolar electric-field on the symmetry axis at t=1 μs and 100 μs. Drift-diffusion fluxes are computed using a first order upwind-scheme for drift fluxes and a second order centered scheme for diffusion fluxes.*

Figure 3.4 shows the same evolutions using a first order upwind-scheme for drift fluxes and a second order centered scheme for diffusion fluxes. We observe that the numerical diffusion due to the first order upwind scheme leads to the formation of an increasing space charge in the domain. Then the ambipolar constraint is not respected and it can be seen on the density profiles that the electrons are diffusing much faster than positive ions. It seems that the direct simulation of the ambipolar diffusion with the system of Equations (3.21) and (3.23) is very sensitive to the transport scheme and that numerical diffusion has to be avoided strictly in order to ensure the quasi-neutrality of the plasma.

For a two species plasma, the system of Equations (3.21) may be considerably simplified and reduced to the classical expression for the ambipolar diffusion flux given in *Hagelaar and Pitchford* [2005]. For example, if the electron density is very small compared to the density of positive and negative ions (as during the interpulse of a NRPD at 300 K (Section 3.2.1)), we have:

$$\begin{cases} n_\mathrm{n} = n_\mathrm{p} \\ \nabla n_\mathrm{n} = \nabla n_\mathrm{p} \\ n_\mathrm{e} = 0 \end{cases} \tag{3.25}$$

$$\Rightarrow \mathbf{E}_\mathrm{amb} = \frac{D_\mathrm{p}\nabla n_\mathrm{p} - D_\mathrm{n}\nabla n_\mathrm{n}}{n_\mathrm{n}\mu_\mathrm{n} + n_\mathrm{p}\mu_\mathrm{p}} = \frac{D_\mathrm{p} - D_\mathrm{n}}{\mu_\mathrm{p} + \mu_\mathrm{n}}\frac{\nabla n_\mathrm{p}}{n_\mathrm{p}}$$

$$\Rightarrow \mathbf{F}_\mathrm{p} = -D_\mathrm{p}\nabla n_\mathrm{p} - n_\mathrm{p}\mu_\mathrm{p}\mathbf{E}_\mathrm{amb} = -\nabla n_\mathrm{p}\frac{D_\mathrm{p}\mu_\mathrm{n} + D_\mathrm{n}\mu_\mathrm{p}}{\mu_\mathrm{n} + \mu_\mathrm{p}}$$

In air, the diffusion coefficients for positive and negative ions are similar and their mobility are very close ($\simeq$ 20% difference maximum). Then it can be reasonably assumed that in such a plasma both positive and negative ions diffuse almost at the diffusion velocity of positive ions. At 1000 K, as discussed in Section 3.2.1, during the interpulse, the electron density is not negligible in comparison to the densities of positive and negative ions. To estimate the influence of the presence of electrons on the diffusion of charged species at 1000 K, in a first step, we have considered that the electron density is almost equal to the density of positive ions and we neglect negative ions. In this case, the positive ion flux by the ambipolar flux of a two species plasma with only positive ions and electrons is given by :

$$\mathbf{F}_\mathrm{p} = -\nabla n_\mathrm{p}\frac{D_\mathrm{p}\mu_\mathrm{e} + D_\mathrm{e}\mu_\mathrm{p}}{\mu_\mathrm{e} + \mu_\mathrm{p}} \tag{3.26}$$

In air at 1000 K in zero applied electric-field, the electron mobility is $\mu_\mathrm{e} = 51300\ \mathrm{cm}^2\ \mathrm{V}^{-1}\ \mathrm{s}^{-1}$ while the mobility of positive ions is around $8\ \mathrm{cm}^2\ \mathrm{V}^{-1}\ \mathrm{s}^{-1}$.

In Equation (3.26), the positive ion mobility μ_p can then be neglected compared to μ_e and we obtain:

$$\mathbf{F}_\mathrm{p} = -\nabla n_\mathrm{p}(D_\mathrm{p} + \frac{\mu_\mathrm{p}}{\mu_\mathrm{e}} D_\mathrm{e}) \tag{3.27}$$

The term $\mu_\mathrm{p} D_\mathrm{e}/\mu_\mathrm{e}$ is of the order 0.14 cm^2 s^{-1} (D_e $\simeq$900 cm^2 s^{-1}, μ_p $\simeq$7.7 and $\mu_\mathrm{e} \simeq$ 51300 cm^2 V^{-1} s^{-1}) and the diffusion coefficient of positive ions is 0.67 cm^2 s^{-1} in air at 1000 K. Then the assumption stated in *Nijdam et al.* [2011] that all charged species diffuse at the velocity of positive ions leads in our case to underestimate the diffusion velocity of species by $\simeq$ 20%. To estimate more accurately the validity of this simplifying hypothesis, Figure 3.5 shows the same results as Figure 3.3 but in assuming that all charged species diffuse at the velocity of positive ions. We observe that the results are quite similar to the case when the drift-diffusion equations for all charged species are solved and we have checked that the difference is less than 10% at t=100 μs.
As a conclusion, in the following, we have assumed an ambipolar diffusion at the diffusion velocity of positive ions for all charged species.

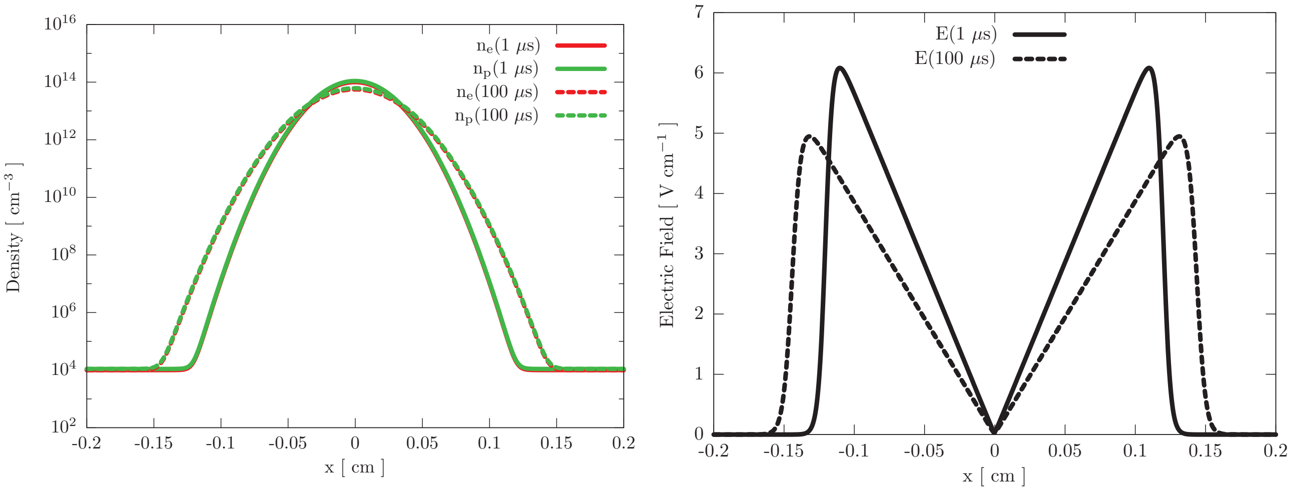

(a) (b)

Figure 3.5: *(a): Electron and positive ion densities and (b): absolute value of the ambipolar electric-field on the symmetry axis at t=1 μs and 100 μs. The same numerical method as Figure 3.3 is used in assuming that all charged species diffuse at the velocity of positive ions.*

3.3 Influence of the preionization at the end of an interpulse on the discharge dynamics of the next voltage pulse at T_g=300 K and T_g=1000 K

3.3.1 At T_g=300 K

As explained in section 3.2.1, at 300 K, the preionization left by successive discharges at the end of an interpulse mainly consists in positive and negative ions. The main negative ion formed in air at 300 K is assumed to be O_2^- even if this point was recently questioned by *Popov* [2010]. These negative ions may be a significant source of seed electrons for the discharge of the next voltage pulse if the detachment process is efficient enough.
In this section, we propose to study in detail the dynamics of a discharge ignited in air at 300 K with a preionization consisting of positive and negative ions, with and without photoionization. As a test-case, we have considered a discharge at T_g=300 K, with an applied voltage of 15 kV with a 2 ns rise-time, a 5 mm gap and point electrodes with R_p=300 μm. The tip of the anode is located at $x = 0$ mm and the tip of the cathode is at $x = 5$ mm. As in Chapter2, to present the different results, Figure 3.6 shows the time evolutions of the axial position of the positive discharge front (position of the maximum electric field E_{max} in the gap) and of E_{max}. The black line corresponds to the reference case used in Chapter2 without photoionization and with a preionization level $n_{p0} = n_{e0} = 10^9\,cm^{-3}$ and $n_{n0} = 0\,cm^{-3}$. The dark blue line corresponds to the same case with photoionization. We observe, that with a preionization level of $n_{p0} = n_{e0} = 10^9\,cm^3$, photoionization has only a small influence on the discharge dynamics and decreases the connection time of 0.3 ns. On the other hand, replacing the electron preionization background by a negative ion preionization brings more significant changes (red line for $n_{e0} = 10^4\,cm^{-3}$ $n_{n0} = 10^9\,cm^{-3}$ $n_{p0} = n_{n0} + n_{e0}$, and dotted black line for $n_{e0} = 10\,cm^{-3}$ $n_{n0} = 10^9\,cm^{-3}$ $n_{p0} = n_{n0} + n_{e0}$): the delay with the reference case is in this case larger (1 ns), and the corresponding electric field is 30% higher as shown in Figure 3.6 (b). This indicates that with a negative ion preionization, the ignition and the propagation of a discharge are more difficult since electrons have first to be detached from negative ions ahead of the discharge front. This effect would be even larger if O_2^- ions are rapidly transformed into negative ions with a larger electron bound energy [*Popov*, 2010]. The black dotted line corresponding to $n_{e0} = 10\,cm^{-3}$ $n_{n0} = 10^9\,cm^{-3}$ $n_{p0} = n_{n0} + n_{e0}$, is a test-case without photoionization. For the same initial densities, the light blue line shows the results obtained with photoionization. We note that with photoionization, the connection time is reduced and that the maximum electric-field is quite similar to the reference case (solid black line with $n_{p0} = n_{e0} = 10^9\,cm^{-3}$ and $n_{n0} = 0\,cm^{-3}$). In these simulations, photodetachment was not taken into account and this process would probably also help the propagation of discharges. Finally, we conclude that when photoion-

ization is taken into account for a level of seed charges of about 10^9cm^{-3}, the dynamics and the characteristics of the discharge are only weakly dependent on the nature of negative charges (either ions or electrons). We have also shown that using directly a preionization with electrons and positive ions at a density of 10^9cm^{-3} without photoionization is a good compromise between complexity and accuracy to study the discharge characteristics at 300 K.

3.3.2 At $\mathrm{T_g}$=1000 K

As explained in Section 3.1, at 1000 K, a significant amount of electrons remains at the end of the interpulse and the role of negative ions on the next discharge dynamics is much less important at 1000 K than at 300 K. We have shown that simulations carried out in Section 2.1 with a $10^9\,\text{cm}^{-3}$ preionization of positive ions and electrons are representative of repetitive discharges in the frequency range 1-10 kHz. However, in the frequency range 10-100 kHz, we have shown that the electron density may be as high as $4 \times 10^{11}\,\text{cm}^{-3}$ and it is important to study how such a high electron density preionization impacts the discharge dynamics. For preionization levels higher than $10^9\,\text{cm}^{-3}$, we have checked that photoionization has no influence on the results and then photoionization has been neglected in this section.

In this section, we suggest to vary the preionization level of the reference discharge case at 1000 K of Chapter2 Section 2.1 (5 kV applied voltage, 2 ns rise-time and $\mathrm{R_p} = 50\,\mu\text{m}$). Figure 3.7 (a) shows the position of the positive streamer for three different preionization levels of positive ions and electrons. The blue dotted line is the reference discharge case of Chapter 2 (Figure (2.1)) with a preionization of electrons and positive ions ($\mathrm{n_{e0}} = \mathrm{n_{p0}} = 10^9\,\text{cm}^{-3}$) and no negative ions ($\mathrm{n_{n0}} = 0\,\text{cm}^{-3}$). When the preionization is increased from 10^9 to $10^{10}\,\text{cm}^{-3}$, we observe that the change of velocity of the positive discharge front before and after the connection with the negative discharge is smoother. With a preionization of $10^{11}\,\text{cm}^{-3}$, the velocity of the positive discharge remains almost constant during all the propagation and is no longer affected by the impact with the negative discharge. This is due to the fact that the preionization level in this case is almost equal to the electron density inside the channel of the negative discharge. Figure 3.7 (b) shows that the increase of the preionization level decreases the maximum electric-field in the streamer head, which corresponds to an easier propagation of the discharge. Non-intuitively, this lower maximum electric-field when the pre-ionization is higher also decreases the electron density in the plasma channel (not shown here) behind the positive streamer head. We have then calculated the energy of the discharge for different preionization levels. Figure 3.8 shows the spatial distribution of the energy density $e_{\mathrm{J}}(t)$ in the whole computational domain for $\mathrm{n_{e0}} = \mathrm{n_{p0}} = 10^9\,\text{cm}^{-3}$, $\mathrm{n_{n0}} = 0\,\text{cm}^{-3}$ (a) and $n_{e0} = n_{p0} = 10^{11}\,\text{cm}^{-3}$, $\mathrm{n_{n0}} = 0\,\text{cm}^{-3}$ (b). The time is shown is $t = 30$ ns, which corresponds to the end of the simulation of the reference discharge case of Chapter2 (case (a)) when the energy released is maximum: The total energy integrated on the whole computational domain E_J is $17\,\mu$J for case (a) (see figure 2.3), and $8\,\mu$J for case (b). Non-intuitively, we observe that the discharge energy after connection is lower when the discharge is ignited with a higher preionization level. The higher discharge energy for case (a) is mostly due to higher current densities due to the combination of the higher electric-field, needed for the discharge propagation in the lower preionization, and the consequent higher electron density in the plasma. Figure 3.8 shows that the energy is concentrated close to the tip of electrodes for cases (a) and (b) and in an additional spot at the middle of the gap for case (a) resulting from the impact of the positive and the negative discharges. For the highly preionized case (b), as the interaction between the two discharges is very smooth, the additional spot in the middle of the gap is absent.

As a conclusion of this section, we have shown that at 1000 K, the discharge dynamics and characteristics remain rather close whatever the preionization level considered in the range 10^9-$10^{11}\,\mathrm{cm}^{-3}$. Then all the conclusions of Chapter 2 on the transitions between discharge regimes are valid for discharges in the frequency range 1-100 kHz.

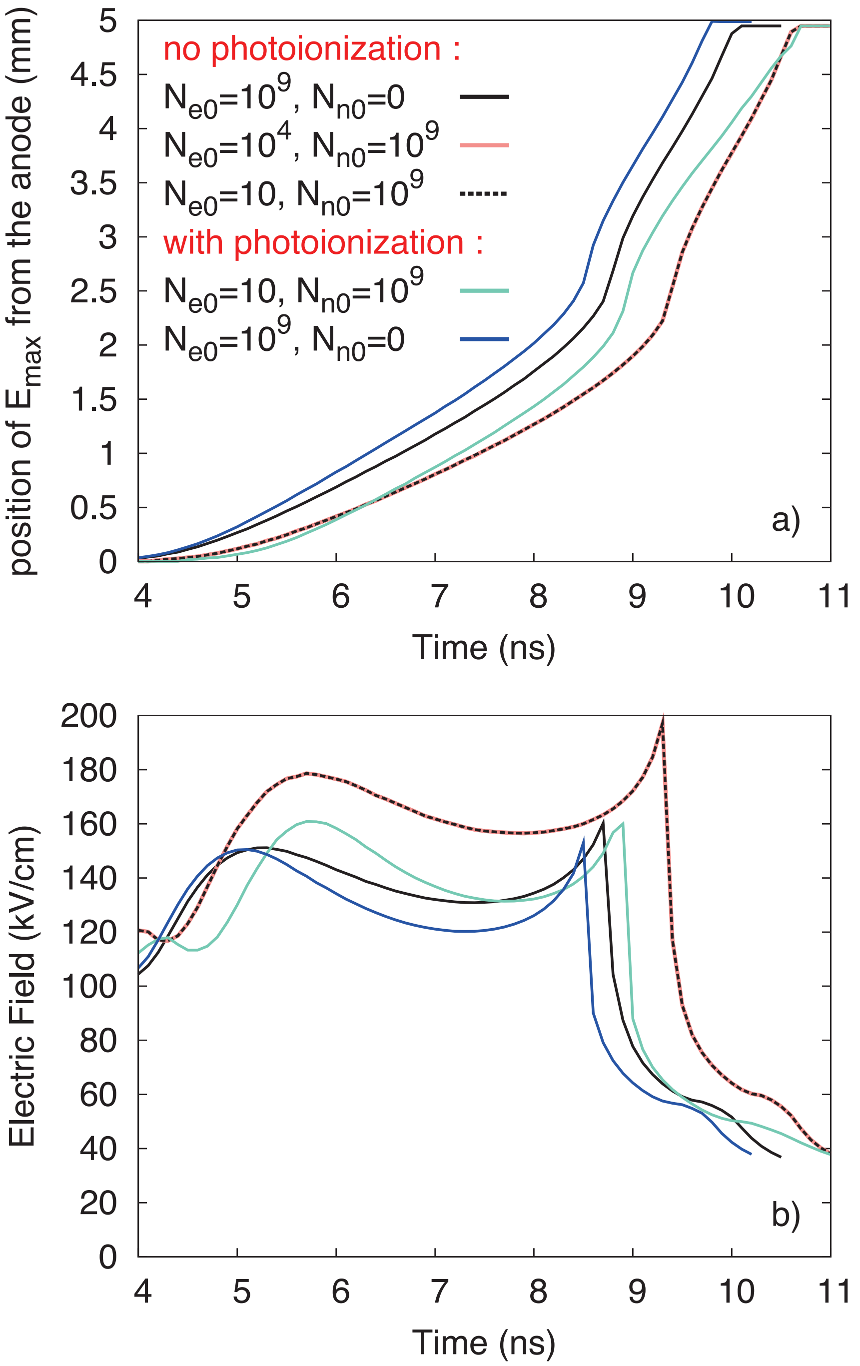

Figure 3.6: *Axial position of the maximum electric-field and then of the positive discharge front (a) and value of the maximum electric-field (b) as a function of time for different preionization levels and with or without photoionization. All discharges start to propagate at t = 4 ns.* $T_g = 300\,K$, $V = 15\,kV$, $R_p = 300\,\mu m$, $Gap = 5\,mm$

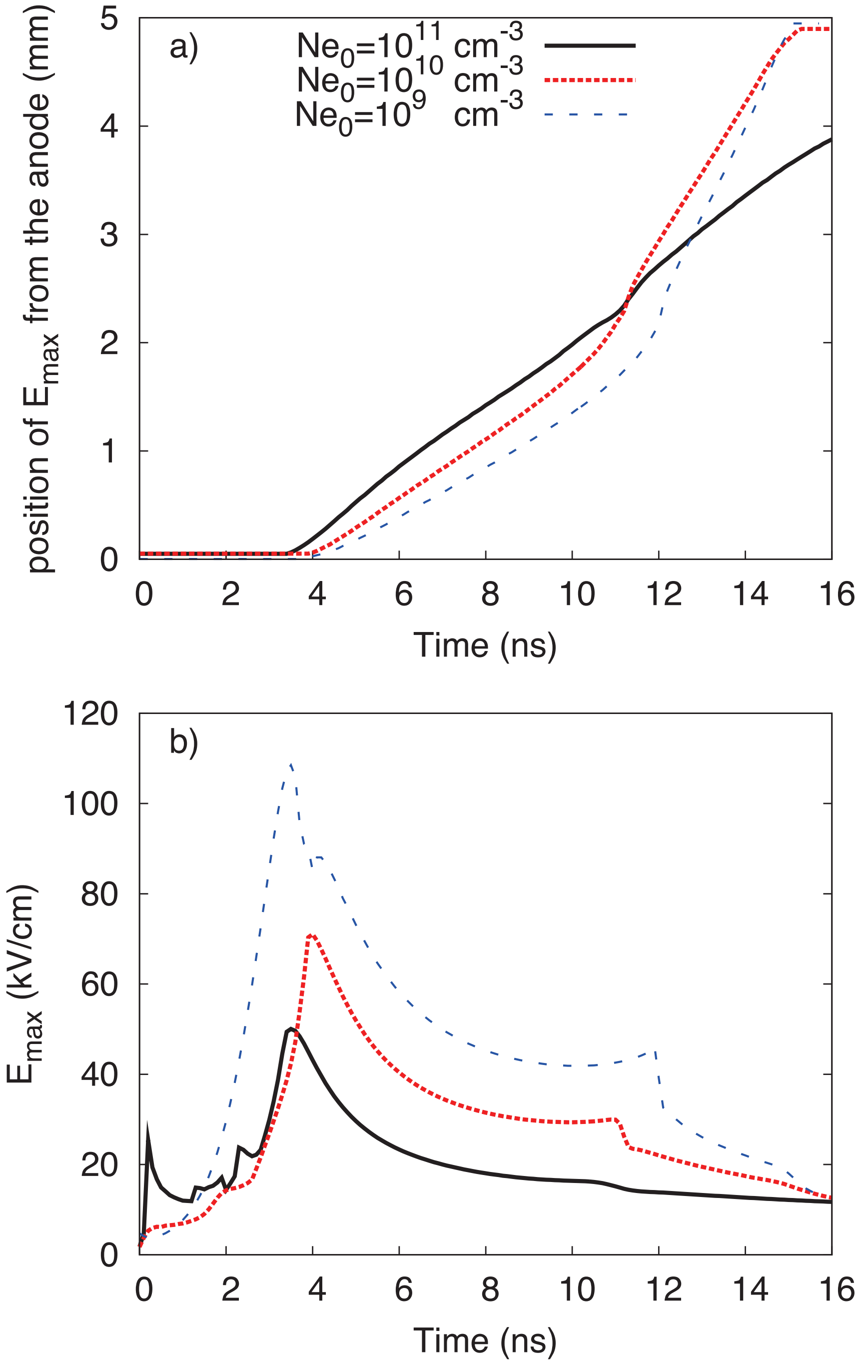

Figure 3.7: *Axial position of the maximum electric-field and then of the positive discharge front (a) and value of the maximum electric-field (b) as a function of time for different preionization levels without photoionization.* $T_g = 1000\,K$, $V = 5\,kV$, $R_p = 50\,\mu m$, Gap $= 5\,mm$.

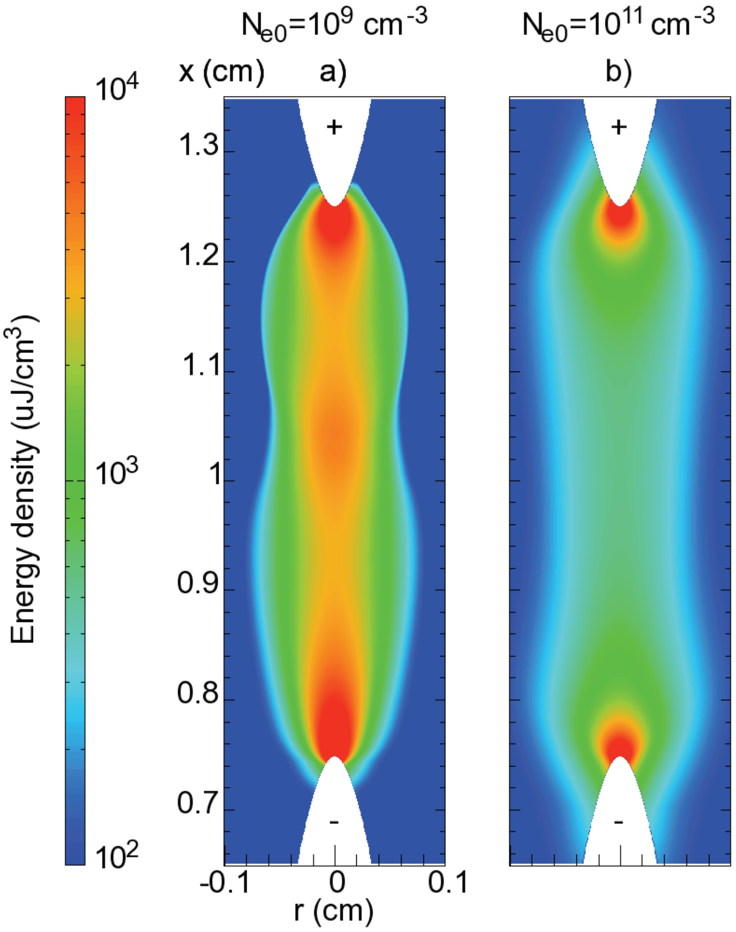

Figure 3.8: *Discharge energy at t = 30 ns for two different preionization levels* $n_{e0} = n_{p0} = 10^9\,cm^{-3}$, $n_{n0} = 0\,cm^{-3}$ *(a) and* $n_{e0} = n_{p0} = 10^{11}\,cm^{-3}$, $n_{n0} = 0\,cm^{-3}$ *(b), without photoionization.* $T_g = 1000\,K$, $V = 5\,kV$, $R_p = 50\,\mu m$, $Gap = 5\,mm$.

3.4 Simulation of several consecutive voltage pulses: formation of a stable glow regime in air at T_g=1000 K

In this section, we propose to simulate several consecutive nanosecond voltage pulses at $T_g = 1000$ K and at 10 kHz to study the dynamics of discharges pulse after pulse and the formation of a stable quasi-periodic glow regime observed in the experiments [*Pai*, 2008]. We use the discharge code based on the 2D axisymmetric fluid model described in section 1.2 during the voltage pulses and we solve the chemistry of the charged species coupled with their diffusion described in Section 3.2 during the inter-pulses, assuming that charged species diffuse at the velocity of positive ions (Section 3.2.2). In this section, we consider a point-to-point geometry with electrodes with a radius of curvature of $\mathrm{R_p} = 300\,\mu$m and a gap size of 2.5 mm. This small size of the gap has been studied in experiments [*Rusterholtz et al.*, 2012]. We have also chosen it as it allows to reduce the size of the computational domain and then the computational time to simulate several consecutive pulses. We have computed 10 voltage pulses at a frequency of 10 kHz and at a temperature of 1000 K with an applied voltage of 5 kV. Figure 3.9 shows the shape of the applied voltage.

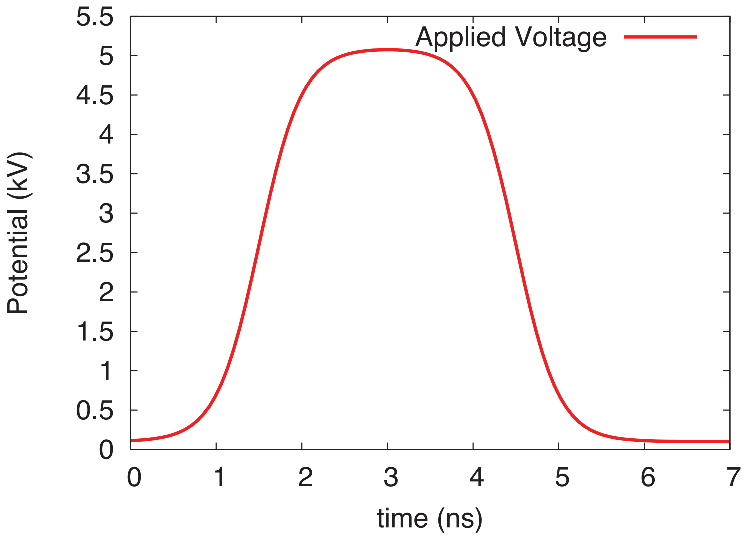

Figure 3.9: *Voltage pulse repeated at a frequency of 10 kHz. The pulse duration is about 5 ns with a rise-time and a decrease-time of 2 ns and a plateau at 5 kV during 1 ns.*

The pulse duration is about 5 ns with a rise-time and a decrease-time of 2 ns and a plateau at 5 kV during 1 ns. This pulse shape has been chosen such that the voltage starts to decrease 0.5 ns after the connection of discharges during the 3^{rd} voltage pulse (and all consecutive pulses as will be shown in the following) to be in the glow regime as discussed in Section 2.1. As initial condition of the first voltage pulse, we have considered a low uniform preionization of electrons and positive ions at 10^4 cm^{-3} in air, due to cosmic rays and ambient radioactivity as discussed in *Pancheshnyi* [2005]. We have taken into account photoionization in these simulations and we have checked that it has a significant influence for the first pulse but its influence becomes negligible for other pulses.

Figure 3.10 shows the 2D distributions of the electron density just before

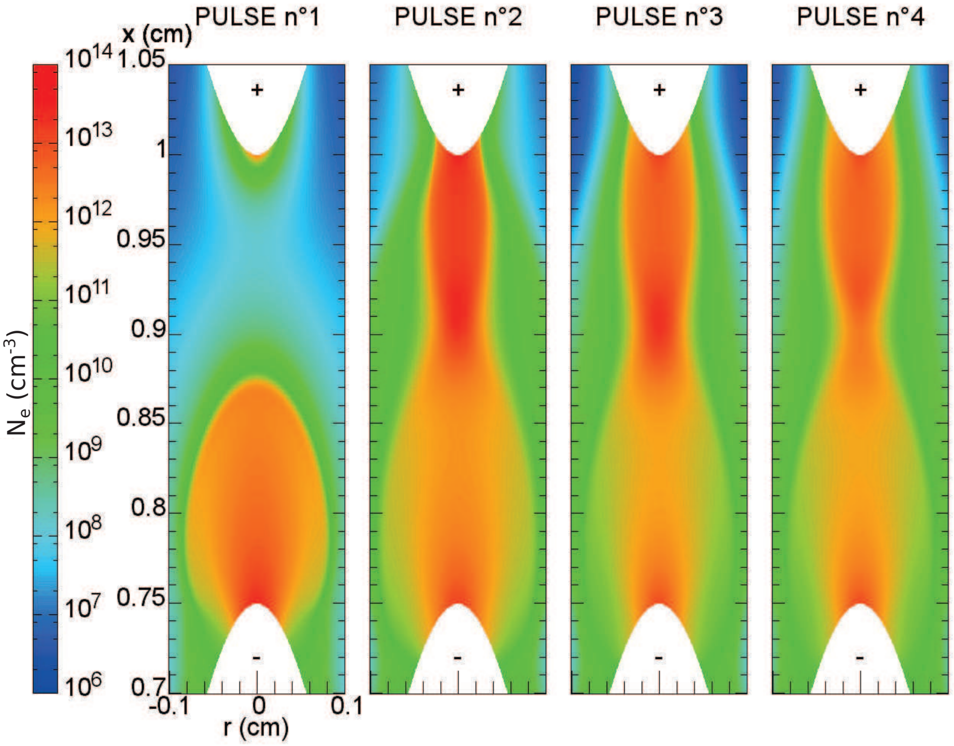

Figure 3.10: *Cross-sectional views of the electron density at the end of the first four pulses of a NRPD in air at atmospheric pressure at 10 kHz and 1000 K. The voltage is a 5 kV pulse of 5 ns, and the inter-electrode gap is 2.5 mm.*

the decrease of the applied voltage, for the first 4 consecutive voltage pulses. We note that the discharges are almost identical after the three first pulses which means that a stable regime is obtained very quickly. It is a consequence of the fact that the final preionization level obtained at the end of an inter-pulse is almost independent of the densities of charged species obtained during previous pulses in the range 1-100 kHz (Section 3.2.1). Consequently in our simulation at 10 kHz, the dynamics of the discharge is only changing during the first pulses of the NRPD and then remains always the same and we obtain a stable glow regime as observed in the experiments [*Pai*, 2008]. Figure 3.10 shows that during the first pulse, there is no connection between the positive and the negative discharges. The connection occurs during the second pulse because the discharge is able to ignite a little earlier thanks to the increase of the preionization level due to the first discharge. Pulse after pulse, the preionization left by the consecutive discharges diffuses and spreads radially. We have checked that the negative discharge is barely affected by this spreading of the preionization. To study its influence on the positive discharge, Figure 3.11 shows the radial profiles of the electron density at 0.5 mm from the tip of the anode at the beginning of each voltage pulse for the first 8 pulses. We observe that the preionization after the two first pulses is rather high ($n_e = 10^{10}\,\mathrm{cm}^{-3}$) and uniform over a radius of about 2 mm, much larger than the diameter of the positive discharge ignited at the positive point. These results validate the assumption of a uniform pre-ionization in the interelectrode gap used in Section 2.1 to study in detail the discharge dynamics during one voltage pulse.

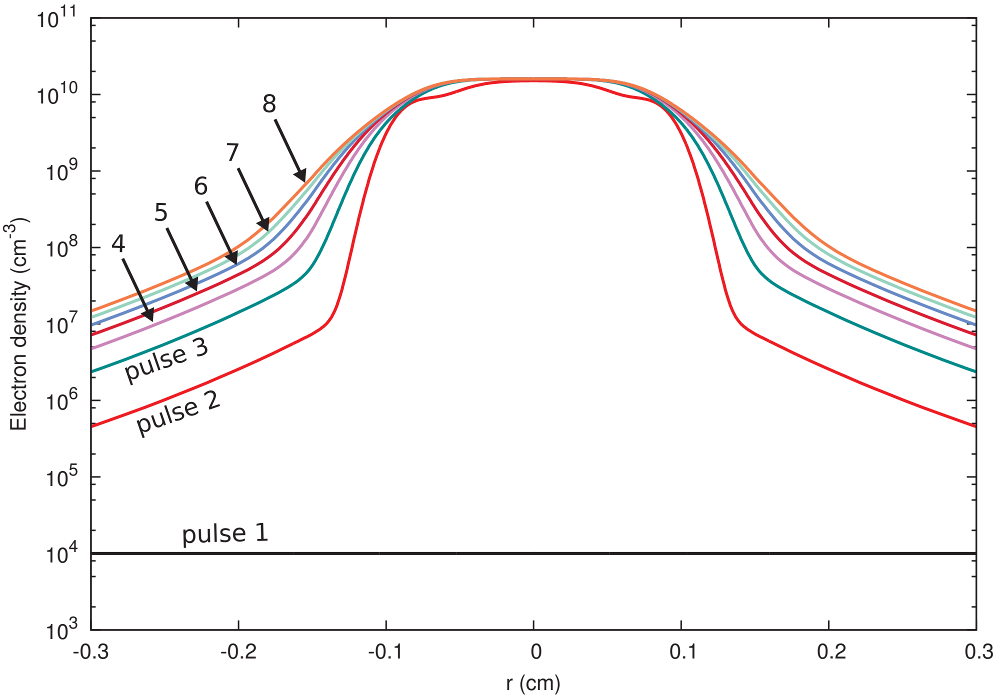

Figure 3.11: *Evolution of the electron density in the radial direction at 0.5 mm from the tip of the anode at the beginning of the first 8 voltage pulses of a point-to-point nanosecond repetitively pulsed discharge at 10 kHz and 1000 K. The voltage is a 5 kV pulse of 5 ns, and the inter-electrode gap is 2.5 mm.*

3.5 Influence of a laminar flow on the stable glow regime at $T_g = 1000$ K

In the experiments, an air flow aligned with the axis of electrodes is used. In this section, we propose to discuss the influence of a laminar flow on the NRPD dynamics and the stable glow regime at $\mathrm{T_g} = 1000$ K. When a laminar flow is added to the NRPD discharge, different cases have to be considered. In this work, we assume that the flow has a negligible impact on the discharge during the voltage pulses. This assumption remains valid as long as the flow is slow enough not to move the gas significantly during the voltage pulses: this means that $\mathrm{V}\times\mathrm{T_p} \ll G$ where $\mathrm{T_p}$ is the pulse duration, G the gap size and V the velocity of the flow. This is verified in almost all experimental conditions studied in the literature with nanosecond voltage pulses, and in our case it is valid up to very high velocities (up to 10 km s^{-1}) which are beyond the scope of this study. Assuming that the flow has only an influence during interpulses, three cases have to be considered.

First, the case for which the product of the velocity of the flow (V) and the interpulse duration $\mathrm{T_i}$ is small compared to the gap size (G) : $\mathrm{V}\times\mathrm{T_i} \ll \mathrm{G}$. In this case, the influence of the flow can be considered as negligible and the multipulse discharge is exactly the same with and without the flow.

The second case is $\mathrm{V}\times\mathrm{T_i} \gg \mathrm{G}$. In this case, the flow blows all the seed charges left by previous discharges, then pulses are really independent and each pulse is identical to the first one.

The last case of interest is intermediate, with $\mathrm{V}\times\mathrm{T_i} \simeq \mathrm{G}$. The flow is then able to change the distribution of the seed charges in the gap from one pulse to another. In this section, we propose to study this particular case.

We have considered the same point-to-point geometry as in previous section: electrodes with a radius of curvature of $\mathrm{R_p} = 300\,\mu$m and a gap size of 2.5 mm. We study the discharge at 1000 K and we use the same voltage shape given on Figure 3.9 with a maximum voltage of 4.5 kV. This value is chosen to be slightly less than in the previous section (5 kV). As already mentioned in Chapter 2, the discharge dynamics and structure are very sensitive to the applied voltage. Figure 3.12 shows that with a maximum voltage of 4.5 kV and the quite large radius of electrodes, only the negative discharge is able to ignite at the cathode and to propagate during the first voltage pulse. At $t = 3$ ns, we observe that ionization takes place close to the tip of the anode and a space charge starts to form but no positive discharge is really ignited in those conditions. The discharge regime is then a corona discharge with very small light emission close to electrode tips due to the absence of positive streamer. In these conditions, the amount of electrons produced between the head of the negative discharge and the anode tip is too small to significantly preionize the interelectrode gap. As a consequence, at a repetition frequency of 10 kHz we have simulated 12 consecutive voltage pulses and we have checked that this discharge remains in the corona regime pulse after pulse and that the positive discharge never ignites.

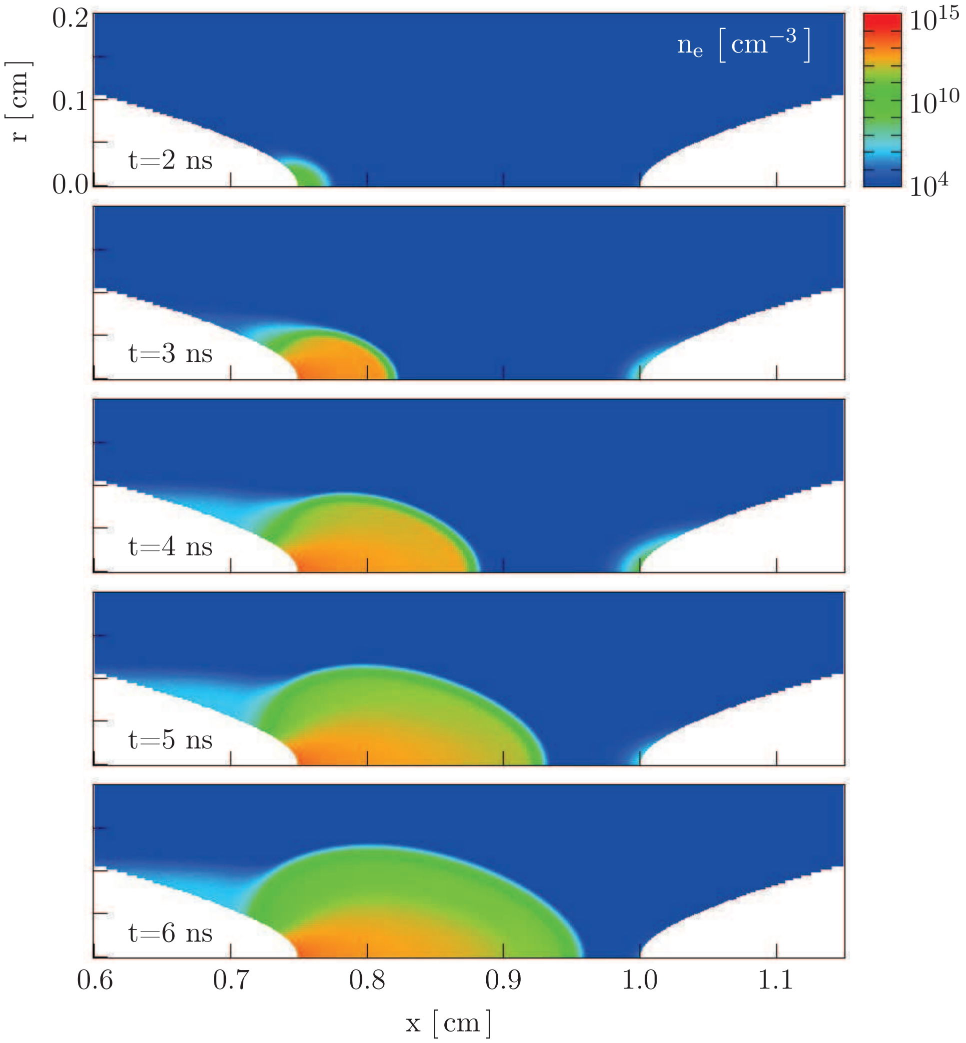

Figure 3.12: *Electron density evolution during the first pulse of a multipulse discharge at 10 kHz, 1000 K, with an applied voltage of 4.5 kV (same voltage shape as on Figure 3.9) and a 2.5 mm gap. The cathode is on left and the anode on the right. This discharge is in the corona regime with only a negative discharge. The positive discharge is not able to ignite due to the too low applied voltage. In the absence of an external flow, all following discharges are similar to the first discharge.*

Figure 3.13 shows the evolution of the electron density during the first interpulse of 100 μs ($f = 10$ kHz) in presence of a laminar flow at 10 m s^{-1} aligned with the axis of electrodes and flowing from the cathode to the anode. The flow is assumed here to act as a simple convection from left to right and we do not take into account the complex flow structure that could exist with stagnation points and boundary layers close to electrodes, and potentially also turbulences at higher flow velocities. During the interpulse, we observe that the electron cloud resulting from the negative discharge is convected over one third of the gap ($\mathrm{V{\cdot}T_i} = 0.3\,\mathrm{G}$) and spreads radially due to ambipolar diffusion. Then at t =100 μs, this electron cloud provides a high preionization of electrons of 10^{10} $\mathrm{cm^{-3}}$ all around the anode, able to promote the ignition of the positive discharge during the next voltage pulse.

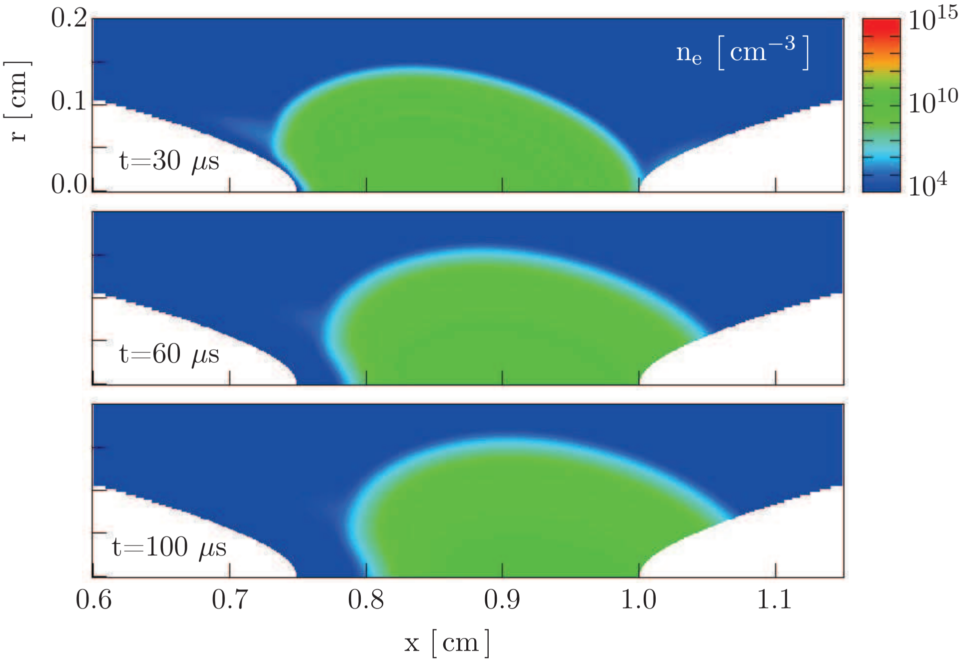

Figure 3.13: *Evolution of the electron density during the first interpulse of the multipulse discharge defined in Figure 3.12 in presence of an external flow at 10 m* s^{-1} *flowing from the cathode (left electrode) to the anode (right electrode).*

Figure 3.14 shows the ignition and the propagation of the discharge during the second voltage pulse. This time, thanks to the redistribution of the preionization by the external flow, the positive discharge is able to ignite and propagate at $t = 3$ ns. Then, at $t = 5$ ns, the positive and the negative discharges impact each other and the discharge transits into the glow regime. We have checked that consecutive pulses are in the stable glow regime at 1000 K. Then the flow is able to induce transitions between discharge regimes as observed in experiments [*Rusterholtz*, 2012].

We have carried out different discharge simulations with an external flow. We have noted that in simulations, the corona-to-glow transition induced by a flow occurs only in a very narrow set of parameters with both low voltages, and flow velocities such that $\mathrm{V{\times}T_i} \simeq \mathrm{G}$. As already mentioned, some other parameters as the applied voltage, have a much more significant influence on the discharge ignition and propagation than the preionization level. For example, with an applied voltage of 4 kV instead of 4.5 kV, the discharge remains in the corona regime during all the pulses (we simulated more than 10 voltage pulses) even if a flow is added. With a voltage of 5 kV, results remain the same as in Section 3.4 even with a 10 m s^{-1} flow from the cathode to the anode. However, if the direction of the flow is reversed (from the anode to the cathode), the positive discharge is never able to ignite and the corona to glow transition observed in Section 3.4 is in this case prevented.

In experiments, the effect of the flow on the corona-to-glow transition seems to be more significant than in the simulations. We would like to point out that the work presented in this section is only a first step to study the influence of a flow on the discharge dynamics and further studies are required.

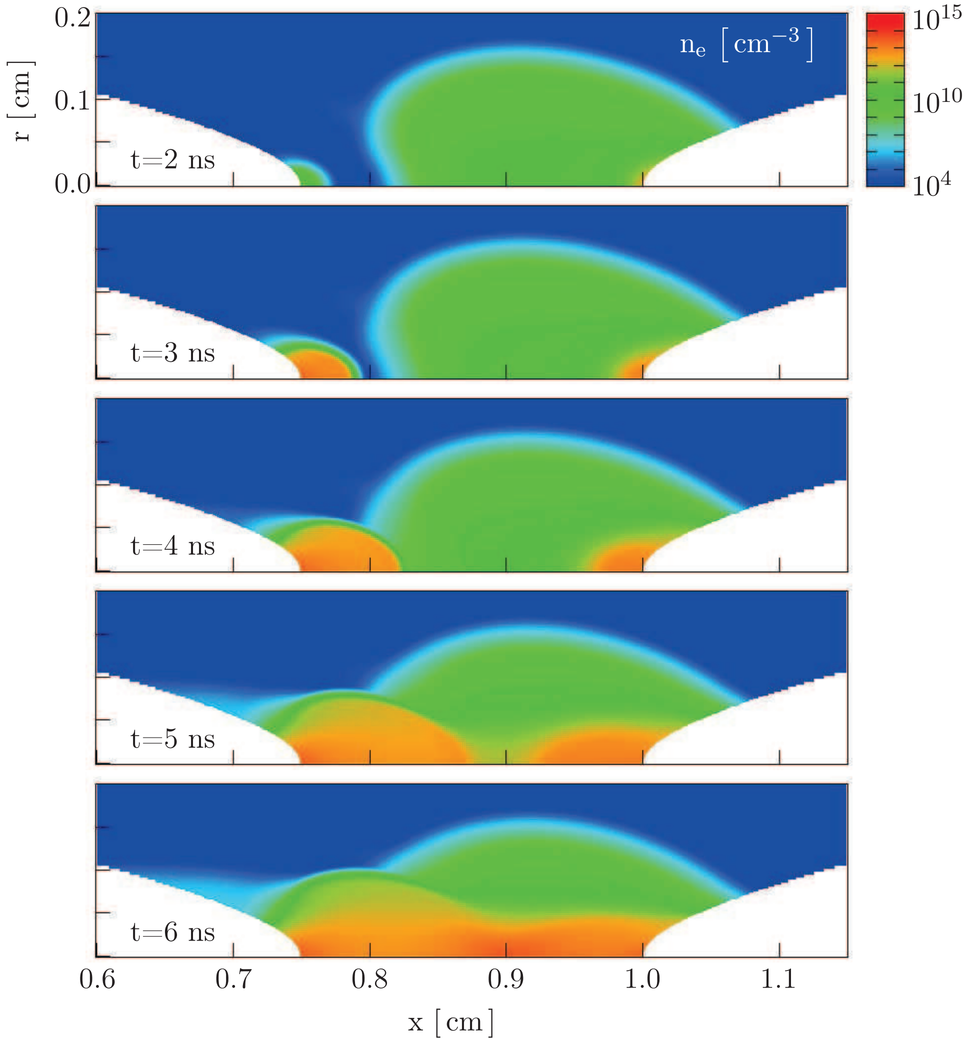

Figure 3.14: *Evolution of the electron density during the second pulse of the multipulse discharge defined in Figure 3.12 in presence of an external flow at 10 m* s^{-1} *flowing from the cathode (left electrode) to the anode (right electrode). Thanks to seed electrons convected by the flow close to the anode, the positive discharge ignites and propagates. The connection occurs at* $t = 5.5$ *ns and the discharge transits into the glow regime.*

3.6 Conclusion

In this chapter, we have first studied the chemistry and diffusion of charged species during interpulses of nanosecond repetitively pulsed discharges. We have shown that in the frequency range 10-100 kHz, at 300 and 1000 K the highest preionization level at the end of an interpulse is between 10^{10} and 4×10^{11} cm^{-3}. The preionization level of 10^9 cm^{-3} taken into account in Chapter 2 corresponds to repetition frequencies in the range 1-10 kHz. We have shown that at 300 and 1000 K for repetitive discharges with frequencies in the range 1-100 kHz, the final value of seed charges at the end of the interpulse is independent on charged species densities at the end of the previous voltage pulse. At 300 K, we have shown that the preionization left by previous discharges consists in positive and negative ions. These negative ions may be a significant source of seed electrons for the discharge of the next voltage pulse if the detachment process is efficient enough. We have studied the dynamics of a discharge ignited in air at 300 K with a preionization consisting of positive and negative ions, with and without photoionization. We have shown that when photoionization is taken into account for a level of seed charges of about 10^9 cm^{-3}, the dynamics and the characteristics of the discharge are only weakly dependent on the nature of negative charges (either ions or electrons). We have also shown that using directly a preionization with electrons and positive ions at a density of 10^9 cm^{-3} without photoionization is a good compromise between complexity and accuracy to study the discharge characteristics at 300 K.

At 1000 K, a significant amount of electrons remains at the end of the interpulse and the role of negative ions on the next discharge dynamics is much less important at 1000 K than at 300 K. However, in the frequency range 10-100 kHz, we have shown that the electron density may be as high as 4×10^{11} cm^{-3} and then we have studied how such a high electron density preionization impacts the discharge dynamics. At 1000 K, we have shown that the discharge dynamics and characteristics remain rather close whatever the preionization level considered in the range 10^9-10^{11} cm^{-3}. Then all the conclusions of Chapter 2 on the transitions between discharge regimes are valid for discharges in the frequency range 1-100 kHz.

For the diffusion of charged species during the interpulse, the assumption that all charged species diffuse at the velocity of positive ions is a good compromise between accuracy and complexity for the simulation of the air plasma in interpulses of nanosecond repetitively pulsed discharges in air at 300 and 1000 K.

Then we have simulated several consecutive nanosecond voltage pulses at $T_g =$ 1000 K and at a frequency of 10 kHz. We have observed that in a few voltage pulses, the discharge reaches a 'stable' glow regime also observed in the experiments [*Pai*, 2008]. The shape of the voltage pulse has been chosen such that the voltage starts to decrease 0.5 ns after the connection of discharges to be in the glow regime as discussed in Chapter 2. We have also observed that the preionization is after the two first pulses rather high ($\mathrm{n_e} = 10^{10}\,cm^{-3}$) and uniform over a radius of about 2 mm, much larger than the diameter of the positive discharge ignited at the positive point. These results validate the assumption of a uniform pre-ionization of the interelectrode gap used in Chapter 2 to study in detail the discharge dynamics during one voltage pulse. Finally, we have taken into account the convection of charged species during the interpulse due to an external air flow. We have shown that the flow may reduce or increase the ignition time of the positive discharge by enhancing or removing the preionization around the anode. We have found that the external air flow may promote the corona-to-glow transition in a very narrow range of parameters.

Chapter 4

Simulation of the spark regime with fast gas heating and compressible flow dynamics

4.1 Introduction

In Chapter 3, we have studied the glow regime of nanosecond repetitively pulsed discharges in air. In this chapter, we propose to study the nanosecond spark regime. As shown in the experiments [*Xu et al.*, 2012], the nanosecond spark discharge may significantly heat the ambient air on short timescales and induce shockwave propagation. In this chapter we will discuss several models for the fast-heating of air by the nanosecond spark and we will study the formation and propagation of shockwaves induced by the discharge. The numerical results obtained will be compared to experiments.

4.2 Simulation of the nanosecond spark regime

4.2.1 Numerical model of the nanosecond spark

In Chapter 2, we have shown that during the glow to spark transition, the electric field in the gap becomes rather uniform. If the average value of the Laplacian electric field (*i.e.* the applied voltage divided by the gap length) is higher than the breakdown field at the considered temperature, we have over-voltage condition. In this case, the electron density increases during the spark phase while the electric field remains constant. This results in a very fast increase of the conductive current and the energy released in the discharge. As the electron density increases, the dielectric relaxation time of the plasma defined in Section 1.2 decreases (see Equation (1.5)). In the spark regime, we have noted that the Maxwell time becomes rapidly of the order of 10^{-16} s, *i.e.* much less than the other time scales of relevance for the selection of the simulation time step. With so small time steps, it is very time consuming to simulate the spark phase of a nanosecond pulsed discharge with the fluid model and the explicit numerical method described in Section 1.3. This difficulty could be considered as non-intuitive as in comparison to the streamer phase, in the spark phase the electric field remains rather constant and the chemistry of charged species is much slower. However, the timestep limitation is due to thin regions with space charges close to electrodes and on the wings of the discharge filament.

In the literature, most of the studies on nanosecond spark discharges have been done in 0D or 1D. In these studies, it is assumed that the electric field is uniform over the cross-section of the discharge and is constant or derived from an experimental current distribution as in *Popov* [2011b] and *Naidis* [2008]. In this work, in order to simulate the nanosecond spark discharge in 2D, we have used a simple approach, which we propose to validate *a posteriori*, based on the comparison of simulation results with experiments. We have assumed that after the connection, the discharge structure remains the same, then the electric field in the spark phase is varying proportionally to the applied voltage:

$$|\vec{\mathrm{E}}| = \mathrm{AV(t)} \tag{4.1}$$

Where V(t) is the applied voltage, and A is a constant. Combining Equation (4.1) to the Maxwell-Gauss equation, one finds that the space charge density ρ during the spark phase has to evolve proportionally to the applied voltage:

$$\rho = \mathrm{AV(t)} \tag{4.2}$$

This forced evolution of the space charge density can be obtained by adding a source term for charged species in each cell of the computational domain. In a first approximation, it is reasonable to assume that only electrons have a sufficiently high mobility to ensure the fast variation of the space charge proportionally to the applied voltage. The added source term is then an electron source term. According to the conservation equation of current, this source term can be seen as the divergence of the conductive current:

$$\partial_{\mathrm{t}}\rho + \vec{\nabla} \cdot \vec{\mathrm{j_c}} = 0 \tag{4.3}$$

More details about the model are given in appendix A.4. This simple approach is non conservative due to the additional electron source term. However, the lack or excess of electrons in the regions with space charges during the spark regime is relatively small compared to the total electron density which increases by orders of magnitude during the spark phase. Then, as a first step, we propose to add an electron source term to modify the space charges when the voltage varies without solving consistently all the charged species fluxes according to equation4.3. Furthermore, as nanosecond spark discharges last

only a few nanoseconds, we have neglected diffusion processes and thermal conduction in the gas and in metallic electrodes.
As the current increases significantly in the spark phase, the magnetic field could play a role on the transport of charged species and on the discharge structure. We have then estimated the maximum value of the magnetic field during the spark discharge assuming that the discharge is equivalent to a plasma channel of constant radius R, of length equal to the gap size G, and with a total conductive current I (see Appendix A.1):

$$B_{max} = \frac{\mu_0 I G}{4\pi R\sqrt{(\frac{G}{2})^2 + R^2}} \tag{4.4}$$

For a typical conductive current $I = 40$ A, a radius of curvature $R = 500\,\mu$m, and a gap size $G = 2.5$ mm, the maximum magnetic field is about 0.01 T. The Lorentz force $\mathrm{F_e}$ on electrons resulting from the electric and the magnetic fields is given by:

$$\vec{F}_{\mathrm{e}} = q_{\mathrm{e}}(\vec{E} + \vec{v}_{\mathrm{e}} \times \vec{B}) \tag{4.5}$$

In the spark regime, we have $v_{\mathrm{e}} \simeq 7 \times 10^6$ V cm^{-1}, and a magnetic field of $\simeq$ 0.01 T, the induced electric field $|\vec{v}_{\mathrm{e}} \times \vec{\mathrm{B}}|$ is then $\simeq$ 700 V cm^{-1} which is relatively small compared to the electric field in the discharge ($\simeq$ 20 kV cm^{-1}). The Hall parameter of the discharge gives an estimation of the angle of deflection of electrons θ due to the presence of the magnetic field:

$$\frac{q_{\mathrm{e}} B}{m_{\mathrm{e}} \nu} = \tan(\theta) \tag{4.6}$$

For $\nu = 10^{13}$ s^{-1}, and a magnetic field of 0.01T, the Hall parameter is very small and $\theta \simeq 0.01\,^{\circ}$. In this case, the magnetic effects have a negligible influence on the electron trajectories and the discharge structure. We have checked that this assumption is valid for currents up to 100 A and the same discharge radius.

4.2.2 Reference test-case of a nanosecond spark discharge at 1000 K

As a reference test-case of a nanosecond spark discharge, in this section and in Sections 4.3, 4.5 and 4.6, we consider a point-to-point discharge in air at 1000 K with a gap size of 2.5 mm, an applied voltage of 5100 V and electrodes with a radius of curvature of 300 μm. This test-case is very close to the spark multi-pulse discharge obtained experimentally in *Rusterholtz et al.* [2012] with a maximum conductive current of 40 A (Figure 4.1). As explained in Section 1.7, during the voltage pulse, we compute the 2D distribution of the discharge energy as a function of time $e_{\mathrm{J}}(t)$. Figure 4.2 shows the distributions of the absolute value of the electric field, the electron density and the discharge energy at $t = 0, 2, 4, 6, 8$ and 10 ns. We note that the discharge energy density increases significantly after the connection for t>4 ns. In particular, we observe two peaks close to both point electrodes. In fact, as the discharge radius is smaller close to the point than in the middle of the gap, the conductive current is higher in these regions, due to the continuity of the current.

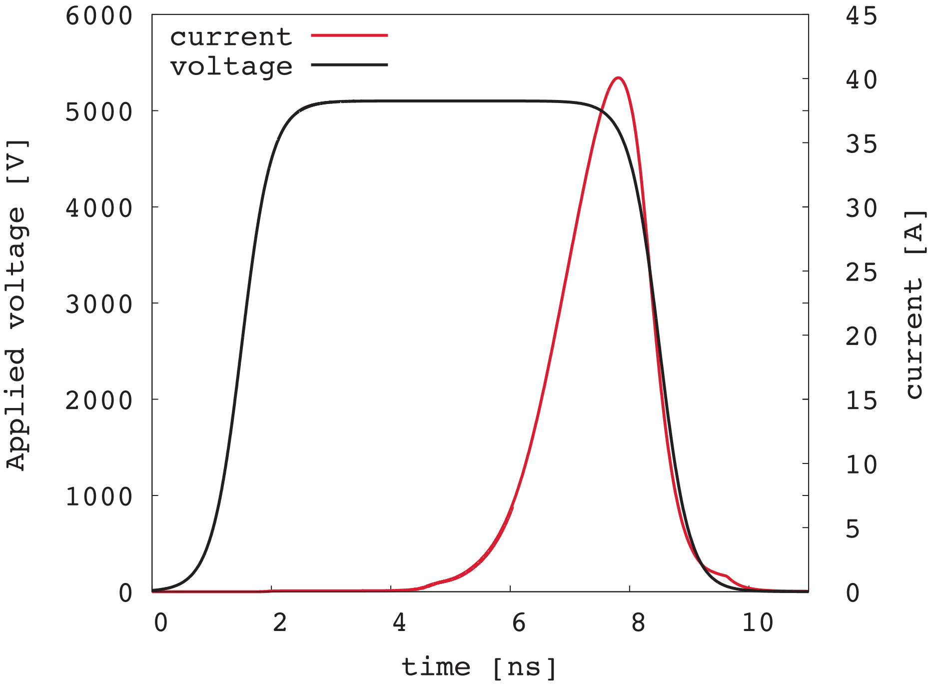

Figure 4.1: *Reference test-case of a nanosecond spark discharge in air at 1000K for an applied voltage of 5100 V and a maximum conductive current of 40 A. The pulse duration is 10 ns with a rise and a decrease time of 2 ns. The connection time between positive and negative discharges is 4.5 ns. The spark phase duration is around 3 ns.*

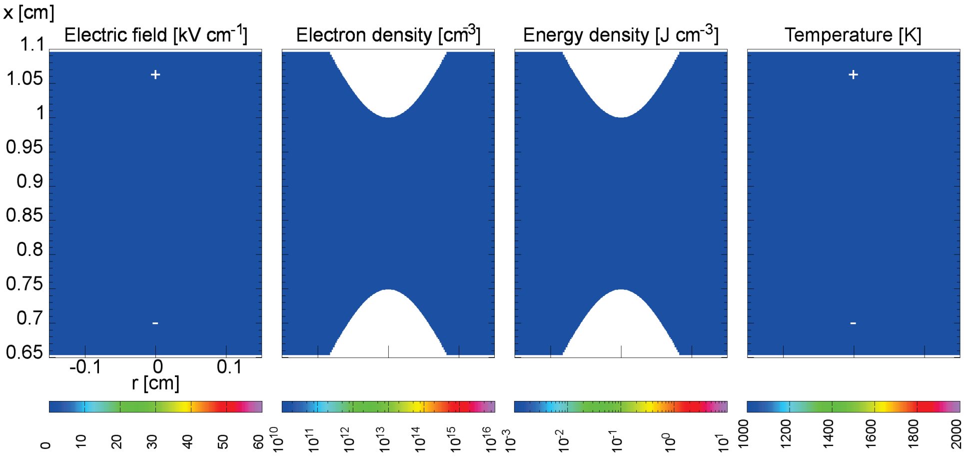

t=0 ns

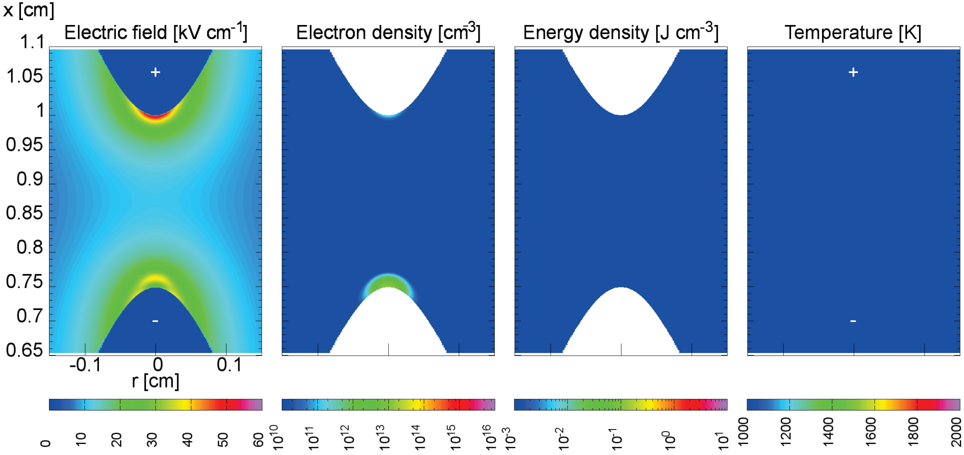

t=2 ns

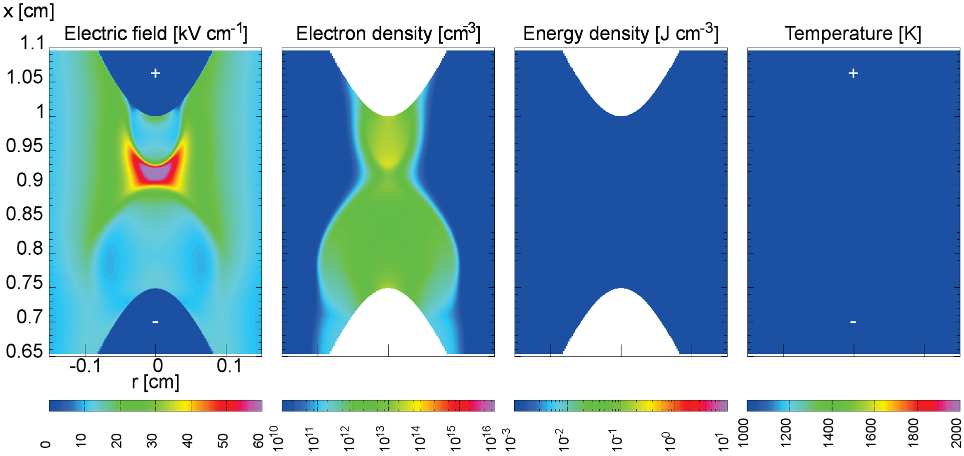

t=4 ns

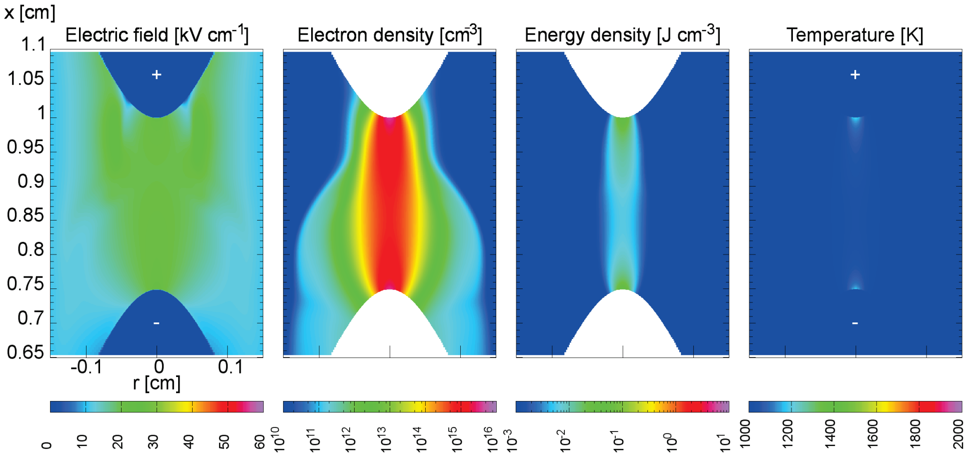

t=6 ns

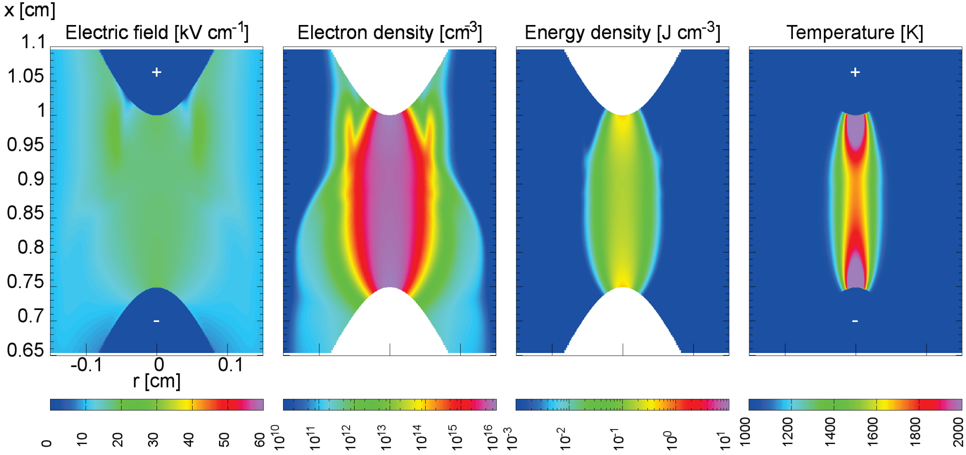

t=8 ns

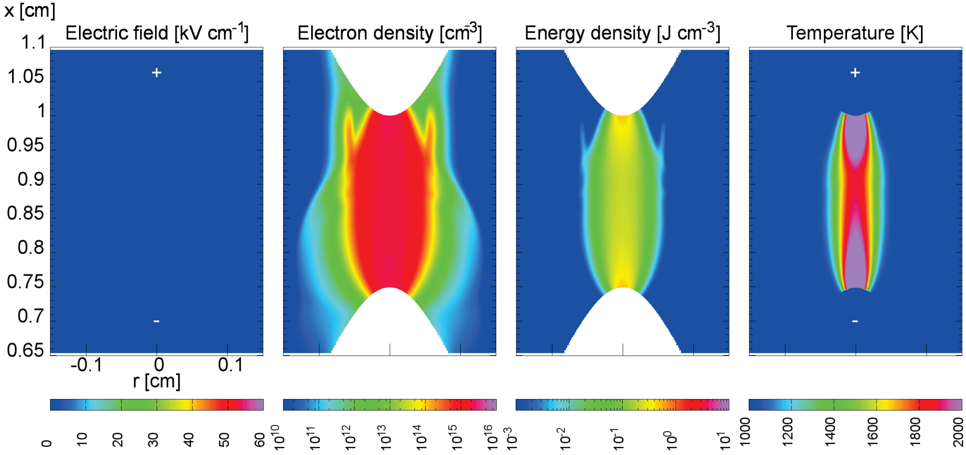

t=10 ns

Figure 4.2: *Cross-sectional views of the magnitude of the electric field, electron density, discharge energy density and neutral gas temperature for the reference nanosecond spark of Figure 4.1. The neutral gas temperature is obtained assuming an instantaneous gas-heating with* $\eta_R = 30\%$ *(see Section 4.3.3).*

4.3 Coupling of nanosecond repetitively pulsed discharges with a gas flow

4.3.1 Introduction

Different experimental studies have shown that nanosecond repetitively pulsed discharges have a significant influence on flows even at supersonic velocities [*Nishihara et al.*, 2011; *Ivanov et al.*, 2009]. NRPD are then very promising for flow control applications. Recently, *Xu et al.* [2012] have shown using fast Schlieren imaging that the spark regime of nanosecond repetitively pulsed discharges produce shockwaves in a wide range of air temperature conditions (between 300 K and 1000 K) at atmospheric pressure.

The influence of a plasma discharge on a flow is due to two processes: the first one is the momentum transfer from accelerated charged species to the neutral gas, generating the EHD (Electro Hydro Dynamic) and MHD (Magneto Hydro Dynamic) forces. The second one is the heating of the neutral gas and its thermal expansion. EHD forces are very important for DBD actuators [*Starikovskii et al.*, 2009; *Boeuf et al.*, 2007], and MHD forces are promising for supersonic flight applications [*Nishihara et al.*, 2005; *Adamovich et al.*, 2008]. However, these two effects are negligible in the case of nanosecond pulsed discharges. Indeed, using NRPD, no ionic wind has been measured experimentally and the shockwaves propagating in all directions are hardly compatible with a directional force as the EHD force. We have estimated the maximum velocity due to momentum transfer from positive ions to the neutral gas during a positively pulsed nanosecond discharge as in *Boeuf et al.* [2007]. First, the force applied by positive ions on the neutral gas through collisions is $f_{\mathrm{p}\to\mathrm{g}} = \rho_\mathrm{p} V_\mathrm{p} \nu_{\mathrm{p}\to\mathrm{g}}$ where indexes p and g refer to the positive ions and to the neutral gas. ρ_i and V_i are respectively the mass density and the velocity of specie i and $\nu_{\mathrm{p}\to\mathrm{g}}$ is the collision frequency between positive ions and neutral molecules. To estimate the maximum velocity that positive ions provide to the neutral gas during a positively pulsed nanosecond discharge, we have simplified the momentum equation to:

$$\rho_\mathrm{g} \partial_t V_\mathrm{g} = f_{\mathrm{p}\to\mathrm{g}} \tag{4.7}$$

For a pulse duration of $\mathrm{T}_\mathrm{pulse}$, we have a maximum velocity of:

$$V_\mathrm{g}(\mathrm{T}_\mathrm{pulse}) \simeq \mathrm{T}_\mathrm{pulse} \frac{f_{\mathrm{p}\to\mathrm{g}}}{\rho_\mathrm{g}} \tag{4.8}$$

For a rather intense nanosecond spark discharge, we have $\nu_{\mathrm{p}\to\mathrm{g}} = 10^{13} s^{-1}$, a positive ion density of 10^{15} cm^{-3} and a neutral gas density of the order of 10^{19} cm^{-3}. With an ion velocity $V_\mathrm{p} = 1000$ km s^{-1}, and a pulse duration of 10 ns, Equation (4.8) gives a maximum velocity of the neutral gas of 10^{-5} m s^{-1}, which is negligible.

As shown in several numerical simulations [*Bityurin et al.*, 2008] and experiments [*Starikovskii et al.*, 2009], the main mechanism by which NRP discharges influence a flow is through the fast heating of the neutral gas. Indeed, during a nanosecond discharge, a significant part of the discharge energy is used to produce vibrationally excited molecules and electronically excited atoms and molecules. If the relaxation of these internal energy modes is fast enough, the translational temperature of the gas increases rapidly in the discharge channel and shockwaves are generated. Different experimental and theoretical works on the evolution of the gas temperature just after the voltage pulse of a NRP discharge in air at atmospheric pressure have shown that the heating rate may be very high, of the order of 10^{10} K s^{-1} [*Rusterholtz et al.*, 2012]. Then the fast heating is the best scenario to explain the formation of shockwaves observed in experiments on NRPD [*Xu et al.*, 2011].

4.3.2 Constant gas density approximation

To study the coupling of fast heating nanosecond repetitively pulsed discharges with ambient air, we have to question the necessity to solve flow equations (Navier-Stokes or Euler equations) during the voltage pulse. If the temperature increase during the voltage pulse is very small ($< 10\,^\circ$), the neutral gas density remains constant and then, there is no need to solve flow equations during the voltage pulse. If the temperature increase during the voltage pulse is more significant, the gas density may vary during the pulse and then change the reduced electric field. In this case, the gas heating has a significant influence on the discharge dynamics. We have then compared the duration of the pulse T_{pulse} with the characteristic time for the change of neutral gas density due to heating, defined as $R_{\text{s}}/c_{\text{max}}$ where R_{s} is the typical radius of the discharge, and c_{max} is the maximum of the sound velocity in the path of the discharge. The increase of the neutral gas temperature leads to an increase of the speed of sound: $c_{\text{max}} \propto \sqrt{T_{\text{max}}}$. Then, the time necessary for acoustic waves to propagate inside the heated region is a good approximation for the time-scale of the neutral gas density variation. It is interesting to note that if

$$T_{\text{pulse}} \ll \frac{R_{\text{s}}}{c_{\text{max}}} \tag{4.9}$$

neutral species are immobile during the voltage pulse. Then even if the temperature increases during the voltage pulse, the neutral gas density remains the same [*Naidis*, 2008]. In this case, the temperature increase has an influence on chemical rates and transport parameters, but its impact on the discharge dynamics is small. It is important to note that the condition given by Equation (4.9) is rather strict as the temperature field generated by the discharge is highly non-uniform. For an intense spark discharge condition with a temperature increase up to 3000 K and a discharge diameter of 500 μm, we have checked that the condition given by Equation (4.9) is valid for $\text{T}_{\text{pulse}} \ll 500$ ns.

As in our case, the durations of voltage pulses are in the range of 5 to 10 ns, the condition given by Equation (4.9) is valid. Then in our conditions, there is no need to solve the flow equations during the voltage pulse and we have used the approximation of a constant neutral gas density during the voltage pulse.

4.3.3 First simplified model for fast gas heating : instantaneous heating and its coupling with the flow

In the literature, these last years, several works [*Popov*, 2011a; *Mintoussov et al.*, 2011; *Rusterholtz et al.*, 2012; *Aleksandrov*, 2010], have been devoted to the study of the fast relaxation of the energy stored in internal modes of molecules and atoms in air and the subsequent increase of the translational temperature of the neutral gas. However, there are still some uncertainties on the chemical processes involved and the reaction rate coefficients of some reactions involving excited states. Therefore as a first step, we have assumed in this section that a fraction η_R of the discharge energy instantaneously heats the neutral gas. In Section 4.5.2 a parametric study will be carried out on the influence of the value of η_R on the results. Then, in Section 4.5.3, the heating of the neutral gas by the discharge will be considered to occur at a finite rate. Finally in Section 4.6, the energy stored in the different internal modes will be studied and a chemical model based on the two-step mechanism initially proposed by *Popov* [2011b] will be used to model more accurately the dynamics of fast heating in nanosecond pulsed discharges and its coupling with an air flow.

First, if the gas heating is considered as infinitely fast, at each point of the computational domain during the integration timestep dt, the discharge energy density $e_{\mathrm{J}}(t)$ during the voltage pulse is converted instantaneously into an increase of the translational temperature of the neutral gas T_{g} by:

$$\int_{t-\mathrm{d}t}^{t} C_{\mathrm{v}}(t)\mathrm{d}T_{\mathrm{g}}(t) = \frac{\eta_R}{\rho_0}(e_{\mathrm{J}}(t) - e_{\mathrm{J}}(t-\mathrm{d}t)) \qquad (4.10)$$

Where C_{v} is the specific thermal capacity at constant volume (J kg^{-1} K^{-1}) and ρ_0 the density of the neutral gas which is assumed to be constant during the discharge. Equation (4.10) is solved assuming that C_{v} is constant during an integration timestep dt and using a predictor-corrector method:

$$\mathrm{d}T_{\mathrm{g}}(t) = \frac{\eta_R}{\rho_0 C_{\mathrm{v}}^{\mathrm{corrected}}}(e_{\mathrm{J}}(t) - e_{\mathrm{J}}(t-\mathrm{d}t)) \qquad (4.11)$$

In the following of this chapter, we will discuss the influence of the value of η_R on the results. As a reference, we have used the value of $\eta_R = 30\%$ which seems to be a reasonable value for the discharge condition we study, based on the works of *Aleksandrov* [2010]. Then, Figure 4.2 shows for the reference nanosecond spark of Section 4.2.2 and $\eta_R = 30\%$, the temperature distribution during the pulse, assuming a instantaneous gas heating. We note that the temperature increases after the connection of the discharge, close to point electrodes where the discharge energy is the highest. At the end of the pulse at $t = T_{\text{pulse}} = 10$ ns, we observe a heated channel. In this work, the temperature $T_{\text{g}}(t = T_{\text{pulse}})$ obtained at the end of the voltage pulse will be used as a source term for the gas-dynamic Euler equations. This initial temperature distribution will generate pressure gradient source terms for the momentum conservation equations of the Euler equations given by:

$$\left\{\begin{array}{ll} \partial_t \rho + \vec{\nabla} \cdot (\rho \vec{V}) & = 0 \\ \partial_t (\rho V_x) + \vec{\nabla} \cdot (\rho V_x \vec{V}) & = -\partial_x p \\ \partial_t (\rho V_r) + \vec{\nabla} \cdot (\rho V_r \vec{V}) & = -\partial_r p \\ \partial_t (\rho e) + \vec{\nabla} \cdot (\rho h \vec{V}) & = 0 \end{array}\right. \tag{4.12}$$

$$\text{with :} \qquad e = \frac{1}{2} V^2 + u \qquad u = C_v T = \frac{RT}{(\gamma - 1)} \qquad h = u + \frac{p}{\rho}$$

where ρ is the density of the neutral gas, V_x and V_r are respectively the axial and the radial components of the fluid velocity $\vec{V}$, e is the energy density of the neutral gas, sum of the specific kinetic energy and the specific internal energy u (J cm^{-3}). The system given by Equations (4.12) is closed by the ideal gas state equation:

$$p = \rho R_s T = \rho u (\gamma - 1) \tag{4.13}$$

where R_s is the specific constant and γ is the isentropic coefficient of the neutral gas, assumed to be constant. The system given by Equations (4.12) can be also written as:

$$\partial_t \mathbf{U} + \partial_x \left(\mathbf{F_x}(\mathbf{U}) \right) + \frac{1}{r} \partial_r \left(r \mathbf{F_r}(\mathbf{U}) \right) = -\partial_x \mathbf{P_x} - \partial_r \mathbf{P_r} \tag{4.14}$$

with:

$$\mathbf{U} = \begin{pmatrix} \rho \\ \rho V_x \\ \rho V_r \\ \rho e \end{pmatrix} \quad \mathbf{P_x} = \begin{pmatrix} 0 \\ p \\ 0 \\ 0 \end{pmatrix} \quad \mathbf{P_r} = \begin{pmatrix} 0 \\ 0 \\ p \\ 0 \end{pmatrix}$$

$$\mathbf{F_x}(\mathbf{U}) = \begin{pmatrix} \rho V_x \\ \rho V_x^2 \\ \rho V_r V_x \\ (\rho e + p) V_x \end{pmatrix} \quad \mathbf{F_r}(\mathbf{U}) = \begin{pmatrix} \rho V_r \\ \rho V_x V_r \\ \rho V_r^2 \\ (\rho e + p) V_r \end{pmatrix}$$

In the following Section 4.4, we present and validate the numerical model used to solve Euler equations in this work. In Section 4.5 and following sections, we present the results of the simulation of the fast heating of the flow by the discharge.

4.4 Numerical models for Euler equations

4.4.1 Dimensional Splitting

As explained in the previous section, the instantaneous heating of a nanosecond pulsed discharge can be modeled as an initial temperature field applied instantaneously to the neutral gas (assuming a constant mass density). Then, according to Equation (4.13), the pressure increases proportionally to the temperature in the heated region. This approximation of an instantaneous heating will be discussed in the following sections and is equivalent to an explosion problem with a fast relaxation of a high pressure, high temperature heated region. As experimental Schlieren images show clearly that there are no significant turbulences and 3D effects during the neutral gas expansion, we have used a 2D axisymmetric model. Therefore, we have assumed that the 2D temperature field is an output from the discharge code and an input of 2D axisymmetric Euler equations (Equations (4.14)). To solve 2D Euler equations, a dimensional splitting in axial and radial directions is carried out. For the axial direction the 1D Euler equations can be written in the form:

$$\partial_t \mathbf{U} + \partial_x \left(\mathbf{F_x}(\mathbf{U})\right) = -\partial_x \mathbf{P_x} \tag{4.15}$$

This equation can be rewritten as:

$$\partial_t \mathbf{U} + \partial_x \left(\mathbf{F_x}(\mathbf{U}) + \mathbf{P_x}\right) = 0 \tag{4.16}$$

with no more source term in the right side of the equation. In this case, the finite difference or finite volume discretizations of Equation (4.16) are rigorously equivalent:

$$\frac{\mathbf{U}_i^{t+\Delta t} - \mathbf{U}_i^t}{\Delta t} + \frac{\left(\mathbf{F_x}(\mathbf{U}) + \mathbf{P_x}\right)^t_{i+\frac{1}{2}} - \left(\mathbf{F_x}(\mathbf{U}) + \mathbf{P_x}\right)^{\mathrm{t}}_{\mathrm{i}-\frac{1}{2}}}{\Delta x} = 0 \tag{4.17}$$

The fluxes $\mathbf{F_x}(\mathbf{U}) + \mathbf{P_x}$ at cell interfaces $i - \frac{1}{2}$ and $i + \frac{1}{2}$ are the solutions of a Riemann problem: a discontinuity of primitive variables between the two adjacent cells. The fluxes can then be computed with any four component 1D Riemann solver.

In the radial direction, the 1D Euler equations are given by:

$$\partial_t \mathbf{U} + \frac{1}{r}\partial_r \left(r\mathbf{F_r}(\mathbf{U})\right) = -\partial_r \mathbf{P_r} \tag{4.18}$$

Similarly to the axial direction, this equation can be rewritten as:

$$\partial_t \mathbf{U} + \partial_r \left(\mathbf{F_r}(\mathbf{U}) + \mathbf{P_r} \right) = \frac{-\mathbf{F_r}(\mathbf{U})}{r} \tag{4.19}$$

The left side of Equation (4.19) is the same as for the axial direction and then all the numerical methods available for the 1D axial problem can be used. However, in the radial direction, there is a geometric source term in the right side of Equation (4.19). As mentioned by *Li* [2003] there is a severe drawback to solve Equation (4.19) as the original multidimensional conservation law is not preserved, i.e., the numerical schemes may not be conservative in multidimensional sense. Therefore, Equation (4.18) can be rewritten as:

$$\partial_t \mathbf{U} + \frac{1}{r} \partial_r \left(r(\mathbf{F_r}(\mathbf{U}) + \mathbf{P_r}) \right) = \frac{\mathbf{P_r}}{r} \tag{4.20}$$

This second approach is conservative with a finite volume discretization approach. The finite volume discretization is obtained by integrating Equation (4.20) over the volume V of a cell and by applying the Ostrogradsky's theorem:

$$\frac{1}{V} \iiint_V \partial_t \mathbf{U} \mathrm{d}V + \frac{1}{V} \iint_S \left(\mathbf{F_r}(\mathbf{U}) + \mathbf{P_r} \right) \mathrm{d}S = \frac{1}{V} \iiint_V \frac{\mathbf{P_r}}{r} \mathrm{d}V \tag{4.21}$$

Assuming that the pressure is uniform inside the volume of the cell we can compute the source term as:

$$\frac{\overline{\mathbf{U}}_j^{t+\Delta t} - \overline{\mathbf{U}}_j^t}{\Delta t} + \frac{\left[\left(\mathbf{F_r}(\mathbf{U}) + \mathbf{P_r} \right)^t S \right]_{j+\frac{1}{2}} - \left[\left(\mathbf{F_r}(\mathbf{U}) + \mathbf{P_r} \right)^t S \right]_{j-\frac{1}{2}}}{V} = \frac{\mathbf{P_r}^t}{r_j} \tag{4.22}$$

where $\overline{\mathbf{U}}$ is the space averaged value of $\mathbf{U}$ on the volume of the cell.

4.4.2 Validation test cases

4.4.2.1 The Sod shock-tube problem

The Sod shock-tube problem is a particular 1D Riemann problem widely used to test compressible fluid-dynamics codes. As for any Riemann problem, the space in the axial direction (x axis) is split into two different regions with different physical quantities separated by a discontinuity in $x = 0$. The Sod conditions are characterized by a high pressure, high density gas on the left region $x < 0$ and a right region ($x > 0$) with a 10 times smaller pressure and a 8 times smaller density. The Sod shock tube problem is rather stiff due to this discontinuity and is very useful to test the stability and the accuracy of a compressible fluid-dynamics code since the exact solution of the Riemann problem can be computed [*Toro*, 2009; *Munafo*, 2011]. Figure 4.3 shows the time evolution of the primitive variables of a Sod shock-tube problem. It compares the exact solution with the numerical solution computed with the approximate Riemann solver HLLC [*Toro*, 2009] on a 1.6 cm domain with 500 cells ($\Delta x = 3.2\,\mu$m).

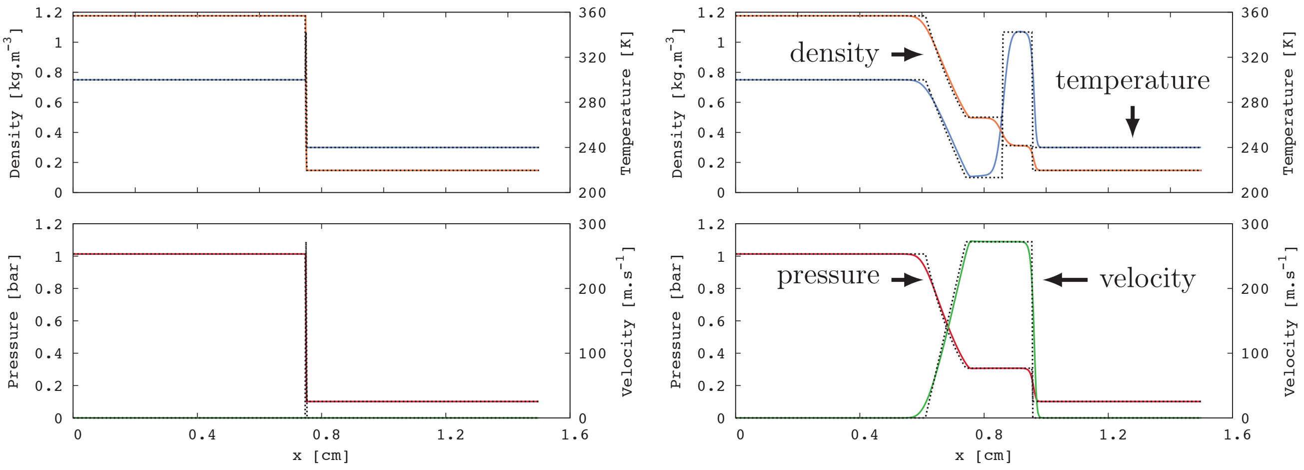

t=0 μs

t=4 μs

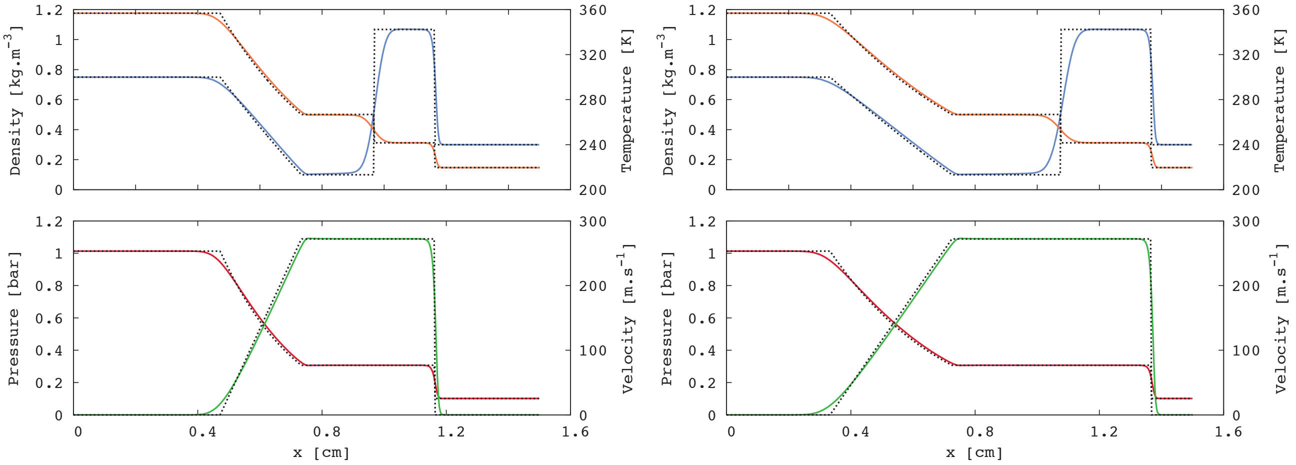

t=8 μs

t=12 μs

Figure 4.3: *Simulation of a 1D Sod shock tube problem in air with a HLLC Riemann solver on 500 cells and a second order Runge-Kutta time integration: Comparison of the 1D profiles of density (orange line), temperature (blue line), pressure (red line) and velocity (green line) with the exact solution (dotted black line) at t=0, 4, 8 and 12μs.*

The accuracy of the solution can be significantly improved using reconstruction methods on conservative variables. The reconstructed values at cell interfaces define new Riemann problems which can be solved with any Riemann solver.

WENO and ENO reconstruction methods are non-oscillatory schemes that can achieve high order accuracy. In this case the choice of the Riemann solver to compute the fluxes at cell interfaces has a small influence on the results and a very simple and inexpensive Lax-Friedrichs method gives satisfactory results [*Shu*, 1997]. Unfortunately ENO and WENO reconstruction methods can not be applied easily for the radial direction [*Li*, 2003]. For this reason a much simpler MUSCL reconstruction has been applied to conservative variables U in order to build at each cell interface the left and right reconstructed values $\mathbf{U}^{\mathrm{L}}$ and $\mathbf{U}^{\mathrm{R}}$:

$$\left\{\begin{aligned} \mathbf{U}^{\mathrm{L}}_{i+\frac{1}{2}} &= \mathbf{U}_i + \frac{1-\phi}{4}\left(\mathbf{U}_i - \mathbf{U}_{i-1}\right) + \frac{1+\phi}{4}\left(\mathbf{U}_{i+1} - \mathbf{U}_i\right) \\ \mathbf{U}^{\mathrm{R}}_{i+\frac{1}{2}} &= \mathbf{U}_{i+1} - \frac{1+\phi}{4}\left(\mathbf{U}_{i+1} - \mathbf{U}_i\right) - \frac{1-\phi}{4}\left(\mathbf{U}_{i+2} - \mathbf{U}_{i+1}\right) \end{aligned}\right. \tag{4.23}$$

where ϕ is a free parameter between -1 (decentered evaluation) and 1 (centered evaluation). In the following, we will consider that $\phi = 1/3$ which corresponds to a third order MUSCL reconstruction. MUSCL schemes are not TVD (Total Variation Diminishing) and a slope limiter has to be used to prevent oscillations in regions with steep gradients. Figure 4.4 shows the same Sod shock-tube problem as Figure 4.3 but with a third order MUSCL reconstruction, a Lax-Friedrichs Riemann solver and a Minmod slope limiter. It has been checked that the choice of the Riemann solver has a negligible influence on the results.

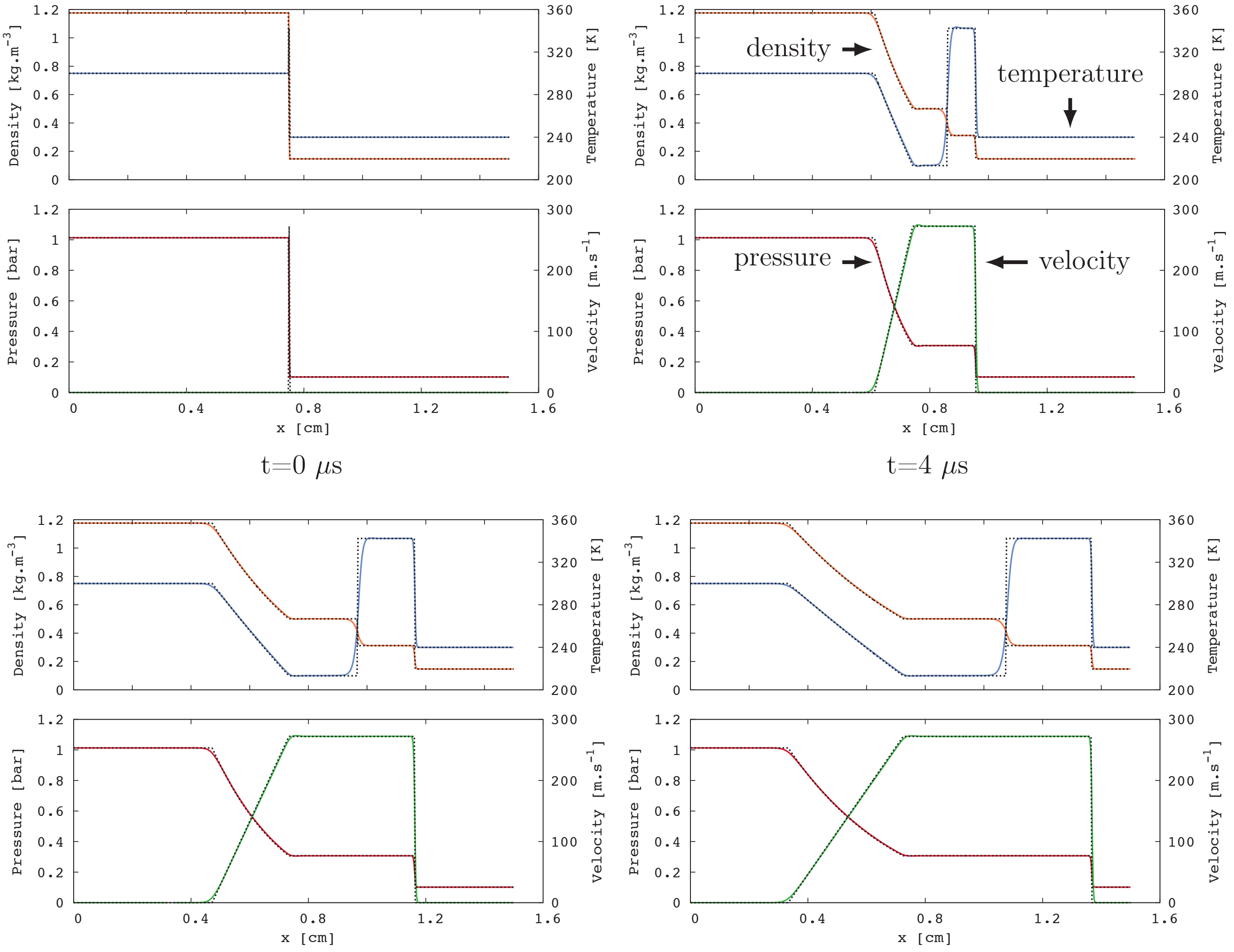

t=0 μs

t=4 μs

t=8 μs

t=12 μs

Figure 4.4: *Simulation of a 1D Sod shock tube problem in air with a Lax-Friedrichs Riemann solver on 500 cells, a 3^{rd} order MUSCL reconstruction with a Minmod slope limiter and a second order Runge-Kutta time integration: Comparison of the 1D profiles of density (orange line), temperature (blue line), pressure (red line) and velocity (green line) with the exact solution (dotted black line) at t=0, 4, 8 and 12μs.*

4.4.2.2 The Sedov explosion

The Sod shock-tube problem is a pure 1D problem and a different test-case has to be studied in order to validate the Euler code in the radial direction. The Sedov explosion problem provides very stiff test-cases for 1D, 2D and even 3D compressible codes [*Kamm*, 2000]. The Sedov explosion deals with the fast relaxation of an initial amount of energy E_0 deposited in an infinitely small volume in a steady ideal fluid with an initial density of the form $\rho = \rho_0 r^w$

where ρ_0 and w are constant and r is the radial position. The interest of this test-case is that the amplitude and the position R of the generated shockwave as a function of time follow analytic similarity relations. For example, the position R of the shockwave as a function of time is given by:

$$R = \lambda(\frac{E_0 t^2}{\rho_0 \alpha})^{\frac{1}{(j+2-w)}} \tag{4.24}$$

where j is the dimensionality index: $j = 1$ corresponds to the planar geometry, the initial energy E_0 is then deposited on a plane at $r = 0$. $j = 2$ corresponds to the cylindrical geometry, with an initial energy deposited on a wire at $r = 0$. $j = 3$ corresponds to the spherical geometry, which is the closest to a realistic explosion, with E_0 deposited on a single point at $r = 0$. In the following, we will focus on the "Standard Sedov problem": a uniform initial background density ($w = 0$). The analytical solution of the Sedov problem at a given time is difficult to obtain and it requires to evaluate numerically several integrals. A numerical algorithm has been developed in *Kamm* [2000]. These authors have computed the solution at t=1 s for $\rho_0 = 1$ g cm^{-3} and $E_0 = 0.0673185$, 0.311357, and 0.851072 ergs respectively for planar, cylindrical and spherical geometries. Figure 4.5 shows that strong shockwaves propagate from the origin with very large density gradients in their front followed by a very low density region.

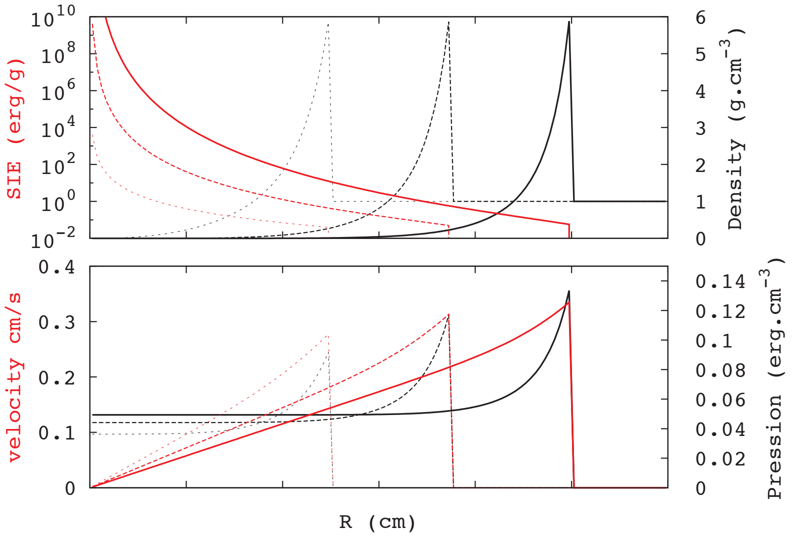

Figure 4.5: *Solution of the standard Sedov explosion problem at t=1 s: the background density is 1 g cm*$^{-3}$ *with an initial energy* $E_0 = 0.0673185$, 0.311357, *and* 0.851072 *ergs respectively for the planar (dotted lines), cylindrical (dashed lines) and spherical geometry (solid lines)*

However, this test case is rather academic since it requires a singular initial energy distribution, and a background fluid without any initial pressure and a rather high density. Then, in order to validate the Euler code, a more physical situation has to be considered. The analytical solution of the Sedov problem is valid only under the hypothesis of an infinitely strong shockwave: if the pressure inside the shockwave is much higher (ratio of 10^5) than the one of the steady fluid. If the background fluid pressure is zero this assumption is correct at any time. If the background fluid has some static pressure, the hypothesis is valid if the explosion is strong enough. Moreover, for the cylindrical and the spherical geometries the amplitude of the shockwave is decreasing as it propagates. Then the hypothesis of an infinitely strong shockwave is valid only during a short time. To verify this hypothesis in a cylindrical test-case, a very strong explosion is considered in a low density air of 0.1 kg m^{-3} with a constant polytropic coefficient $\gamma = 1.4$, and a background specific energy of 1 erg g^{-1} which corresponds to a background pressure and temperature both very close to zero (4 μPa and 1.39×10^{-7} K). The length of the domain is 0.2 m discretized on 1000 cells of 200μm. The initial singular energy is set to $E_0 = 10^4$ erg. Figure 4.6 shows the analytical solution computed at t=50 ns (dotted black line). This solution is used as an initial condition for the 2D axisymmetric Euler code (solid lines). As the analytical solution of the SIE (Specific Internal Energy) is singular on the axis of symmetry, there is a significant difference with the SIE considered in the Euler code very close to the axis. However, other quantities as density, velocity and pressure are not affected and we have checked that this difference on SIE has a negligible influence on the propagation of the shockwave. Figure 4.7 shows the evolution of the solution every 50 ns using the diffusive Lax-Friedrichs scheme. It can be seen clearly that the error increases with time and that the maximum amplitude of the density of the shockwave is not solved properly with an error of 25% at t=450 ns. However, the position of the maximum and the velocity of the front is well resolved by the scheme. Figure 4.8 shows the same test-case using the third order MUSCL reconstruction on the Lax-Friedrichs scheme. The error on maximum density in the shockwave is around 10% and the position and the shape of the wave is very well resolved without significant numerical diffusion. As a conclusion of this section, the good agreement obtained between the analytical solution of the Sedov test-case and our numerical model, validates the numerical resolution we have used for Euler equations in the radial direction.

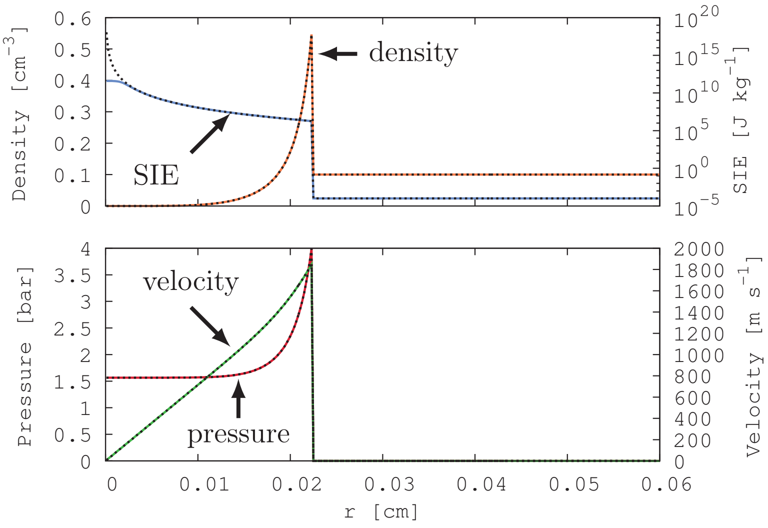

t=50 ns

Figure 4.6: *Standard Sedov problem solution at t=50 ns for the cylindrical geometry with* $E_0 = 10^4$ *erg,* $\gamma = 1.4$*, and a low background specific energy of 1 erg* g^{-1} *(dotted lines). The solution is used to compute the initial solution of the validation test-case of the 2D Euler code (solid lines)*

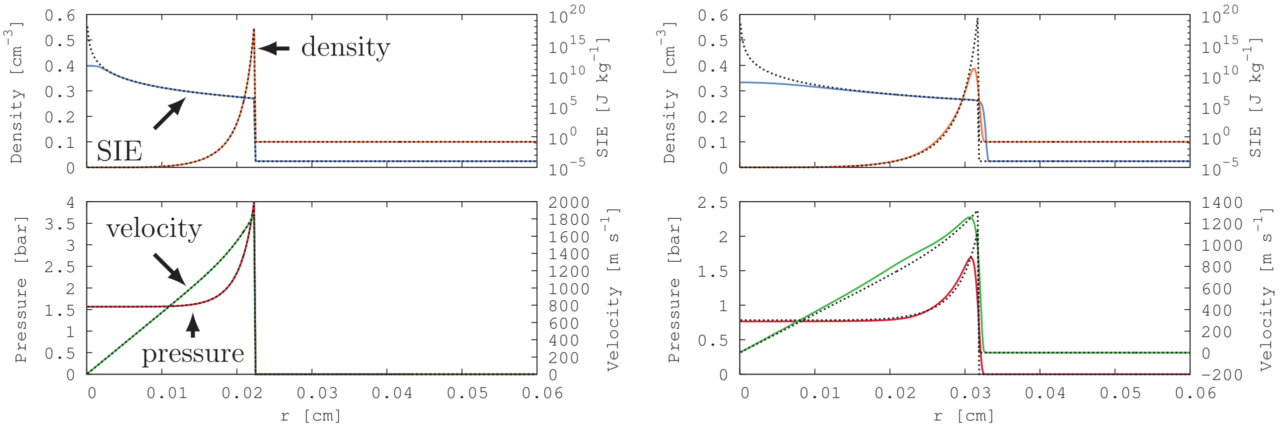

t=50 ns t=100 ns

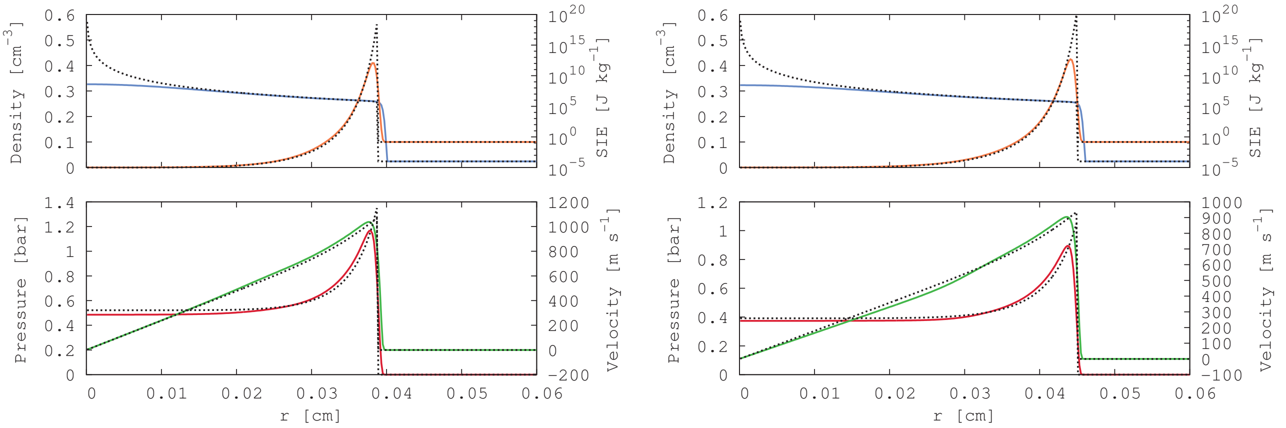

t=150 ns t=200 ns

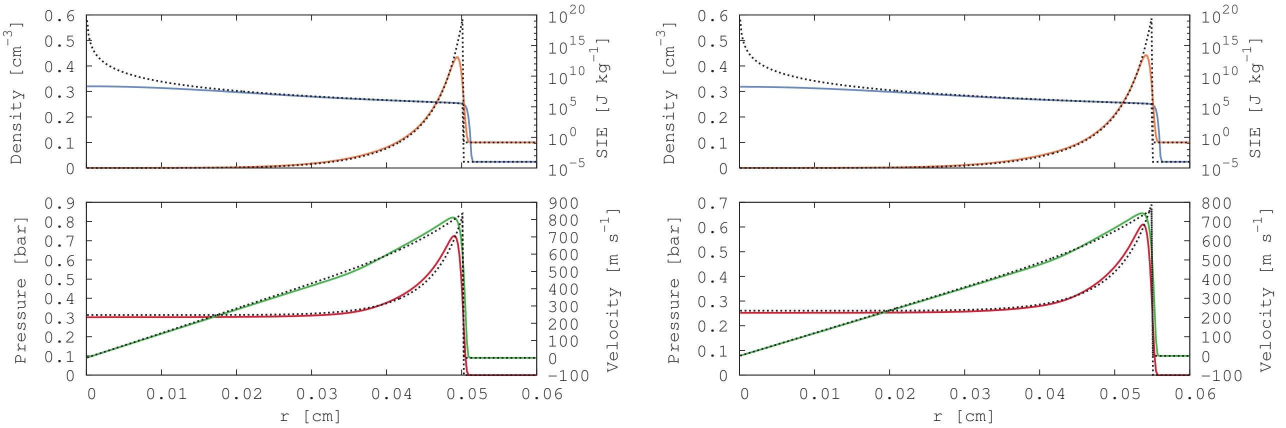

t=250 ns t=300 ns

Figure 4.7: *Cylindrical test-case. Results of the Euler 2D axisymmetric code with a Lax-Friedrichs scheme. Comparison with the analytical solution of the corresponding Sedov problem (dotted lines).*

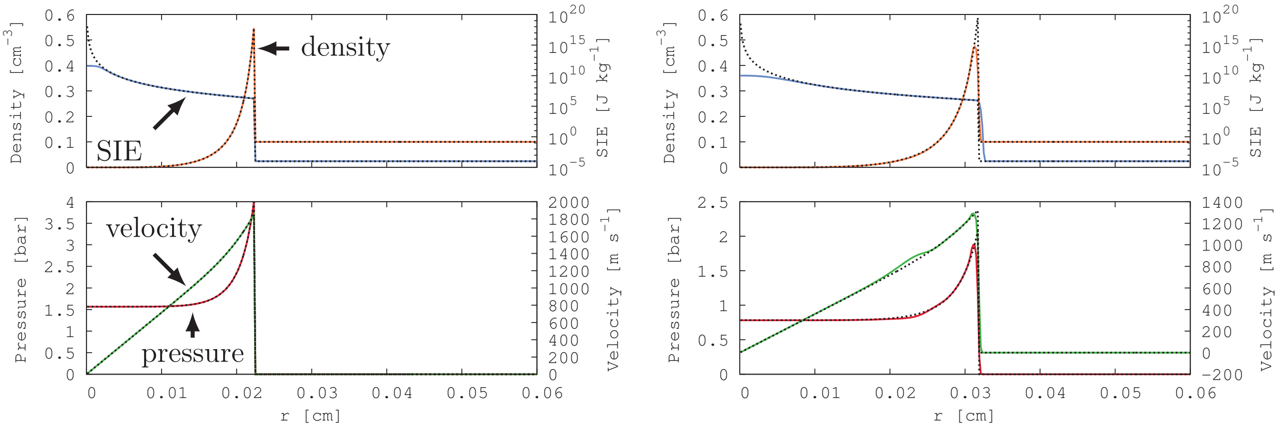

t=50 ns

t=100 ns

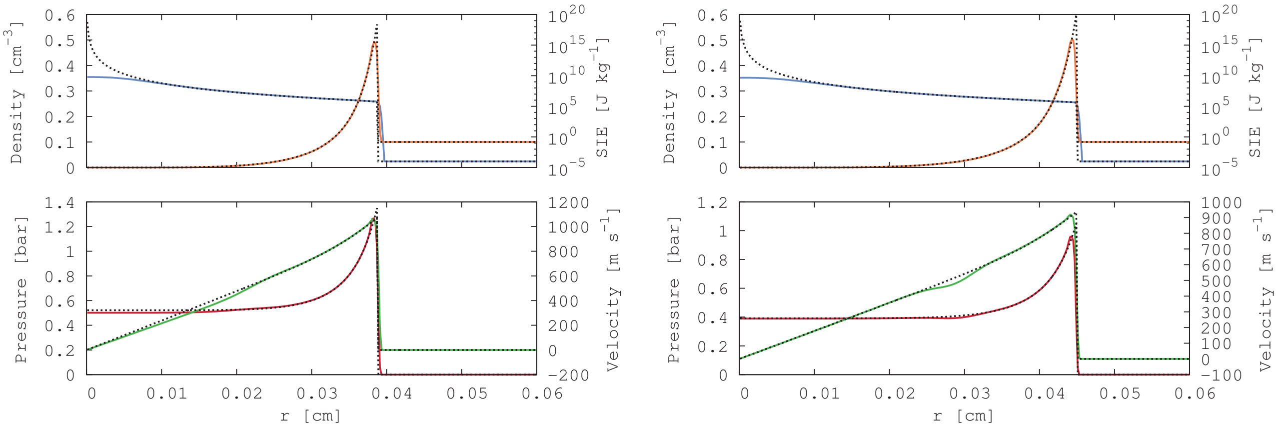

t=150 ns

t=200 ns

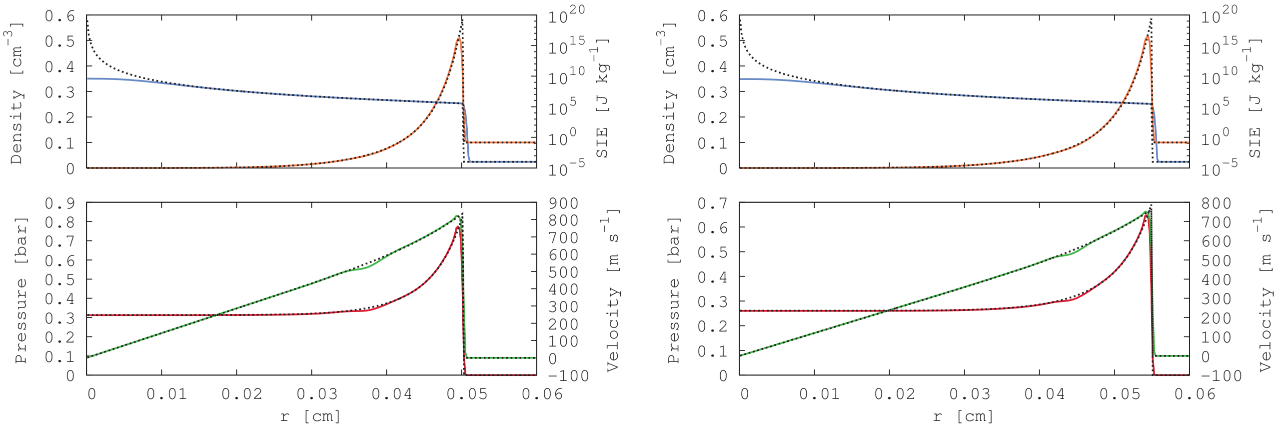

t=250 ns

t=300 ns

Figure 4.8: *Cylindrical test-case. Results of the Euler 2D axisymmetric code with a MUSCL scheme. Comparison with the analytical solution of the corresponding Sedov problem (dotted lines).*

4.5 2D simulation of shock-waves produced by a nanosecond spark discharge

4.5.1 Instantaneous heating of air at 1000K by a nanosecond spark discharge

Following the method described in Section 4.3.3, Figure 4.9 shows the 2D temperature field resulting from the reference nanosecond spark discharge in air at 1000 K (Section 4.2.2) in assuming that η_{R}=30% of the discharge energy instantaneously heats the air.

The resulting 2D temperature field at the end of the voltage pulse is an initial condition for the Euler code. The pressure is computed using the ideal gas law assuming a density of 0.35 kg cm^{-3}, which is the density of air at 1000 K, and an isentropic coefficient $\gamma = 1.4$. Figure 4.9 shows that the initial condition then consists in an homogeneous density in the whole domain, and a channel on the discharge path with high pressure and temperature and two hot spots close to electrode tips. Figure 4.10 shows the time sequence every 200 ns of the gas dynamics resulting from this infinitely fast heating up to 1.2 μs. At t =200 ns, we note that due to the very fast heating, the density has decreased very quickly close to the tip of the electrodes compared to the initial density (Figure 4.9). The density drops from 0.35 kg cm^{-3}, which is the air density at 1000 K to a minimum of 0.1 kg cm^{-3}. The velocity of the fluid has a cylindrical shape all around the heated channel with a higher value close to the hot spots. For $t > 400$ ns, a cylindrical shockwave characterized by jumps in pressure, density, temperature and velocity propagates radially. These jumps are more significant in the region close to the electrode tips due to the higher initial temperature. However, the shockwave propagation velocity is at every point of the wave front equal to the speed of sound in the unperturbed air at 1000 K (650 m s^{-1}). Behind the shockwave, a low density region remains with a pressure even less than the atmospheric pressure. This depletion is due to the displacement of air due to the velocity induced by the shockwave on the fluid. It can be interpreted as the fast dilatation of the hot channel produced by the discharge. Between t =800 ns and 1.2 μs two other shockwaves propagate from the tip of the electrodes inside the low pressure, low density channel. These shockwaves are reflections of the first cylindrical shockwave on the electrode tips. These successive shockwaves will increase the density in the channel and the pressure will finally converge to the atmospheric pressure. Figure 4.11 shows the 1D time evolution of the air density and temperature in the radial direction in the middle of the inter-electrode gap every 100 ns up to 900 ns. We note the fast depletion of the air density inside the hot channel and that the shockwave forms on the wings of the heated channel before propagating towards the surrounding air. Due to the cylindrical symmetry, the amplitude of the shockwave decreases as it propagates. The maximum density inside the shockwave is around 0.4 kg cm^{-3} which corresponds to an increase of 15% in comparison of the density of the surrounding ambient air. The maximum temperature in the shockwave on Figure 4.11 is around 1040 K and we have checked on 2D plots (Figure 4.10) that it remains less than 1200 K. The maximum temperature jump inside the shockwave is then about 20%, but as the shockwave propagates this temperature jump becomes very small. As a consequence, the speed of sound of the steady air is barely affected by the presence of the shockwave because sound velocity is proportional to the square root of the air temperature. This may be the reason why shockwaves propagate at velocities very close to the speed of sound at 1000 K. Figure 4.11 also shows that the hot channel increases in size as a function of time. If we define the radius of the hot channel as the distance from the axis of symmetry at which the density is equal to the density of the steady air (in our case 0.35 kg cm^{-3}), our results show that this radius increases between 300 ns and 900 ns by 65%. The expansion velocity of the heated channel is around 660 m s^{-1} which is a little higher than the speed of sound at 1000 K.

Figure 4.12 shows the 1D time evolution of the density and the temperature in the axial direction on the symmetry axis. We note that the temperature decrease is more significant close to the tip of the electrodes than in the middle of the gap: the temperature decrease during the hot channel formation is around 400 K in the middle of the gap and around 1000 K at the tip of the electrodes. This decrease would be even faster if heat transfer to the electrodes was taken into account, but due to the very short time-scales considered in this work, we have neglected its influence. This faster decrease of temperature close to the electrodes is due to the higher pressure and the faster formation of shockwaves, able to remove a significant amount of the deposited energy. Then, the difference between the temperature at the tip of the electrodes and in the middle of the gap decreases during the hot channel formation. As a consequence, both the 2D temperature and density fields in the fully developed hot channel are more homogeneous than the initial discharge energy distribution. It is interesting to note that shockwaves are able to remove a significant amount of the discharge energy deposited in the gas: the ratio of the temperature decrease due to the shockwave formation to the temperature increase due to the discharge energy deposition is around 30% at the tip of the electrodes and 20% in the middle of the gap. It means that during the permanent regime of a multi-pulse spark discharge, thermal losses have to compensate exactly the energy deposition by the successive discharges and the shockwave formation and propagation is a significant dissipative process. However, other mechanisms may also play a role on longer timescales as heat transfer to walls and thermal diffusion.

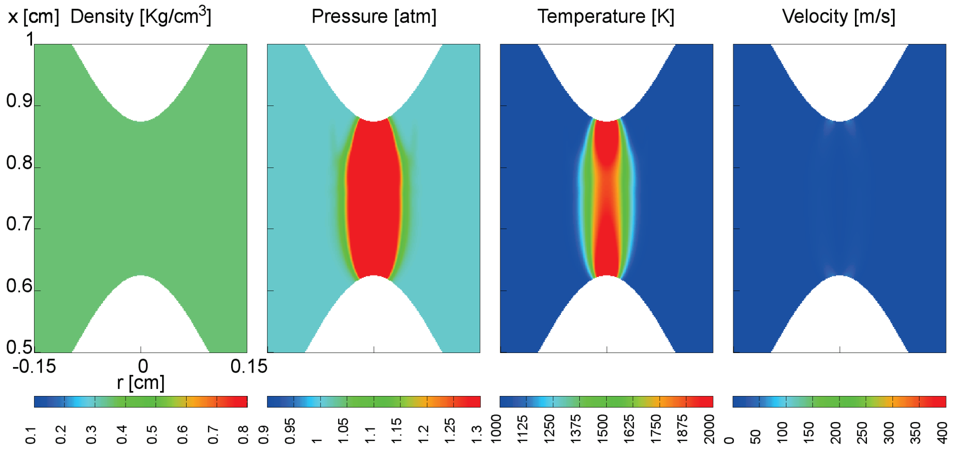

t=0 μs

Figure 4.9: *Initial condition for the Euler 2D axisymmetric code: it corresponds to the density, pressure, temperature and velocity fields at the end of the reference nanosecond spark discharge in air at 1000 K defined in section 4.2.2*

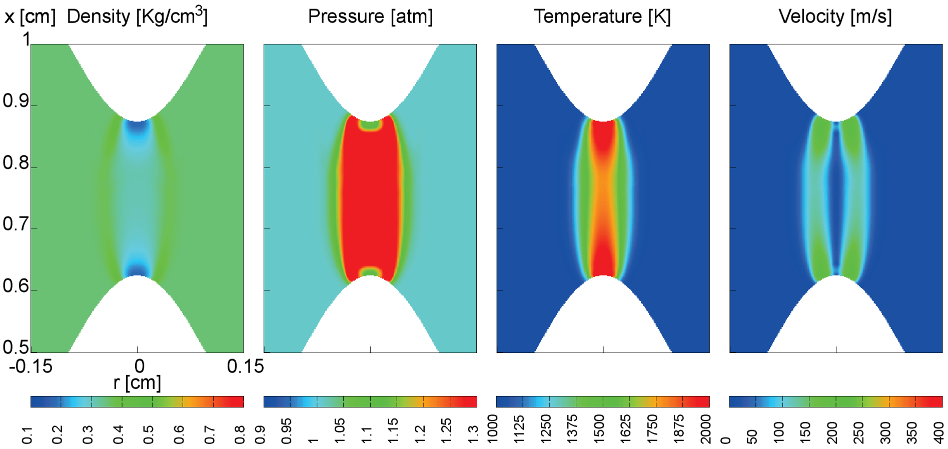

t=200 ns

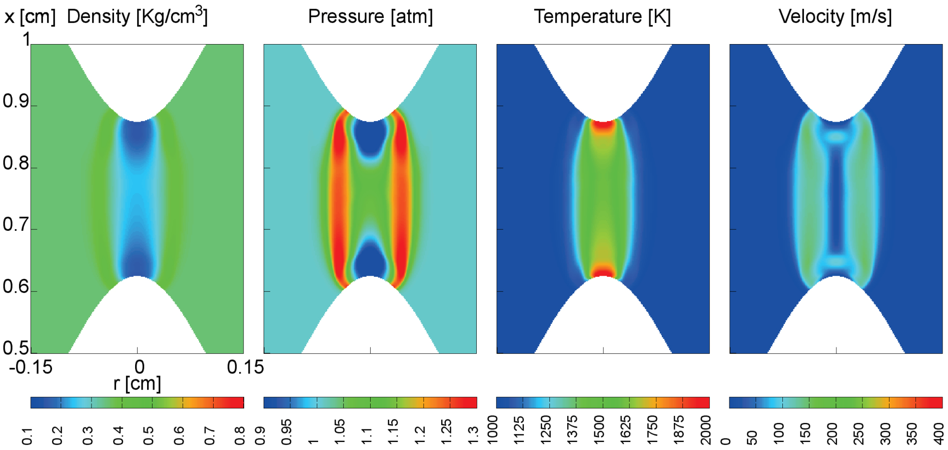

t=400 ns

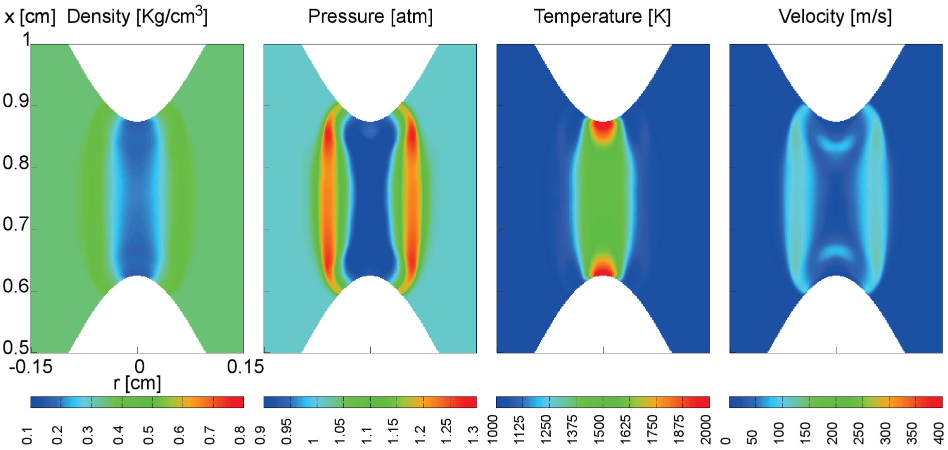

t=600 ns

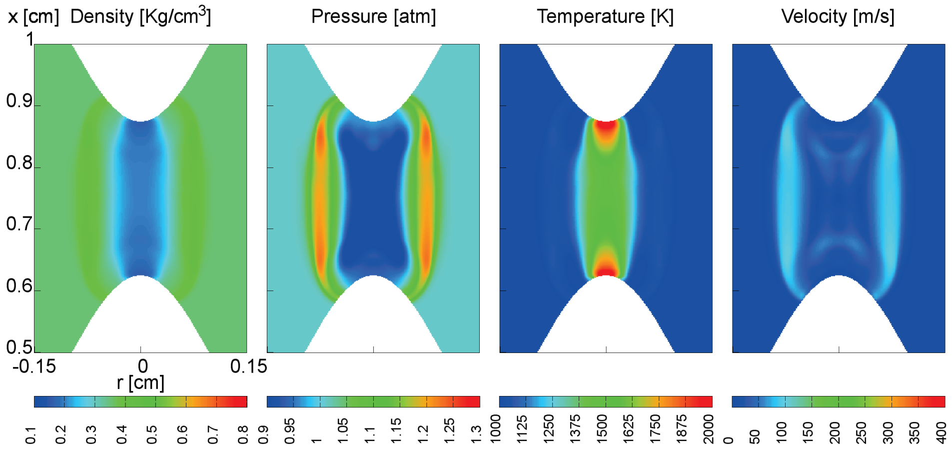

t=800 ns

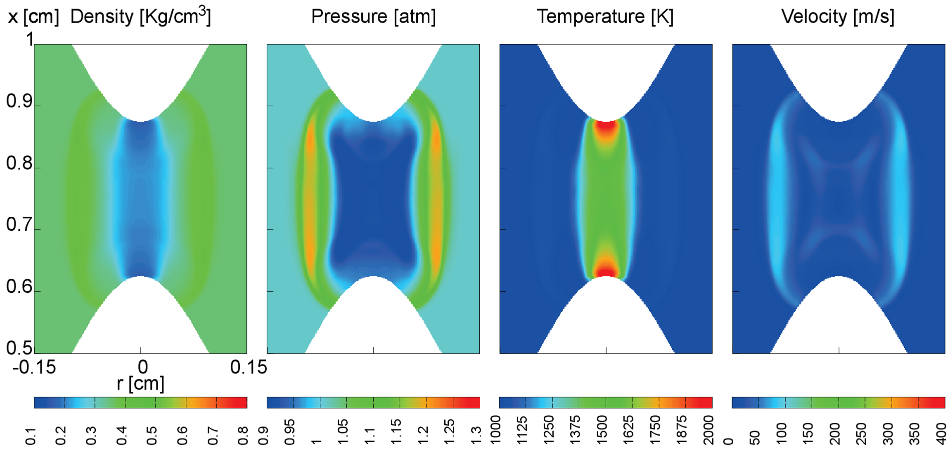

t=1 μs

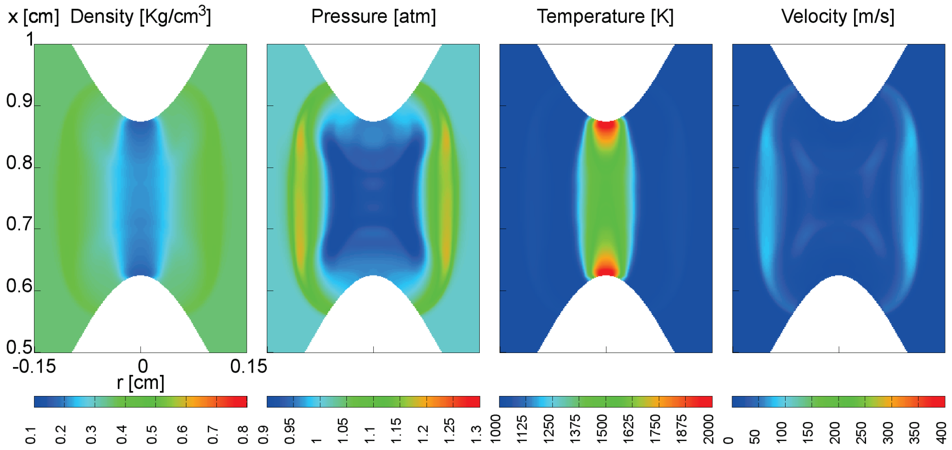

t=1.2 μs

Figure 4.10: *Dynamics of the shock wave in air at 1000 K produced by the reference nanosecond spark discharge defined in section 4.2.2. Cross-sectional views of density, pressure, temperature and velocity every 200 ns.*

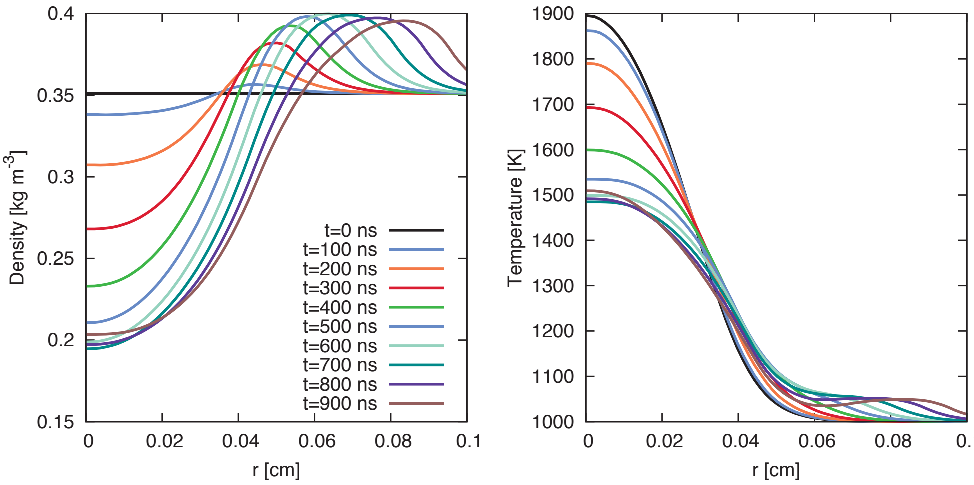

Figure 4.11: *Evolution of the air density and the air temperature in the radial direction in the middle of the gap every 100 ns for the same condition as Figure 4.10.*

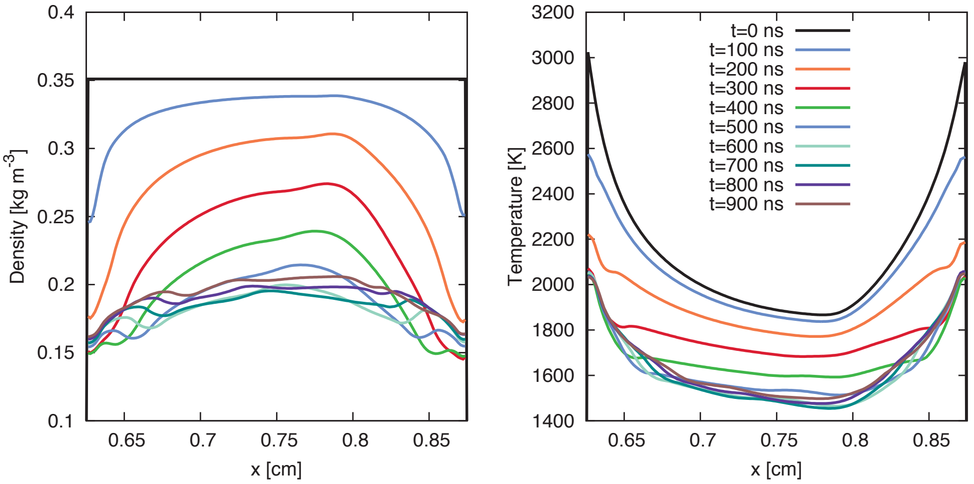

Figure 4.12: *Evolution of the air density and the air temperature in the axial direction on the symmetry axis every 100 ns for the same condition as Figure 4.10.*

In experiments carried out at EM2C laboratory on nanosecond spark discharges, *Xu et al.* [2011] have shown that nanosecond repetitively pulsed discharges can generate shockwaves by Schlieren imaging. This optical technique is based on the deviation of the light beams emitted by a collimated source placed behind the flow and allows to observe locations of density gradients in the flow. In *Hadjadj and Kudryavtsev* [2005] different methods to generate numerical Schlieren images, which look close to those experimentally obtained are discussed and compared. In order to highlight the weak non-uniformities of the flow field [*Hadjadj and Kudryavtsev*, 2005], we have used the non-linear expression proposed by *Quirk* [1994], based on the absolute value of the density gradient, and we have plotted the quantity:

$$S(x,y) = \beta exp\left(-\kappa\frac{|\nabla\rho|}{|\nabla\rho|_{max}}\right) \tag{4.25}$$

where the subscript max denotes the maximum values of the density gradient over the whole flow field and κ and β are parameters. The parameter β determines the shade of grey colour that corresponds to the zero gradient and the parameter κ governs the amplification of small gradients. In this work, we have used the recommended values of $\kappa = 15$ and $\beta = 0.8$ given in *Hadjadj and Kudryavtsev* [2005].
Figure 4.13 shows the time sequence of the numerical Schlieren images of the shockwave formed due to the instantaneous heating of the air at 1000 K for the reference discharge case defined in Section 4.2.2. As expected, the most significant density gradients are observed on the wings of the hot channel. Figure 4.13 also shows more in detail the shockwave structure: as already mentioned, a first shockwave related to the thermal expansion of the hot channel is generated and propagates with a cylindrical geometry at the speed of sound of air at 1000 K. Just after, two spherical shockwaves due to reflections on the two point electrodes propagate in the hot channel. These two reflected shockwaves have exactly the same radius and propagate at a velocity very close to the speed of sound. These two spherical shockwaves impact each other at the middle of the inter-electrode gap at t=3 μs. Then, they cross each other and go on their propagation in the gap, removing all gradients in the axial direction in their wakes.

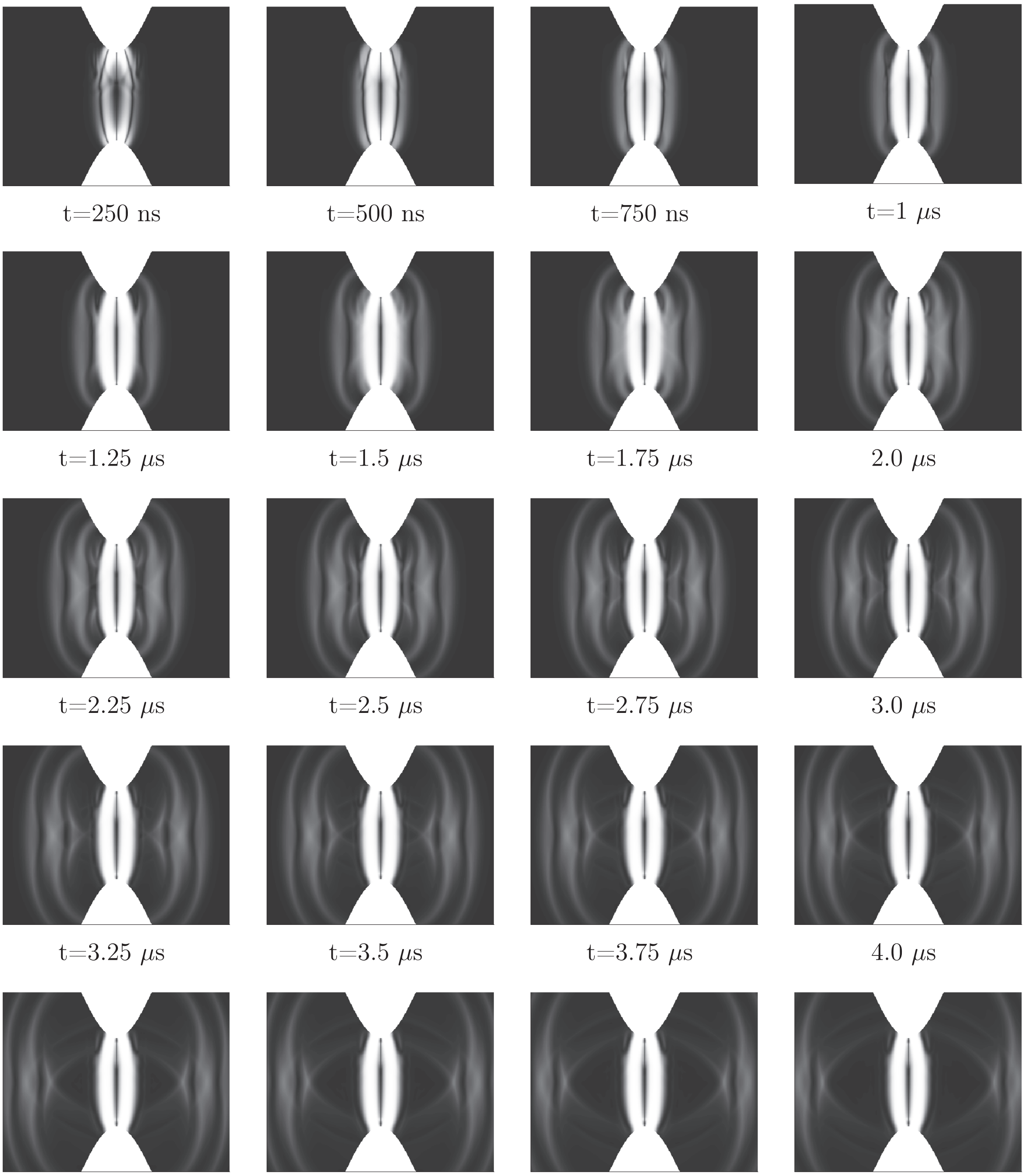

t=250 ns t=500 ns t=750 ns t=1 μs

t=1.25 μs t=1.5 μs t=1.75 μs 2.0 μs

t=2.25 μs t=2.5 μs t=2.75 μs 3.0 μs

t=3.25 μs t=3.5 μs t=3.75 μs 4.0 μs

t=4.25 μs t=4.5 μs t=4.75 μs 5.0 μs

Figure 4.13: *Numerical Schlieren images of the shockwave formation due to the instantaneous heating of air at 1000 K for the reference nanosecond spark discharge defined in section 4.2.2. The sequence of pictures shows the formation and the time evolution of the shockwaves every 250 ns.*

4.5.2 Influence of the amount of the instantaneously deposited energy on the gas dynamics

In previous sections, we have assumed that $\eta_{\mathrm{R}} = 30$ % of the total discharge energy instantaneously heats the ambient air. In this section, we have varied this value to check its influence on the gas dynamics. Figure 4.14 shows the 2D time evolutions of Schlieren images every 400 ns up to $t = 2$ μs after the reference nanosecond spark discharge for four different values of η_{R}: 15, 30, 45 and 60%. It is interesting to note that for these different values of η_{R}, we observe very similar shockwave structures and a very similar dynamics of the flow. The propagation velocity of shockwaves is almost equal in all cases as it corresponds to the velocity of sound in the steady air at 1000 K. The only parameter which changes is the density jump in shockwaves. As expected, as the value of η_{R} increases, more energy is put into the air and the shockwaves generate higher density, pressure, and temperature gradients. To compare more in detail the results for the different values of η_{R}, Figure 4.15 shows the radial evolutions of the density and the temperature up to 900 ns in the middle of the inter-electrode gap for $\eta_{\mathrm{R}} = 15\%$ and $\eta_{\mathrm{R}} = 60\%$. Figure 4.16 shows for the same conditions the axial evolutions of the density and the temperature on the symmetry axis. As expected, the temperature increase (and the corresponding density decrease) are four times higher for $\eta_{\mathrm{R}} = 60\%$ than for $\eta_{\mathrm{R}} = 15\%$. On Figure 4.15, we also note that the shockwave generated by the low density channel seems to propagate slightly faster at the beginning of its propagation for $\eta_{\mathrm{R}} = 60\%$. On the radial profiles of the density, we observe that between 100 ns and 900 ns, the radius of the channel increases by 50% for $\eta_{\mathrm{R}} = 15\%$. However, for $\eta_{\mathrm{R}} = 60\%$, the radius of the channel increases by a factor 2 in the same time, meaning a much faster and more significant dilatation of the hot channel. This dilatation of the hot channel has been observed experimentally in *Xu et al.* [2012] and then seems to confirm a significant very fast heating of the air by the nanosecond spark discharge.

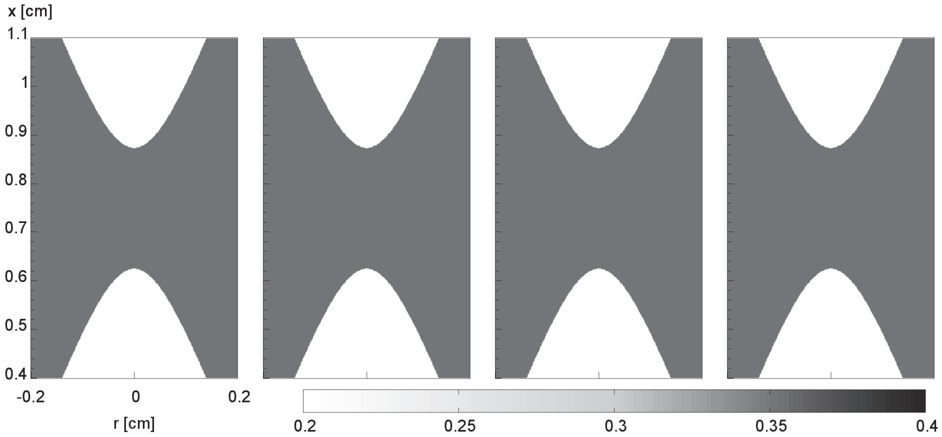

t=0 μs

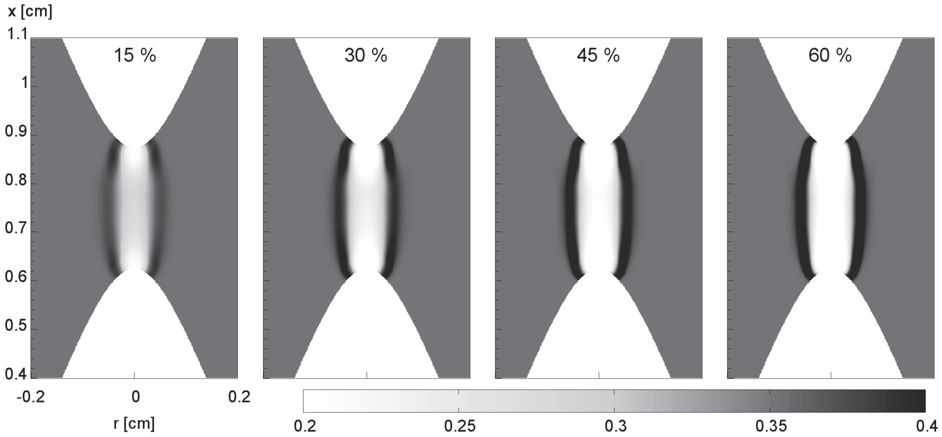

t=400 ns

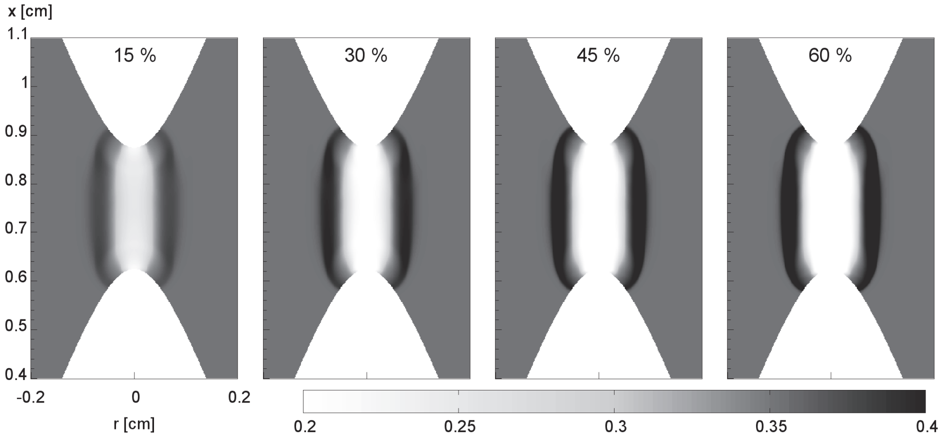

t=800 ns

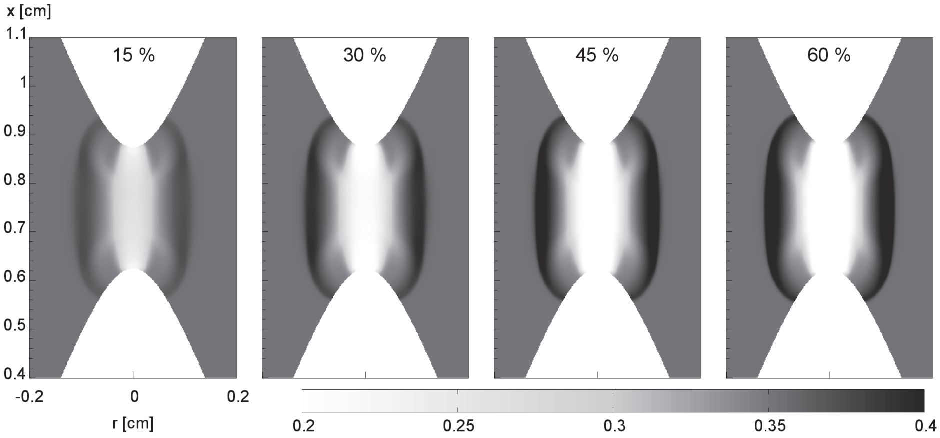

t=1.2 μs

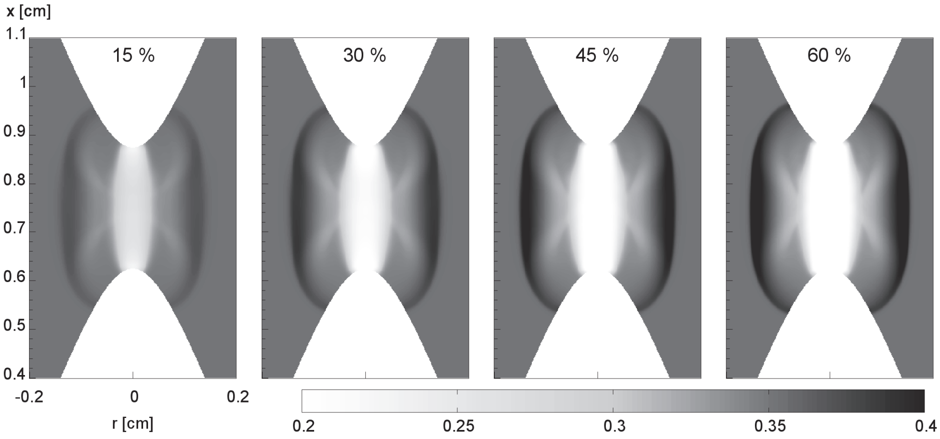

t=1.6 μs

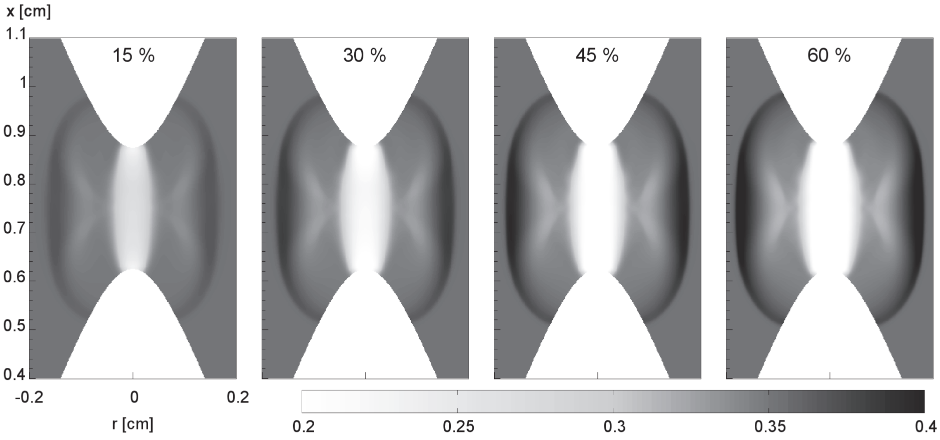

t=2.0 μs

Figure 4.14: *Numerical Schlieren images of the shockwave formation due to the instantaneous heating of air at 1000 K for the reference nanosecond spark discharge defined in section 4.2.2 for* η_R = *15, 30, 45 and 60%. The sequence of pictures shows the formation and the time evolution of the shockwaves every 400 ns.*

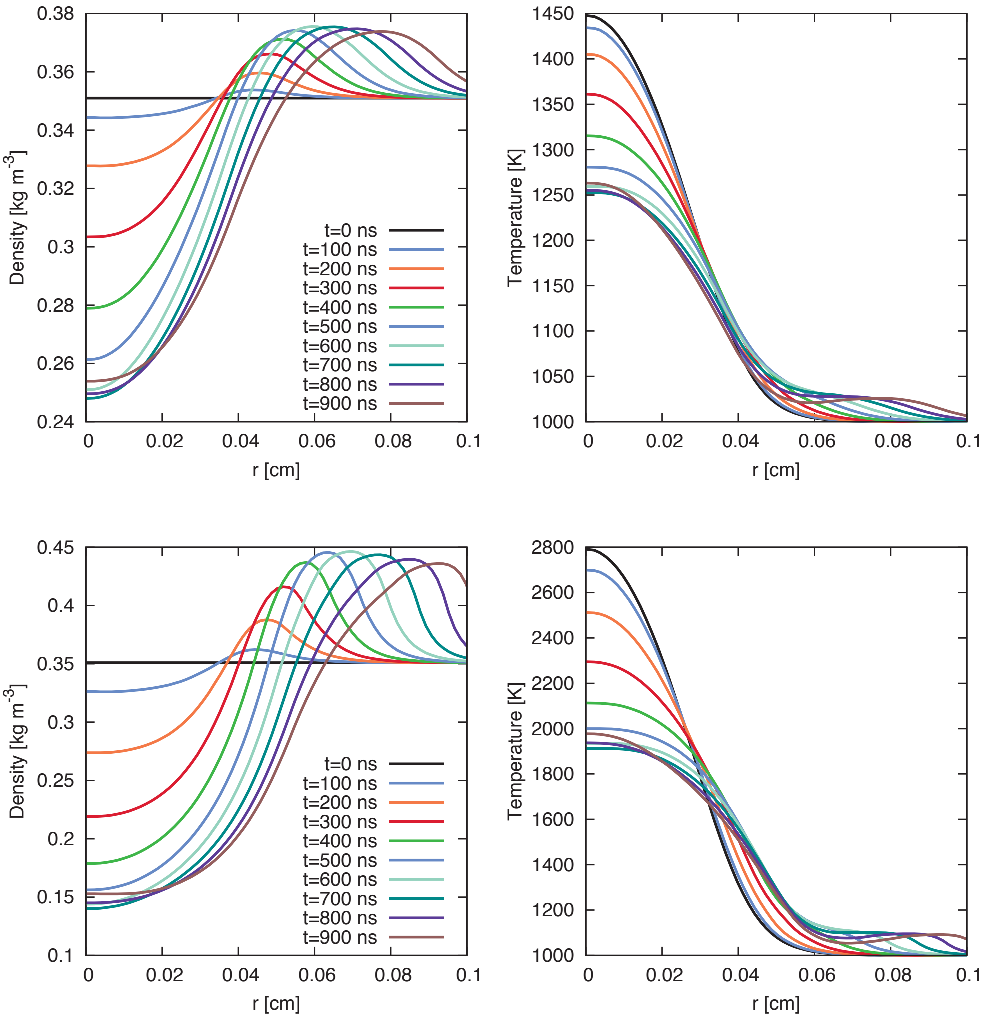

Figure 4.15: *Evolution of the air density and the air temperature in the radial direction in the middle of the gap due to the instantaneous heating of air at 1000 K for the reference nanosecond spark discharge defined in section 4.2.2 for* $\eta_R = 15\%$ *(top images) and* $\eta_R = 60\%$ *(bottom images).*

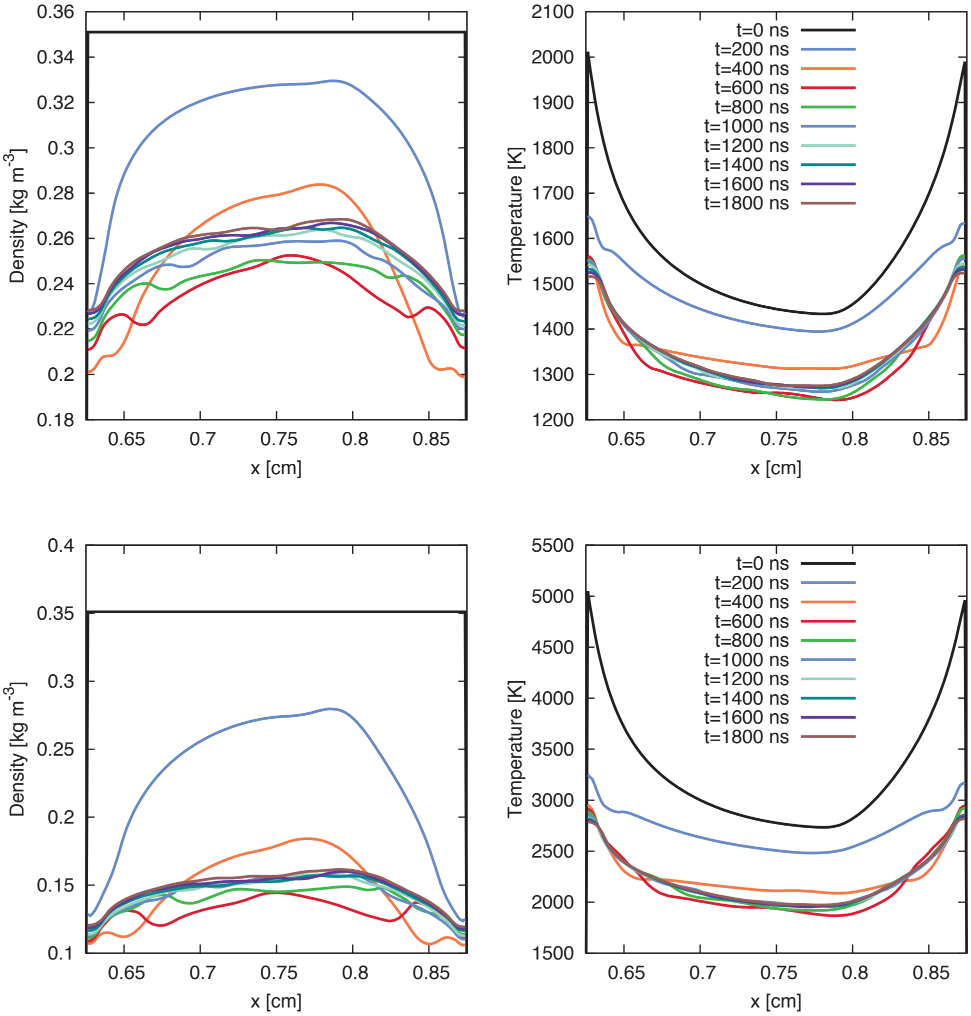

Figure 4.16: *Evolution of the air density and the air temperature in the axial direction on the symmetry axis due to the instantaneous heating of air at 1000 K for the reference nanosecond spark discharge defined in section 4.2.2 for* $\eta_{\mathrm{R}} = 15\%$ *(top images) and* $\eta_{\mathrm{R}} = 60\%$ *(bottom images).*

4.5.3 Influence of the fast-heating rate of the deposited energy on the gas dynamics

In previous sections, we have assumed that the fraction η_R of the total discharge energy instantaneously heats the ambient air. The hypothesis of an infinitely fast heating rate is valid only if the fast-heating process occurs on a characteristic time which is much less than the diameter of the discharge divided by the speed of sound in the hot channel, which is around 500 ns for a strong spark discharge (see section 4.3.2). However, as fast heating is due to the relaxation of the energy stored in internal modes of molecules and atoms, which may have different timescales, we have studied the influence of a heating phase longer than the characteristic time of 500 ns. In this section, we have computed the gas dynamics generated by the reference nanosecond spark discharge, assuming a linear increase of the temperature just after the discharge. We have considered that 30% of the discharge energy at the end of the pulse $e_\mathrm{J}(\mathrm{T}_\mathrm{pulse})$ is put into the air heating with a characteristic time of $\tau_\mathrm{h} = 1\,\mu$s taken from experiments in air surface dielectric barrier discharges at atmospheric pressure [*Aleksandrov*, 2010]. Then, the temperature is derived from:

$$\mathrm{T_g}(t + \mathrm{d}t) = \mathrm{T_g}(t) + \mathrm{d}t\,\frac{\eta_\mathrm{R} e_\mathrm{J}(\mathrm{T}_\mathrm{pulse})}{\rho(t) C_\mathrm{v}(t) \tau_\mathrm{h}} \qquad \text{for } t \leq \tau_\mathrm{h} \tag{4.26}$$

where dt is a time-step chosen to ensure that $\rho(t)C_\mathrm{v}(t)$ is not varying too much between t and t+dt. Practically, we have chosen dt such that the temperature increase is less than 10 K during one time-step. The heating rate is then varying between 10^9 K s^{-1} in the middle of the gap and 2.10^9 K s^{-1} close to the tip of the electrodes where the temperature increase is more significant. These heating rates are in qualitative agreement with the fast-heating timescales obtained in air surface dielectric barrier discharges at atmospheric pressure in *Aleksandrov* [2010]. On the other hand they are one order of magnitude less than the heating rates obtained by *Rusterholtz et al.* [2012] and then, they can be considered as low limit values of heating rates for the nanosecond spark discharge studied in this work. It is interesting to note that a simulation with a characteristic time of $\tau_\mathrm{h} = 20$ ns, close to the values obtained by *Rusterholtz et al.* [2012] has been carried out and no significant differences have been observed with the infinitely fast heating case (Section 4.5.1). Figure 4.17 shows the time evolutions of the air density and the temperature in the radial direction in the middle of the gap for $\tau_\mathrm{h} = 1\,\mu$s up to $t = 5\,\mu$s. Figure 4.18 shows the time evolutions of the air density and the temperature in the axial direction on the symmetry axis for the same conditions. Both figures show that the temperature at t=0 s is equal to 1000 K and then increases progressively during 1 μs. Conversely, the air density decreases progressively and a pressure wave is generated around the hot channel. On Figure 4.17, at t=1 μs, when all the energy has been put into the air, we note that the maximum temperature in the hot channel is less than the maximum initial temperature for the case of an infinitely fast heating (see Figure 4.11). This is probably due to the fact that the pressure wave is generated and starts to propagate during the temperature increase. Then, due to the shock wave propagation, some energy is removed from the hot channel during the heating phase and the final temperature is lower. After 1 μs, the temperature starts to decrease and the density increases slowly up to t=5 μs. It is interesting to note that there are two major differences between the case of a fast-heating at a finite rate and an instantaneous heating: First, due to the slow increase of the temperature when a finite heating rate is considered, the amplitude of the pressure wave generated is smaller than the one obtained for an instantaneous heating. With a rather long characteristic time of heating of $\tau_{\mathrm{h}} = 1\,\mu$s, it is even not clear that a real shock wave is formed as no discontinuity is clearly observed. Second, no expansion of the hot channel is observed with $\tau_{\mathrm{h}} = 1\,\mu$s. The experimental results from *Xu et al.* [2011] showing the fast expansion of the hot channel and the propagation of a shockwave seem to validate the hypothesis of a fast heating on short time-scales much less than 1 μs in the nanosecond spark discharge studied in this work.

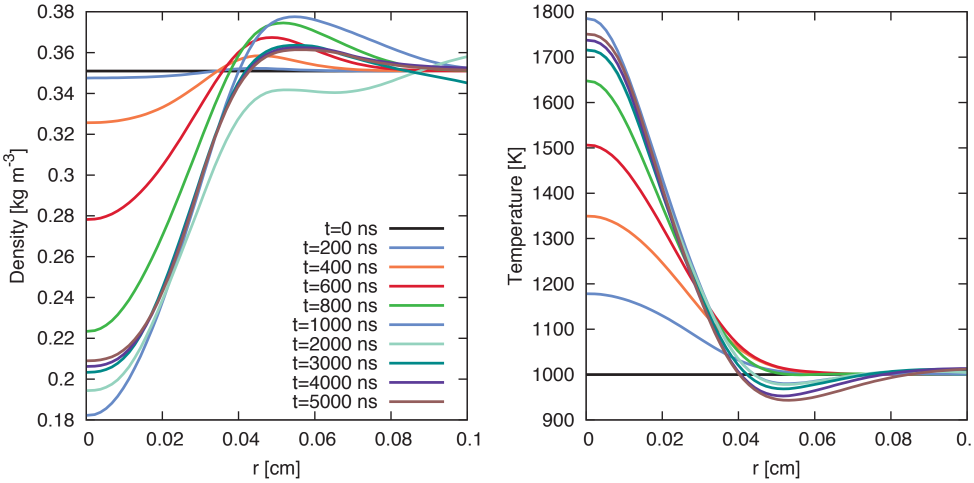

Figure 4.17: *Evolution of the air density and the air temperature in the radial direction in the middle of the inter-electrode gap up to $t = 5\,\mu s$ for the reference nanosecond spark discharge defined in section 4.2.2. In this case, 30% of the discharge energy is put into the air heating with a characteristic time of $\tau_h = 1\,\mu s$.*

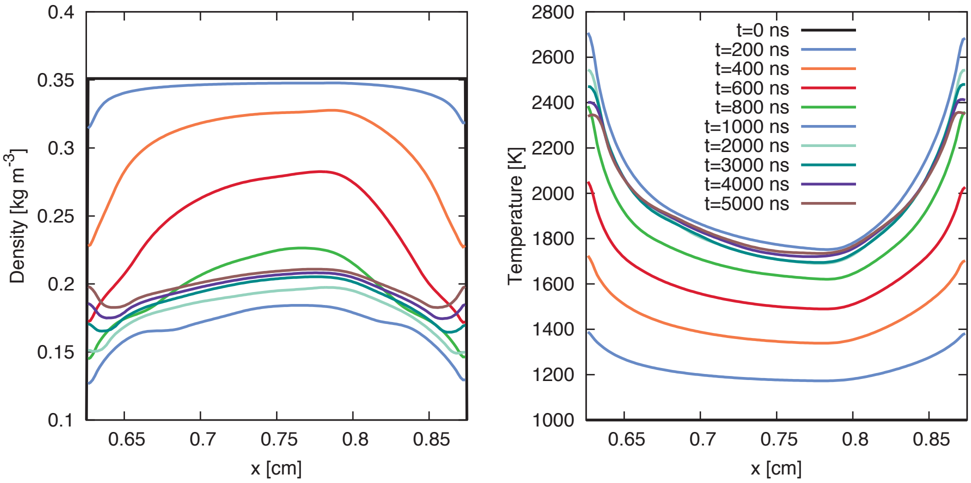

Figure 4.18: *Evolution of the air density and the air temperature in the axial direction on the symmetry axis up to $t = 5\,\mu s$ for the reference nanosecond spark discharge defined in section 4.2.2. In this case, 30% of the discharge energy is put into the air heating with a characteristic time of $\tau_h = 1\,\mu s$.*

4.5.4 Instantaneous heating of air at 300 K by a nanosecond spark discharge

As explained in Section 2.7, the glow to spark transition is much faster at 300 K than at 1000 K for scaled voltage conditions. Gas heating and compressible flow dynamics are then very important for repetitively pulsed nanosecond discharges at 300 K. In this section, we consider the same geometry and conditions as for the reference nanosecond spark discharge defined in Section 4.2.2 at 1000 K but with an applied voltage of 15 kV, scaled relatively to the air density at 300 K and with a pulse duration is of 5 ns (with a rise and a decrease time of 2 ns), shorter than for the reference case at 1000 K. Figure 4.19 shows the 2D temperature field generated by this discharge up to t =5 ns, assuming that 30% of the discharge energy instantaneously heats the ambient air. We note that the maximum temperature obtained is less than for the reference spark discharge at 1000 K (Figure 4.2). The 2D distributions of the discharge energy and temperature are also different with at $t = 4$ ns at 300 K, two hot spots close to the electrode tips and a third one in the middle of the gap. At 1000 K (Figure 4.2), only the two hot spots close to the electrode tips are observed. At 300 K, the third hot spot in the middle of the gap is directly linked to the discharge structure: indeed, on Figure 4.19, we observe at t =3.5 and 4 ns a constriction of the discharge radius in the middle of the gap (which is not seen in the reference case at 1000 K). This constriction of the discharge increases the local current density and then the deposited energy density. At t =5 ns on Figure 4.19, we observe a hot cylinder from the middle of the gap up to the anode tip and a hot spot close to the cathode tip.

Figure 4.20 shows the gas dynamics resulting from this temperature field. Conversely to the reference case at 1000 K, at 300 K we observe at t =600 ns a fast depletion of the density not only close to electrode tips but also in the hot region between the anode and the middle of the inter-electrode gap. On the pressure and velocity fields, we note that three shockwaves are emerging at the same time from the three initial hot spots. At t =1.2 μs the three spherical shockwaves merge into a cylindrical shockwave propagating radially at approximately 360 m s^{-1} i.e. a velocity very close to the speed of sound at 300 K. Then the conclusions derived for the reference nanosecond spark discharge at 1000 K remain valid for the studied case at 300 K: when one assumes an instantaneous heating of the gas by the discharge, a radial expansion of the hot channel is observed on short timescales. We have noted that no significant changes are observed in the gas dynamics when the amount of the deposited energy varies.

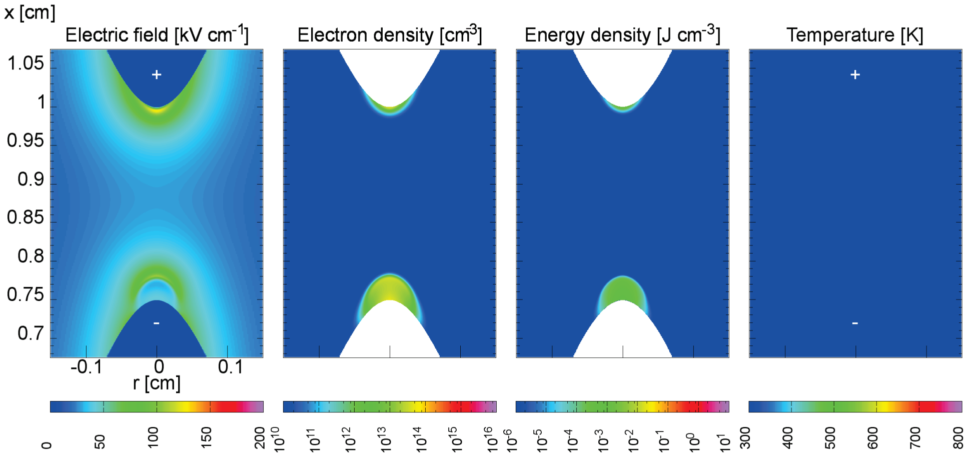

t=2 ns

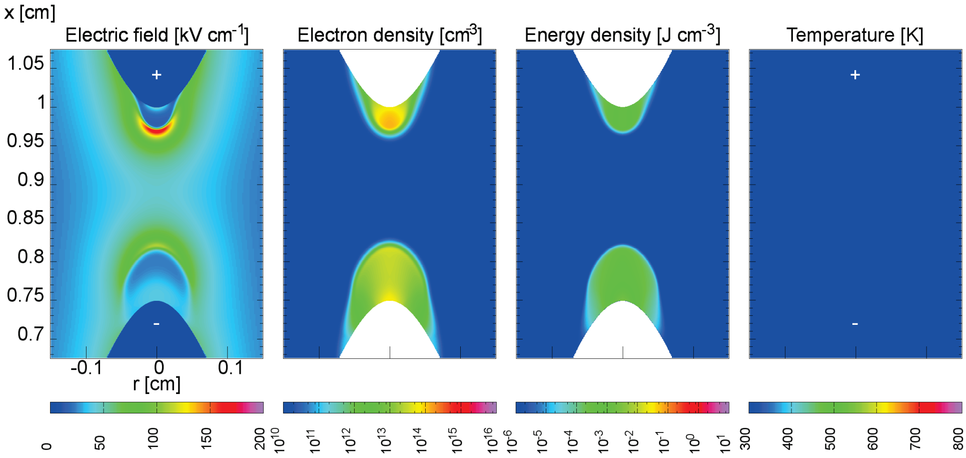

t=2.5 s

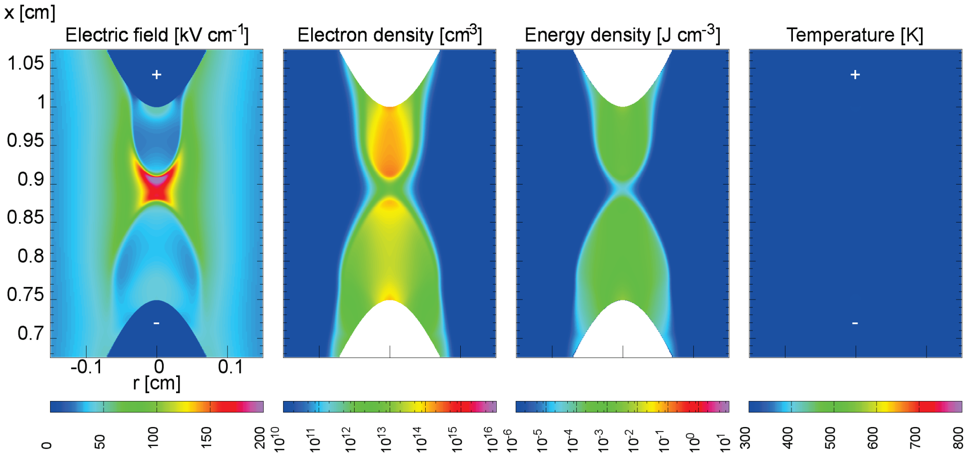

t=3 ns

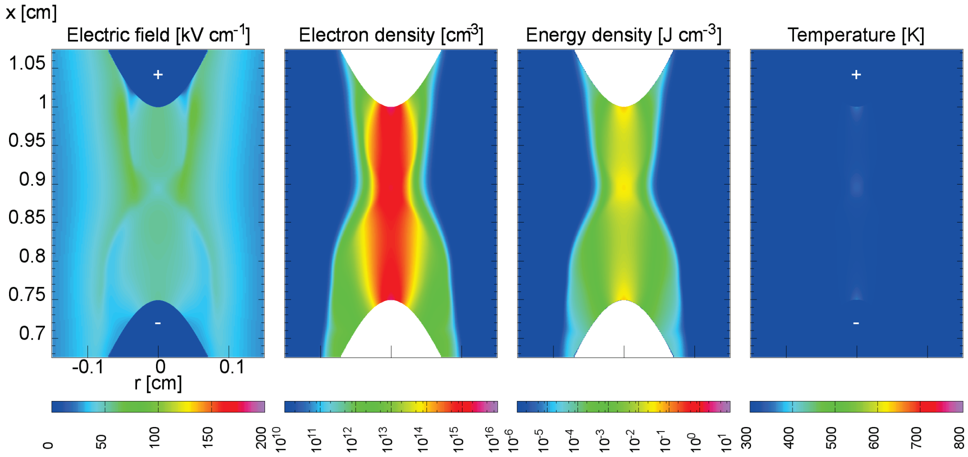

t=3.5 ns

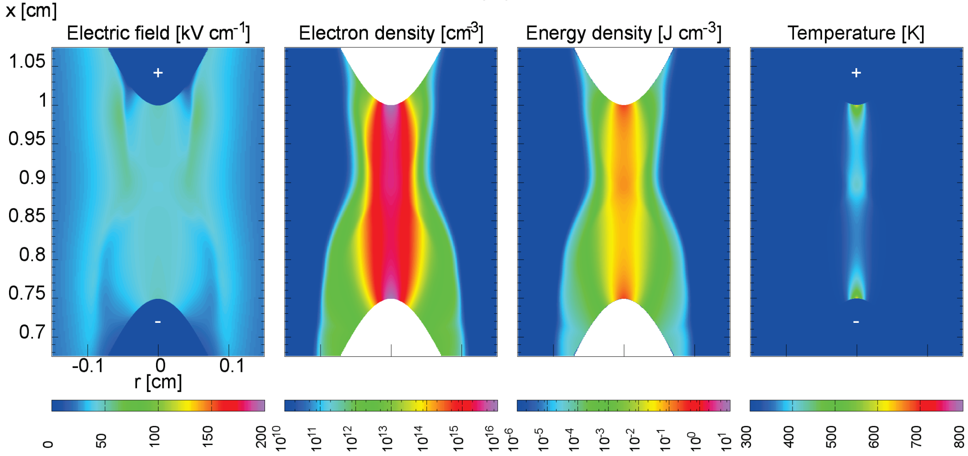

t=4 ns

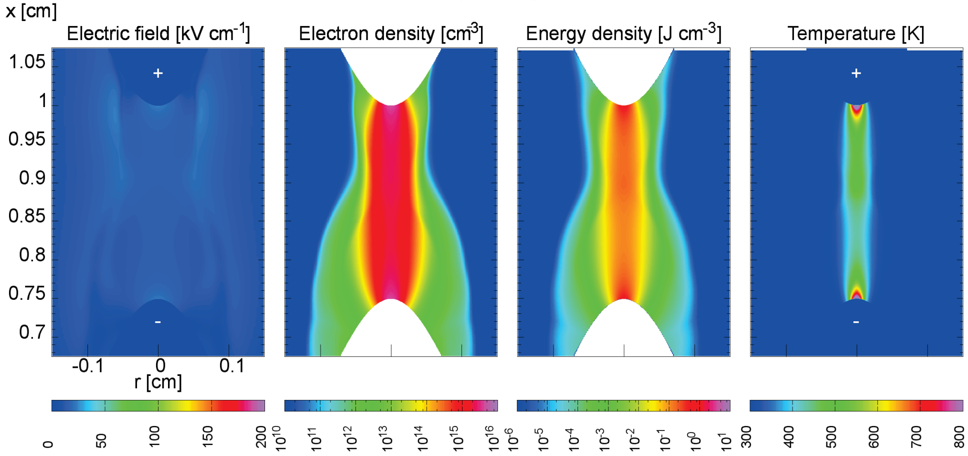

t=5 ns

Figure 4.19: *Cross-sectional views of the magnitude of the electric field, electron density, discharge energy density and neutral gas temperature for an 'energetic glow discharge' at 300 K. The neutral gas temperature is obtained assuming an instantaneous gas-heating with* $\eta_R = 30\%$

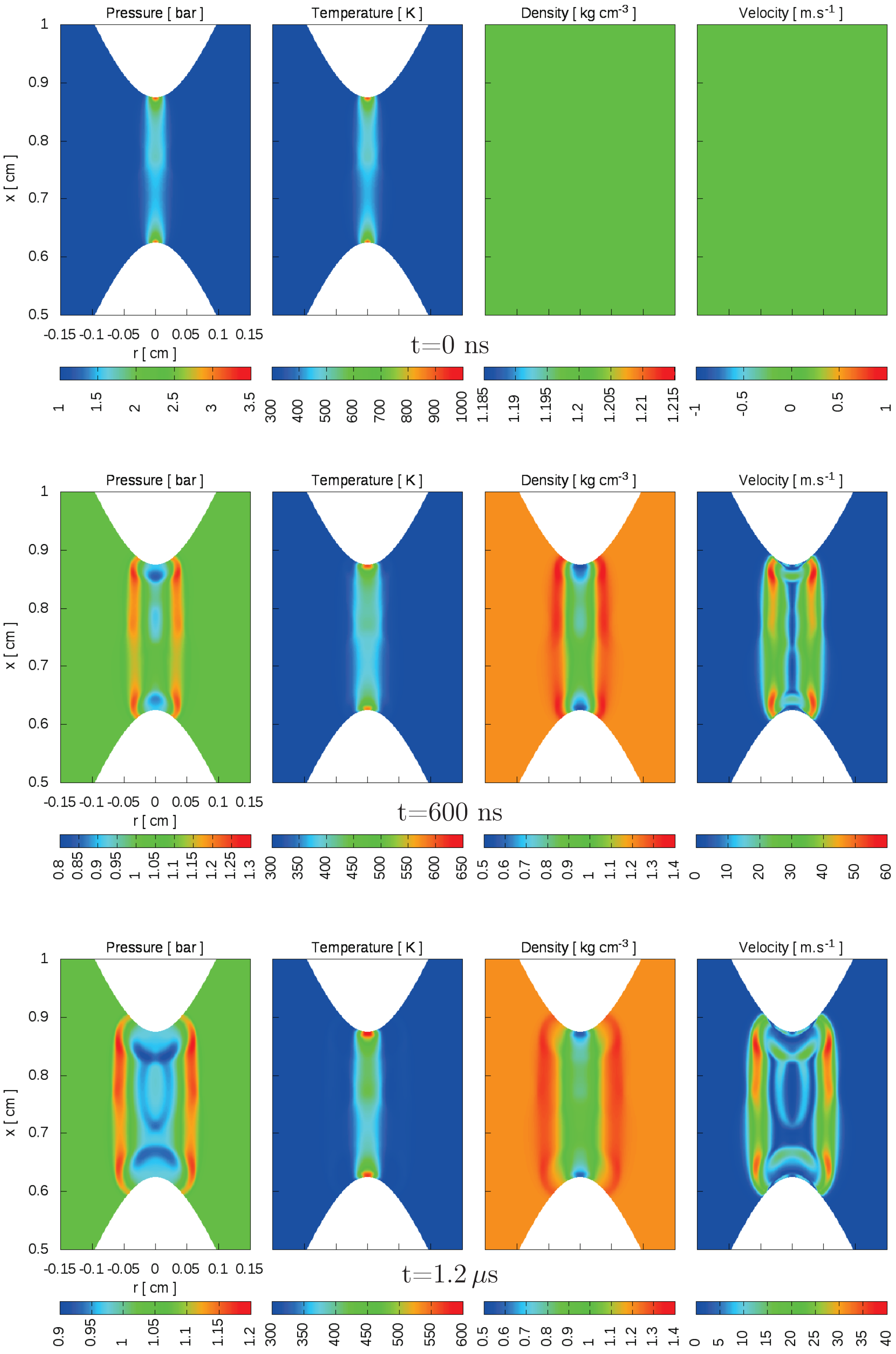
Pressure [bar]
Temperature [K]
Density [kg cm-3]
Velocity [m.s-1]
x [cm]
1
0.9
0.8
0.7
0.6
0.5
-0.15 -0.1 -0.05 0 0.05 0.1 0.15
r [cm]
t=0 ns
1 1.5 2 2.5 3 3.5
300 400 500 600 700 800 900 1000
1.185 1.19 1.195 1.2 1.205 1.21 1.215
-1 -0.5 0 0.5 1
t=600 ns
0.8 0.85 0.9 0.95 1 1.05 1.1 1.15 1.2 1.25 1.3
300 350 400 450 500 550 600 650
0.5 0.6 0.7 0.8 0.9 1 1.1 1.2 1.3 1.4
0 10 20 30 40 50 60
t=1.2 μs
0.9 0.95 1 1.05 1.1 1.15 1.2
300 350 400 450 500 550 600
0.5 0.6 0.7 0.8 0.9 1 1.1 1.2 1.3 1.4
0 5 10 15 20 25 30 35 40

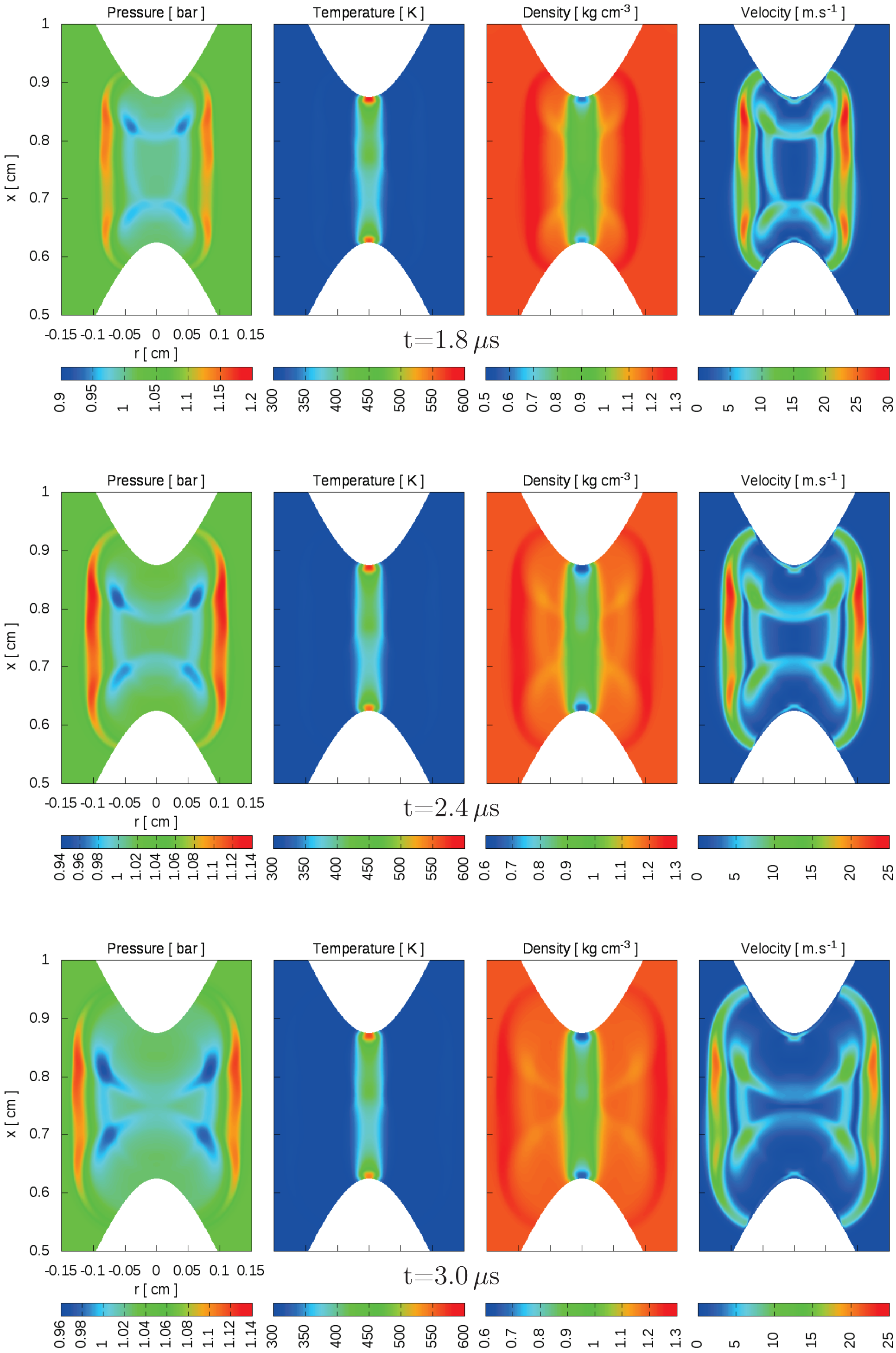

Figure 4.20: *Dynamics of the shock wave in air at 300 K produced by the 'energetic glow discharge' of Figure 4.19. Cross-sectional views of density, pressure, temperature and velocity every 600 ns.*

4.6 More detailed models for fast gas heating

In previous sections, we have assumed based on the work of *Popov* [2011a] and *Aleksandrov* [2010] that 30% of the discharge energy goes to fast heating and we have considered that the heating is either instantaneous or with a characteristic time of 1 μs. To model more accurately the fast gas heating, it is important to note that the fraction of the discharge energy going to fast heating depends on the relaxation of vibrationally excited molecules and electronically excited atoms and molecules produced by the nanosecond discharge. These excited species are mostly produced by electron impact collisions during the discharge and then their production depends strongly on the electric field in the discharge. As already mentioned in previous sections, the 2D electric field is varying significantly in time during the voltage pulse and is also non-uniform in the interelectrode gap. Then, as a first step to improve the modeling of fast heating in Section 4.6.1, we have considered that the production of excited species and then the amount of energy stored in these species depends on the local value of the electric field. The relaxation of the energy stored in the different internal modes of molecules and atoms will relax in time and finally increase the gas translational temperature. However the relaxation of the different internal modes may have different characteristic timescales. Then, in Section 4.6.2, we have implemented a chemical model for excited species in air to take into account more in detail the dynamics of formation of excited species during the discharge phase and the relaxation of their internal energy. In Section 4.6.3, the results obtained with these two more detailed models will be compared to the reference model used in previous sections (in which we consider that 30% of the discharge energy instantaneously heats the ambient air).

4.6.1 Fast heating model depending on the electric field

The electron energy losses in the different collisional processes in air (elastic collisions, rotational, vibrational and electronic excitations, ionization and attachment processes...) depend on the value of the reduced electric field E/N. Using the two-term Boltzmann solver Bolsig+ [*Hagelaar and Pitchford*, 2005], *Riousset et al.* [2010] have computed and tabulated the fractions of energy losses as a function of the reduced electric field for air at 300 K. Following their approach, we have estimated that the fraction of the discharge energy that instantaneously goes into air heating is:

$$\eta_R = \eta_{\mathrm{ela}} + \eta_{\mathrm{rot}} + \eta_{\mathrm{vib}}^{\mathrm{O_2}} + 0.3 \times \eta_{\mathrm{elec}} \qquad (4.27)$$

where η_{ela} is the part going in elastic collisions, η_{rot} in rotational excitation of N_2 and O_2 molecules, $\eta_{\mathrm{vib}}^{\mathrm{O_2}}$ in vibrational excitation of the O_2 molecules and η_{elec} in electronic excitation of N_2 and O_2 molecules. At low reduced electric field, rotational modes of N_2 and O_2 molecules are excited. The relaxation

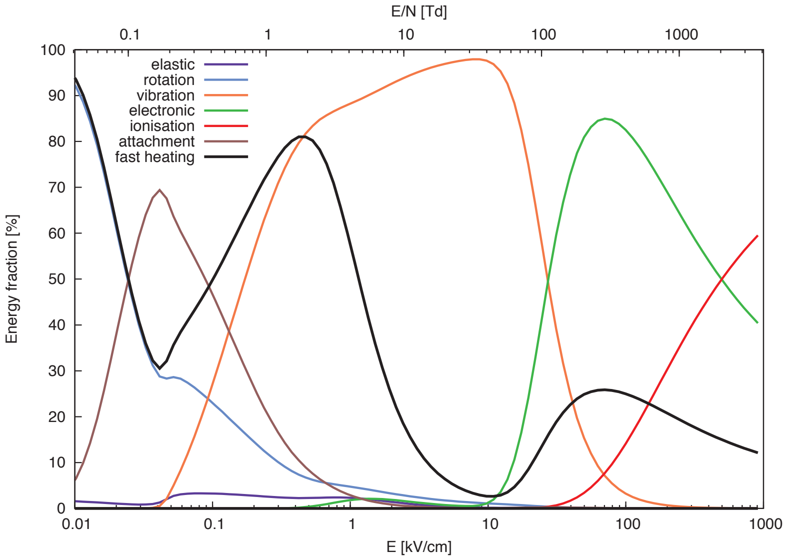

Figure 4.21: *Fractions of the electron energy spent in different collisional processes in air at 1000 K at atmospheric pressure as a function of the electric-field. The fast heating (black line) corresponds to η_R in Equation (4.27).*

of these modes in air at atmospheric pressure is very fast (few collisions) and then can be considered as instantaneous. At higher values of reduced electric field, vibrational modes of N_2 and O_2 molecules are excited. The relaxation of the energy stored in vibrationally excited O_2 molecules is fast at atmospheric pressure and than can also be considered as instantaneous. However, in air, the most significant part of the vibrational energy is stored in N_2 vibrational energy. If air is only weakly dissociated, the relaxation of this vibrational energy is relatively slow and occurs with a relaxation time of about 100 μs [*Mnatsakanyan and Naidis*, 1985; *Millikan and White*, 1963], which is too slow to play a role in fast heating. Therefore the term $\eta_{\text{vib}}^{N_2}$ is not included in Equation (4.27). However, if air is dissociated, one has to take into account the very efficient relaxation of N_2 vibrational energy through inelastic collisions with O atoms [*Taylor*, 1974; *Doroshenko,V.M., Kudryavtsev and Smetanin*, 1991]. In this case, a significant part of $\eta_{\text{vib}}^{N_2}$ could be also considered in Equation (4.27). Finally, at higher reduced electric field, electronic modes are excited. Following the approach of *Popov* [2001] we have considered that 30% of the energy expended on the excitation of the electronic degrees of freedom of the molecules is directly transferred to gas heating.

As we study discharges in air at 1000 K, we have checked that in the range 300-1500 K the neutral gas temperature has only a small influence on the electron distribution function and therefore, we have used the tabulated energy fractions derived by *Riousset et al.* [2010] at 300 K, in simply scaling them in density at 1000 K. Figure 4.21 shows the different energy fractions as a function of the magnitude of the electric field at 1000 K and the value of η_R (black line) considered for the fast-heating with this model. We note that the value of η_R varies significantly with the value of the electric field.

4.6.2 A chemical model for the fast gas heating: the two-step mechanism

As initially proposed by *Popov* [2001], an important process for fast gas heating in air at atmospheric pressure seems to be the fast quenching of electronic excited levels of nitrogen in the so-called the two-step mechanism. In a first step, during the voltage pulse, electronically excited nitrogen molecules are produced by electron impact due to the high electric field present in the discharge. In a second step, these molecules are quenched by neutral particles and mainly by O_2 molecules. These quenching reactions are very efficient and occur quickly after the discharge in less than a few tens of nanoseconds [*Rusterholtz et al.*, 2012]. As a consequence, O_2 molecules are dissociated and part of the energy stored in the electronic excited levels of nitrogen molecules is transferred into kinetic energy of the oxygen atoms produced. In a few collisions, these oxygen atoms thermalize and then increase the neutral gas temperature. In this work, we have considered a simple chemical model for air in order to take into account the two-step mechanism based on the works of *Popov* [2001]. This model takes into account 9 species: $N_2(X^1\Sigma_g^+)$, $N_2(A^3\Sigma_u^+)$, $N_2(B^3\Pi_g)$, $N_2(C^3\Pi_u)$, $N_2(a'^1\Sigma_u^-)$, O_2, N_2, O, O^- and electrons e^- and 18 reactions given in Table 4.1 with the references for the reaction rates. In this model, we have taken into account four exothermic reactions that may heat efficiently the ambient air: R9, R12, R13 and R14. It is important to note that other processes (as the relaxation of the rotational and vibrational energy of air molecules) or other reactions and species (as those involving H atom formation in humid air [*Zuzeek et al.*, 2011]) could also contribute to the gas heating but are not taken into account in this simple chemical model. Therefore, the chemical model proposed in this section certainly underestimates the fast-heating produced by a NRPD in air at atmospheric pressure. However, increasing the complexity of the chemical model (for example in taking into account the vibrational levels of electronic states of N_2 molecules) increases the number of species and reactions in air [*Piper*, 1992]. As many reactions involving excited states are not known accurately, as a first step, we have used a rather simple chemical model, with global reactions for the quenching of electronic states of N_2 molecules. The values of the energy release ϵ_i of these global quenching reactions are also difficult to determine accurately as the dissociation energy of O_2 molecules may depend on its vibrational distribution. Furthermore, we assume that the oxygen atoms produced are on their electronic ground state. Values of ϵ_i used in this work are taken from different works, and are given in Table 4.1.

	Reaction	Reference
	Electron impact excitation of N_2	
R1	$N_2 + e^- \rightarrow N_2(A^3\Sigma_u^+) + e^-$	k_1
R2	$N_2 + e^- \rightarrow N_2(B^3\Pi_g) + e^-$	k_2
R3	$N_2 + e^- \rightarrow N_2(a'^1\Sigma_u^-) + e^-$	k_3
R4	$N_2 + e^- \rightarrow N_2(C^3\Pi_u) + e^-$	k_4
	Quenching of electronically excited N_2 by N_2	
R5	$N_2(A^3\Sigma_u^+) + N_2 \rightarrow N_2(X^1\Sigma_g^+) + N_2$	k_{105}
R6	$N_2(B^3\Pi_g) + N_2 \rightarrow N_2(A^3\Sigma_u^+) + N_2$	k_{110}
R7	$N_2(C^3\Pi_u) + N_2 \rightarrow N_2(a'^1\Sigma_u^-) + N_2$	k_{118}
R8	$N_2(a'^1\Sigma_u^-) + N_2 \rightarrow N_2(B^3\Pi_g) + N_2$	k_{114}
	Quenching of electronically excited N_2 by O_2 and O	
R9	$N_2(A^3\Sigma_u^+) + O_2 \rightarrow N_2(X^1\Sigma_g^+) + 2O + \epsilon_1$	k_{100}
R10	$N_2(A^3\Sigma_u^+) + O_2 \rightarrow N_2(X^1\Sigma_g^+) + O_2$	k_{106}
R11	$N_2(A^3\Sigma_u^+) + O \rightarrow N_2(X^1\Sigma_g^+) + O$	R10
R12	$N_2(B^3\Pi_g) + O_2 \rightarrow N_2(X^1\Sigma_g^+) + 2O + \epsilon_2$	k_{113}
R13	$N_2(C^3\Pi_u) + O_2 \rightarrow N_2(X^1\Sigma_g^+) + 2O + \epsilon_3$	k_{119}
R14	$N_2(a'^1\Sigma_u^-) + O_2 \rightarrow N_2(X^1\Sigma_g^+) + 2O + \epsilon_4$	k_{115}
	Radiative desexcitation of N_2 electronically excited states	
R15	$N_2(B^3\Pi_g) \rightarrow N_2(A^3\Sigma_u^+)$	
R16	$N_2(C^3\Pi_u) \rightarrow N_2(B^3\Pi_g)$	
	electron impact dissociation of O_2	
R17	$O_2 + e^- \rightarrow 2O + e^-$	$\Sigma\ k_{13}, k_{14}, k_{15}$
R18	$O_2 + e^- \rightarrow O + O^-$	k_{23}

Table 4.1: *Two-step chemical model implemented in the discharge code in order to compute the ultra-fast heating of a nanosecond discharge in air at atmospheric pressure. All the reaction rates are taken from Kossyi et al. [1992] except for the reaction R11 which is taken from Brandenburg et al. [2005] and the reactions R15 to R18 which are taken from Liu and Pasko [2004]. The references column indicates the name given to the reaction rates in the cited articles. The energy releases* ϵ_1 *and* ϵ_4 *in reactions R9 and R14 are taken from Popov [2001] :* $\epsilon_1 = 1.1$ *eV and* $\epsilon_2 = 1.4$ *eV. In reaction R13* $\epsilon_3 = 2.2$ *eV is taken from Piper [1992]. In reaction R14* $\epsilon_4 = 5.9$ *eV is taken from Pancheshnyi et al. [2000].*

4.6.3 Comparison of the different fast-heating models

In this section, we compare the reference model used in previous Sections assuming that 30% of the discharge energy instantaneously heats the ambient air with the energy model presented in Section 4.6.1 and the chemical model in Section 4.6.2. We consider the reference nanosecond spark discharge defined in section 4.2.2 in air at 1000 K. Figure 4.22 shows the applied voltage as a function of time and for each of the three models, the time evolution of the gas temperature in the middle of the gap on the symmetry axis. For the reference model and the energy model of Section 4.6.1, the energy release is instantaneous, therefore the maximum temperature increase is obtained at the end of the voltage pulse and is of about 900 K for the reference model and 780 K for the energy model of Section 4.6.1. With the chemical model of Section 4.6.2, the heating starts at t =4 ns with the spark phase during which the electron density and then the production of excited nitrogen increases quickly. The temperature increase at the end of the pulse is about 200 K. With this model, the temperature goes on increasing after the voltage pulse during a few tens of nanoseconds up to 1550 K which corresponds to a fraction of 20% of the total discharge energy. It is interesting to note that with this two-step mechanism, half of the temperature increase seems to take place during the spark phase of the pulse, which is in qualitative agreement with the temperature measurements obtained by *Rusterholtz et al.* [2012]. The maximum temperature increase is less than in the experiments but this may be due to the fact that the initial background temperature is higher in the experiments (1400 K) and also because the simple chemical model we have considered gives a low estimation of the fast-heating. When the discharge is in the spark regime, the electric-field is rather uniform in the plasma channel and close to the applied voltage divided by the gap size which gives 20.4 kV cm^{-1}. According to Figure 4.21, for a field of 20 kV cm^{-1} at 1000 K the fraction of the discharge energy going to fast heating is around 25%. As a consequence, the model proposed in Section 4.6.1 based on the energy fractions gives a final temperature increase around 800 K which corresponds to a energy fraction of 27% of the total discharge energy.

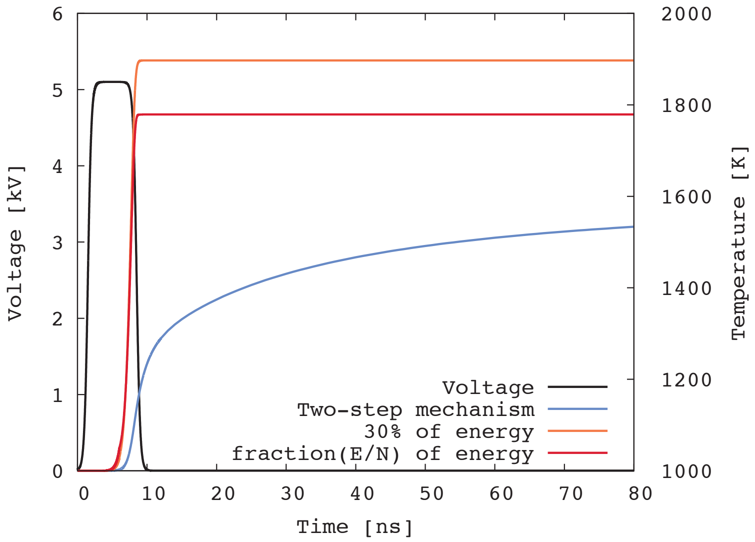

Figure 4.22: *Fraction of the electron energy as a function of the electric-field in air at 1000 K. The fast heating (black line) corresponds to the summation of the energy spent into elastic collisions, rotational excitation and 30% of the electronic excitation.*

This indicates that the magnitude of the electric-field in the spark regime is really a key parameter for the energy deposition on short time-scales. Based on these results, it seems that a good way to prevent a fast temperature increase in nanosecond repetitively pulsed discharges could be to ignite discharges in under-voltage conditions (as will be discussed in Section 6.6). In this case, most of the discharge energy goes to vibrational excited levels of N_2, and for weakly dissociated air, the relaxation of N_2 vibrational energy is rather slow and of the order of 100 μs. This stored energy could be easily removed by an air flow and then allow to keep a low temperature in the discharge channel. In conclusion, it is interesting to note on Figure 4.22 that the three different models give rather close values for the fraction of the energy going to fast heating and indicates that it should be in the range 20%-30%.
Figure 4.23 shows the 2D distribution of the temperature obtained with the three fast-heating models at the end of the voltage pulse (t =10 ns) and at t =1 μs. The comparison between the reference model (30% of the discharge energy instantaneously heats ambient air) on Figure 4.23 (a) and the energy model of Section 4.6.1 in Figure 4.23 (b) reveals a quite similar structure with the two hot spots close to the electrodes. A constriction in the middle of the gap appears on Figure 4.23 (b) but not on Figure 4.23 (a). Figure 4.23 (c) shows the temperature field obtained with the two-step mechanism of Section 4.6.2. With this chemical model, the temperature increases during the pulse but also during the post-discharge and reaches its maximum value at t =1 μs. We note that the temperature distribution for the chemical model is very similar to the distribution obtained with the two other models. It is important to point out that the three models studied in this section are different, but in all cases, the energy release depends on the electric-field and the electron density distribution during the spark phase. As a conclusion, nevertheless, it is interesting to note that the heating model seems to have only a small influence on the temperature distribution.

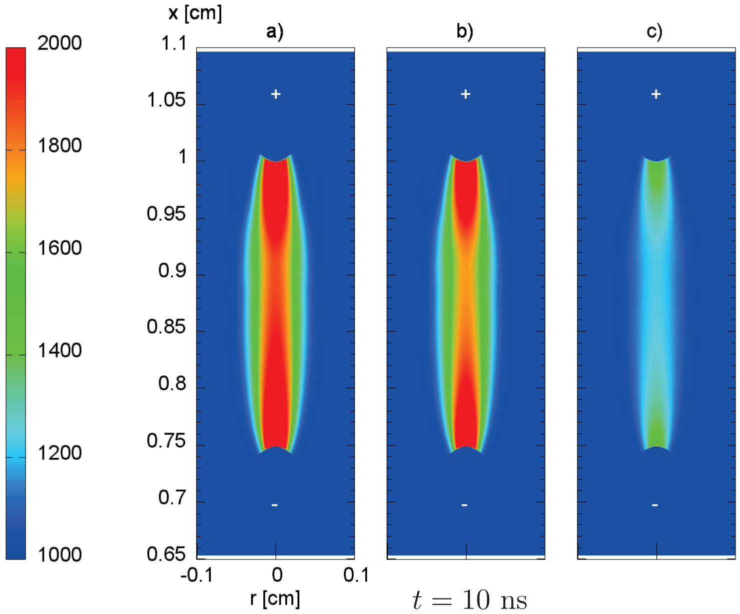

$t = 10$ ns

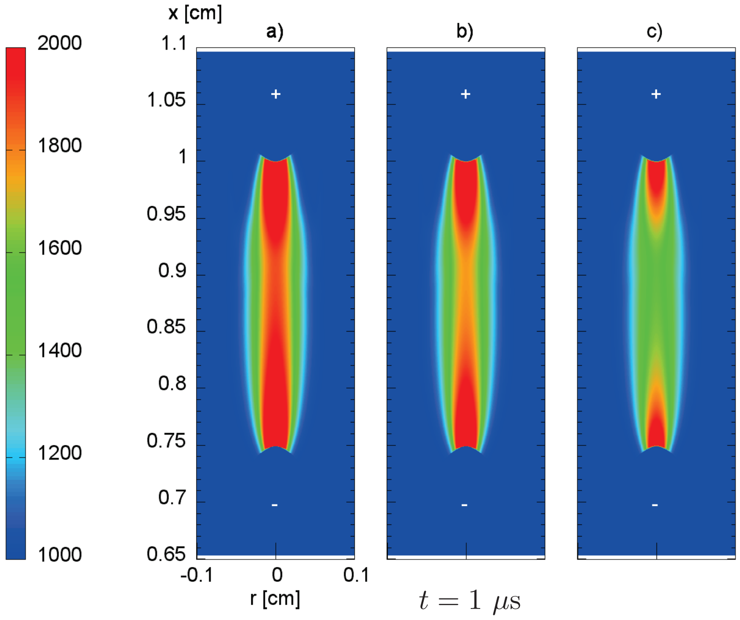

$t = 1$ μs

Figure 4.23: *2D temperature distribution at* $t = 10$ *ns and* $t = 1$ μ*s for three fast heating models for the reference nanosecond spark discharge defined in section 4.2.2 in air at 1000 K. Reference model with 30% of the discharge energy instantaneously heating the ambient air (a), instantaneous heating with the energy model presented in Section 4.6.1 (b), heating model with the two-step mechanism presented in Section 4.6.2 (c).*

4.7 Conclusion

In this chapter, we have proposed a model for a nanosecond spark discharge in air at atmospheric pressure. As shown in the experiments of *Xu et al.* [2012], the nanosecond spark discharge may significantly heat the ambient air on short timescales and induce shockwave propagation. Therefore we have studied the mechanisms of fast heating of the ambient air by the nanosecond spark discharge and we have solved 2D Euler equations to study the compressible gas dynamics induced by this heating. As a reference test case, we have considered a nanosecond spark discharge at 1000 K. For the modeling of the fast heating, as a first step, we have considered that a fixed fraction η_R of the discharge energy instantaneously heats the neutral gas. As a reference, we have used the value of $\eta_R = 30\%$ which seems to be a reasonable value for the discharge condition studied in this work, based on the works of *Popov* [2001] and *Aleksandrov* [2010]. Then we have carried out a parametric study on the influence of the value of η_R on the gas dynamics. For all values of η_R studied in the range 15 to 60%, we have observed the formation and propagation of a cylindrical shockwave and its reflection on the electrode tips. The propagation velocity of these shockwaves is very close to the speed of sound in air at 1000K. We have also noted that the channel heated by the nanosecond spark discharge expands radially on short timescales $t < 1\ \mu$s. These results are in good qualitative agreement with experiments. In a second step, we have considered that the gas heating is much slower (characteristic time of 1 μs) and we have shown that in this case, no clear shockwaves can be observed. Finally, we have studied the energy deposited in the different internal modes of air atoms and molecules by a nanosecond pulsed discharge and we have used a chemical model based on the two-step mechanism initially proposed by Popov [*Popov*, 2001] to model more accurately the dynamics of fast heating in a nanosecond spark discharge and its coupling with the ambient air. This more accurate modeling confirms that the fraction of the discharge energy going to fast heating is in the range 20%-30% and shows that the discharge energy is not deposited uniformly in the air with two hot spots close to electrode tips.

Chapter 5

Influence of the circuit on multipulse spark discharges

5.1 The multi-pulse glow to spark transition: influence of the external circuit

5.1.1 Introduction: need for a circuit model

As explained in Chapter 2 (Section 2.3), the glow-to-spark transition depends strongly on the reduced laplacian electric-field. During a multi-pulse glow discharge, as gas heating is negligible, the applied reduced electric-field remains the same as both the applied voltage, and the density of the neutral gas remain the same. With no significant heating, the effect of previous pulsed discharges on the next one is mostly to change the preionization level at the end of the interpulse period as studied in Chapter 3. If a discharge is able to heat-up the gas significantly, the neutral gas density in the discharge path may change pulse after pulse. In Chapter 4 (Section 4.5.1), we have shown that after a nanosecond spark discharge, the fluid dynamics during the interpulse leads to the fast formation of a hot low density channel in the inter-electrode gap at the location of the nanosecond spark discharge. If the applied voltage remains the same, following discharges will then have to ignite and propagate in a lower density channel with a higher applied reduced electric field. As a consequence, the conductive current will increase pulse after pulse. This current increase leads to higher current densities and a higher gas heating, then the density decrease is more and more significant pulse after pulse. Rapidly, after few pulses, very high discharge currents can be obtained. For example, a simulation has been performed with a 2.5 mm gap, a 8 kV applied voltage, a pulse duration of 5 ns and an initial temperature of 1000 K. The averaged laplacian field in the gas on the symmetry axis is of 32 kV cm^{-1} which is much higher than the breakdown field in air at 1000 K ($\simeq$ 10 kV cm^{-1}). In such over-voltage conditions, the first pulses lead to spark discharges with conductive currents which in a few pulses reach values up to 2000 A.

The fluid model used in this study is not well adapted to simulate such a high current discharge, due to the very high ionization degree, neutral gas temperature and magnetic-fields. Moreover, experimental studies on NRPD deal most of the time with nanosecond spark discharges with maximum conductive currents around 30 A. Then, other physical processes should be included in the model in order to limit the current increase during the nanosecond spark discharges. Thermal conduction and molecular diffusion in the gas are processes which could remove partially the high temperature and low density channel during the inter-pulses. However, these two processes are quite slow and we have checked that in the frequency range 1-30 kHz, they are unable to prevent the fast current increase in the multi-pulse spark discharge. Other processes such as radiative cooling or heat transfer to the electrodes could also play a role. However, in the experiments carried out at EM2C [*Rusterholtz et al.*, 2012] the most important phenomena for the transition between multipulse glow and spark discharges appear to be the convection due to the external air flow, and the current limitation due to the external circuit. Indeed, with an air flow with a high velocity, the hot channel formed after a given voltage pulse could be completely removed and replaced by ambient air between electrodes at the beginning of the next voltage pulse. Therefore an external air flow is a good way to avoid the glow to spark transition and to obtain a stable multipulse glow regime. In this chapter, we neglect the influence of the air flow and we propose to model the external circuit to limit the discharge current. Experimentally [*Pai*, 2008], it has been shown that the voltage power supply may be considered as ideal during a glow discharge, when the conductive current is very low ($\simeq$ mA). However, in the nanosecond spark regime, the applied voltage decreases sharply as the current increases during the glow to spark transition [*Pai*, 2008].

For pulse durations of 10 ns, the propagation distance of a voltage pulse through electric cables is around 3 m. It is then reasonable to assume that the applied voltage on electrodes is independent on the power supply during the discharge. When the voltage pulse reaches the anode, part of the voltage and the current will be transmitted, and some part will be reflected depending on the impedance of the plasma and the impedance of the cable. In this work, we have modeled the circuit to better calculate the applied voltage based on BNC cable theory.

5.1.2 BNC cable circuit model

A BNC cable is characterized by a linear inductance Λ (H m^{-1}) and a linear capacitance Γ (F m^{-1}). If we neglect the linear resistance of the cable, it can be modeled by the simple circuit shown in Figure 5.1:

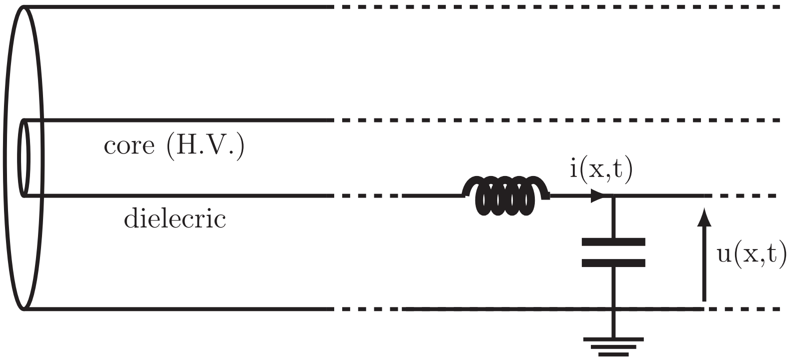

Figure 5.1: *Schematic view of a BNC coaxial cable and its equivalent circuit model*

In the circuit described on Figure 5.1, the voltage $\mathrm{u}(x,t)$ and the intensity $\mathrm{i}(x,t)$ obey the following system of differential equations:

$$\left\{\begin{array}{ll} \partial_x \mathrm{i}(x,t) & = -\Gamma \partial_t \mathrm{u}(x,t) \quad (1) \\ \\ \partial_x \mathrm{u}(x,t) & = -\Lambda \partial_t \mathrm{i}(x,t) \quad (2) \end{array}\right. \tag{5.1}$$

Combining both equations results in a wave equation for both $\mathrm{u}(x,t)$ and $\mathrm{i}(x,t)$:

$$\left\{\begin{array}{ll} \partial_{tt} \mathrm{i}(x,t) - \frac{1}{c^2}\partial_{xx}\mathrm{i}(x,t) & = 0 \quad (1) \\ \\ \partial_{tt} \mathrm{u}(x,t) - \frac{1}{c^2}\partial_{xx}\mathrm{u}(x,t) & = 0 \quad (2) \end{array}\right. \tag{5.2}$$

where $c = 1/\sqrt{\Gamma\Lambda}$ is the speed of light. If we consider a voltage wave propagating in a BNC cable from the power supply to the anode of a point-to-point discharge, the voltage $\mathrm{u}(x,t)$ follows the wave equation (5.2 (2)) which means that it can be written in the form $\mathrm{u}(x-ct)$. Then, using this expression in equation (5.1 (1)) one gets:

$$\begin{aligned} &\mathrm{u}'(x-\mathrm{c}t) = \frac{1}{\Gamma \mathrm{c}}\partial_x \mathrm{i}(x,t) = \frac{1}{\Gamma \mathrm{c}}\partial_{x-\mathrm{c}t} i(x,t) \quad (1) \\ &\Rightarrow u(x,t) = \frac{1}{\Gamma \mathrm{c}}\mathrm{i}(x,t) \qquad\qquad\qquad\quad (2) \end{aligned} \tag{5.3}$$

In equation (5.3 (2)) we have considered that no constant voltage or current is present in the cable. For a reflected voltage wave propagating in the opposite direction, from the anode to the power supply, $\mathrm{u}_{\mathrm{ref}}(x,t)$ can be written in the form $\mathrm{u}_{\mathrm{ref}}(x+ct)$. In this case the relation between $\mathrm{u}_{\mathrm{ref}}(x,t)$ and $\mathrm{i}_{\mathrm{ref}}(x,t)$ is given by:

$$\mathrm{u}_{\mathrm{ref}}(x,t) = -\frac{1}{\Gamma \mathrm{c}}\mathrm{i}_{\mathrm{ref}}(x,t) \tag{5.4}$$

Finally, the total voltage in the BNC cable is given by:

$$\mathrm{u_{tot}}(x,t) = \mathrm{u}(x,t) + \mathrm{u_{ref}}(x,t) = \mathrm{Z_{cable}}(\mathrm{i}(x,t) - \mathrm{i_{ref}}(x,t)) \tag{5.5}$$

where $\mathrm{Z_{cable}}$=1/(Γc) is the real impedance of the BNC cable. The plasma at the anode can be modelled by a impedance $\mathrm{Z_{plasma}}$. Applying the Ohm's law to the plasma one gets:

$$\mathrm{u_{tot}}(x_a,t) = \mathrm{Z_{plasma}}(\mathrm{i}(x_a,t) + \mathrm{i_{ref}}(x_a,t)) \tag{5.6}$$

where x_a is the position of the anode. Combining equation (5.5) with x=x_a and equation (5.6) gives the relation between the transmitted and the reflected components of the voltage and the current at the anode:

$$\frac{\mathrm{i_{ref}}}{\mathrm{i}} = -\frac{\mathrm{u_{ref}}}{\mathrm{u}} = \frac{\mathrm{Z_{cable}} - \mathrm{Z_{plasma}}}{\mathrm{Z_{cable}} + \mathrm{Z_{plasma}}} = \mathrm{r} \tag{5.7}$$

where r is called the reflection coefficient. Several situations can be obtained considering equation (5.7). With no plasma in the inter-electrode gap, we can consider that $\mathrm{Z_{plasma}} \to \infty$. Then, according to equation (5.7) $\mathrm{u_{ref}} = \mathrm{u}$ and the total applied voltage $\mathrm{u_{tot}}$ is two times the voltage of the incident voltage wave u. On the other hand in this case, the transmitted and reflected currents are opposite such that the total conductive current is exactly zero. If we assume a plasma of infinite conductivity, $\mathrm{Z_{plasma}}$=0 Ω, $\mathrm{i_{ref}} = \mathrm{i}$, then the reflected voltage is exactly the opposite of the incident voltage and the total applied voltage in the inter-electrode gap is zero. Finally, if the impedance of the plasma is exactly the same as the impedance of the cable, no reflection is observed and all the incident voltage and current are transmitted into the plasma. The main difficulty of the model is to estimate accurately the plasma impedance. In a general case, the plasma can be modeled by a R$\mathcal{L}$ circuit in series of resistance R and inductance $\mathcal{L}$. The voltage $\mathrm{u_{tot}}$ is then related to the intensity i according to:

$$\mathrm{i} = \frac{\mathrm{u_{tot}}(x,t)}{R}(1 - e^{-\frac{t}{\tau}}) \quad \text{with :} \;\; \tau = \frac{\mathcal{L}}{\mathrm{R}} \tag{5.8}$$

where τ is the time constant of the circuit. In Annex A.2 the inductance of the plasma has been estimated to 10^{-10} H. The minimum resistance of the plasma during the spark regime is about 100 Ω. The time constant τ of the R$\mathcal{L}$ circuit is then on the order 10^{-12} s which is very small compared to the characteristic variation time of the current and the voltage during the discharge ($\simeq 10^{-10}$ s). It is then reasonable to assume that the plasma behaves like a simple resistance. In the discharge code, it is possible to calculate explicitly the resistance of the plasma in considering the total voltage and the transmitted current at the previous time-step:

$$\mathrm{u_{tot}^{\mathit{t+dt}}} = u^{t+dt}(1 - \mathrm{r}^t) \tag{5.9}$$

with:

$$\mathrm{r}^t = \frac{\mathrm{Z_{cable}} - \mathrm{Z}^t_{\mathrm{plasma}}}{\mathrm{Z_{cable}} + \mathrm{Z}^t_{\mathrm{plasma}}} \quad \text{and} \quad \mathrm{Z}^t_{\mathrm{plasma}} = \frac{\mathrm{u}^t_{\mathrm{tot}}}{\mathrm{i}^t_{tot}}$$

where u^t is given by the shape of the voltage delivered by the power supply. In this work it corresponds to the sigmoid shape described in Section 4.2.2. This approach is rather accurate provided that the variation of the plasma resistance $\mathrm{Z_{plasma}}$ remains small during one time-step dt. According to the Drude-Lorentz formula for conductivity, this hypothesis is verified as long as the variations of the averages over the whole plasma volume of the electron density and the collision frequency remain small during one time-step. As explained in Section 1.3, the chemical time-step during the streamer discharge ensures that the variation of the electron density remains less than 10 % during each iteration. During the spark phase, the chemistry is computed implicitly but the electron density varies slowly due to the relatively low homogeneous electric-field, and the applied voltage is updated frequently. It is the same for the collision frequency as the electric-field during the spark phase evolves proportionally to the applied voltage. On the other hand, during the streamer propagation the electric-field may change rapidly but in a very narrow region such that the averaged electric-field in the whole discharge volume is almost proportional to the applied voltage and does not change very rapidly. Moreover during this phase, the conductive current is very small and the reflection coefficient r is almost always equal to -1.

Then, with the circuit model presented in this section, the applied voltage decreases dynamically when the conductivity increases significantly, for example during the spark phase. In the following, we will call "applied voltage", the voltage at the anode when no plasma and a zero conductivity is present between the electrodes. In this case, the applied voltage is two times the voltage delivered by the power supply. In practice, the impedance of the plasma is much higher than the impedance of the cable. When the conductivity of the plasma increases, its impedance decreases and slowly converges to a value close to the cable impedance. In this case, no reflection is observed and the voltage is exactly the one delivered by the power supply, which means two times lower than the applied voltage. The value of the cable real impedance $\mathrm{Z_{cable}}$ is of importance. When $\mathrm{Z_{cable}}$ increases, all other conditions being unchanged, the impedance of the plasma converges more rapidly to this value during the spark phase and a faster voltage decrease and a more significant current limitation can be obtained. The cable impedance can be increased either by changing the BNC cable properties (for example the linear inductance), or in adding a ballast resistance in series with the anode. Adding a ballast resistance is a very well-known experimental method to limit the current of a DC discharge [*Packan*, 2003]. A limitation of the circuit model presented in this section is that the propagation of the applied potential wave inside the plasma volume is considered as instantaneous. A better description would require to compute the potential and the electric-field with Maxwell equations instead of simply Poisson equation. However, the propagation time of light inside an inter-electrode gap of 2.5 mm is around 10^{-12} s and it will be shown in the following that in practice u_{tot} at the anode is varying on much longer time-scales ($\simeq 10^{-10}$ s) and therefore the electrostatic approximation remains reasonable.

5.1.3 Influence of a circuit model on a multipulse nanosecond spark discharge

To simulate a multi-pulse nanosecond spark discharge, we have used the model presented in Section 4.2.1 for the nanosecond spark during the voltage pulse. The temperature during the discharge pulse is computed assuming that 30% of the discharge energy instantaneously heats the ambient air (model of Section 4.3.3. In Section 4.5.1, we have shown that after the nanosecond spark discharge, the pressure goes to equilibrium very quickly in the inter-electrode gap due to the fast propagation of the shockwave. This characteristic time, which is close to the gap size divided by the speed of sound is much smaller than the inter-pulse duration ($\simeq 1\ \mu$s). In order to simulate a multi-pulse spark discharge, it can be reasonably assumed in a first approximation that the neutral gas density is scaled according to the ideal gas law instantaneously, just after the pulse, assuming a constant pressure. It has been shown in section 4.5.1 that the shockwaves generated remove a significant fraction of the energy deposited into the inter-electrode gap ($\simeq$50 %). Then the constant pressure approach overestimates the density decrease in the post-discharge. However, this constant pressure hypothesis allows us to avoid the resolution of all the set of Euler equations during the inter-pulse, and gives qualitative results on the influence of the air density variations. The circuit model described in previous Section 5.1.2 allows to simulate discharges in high over-voltage conditions and with significant air density variations due to the fast heating. Figure 5.2 shows the evolutions of the voltage and current during the first three pulses of the intense spark discharge presented in Section 5.1.2 (with an applied voltage of 8 kV, a pulse duration of 5 ns, a gap size of 2.5 mm and for air initially at 1000 K) coupled with the circuit model. The dashed black line represents the ideal voltage, which means the applied voltage without external circuit model. It clearly appears that the voltage is exactly equal to the ideal voltage during a first phase of the voltage pulse. This phase corresponds to the propagation of the two discharges in the gap up to the connection, and covers both the corona and the glow regime during which the current in the discharge remains very small ($r \simeq -1$). After the connection and during the nanosecond spark phase, the current increases significantly as the electron density and the plasma conductivity increase. For this reason, the applied voltage decreases rapidly compared to the ideal voltage. Then it forms a plateau around a voltage value a little higher than one half of the ideal voltage. As explained in the previous section this phase corresponds to a situation where the plasma resistance gets close to

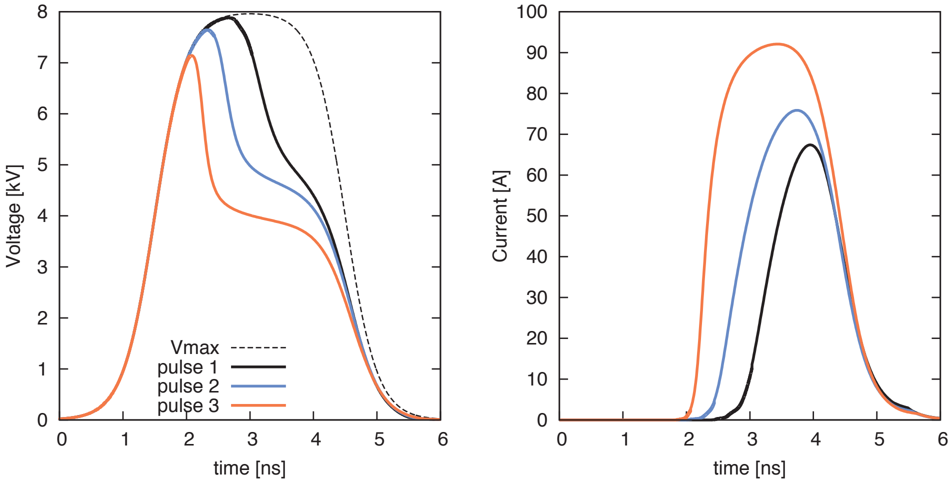

Figure 5.2: *Time evolutions of the applied voltage and the discharge conductive current for 3 consecutive voltage pulses of a nanosecond spark discharge with the circuit model of Section 5.1.2 with no ballast resistance. The applied voltage is 8 kV, the pulse duration is of 5 ns, the gap size is 2.5 mm and air is initially at 1000 K. For each pulse, the origin of time is the beginning of the considered voltage pulse. The black dashed line represents the potential wave delivered by the power supply.*

the cable real impedance. The voltage plateau is maintained until the end of the pulse duration. Between the first pulse and the third one, we note that the plateau gets longer, and at a lower voltage value. This is due to the fact that the connection between the two discharges in the gap and the glow to spark transition occurs sooner for consecutive pulses.

Figure 5.3 shows 1D radial evolutions of the air density and temperature in the middle of the inter-electrode gap at the end of each pulse at t=6 ns. While the air temperature increases significantly pulse after pulse, the air density decreases by almost a factor of three between the first discharge and the third one. For this reason the spark regime occurs sooner and is more and more energetic pulse after pulse. Then the voltage limitation becomes more significant pulse after pulse, and even if the current is still increasing pulse after pulse, it is considerably reduced: the maximum current during the third pulse is 90 A while it is around 2000 A without the circuit model. However, the fact that the current is still increasing indicates that the circuit model is not able to compensate completely the effect of the increasing reduced laplacian electric-field due to the fast-heating.

To show that the air density decrease has a major influence on the discharge structure, Figure 5.4 shows the 2D distribution of the electron density for the three consecutive pulses of Figures 5.2 and 5.3 during the propagation phase of the streamers. The times presented are referring to the beginning of each voltage pulses. For top figures, times are chosen to correspond to the same

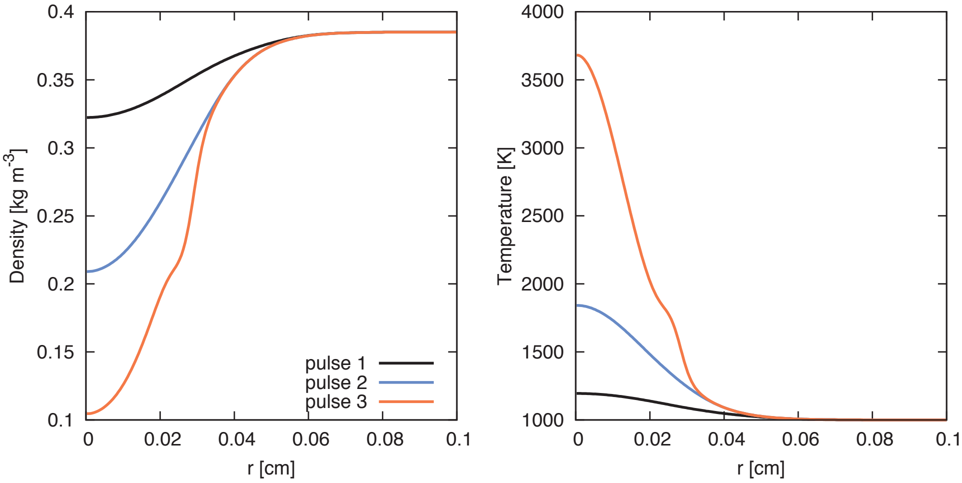

Figure 5.3: *Time evolutions of the air density and temperature in the radial direction in the middle of the gap at the end (t=6 ns) of the 3 consecutive voltage pulses of Figure 5.2.*

position of the positive discharge in the inter-electrode gap for the three pulses. For the bottom figures, times correspond to the arrival of the positive discharge at the anode and the beginning of the spark regime. We observe that both the positive and the negative discharges are influenced by the air density variation pulse after pulse: the discharge tends to ignite and to propagate faster when it is ignited in air with a lower density. We also note that the discharge radius is decreasing pulse after pulse. This constriction of the discharge radius can also be observed on the 2D temperature fields during the nanosecond spark phase on Figure 5.5. As a consequence of this decrease of the plasma filament section and also of the increase of the reduced laplacian electric-field, the current density and the Joule heating increase. This rapid decrease of the discharge radius has also be obtained numerically by *Nikipelov et al.* [2011]. Although the discharge structure is varying significantly, the 2D distribution of the temperature due to the fast-heating is barely affected and the maximum temperature remains located close the tip of the electrodes. The faster propagation and the constriction of the discharge is due to the easier propagation in the lower density and higher temperature plasma channel generated by successive pulses. To prevent this, in the following section we propose to add a ballast resistance to increase the limitation of the current with the circuit model.

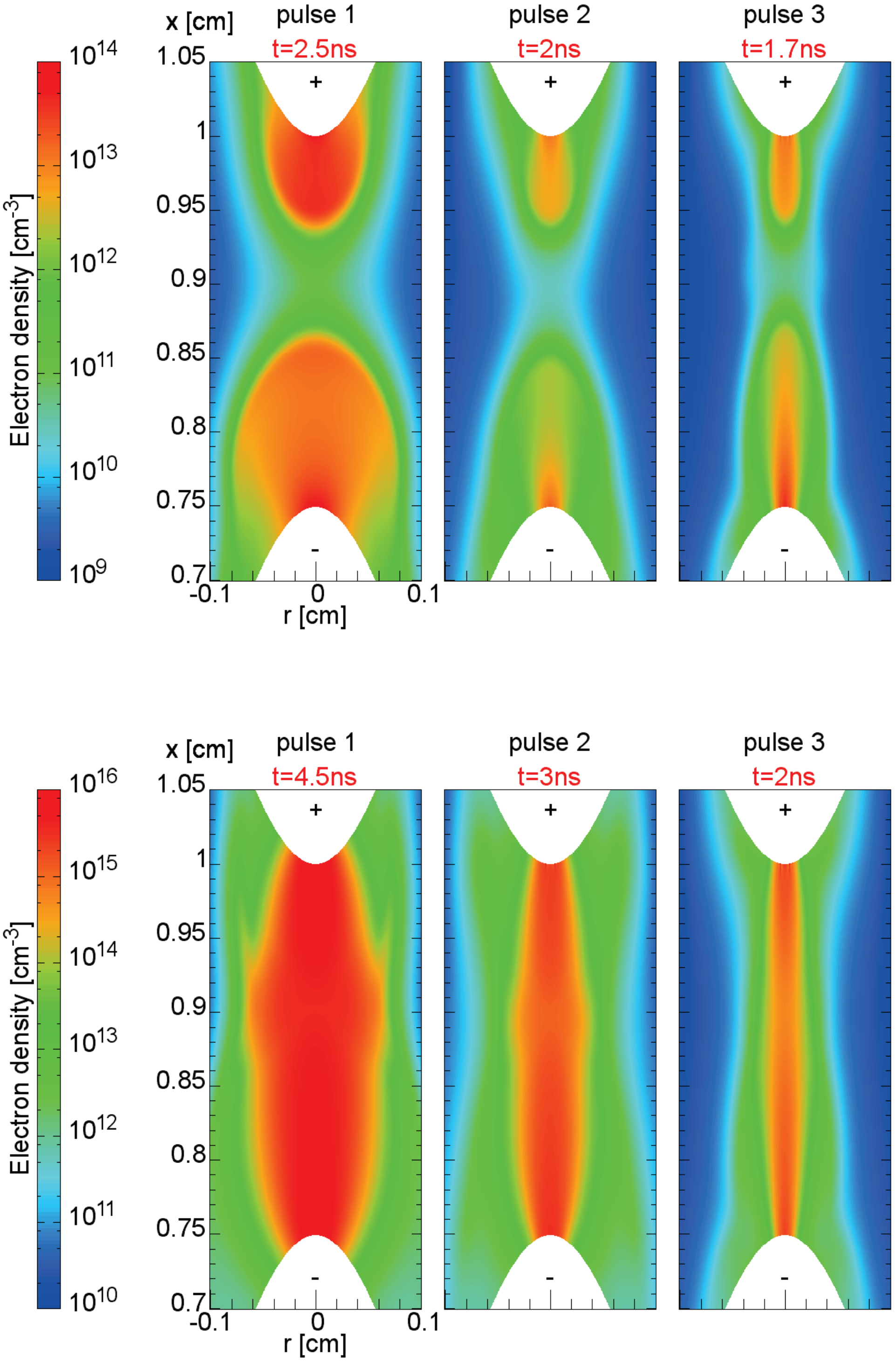

Figure 5.4: *Cross-sectional views of the electron density for 3 consecutive voltage pulses of a nanosecond spark discharge for the same conditions as Figure 5.2. For each pulse, the origin of time is the beginning of the considered voltage pulse. For top figures, times are chosen to correspond to the same position of the positive discharge in the inter-electrode gap for the three pulses. On the bottom figures, times correspond to the arrival of the positive discharge at the anode and the beginning of the spark regime.*

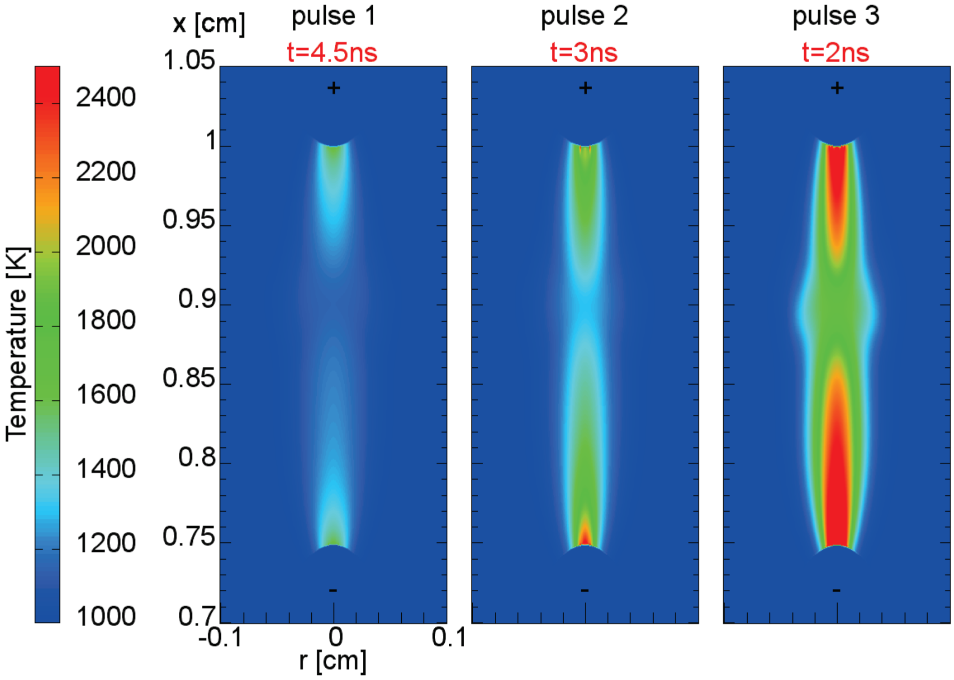

Figure 5.5: *Cross-sectional views of the air temperature for 3 consecutive voltage pulses of a nanosecond spark discharge for the same conditions as Figure 5.2. For each pulse, the origin of time is the beginning of the considered voltage pulse. Times are the same as those of bottom figures on Figure 5.4. The temperature is computed assuming that 30% of the discharge energy instantaneously heats the ambient air (model of Section 4.3.3).*

5.1.4 Influence of adding a ballast resistance in the circuit model on the multipulse nanosecond spark discharge

To prevent the fast formation of a very energetic nanosecond spark discharge due to the fast-heating and the air density decrease, it is possible to add a ballast resistance to the cable impedance Z_{cable} in the circuit model presented in Section 5.1.2. Then, results presented in previous section correspond to the case R=0 Ω. Figure 5.6 shows the voltage and the current evolutions for the same discharge parameters as in the previous section but with a ballast resistance of R=1000 Ω. We have simulated 7 consecutive pulses in this case, as the limitation of the current is higher than with R=0 Ω: the maximum of the current is around 4.5 A while it was close to 90 A without resistance. The resistance has a major influence and the intense spark regime is considerably inhibited. The evolution of the maximum current pulse after pulse shows a complex non-monotonous evolution since it increases between pulse 1 and 4, then it decreases for pulses 5 and 6 and finally it increases again for pulse 7. Such a complex evolution is due to the strong non-linear coupling between the circuit model, the reduced electric-field, the evolution of the discharge structure and the energy released in the discharge. Figure 5.7 shows the 1D evolution of the air density and temperature in the radial direction in the middle of the gap. Compared to figure 5.3, the temperature increase is much smaller: only 60 K instead of 2500 K, and the density variation is rather small (around 10 %). Figure 5.8 shows shows the 2D distribution of the electron density for the three first pulses at two different times during each voltage pulse. The times presented are referring to the beginning of each voltage pulse. For top figures, times are chosen to correspond to the same position of the positive discharge in the inter-electrode gap for the three pulses. For the bottom figures, times correspond to the arrival of the positive discharge at the anode. We note that the the discharge structure looks exactly the same between the first three pulses even if the first positive discharge ignites a little later than the next ones. Figure 5.9 shows the 2D temperature fields during these three first pulses. For the two first pulses, we observe three hot spots (two close to the electrode tips and a third one almost in the middle of the gap at the location of the impact between positive and negative discharges). It is interesting to note that in the case with R=0 on Figure 5.5, only the two hot spots close to the electrode tips are observed. Then discharges calculated with R=1000 Ω seem to have a structure close to the one obtained for nanosecond spark discharges at 300 K in Section 4.5.4. This means that due to the current limitation with R=1000 Ω the intense spark discharge is inhibited and gets closer to an energetic glow discharge during the first two pulses. Due to density variations, this energetic glow discharge becomes a spark discharge with a strong current limitation. This variation of discharge regime is probably the reason why the maximum of the discharge current evolves in a non-intuitive way pulse after pulse. These results indicate that the discharge regime can be changed by varying the resistance of the circuit and that the case R=1000 Ω is a limit case between a multipulse nanosecond spark regime and a multipulse nanosecond glow discharge regime. The temperature increase is around 10 K per pulse and an evolution of this discharge to a more energetic nanosecond spark discharge may occur on much longer timescales and with a larger number of pulses. An increase of 1000 K comparable to the case R=0 Ω could be obtained in 100 pulses which means 10 ms at 10 kHz. However, the permanent regime of this discharge will then depend on other physical processes important on longer timescales such as thermal conduction in the gas and heat transfer to the electrodes and the air flow. In particular, experiments at EM2C [*Rusterholtz et al.*, 2012] have shown that the air flow has also a significant influence on the discharge regime and on the transition between multipulse glow and spark discharges. For example a flow of 10 m s^{-1} would remove completely the hot channel in 10 ms and then the flow would in this case allow to obtain a 'stable' multipulse glow regime.

In our simulations, we have checked that if the ballast resistance is increased to values higher than 1000 Ω, the glow to spark transition after a few discharge pulses may completely disappear. For example, with a ballast resistance of 10000 Ω, Figure 5.10 shows that the current and the voltage evolution of 7 consecutive pulses are almost identical. The maximum of current remains very small for all pulses and is around 0.5 A. Figure 5.11 shows the 2D distribution of the electron density for the three first pulses during each voltage pulse. We note that the the discharge structure looks exactly the same between the first three pulses with a constriction in the middle of the gap and a large variation of the discharge radius as a function of the axial position in the gap. This discharge structure is very different from the one obtained on Figure 5.4 in Section 5.1.3 with the circuit model but no ballast resistance. Figure 5.12 shows the 2D temperature fields during these three first pulses. We observe that the current limitation is so strong with R=10000 Ω that the nanosecond discharge remains in the glow regime at 1000 K with a very small temperature increase of about 6 K at maximum, located in three hot spot regions (close to electrode tips and in the gap). Then, increasing significantly the ballast resistance is also an efficient way to obtain a ’stable’ multipulse glow regime.

5.2 Conclusion

In this chapter, we have taken into account an external circuit model based on the BNC cable used in experiments to limit the discharge current in multipulse nanosecond discharges. With the circuit model used, the applied voltage decreases dynamically when the conductivity of the plasma increases. Therefore we have been able to simulate several consecutive discharge pulses and to study the transition from multipulse nanosecond glow to spark discharges. In the multipulse nanosecond spark regime, the air temperature increases (correspondingly the air density decreases) significantly pulse after pulse in the discharge channel and we have observed that the discharge radius decreases pulse after pulse. To further increase the current limitation, we have added a ballast resistance to the circuit and we have shown that for a value of R=10,000 Ω, the heating after each pulse is negligible and then the multipulse nanosecond discharge in this case remains in a ’stable’ glow regime.

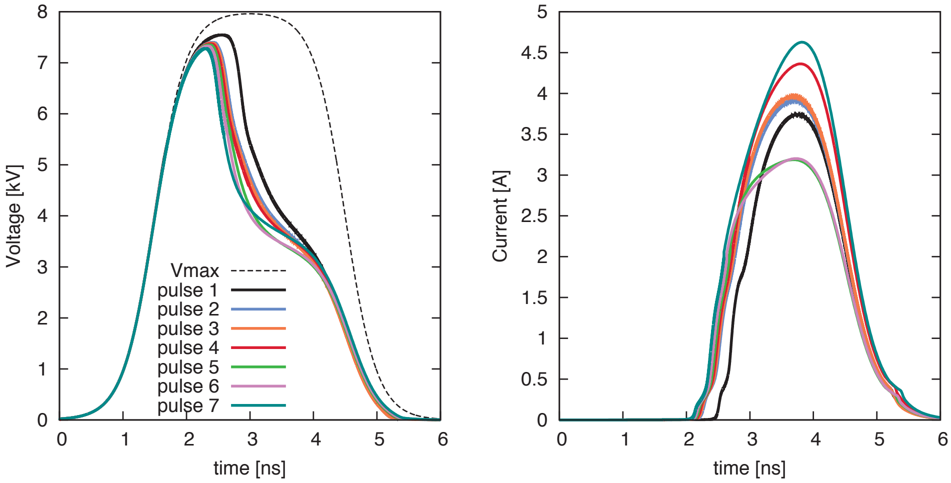

Figure 5.6: *Time evolutions of the applied voltage and the discharge conductive current for 7 consecutive voltage pulses of an naosecond spark discharge with the circuit model of Section 5.1.2 with an additional ballast resistance R=1000 Ω. The applied voltage is 8 kV, the pulse duration is of 5 ns, the gap size is 2.5 mm and air is initially at 1000 K. For each pulse, the origin of time is the beginning of the considered voltage pulse. The black dashed line represents the potential wave delivered by the power supply.*

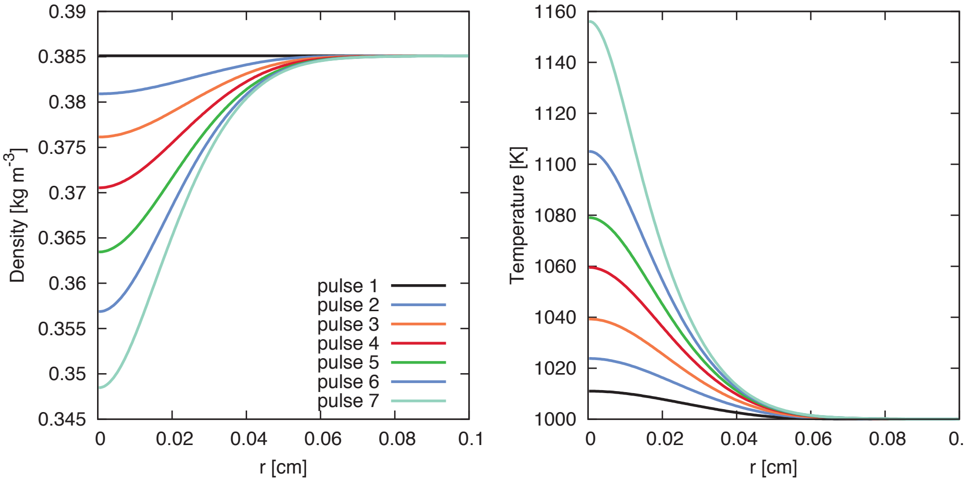

Figure 5.7: *Time evolutions of the air density and temperature in the radial direction in the middle of the gap at the beginning (t=0 ns) of 7 consecutive voltage pulses for the same conditions as in Figure 5.6.*

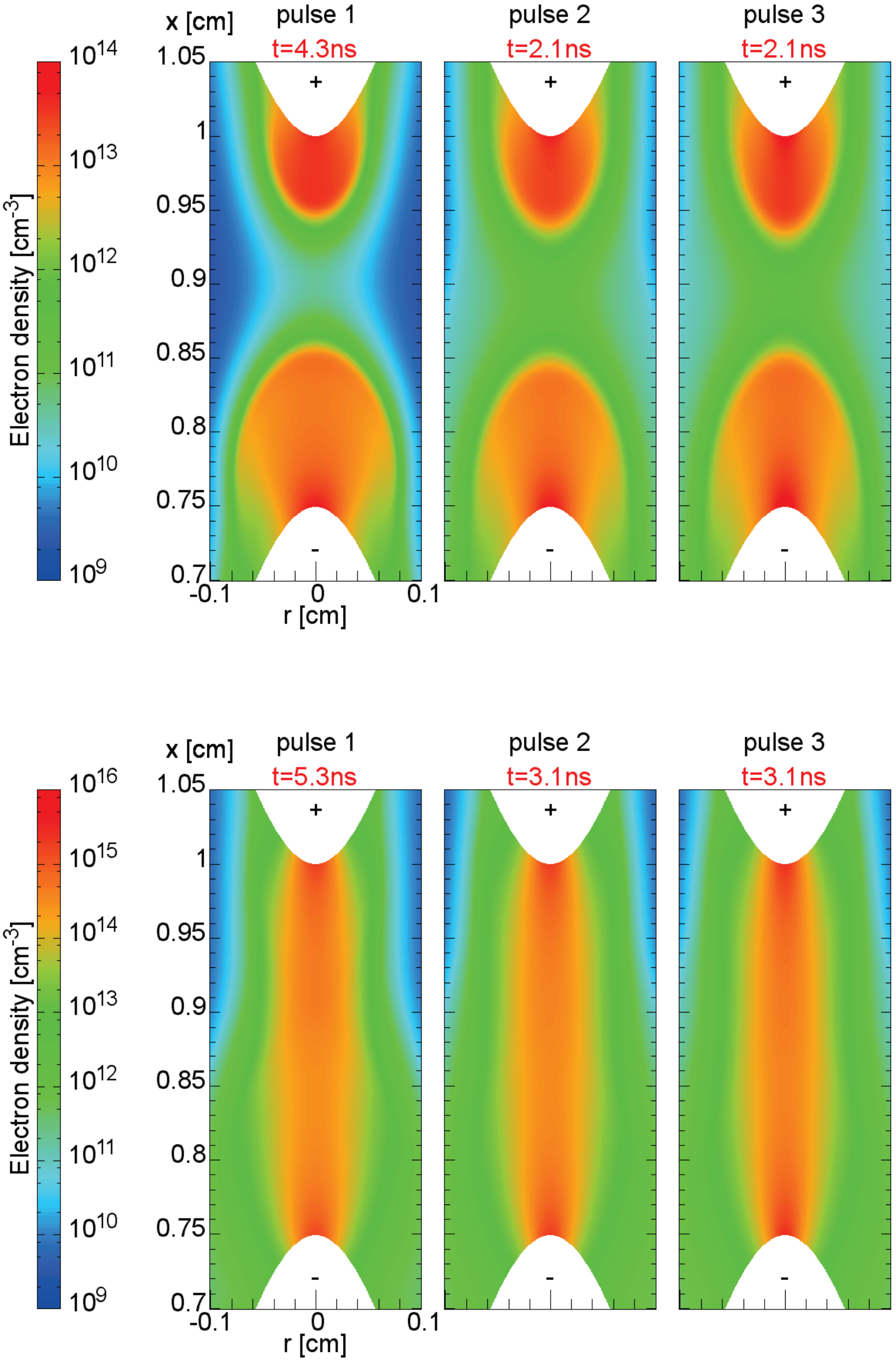

Figure 5.8: *Cross-sectional views of the electron density for the 3 first consecutive voltage pulses of a nanosecond spark discharge for the same conditions as Figure 5.6. For each pulse, the origin of time is the beginning of the considered voltage pulse. For top figures, times are chosen to correspond to the same position of the positive discharge in the inter-electrode gap for the three pulses. For the bottom figures, times correspond to the arrival of the positive discharge at the anode.*

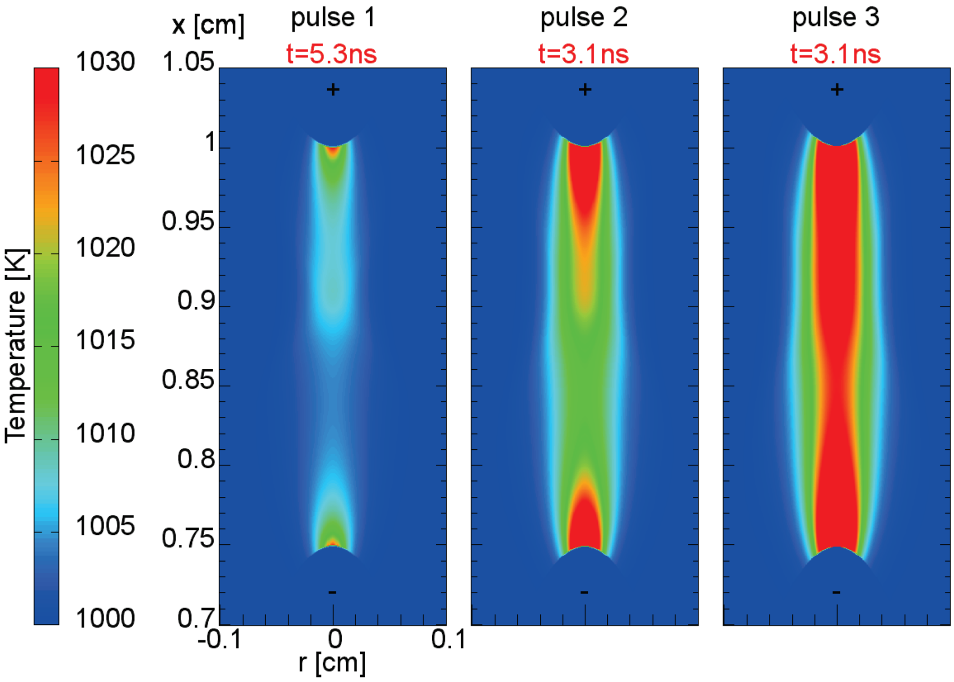

Figure 5.9: *Cross-sectional views of the air temperature for the 3 first consecutive voltage pulses of a nanosecond spark discharge for the same conditions as Figure 5.6. For each pulse, the origin of time is the beginning of the considered voltage pulse. Times are the same as those of bottom figures on Figure 5.4. The temperature is computed assuming that 30% of the discharge energy instantaneously heats the ambient air (model of Section 4.3.3).*

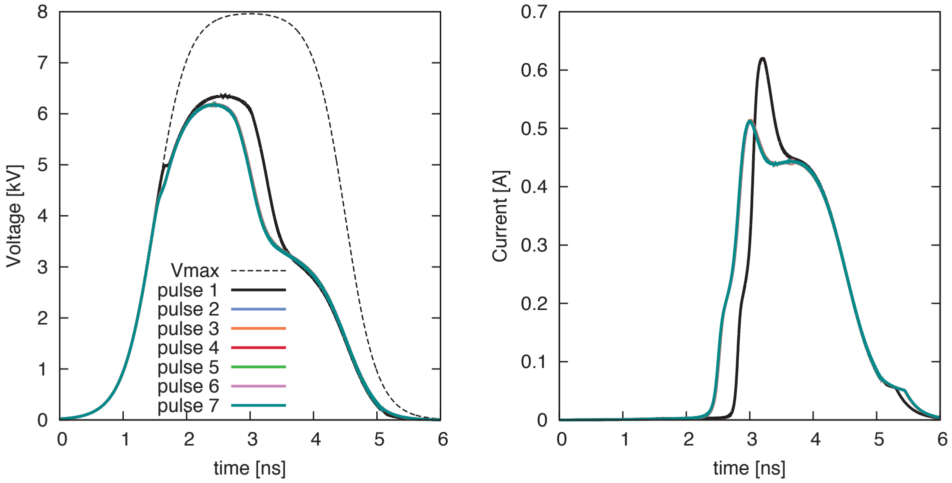

Figure 5.10: *Time evolutions of the applied voltage and the discharge conductive current for 7 consecutive voltage pulses of an naosecond spark discharge with the circuit model of Section 5.1.2 with an additional ballast resistance R=10,000 Ω. The applied voltage is 8 kV, the pulse duration is of 5 ns, the gap size is 2.5 mm and air is initially at 1000 K. For each pulse, the origin of time is the beginning of the considered voltage pulse. The black dashed line represents the potential wave delivered by the power supply.*

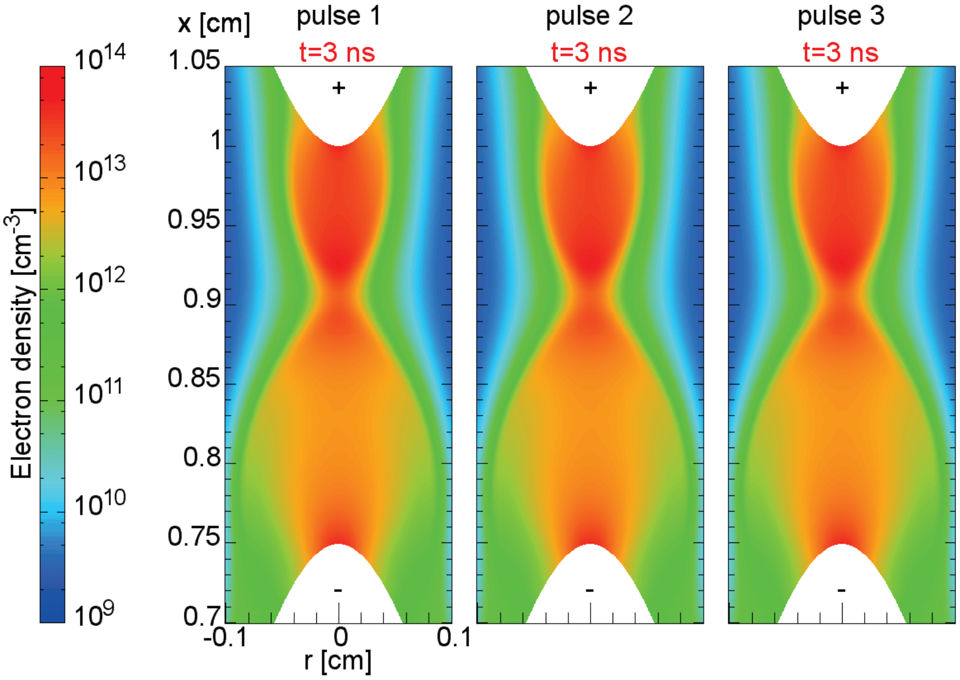

Figure 5.11: *Cross-sectional views of the electron density for the 3 first consecutive voltage pulses of a nanosecond spark discharge for the same conditions as Figure 5.10. For each pulse, the origin of time is the beginning of the considered voltage pulse and 3 ns corresponds to the arrival of the positive discharge at the anode.*

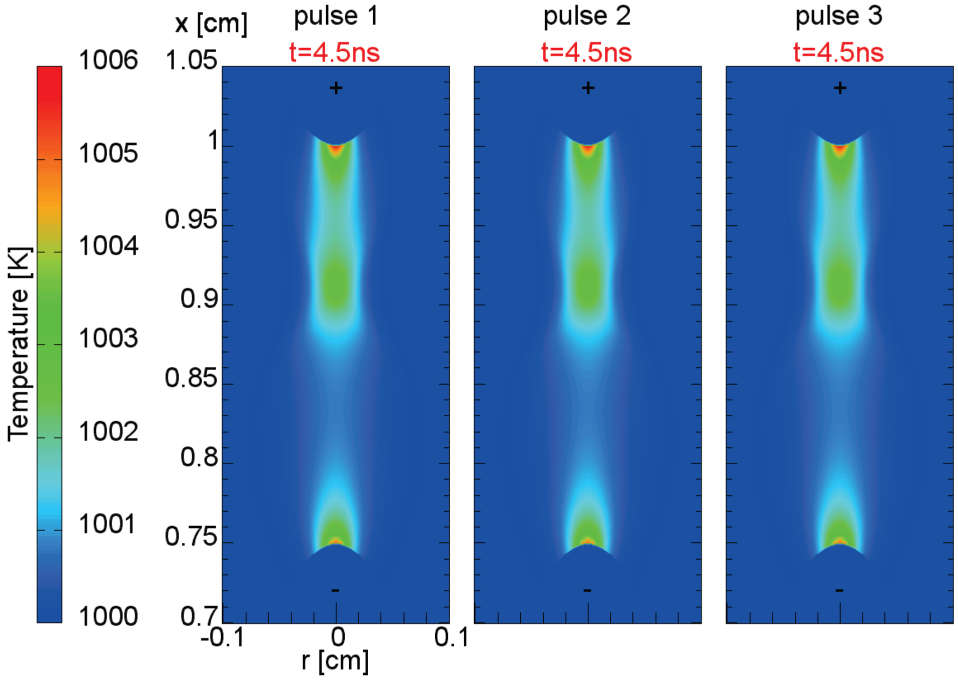

Figure 5.12: *Cross-sectional views of the air temperature for the 3 first consecutive voltage pulses of a nanosecond spark discharge for the same conditions as Figure 5.10. For each pulse, the origin of time is the beginning of the considered voltage pulse and the temperature is at maximum at the end of the pulse at 4.5 ns. The temperature is computed assuming that 30% of the discharge energy instantaneously heats the ambient air (model of Section 4.3.3).*

Part II

Applications of nanosecond pulsed discharges

Chapter 6

Application of NRDP at 300K: Optimization of the conditions to obtain the glow regime

6.1 Introduction

For many applications as biomedical, surface treatment and decontamination, the challenge is to produce a large plasma volume at atmospheric pressure at low power with a low gas temperature and a high chemical reactivity. Therefore, in this chapter, first, we propose to study in detail the conditions to obtain a glow discharge at 300K with a NRPD in air at atmospheric pressure between two point electrodes. Second, we will discuss ways to extend these conditions in order to obtain glow discharges in larger interelectrode gaps. In Section 2.7, as a reference we have studied the dynamics of a single discharge in air at $T_{\mathrm{g}} = 300$ K occurring during one of the nanosecond voltage pulses for an applied voltage of 15 kV, a 5 mm gap and point electrodes with $R_{\mathrm{p}} = 50\,\mu$m using the 2D discharge model presented in Section 1.3. As many discharges have occurred before the simulated one, we have estimated that the density of seed charges is uniform in the interelectrode gap and of 10^9cm^{-3} for $T_{\mathrm{g}} = 300$ K and we have neglected the influence of photoionization. In Sections 6.2 to 6.5, we will carry out a detailed parametric study on the conditions to obtain a glow regime at 300 K. We will vary the applied voltage, the size of the interelectrode gap and the radius of curvature of hyperboloid electrodes. Finally in Section 6.6, we will discuss ways to optimize the volume of the glow discharge obtained with a NRPD between point electrodes at 300 K and at atmospheric pressure.

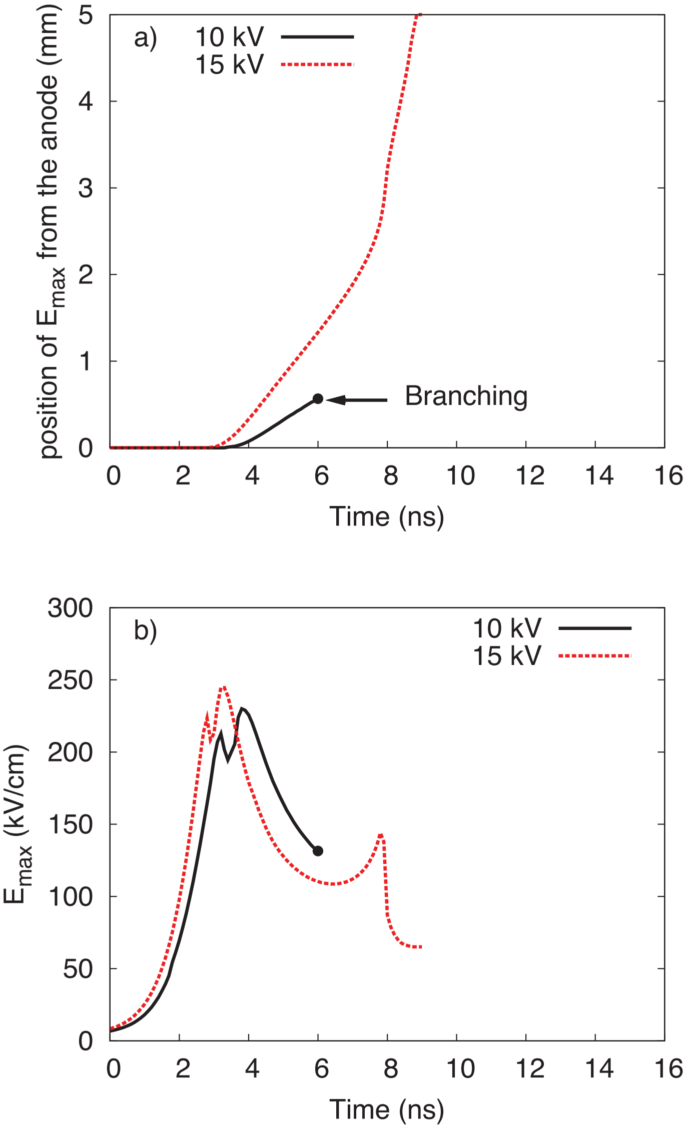

Figure 6.1: *Influence of the applied voltage on the time evolutions of the position of the maximum electric field* E_{max} *(a) and the value of* E_{max} *(b) along the axis of symmetry for* $T_{\mathrm{g}} = 300$ *K,* R_{p}*=50 µm and a 5 mm gap.*

6.2 Influence of the applied voltage on the discharge dynamics at T_g=300 K

Figure 6.1 shows the time evolutions of the position of the positive discharge front, and of the value of E_{max} for two different values of the applied voltage: 10 and 15 kV. In comparison to the reference case for an applied voltage of 15 kV in Section 2.7, we note that for 10 kV, the ignition time of the discharge is slightly increased (3.5 instead of 3 ns) and the velocity of the positive discharge is much less than for 15 kV. At t =6 ns, for 10 kV we have observed that the positive streamer branches with a maximum of electric field out of the symmetry axis of the discharge. The accurate simulation of branching discharges is beyond the scope of this work and would require a 3D discharge code. In this work, as we use a 2D axisymmetric model, we simply stop the simulations when the discharge branching starts. It is interesting to note that in our simulations at T_g=1000 K, no branching has been observed for the range of conditions studied in Sections 2.2 to 2.6. These results are in qualitative agreement with experiments, with no observed branching at T_g=1000 K and many observations of branching discharges at T_g=300 K [*Jarrige*, 2011].

One of the objective of this chapter is to discuss the conditions to obtain a glow regime at T_g=300 K. Following the analysis carried out in *Pai et al.* [2010a], to obtain the glow regime, the average electric field has to be equal to the breakdown field. At T_g=300 K, for the 10 kV case with a 5 mm gap, the average electric field is $E_{gap} \simeq 20$ kV cm^{-1} which is below the breakdown field of 30 kV cm^{-1}. Then, to check the criterion proposed in *Pai et al.* [2010a], we have carried a simulation at T_g=300 K with an applied voltage of 10 kV and an additional uniform axial electric field E_0=10 kV cm^{-1} to have an average field in the gap of 30 kV cm^{-1}, the breakdown field. Figure 6.2 shows that in this case the characteristics of the discharge are very close to the 15 kV reference case with a fast and stable propagation of the positive streamer, the connection of both discharges and the positive streamer arrival at the cathode. We have then checked the sensitivity of the results to the value of E_0 and Figure 6.2 shows that for a small additional uniform field of E_0= 2 kV cm^{-1}, the branching of the positive discharge disappears. In this case, the ignition of the discharge occurs at 3 ns, the velocity of the discharge before connection is about 300 km s^{-1} and the connection occurs at 12.5 ns. Then with a voltage pulse duration of about 12.5 ns, this discharge could be in the glow regime. It is interesting to note that in this case the average electric field in the gap is only E_{gap} =22 kV cm^{-1}, less than the breakdown field. This result seems to indicate that the glow regime at T_g=300 K can be obtained even if the average electric field is less than the breakdown field. Then to better understand the conditions to obtain a glow regime at T_g=300 K, it is important to determine the conditions for a stable propagation of the positive streamer in the gap.

At P_{atm} and T_g=300 K, an external electric field of about 5 kV cm^{-1} is required to have a stable positive streamer propagating in air far from electrodes [*Raizer*,

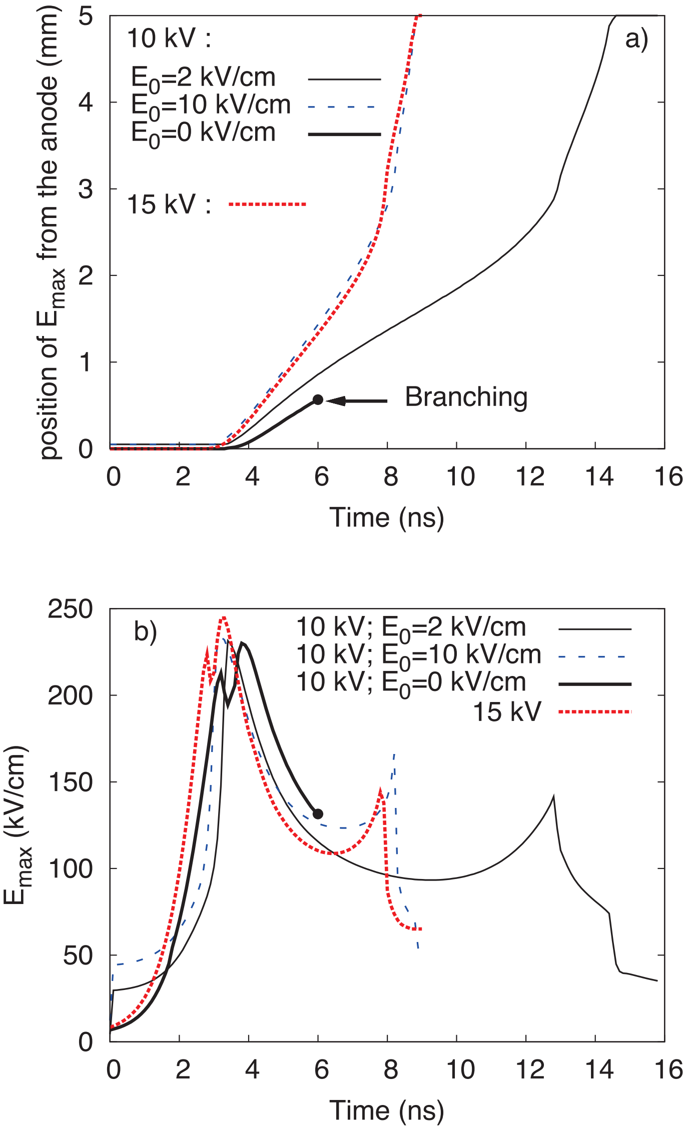

Figure 6.2: *Influence of an additional uniform axial electric field E_0 for the conditions of Figure 6.1.*

1991]. For the point-to-point geometry studied in this work, after the voltage rise, the minimal Laplacian field is obtained in the middle of the gap $E_{L,min}$ by symmetry. For this particular geometry, we have carried out several test runs for different values of the applied voltage, the gap and R_{p} and we have determined that $E_{L,min}$ has to be equal to $E^* \simeq$8-9 kV cm^{-1} to ensure a stable propagation of the positive discharge in the gap. For the two applied voltages studied on Figure 6.1, it is interesting to note that $E_{L,min}$=11 kV cm$^{-1} > E^*$ for the 15 kV reference case of Section 2.7 and is only 7.3 kV cm$^{-1} < E^*$ for the 10 kV case with $E_0 = 0$ kV cm^{-1} which branches. For 10 kV and $E_0 = 2$ kV cm^{-1}, $E_{L,min}$ =9.3 kV cm$^{-1} > E^*$ and Figure 6.2 shows that in this case, a stable propagation of the positive streamer is obtained.

6.3 Influence of the gap on the discharge dynamics at T_{g}=300 K

Figure 6.3 shows the time evolutions of the position of the positive discharge front, and of the value of E_{max} for two different values of the gap: 2.5 and 5 mm. For both cases, we observe a stable propagation of the positive discharge and no branching. Indeed, as mentioned in the previous section, for a 5 mm gap, $E_{L,min}$ is higher than E^* and then this is also the case for a gap of 2.5 mm for the same applied voltage and same value of R_{p}. As already observed at T_{g}=1000 K on Figure 2.5, Figure 6.3 shows that as the gap increases from 2.5 to 5 mm, the connection time increases by a factor 2 and the ignition time remains unchanged. On Figure 6.3, the velocity of the discharge before connection increases from ∼500 km s^{-1} to ∼625 km s^{-1} i.e. by a factor of 1.25 as the gap increases from 2.5 to 5 mm. After connection, Figure 6.3 shows that the velocity of the discharge is increased by a factor 6.9 for the 2.5 mm gap and 4.5 for the 5 mm gap. As already observed at T_{g}=1000 K on Figure 2.5, Figure 6.3 shows that the peak electric field in the positive streamer head is almost the same for the two studied gaps. After the connection the electric field in the gap decreases to the average electric field in the gap $E_{\mathrm{gap}} \simeq$60 kV cm^{-1} for 2.5 mm and 30 kV cm^{-1} for 5 mm (Figure 2.10). Then decreasing the gap at T_{g}=300 K from 5 to 2.5 mm decreases the connection time by a factor of 1.8 and increases the average electric field in the gap to values higher than the breakdown field. Then for T_{g}=300 K, an applied voltage of 15 kV and $R_{\mathrm{p}} = 50\,\mu m$, for a voltage pulse duration of 10 ns, a glow regime will be obtained for a 5 mm gap and a spark regime for 2.5 mm.

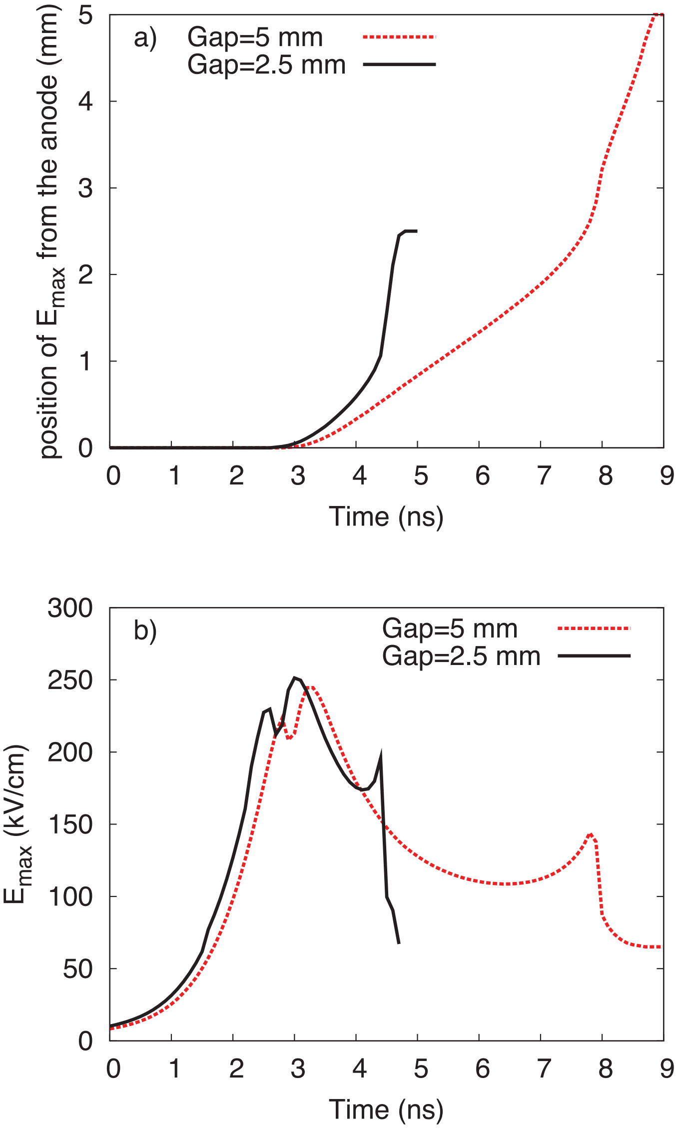

Figure 6.3: *Influence of the gap on the time evolutions of the position of the maximum electric field* $E_{\max}$ *(a) and the value of* $E_{\max}$ *(b) along the axis of symmetry for* $T_{\mathrm{g}} =$ *300 K,* R_{p}=*50 µm and an applied voltage of 15 kV.*

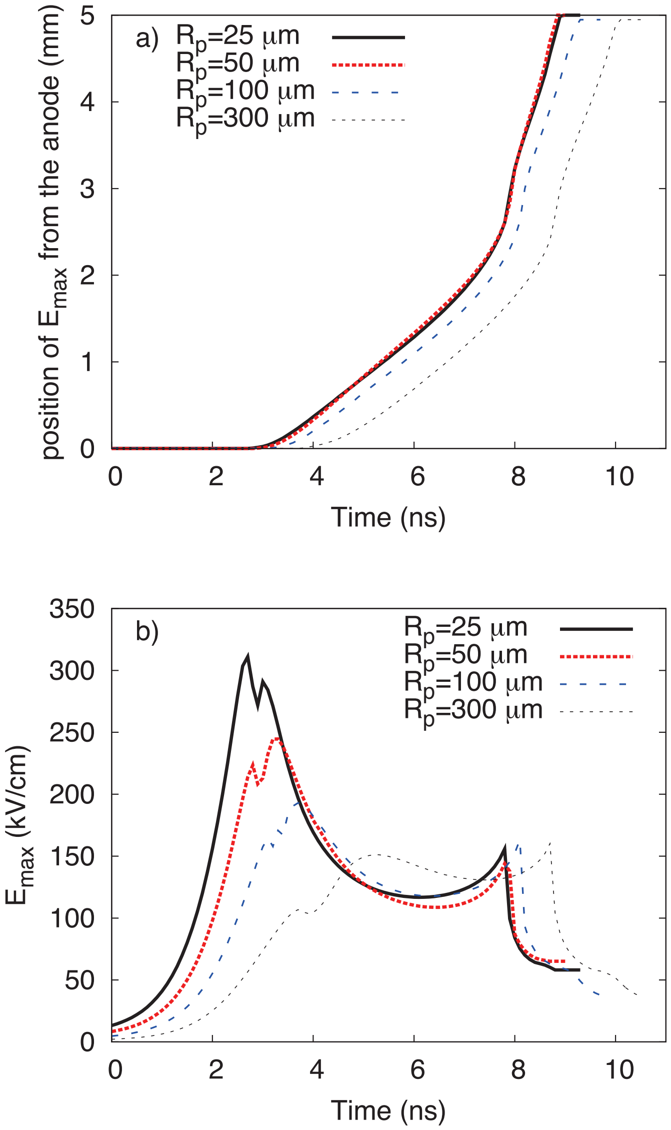

Figure 6.4: *Influence of the radius of curvature of point electrodes R_p on the time evolutions of the position of the maximum electric field E_max (a) and the value of E_max (b) along the axis of symmetry for $T_\mathrm{g} = 300$ K, an applied voltage of 15 kV and a 5 mm gap.*

6.4 Influence of the radius of curvature of electrodes R_{p} on the discharge dynamics at T_{g}=300 K

Figure 6.4 shows the time evolutions of the position of the positive discharge front, and of the value of E_{max} for four different values of $R_{\mathrm{p}} = 25, 50, 100$ and 300 μm for T_{g}=300 K, an applied voltage of 15 kV and a 5 mm gap. We have checked that for the lowest value $R_{\mathrm{p}} = 25\,\mu$m, $E_{L,min}$=9.6 kV cm^{-1} $> E^{*}$. For the same applied voltage and same value of the gap, $E_{L,min}$ increases as the value of R_{p} increases. Then for all values of R_{p} shown on Figure 6.4, $E_{\mathrm{L,min}}$ is higher than E^{*}, and then a stable propagation of the positive discharge is observed. As for T_{g}=1000 K, Figure 6.4 shows that at T_{g}=300 K the increase of R_{p} from 25 to 300 μm has a small influence on the ignition time of the discharge which increases from 3 to 4 ns. At T_{g}=300 K, we note that the velocity of the discharge is independent of the value of R_{p} and is about 500 km s^{-1}. Then the connection time increases only from 8 to 8.75 ns as R_{p} varies by a factor 12 from 25 to 300 μm. Figure 6.4 (b) shows that for all studied values of R_{p}, the peak electric field in the positive streamer head converges towards 120 kV cm^{-1} before connection. It is interesting to note that the electric field in the positive streamer head has the same dependence with R_{p} than the one observed on Figure 2.6 at T_{g}=1000 K. For $R_{\mathrm{p}} = 50\,\mu$m, Figure 6.4 (b) shows that at the start of the positive streamer the peak electric field in the streamer head is higher than 120 kV cm^{-1} and decreases towards this value during the propagation. Conversely for $R_{\mathrm{p}} = 300\,\mu$m, the peak electric field in the streamer head is less than 120 kV cm^{-1} as it starts propagating and then the peak electric field increases during the discharge propagation to reach this value. After connection, the electric field converges towards the average electric field in the gap E_{gap} =30 kV cm^{-1}.

6.5 Summary of the results of the parametric study carried out at T_{g}=300 K

Table 6.1 summarizes the results obtained in the preceding sections at T_{g}=300 K on ignition and connection times, discharge velocity before and after connection and values of E_{gap} and $E_{\mathrm{L,min}}$.

In agreement with experiments, in our simulations we have observed that there is a minimal voltage to be applied for a given pulse duration to have the ignition and propagation of both discharges until the connection. At T_{g}=300 K, with R_{p}=50 μm, a 5 mm gap and a voltage pulse duration of about 10 ns, this minimal voltage is about 15 kV. For the range of conditions studied, we note that the ignition time of the discharge appears to be almost independent of the gap, the applied voltage and R_{p}. Table 6.1 shows that the connection time increases as the gap increases. Conversely, the radius of curvature of electrodes has a smaller effect on the connection time which slightly decreases as the radius of curvature of electrodes decreases. The main difference between the results at T_g=1000 K and T_g=300 K is the fact that in the range of parameters studied in this work, branching of discharges has been observed at T_g=300 K and not at T_g=1000 K. Based on our simulations, a minimal value of $E^* \simeq$8-9 kV cm^{-1} at P_{atm} and T_g=300 K of $E_{\text{L,min}}$ the Laplacian electric field in the middle of the gap is necessary to have a stable propagation of the positive streamer without branching in the point-to-point geometry studied in this work. This field is slightly higher than the minimal external field required to have a stable positive streamer propagating in air far from electrodes at P_{atm} and T_g=300 K. Using similarity relations, we assume that this minimal value is N_{300}/N_{1000} times less at T_g=1000 K and then $E^* \simeq$2.4-2.7 kV cm^{-1} at T_g=1000 K. In Table 2.1, in Section 2.6, we note that for all cases $E_{\text{L,min}} > 2.5 - 3$ kV cm^{-1} except the case R_p=50 μm, for a 5 mm gap and 3 kV. In this case $E_{\text{L,min}} = 2.2$ kV cm^{-1} and then this discharge may branch. In this work, for T_g=1000 K, we have carried out simulations with voltage pulse durations of the order of 10 ns to be close to experimental conditions and during the 16 ns simulated for this case (R_p=50 μm, for a 5 mm gap and 3 kV), Figure 2.4 shows that the positive streamer propagates very slowly with no branching. As mentioned earlier these results are in qualitative agreement with experiment using 10 ns voltage pulses, with no observed branching at T_g=1000 K and many observations of branching discharges at T_g=300 K [*Jarrige*, 2011].

R_p(μm)	50	50	50	50	25	100	300	300
Applied Voltage (kV)	15	15	10	15	15	15	15	15
Gap (mm)	2.5	5	5	10	5	5	5	10
Ignition-time (ns)	3	3	3.5	3.6	3	3.25	4	5
connection-time (ns)	4.5	8	-	-	8	8.25	8.75	28
V before connection (km s^{-1})	625	500	200	375-92	500	500	500	260
Velocity increase after connection	6.9	4.5	-	-	4.5	4.5	4.6	1.6
E_{gap} (kV cm^{-1})	60	30	20	15	30	30	30	15
$E_{\text{L,min}}$ (kV cm^{-1})	24.5	11	7.3	7.5	9.6	12.5	15.9	9.2

Table 6.1: *Discharge characteristics at T_g =300 K for different applied voltages, gaps and values of R_p*

In *Pai et al.* [2010a], they have considered that to have a glow regime, the electric field in the gap during the conduction phase has to be at least equal to the breakdown field, which is 30 kV cm^{-1} for P_{atm} and T_g=300 K. For all the conditions studied in the preceding sections for P_{atm} and T_g=300 K, we have found that after the connection of positive and negative discharges, the electric field becomes rather uniform in the gap and converges towards the average electric field for the given applied voltage and gap size. For all the studied conditions for P_{atm} and T_g=300 K with a gap distance less or equal to 5 mm, we have noted that if the average electric field in the gap is equal or higher than the breakdown field, the propagation of the discharge occurs in less than or almost 10 ns, that is to say during the voltage pulse duration used in the experiments [*Pai et al.*, 2010a]. To obtain the glow regime, it is important that the connection time of the discharge be almost equal to the duration of the voltage pulse. In this case, the discharge has just the time to fill the interelectrode gap and no heating is observed.

6.6 Discussion on the conditions to obtain a glow discharge in large gaps at $T_{\rm g}$=300 K

In the preceding sections, we have studied the conditions to obtain the glow regime of discharges in interelectrode gaps up to 5 mm. As mentioned in the introduction, for various applications, it would be of great interest to obtain the glow regime at $T_{\rm g}$=300 K for larger gaps.

However, based on our results, if the gap is increased for a fixed geometry of electrodes, $E_{\rm L,min}$ decreases and may become less than E^*. As an example, Figure 6.5 shows the time evolutions of the position of the positive discharge front, and of the value of $E_{\rm max}$ for $T_{\rm g}$ = 300 K, $R_{\rm p}$=50 μm, an applied voltage of 15 kV and a 10 mm gap. In this case $E_{\rm L,min} = 7.5$ kV cm$^{-1} < E^*$ and we note that the velocity of the positive discharge decreases as it propagates from 392 to 375 km s^{-1} and as expected, the positive streamer finally branches at t =15 ns as the positive streamer front is at 2 mm from the anode. As mentioned in section 6.2, adding an uniform axial Laplacian electric field to be above E^* allows a stable propagation of the discharge and then may allow to generate the glow regime in large gaps at $T_{\rm g}$=300 K. This can be done by different ways and for example by increasing the radius of curvature of the electrodes as shown on Figures 6.5 and 6.6 with $R_{\rm p}$=300 μm an applied voltage of 15 kV and a 10 mm gap. In this case, $E_{\rm L,min} = 9.2$ kV cm$^{-1} > E^*$ and the positive discharge ignites at t =5 ns and propagates with a rather constant velocity of about 260 km s^{-1} until the connection at t =28 ns. After connection, the discharge velocity is 1.6 times higher than before connection and the electric field in the gap rapidly decreases to converge towards the average electric field value which is 15 kV cm^{-1} in this case.

Figure 6.6 shows the time sequence of the distributions of the electron density at t =13, 20, 27, 31 and 34 ns. After the initiation of the discharge, we observe a stable propagation of the positive discharge in the gap from t =10 to 25 ns before the connection of both discharges. As expected, as the gap is increased, we note that the propagation times of discharges in the gap increase and then longer pulse durations have to be used. Figure 6.5 shows that the peak electric field in the positive streamer head during its stable propagation is constant and about 120 kV cm^{-1}. Conversely, for the branching case with $R_{\rm p}$=50 μm, the electric field at the ignition time is very high but decreases rapidly as the

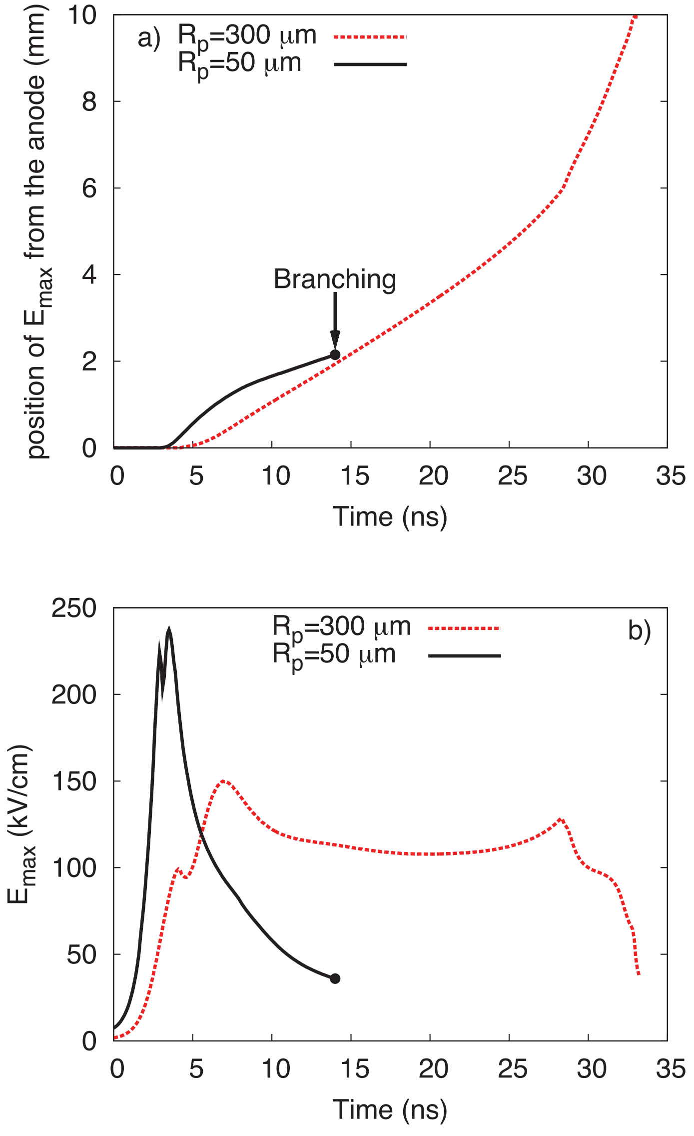

Figure 6.5: *Influence of the radius of curvature of point electrodes* R_p *on the time evolutions of the position of the maximum electric field* E_max *(a) and the value of* E_max *(b) along the axis of symmetry for* T_g *=300 K, an applied voltage of 15 kV and a 1 cm gap.*

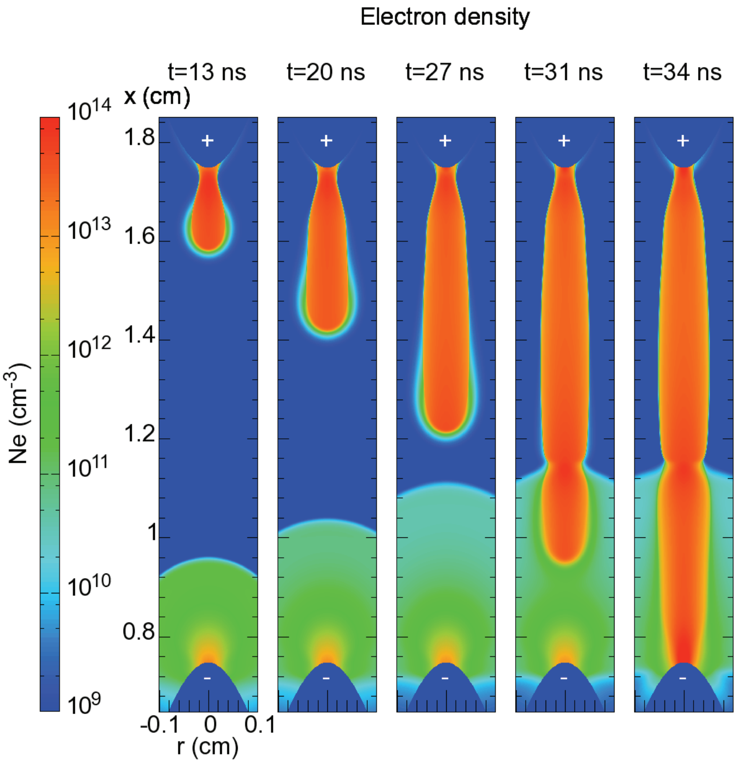

Figure 6.6: *Dynamics of the discharge at* $T_g = 300$ *K for an applied voltage of 15 kV, a 1 cm gap and point electrodes with* $R_p = 300\,\mu m$*. Cross-sectional views of the electron density at* t *=13, 20, 27, 31 and 34 ns.*

streamer propagates and the peak electric field in the positive streamer head is only 40 kV cm^{-1} at the moment of branching. Table 6.1 shows that for $R_p = 300\,\mu$m and an applied voltage of 15 kV, the velocity of the discharge is about 1.9 times less with a 10 mm gap than for 5 mm and that the connection time is 3 times longer for 10 mm than for 5 mm.

Figure 6.7 (a) shows the time evolution of the axial electric field after the positive streamer arrival at the cathode from t =34.5 to 43.5 ns. As observed in preceding sections, we note that the electric field becomes rapidly rather uniform in the inter-electrode gap and converges towards 15 kV cm^{-1}, the average electric field in the gap which is less than the breakdown field for P_{atm} and T_g=300 K. Then, after the connection the electron density decreases in the 10 mm gap whereas it is increasing for a 5 mm gap with the same applied voltage as the average electric field in this case is higher than the breakdown field.

Consequently, Figure 6.7 (b) shows that after the connection, the energy e_J derived from the time integrated Joule heating term (Eq. (1.24)) is about 20 times smaller for the 10 mm gap than for the 5 mm gap (Figure 2.10 (b)).

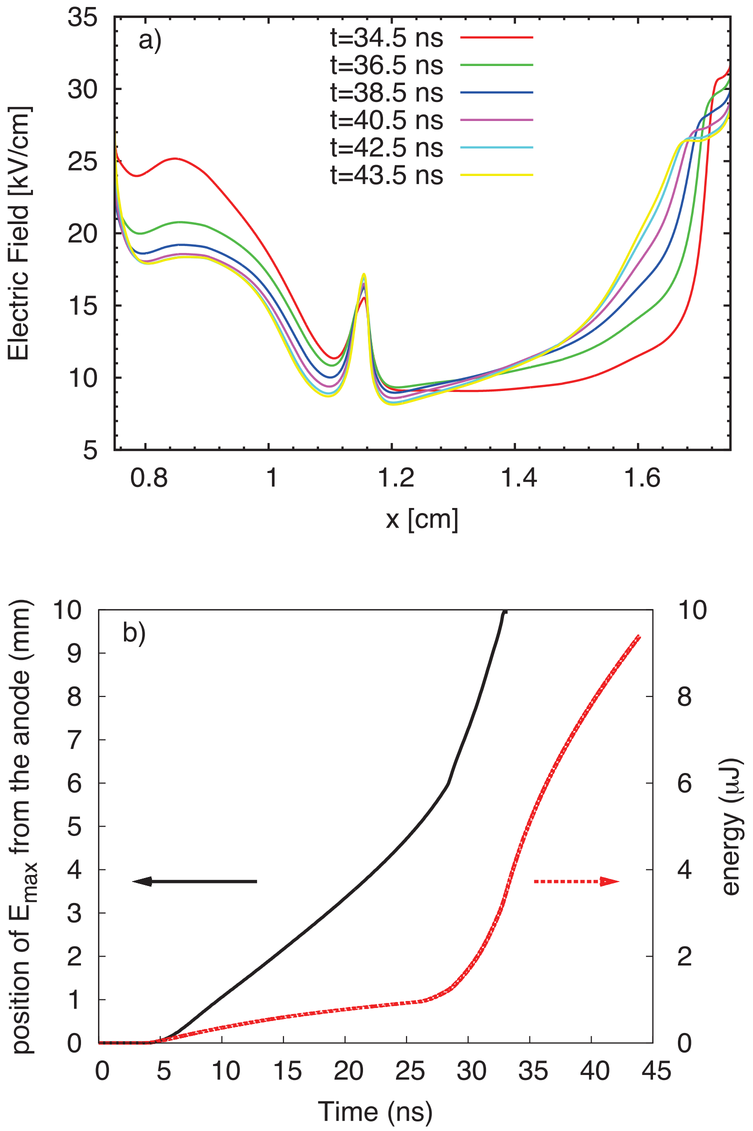

Figure 6.7: *Time evolutions of the value of the electric field along the axis of symmetry after the arrival of the positive streamer at the cathode (a) and of the energy* e_J *given by Eq. (1.24) and the position of* $E_{\max}$ *(b) for the same conditions as Figure 6.5. The tip of the cathode is located at* $x_C = 0.75$ *cm, and the tip of the anode is at* $x_A = 17.5$ *mm.*

As mentioned in Section 2.7, for the 5 mm gap with R_{p}=50 μm and 15 kV, to have the glow regime, the voltage pulse duration has to be almost equal to the connection time to avoid the gas heating by the discharge after the connection. Conversely, Figure 6.7 (b) shows that for a 10 mm gap at T_{g}=300 K, with R_{p}=300 μm and an applied voltage of 15 kV, the heating of the gas after connection is reduced and then, even if the pulse duration is longer than the connection time, a glow regime could be obtained.

6.7 Conclusion

In this chapter, we have studied the dynamics of an air discharge in a point-to-point geometry at atmospheric pressure during one voltage pulse at $T_{\mathrm{g}} = 300$ K to optimize the conditions to obtain a glow regime. We have found that after the connection of positive and negative discharges, the electric field becomes rather uniform in the gap and converges towards the average electric field for the given applied voltage and gap size. For all the conditions studied at T_{g}=300 K with a gap distance less or equal to 5 mm, we have noted that if the average electric field in the gap is equal or higher than the breakdown field, the propagation of the discharge occurs in less than or almost 10 ns, that is to say during the voltage pulse duration used in the experiments. In these conditions, in agreement with conclusions in Section 2.9 at $T_{\mathrm{g}} = 1000$ K, to obtain the glow regime, it is important that the connection time of the discharge be almost equal to the duration of the voltage pulse. Then, the discharge has just the time to fill the interelectrode gap and no heating is observed.

At $T_{\mathrm{g}} = 300$ K, for a 10 ns duration voltage pulse, when the average electric field in the gap is less than the breakdown field, we have observed that discharges may branch. Based on our simulations, we found that a minimal value of the Laplacian electric field of 8-9 kV cm^{-1} at P_{atm} and T_{g}=300 K is necessary to have a stable propagation of the positive streamer without branching in the point-to-point geometry studied in this work. This field is slightly higher than the minimal external field required to have a stable positive streamer propagating in air far from electrodes at P_{atm} and T_{g}=300 K.

Finally, we have shown that it is possible to extend the glow regime at $T_{\mathrm{g}} = 300$ K to larger interelectrode gaps using longer voltage pulse duration for conditions in which the average electric field in the gap is less than the breakdown field. In these cases, the heating of the gas after connection is limited and then, even if the pulse duration is longer than the connection time, a glow regime may be obtained.

Chapter 7

Application of NRPD to plasma assisted combustion of a H_2-air mixture

7.1 Introduction

In this chapter we study the ignition by a nanosecond spark discharge of a lean (equivalence ratio of $\Phi = 0.3$) H_2-air mixture at 1000 K and atmospheric pressure. In Section 7.2, we present the simple model used in this work to study the coupling between plasma and combustion. Then, in Section 7.3, we describe the numerical method used for the 2D simulation of the ignition. In Section 7.4 we validate the combustion code with two test-cases: a 0D auto-ignition test-case at 1200 K and a 1D flame propagation test-case at 600 K. Finally, in Sections 7.5 and 7.6 we simulate in 2D the ignition of a H_2-air mixture by a nanosecond spark discharge between two point electrodes. As a reference, we consider the nanosecond spark discharge at 1000 K and atmospheric pressure in air studied in Chapter 4. As the equivalence ratio of the H_2-air mixture is of $\Phi = 0.3$, we assume that the heating of the H_2-air mixture and the production of active species by the plasma discharge are the same as in air. In Section 7.5, we study the ignition in taking into account only the fast-heating of the gas by the nanosecond spark discharge. In Section 7.6, we assume no heating by the discharge and we take into account only the production of atomic oxygen by the nanosecond spark discharge to ignite the H_2-air mixture. Then we compare the relative importance of fast-heating and production of active species by the nanosecond spark discharge for the ignition of a lean H_2-air mixture.

7.2 Coupling between nanosecond pulsed discharges and combustion

Since several decades, classical spark discharges are used for ignition and flame stabilization. Although as little as 0.2 mJ of energy is required to ignite a quiescent stoichiometric mixture, only a small fraction of the electrical energy is transmitted to the gas mixture. Hence, conventional ignition systems deliver about 30-50 mJ to the spark in typically 100 μs [*Maly*, 1984].

The aim of this chapter is to study the plasma-assisted-ignition of a lean H_2-air mixture at 1000 K, using a nanosecond spark discharge. Basically, nanosecond pulsed discharges can ignite lean mixtures through three distinct processes: the fast-heating of the mixture, the production of active chemical species, and VUV radiations.

Plasma discharges in air are known to emit VUV radiations that may induce photolysis of fuel molecules or photodissociation of molecular oxygen:

$$\mathrm{O_2} + \gamma \rightarrow \mathrm{O} + \mathrm{O} \tag{7.1}$$

and then may play a role in plasma assisted combustion. Effects of VUV radiations on combustion have been studied in [*Cerkanowicz*, 1979] and more recently in [*Berezhetskaya et al.*, 2005]. It has been shown that VUV radiations from discharges are able to extend the limits of ignition of hydrogen-air mixtures at low pressure [*Popov*, 2007]. However, even if it may induce non local effects, the photodissociation of oxygen molecules is probably a secondary process compared to the the other mechanisms as explained in *Starikovskiy et al.* [2012].

It is possible to estimate the production of atomic oxygen through dissociation of oxygen molecules by VUV photons in the range 205-240 nm. Assuming that the maximum emission intensity of an air nanosecond spark discharge in this frequency range is around $\mathrm{F}_\gamma \simeq 10^{13}$ Ra, (typical value of the emission of $2\mathrm{PN}_2$ by the discharges studied in this work) the maximum photodissociation rate $\mathrm{k}_{\gamma\mathrm{diss}}$ can be estimated by:

$$k_{\gamma \mathrm{diss}} = n_{\mathrm{O_2}} F_\gamma \sigma \tag{7.2}$$

where σ, the absorption cross section in the range 205 nm-240 nm is between 7.35×10^{24} cm^2 and 1.01×10^{24} cm^2 respectively [*Demore et al.*, 1997] and $\mathrm{n_{O_2}}$ is the molecular oxygen density in air at the considered temperature. Then, for $\sigma = 7.35 \times 10^{24}$ cm^2 and $\mathrm{T_g}$=1000 K, the photodissociation rate is around 2×10^{18} cm^{-3} s^{-1}. For a pulse of 10 ns, the maximum atomic oxygen density created by this mechanism is of the order 2×10^{10} cm^{-3}, which is very small compared to the gas density at 1000 K and atmospheric pressure. Then, it seems reasonable in a first approximation to neglect this radiative effect on combustion for conditions studied in this work.

As explained in Chapter 4, according to the two-step mechanism, the fast-heating of a nanosecond pulsed discharge may occur on very short timescales of a few tens of nanoseconds right after a voltage pulse. This fast-heating time is then much smaller than the characteristic auto-ignition times for the combustion reactions that are of the order of a few μs for the fastest to a few ms in most conditions. As a consequence it can be reasonably assumed for combustion that the fast heating is infinitely fast during the voltage pulses. For nanosecond spark discharges able to increase the temperature by hundreds or thousands of degrees, fast-heating may play a very significant role in the reduction of the ignition time. The compressible flow dynamics generated by such a high heating rate (discussed in chapter 4), is also important for the ignition mechanism since the fast expansion of the hot plasma channel leads to a significant temperature decrease during the first microseconds by $\simeq 50\,\%$ (as discussed in chapter 4), and an increase of the radius of the plasma channel. As discussed in chapter 4, for conditions studied in this work, we can assume that 30 % of the discharge energy is going instantaneously to fast-heating, and we need to solve Euler equations to study the fluid dynamics during the ignition process.

The chemical species produced by a plasma discharge are also very important for ignition. Indeed, production by the discharge of electronic excitation of atoms and molecules and vibrational excitation of molecules, and of radicals, positive and negative ions increase the chemical reactivity of a mixture and may play a significant role in ignition. In our conditions, electron and ion densities after a voltage pulse are very low compared to the density of neutrals (as discussed in chapter 3) and we have assumed that their influence on the combustion chemistry is negligible. During the rise and the decrease of the voltage, some singlet oxygen molecules $O_2(a^1\Delta_g)$ may be formed due to the low applied reduced electric-field. It has been shown that this specie is able to enhance significantly ignition reactions and flame propagation in low pressure and lean hydrogen-air mixture [*Smirnov et al.*, 2008]. However, the excitation of molecular oxygen may be neglected in our case, since in air at atmospheric pressure most of the discharge energy spent on electronic excitation goes into the excitation of nitrogen molecules [*Wu et al.*, 2010].

Among the vibrationally excited molecules produced by the discharge, $H_2(v)$ could be involved in chain initiation and branching reactions. However, based on the work of *Popov* [2007], we have considered that in our lean studied condition and at atmospheric pressure, the influence of $H_2(v)$ is negligible. As explained in *Zuzeek et al.* [2011], dissociation of hydrogen molecules may also play an important role as a source of H radicals. However, as we consider a lean mixture with an equivalence ratio of 0.3, we have neglected the production of H atoms by the discharge.

Finally, for our studied conditions, the main chemical mechanisms for plasma assisted combustion seem to be the production of atomic oxygen through direct electron impact dissociation, and the dissociative quenching of electronically excited N_2 [*Starikovskiy and Aleksandrov*, 2013].

In the following, as a reference, we consider the nanosecond spark discharge at

Nos	Reaction	Ref
R1	$H + O_2 \rightleftharpoons OH + O$	Boivin [2011]
R2	$H_2 + O \rightleftharpoons OH + H$	-
R3	$H_2 + OH \rightleftharpoons H_2O + H$	-
R4	$H + O_2(+M) \rightleftharpoons HO_2(+M)$	-
R5	$HO_2 + H \rightleftharpoons 2OH$	-
R6	$HO_2 + H \rightleftharpoons H_2 + H_2$	-
R7	$HO_2 + OH \rightleftharpoons H_2O + O_2$	-
R8	$H + OH + M \rightleftharpoons H_2O + M$	-
R9	$2H + M \rightleftharpoons H_2 + M$	-
R10	$2HO_2 \rightleftharpoons H_2O_2 + O_2$	-
R11	$HO_2 + H_2 \rightleftharpoons H_2O_2 + H$	-
R12	$H_2O_2 + M \rightleftharpoons 2OH + M$	-

Table 7.1: *12-step mechanism for hydrogen-air combustion with a total of 9 species.*

1000 K and atmospheric pressure in air studied in Chapter 4. As the equivalence ratio of the H_2-air mixture is of $\Phi = 0.3$, we assume that the heating of the H_2-air mixture and the production of O atoms by the plasma discharge are the same as in air. The outputs from the discharge code at the end of the voltage pulse are the temperature field resulting from the fast-heating and the atomic oxygen density produced by electron impact and dissociative quenching of excited nitrogen. These 2D fields are used as an inputs for the hydrogen-air combustion model presented in the next section. Results of the influence of the nanosecond spark discharge on the ignition of a H_2-air mixture will be presented in Sections 7.5 and 7.6.

7.3 Model for the combustion of a H_2-air mixture

The main chemical effect of the nanosecond spark discharge on the chemistry useful for plasma assisted combustion is assumed to be the production of atomic oxygen. Then it is important to have a chemical model for combustion that takes into account atomic oxygen in the kinetics. *Boivin et al.* [2011] have successfully tested several kinetic models for combustion of hydrogen-air mixtures in a wide range of conditions. In particular they have studied a reduced 12-step chemical model. This model takes into account 9 species including atomic oxygen: H_2, O_2, H_2O, H, O, OH, HO_2, H_2O_2, and N_2 and the 12 reactions are given in Table 7.1. *Boivin et al.* [2011] have shown that this reduced 12-step chemical model is able to predict accurately burning rates and flammability limits in steady planar deflagrations, and peak temperatures and extinction strain rates in non-premixed counterflow flames. Results obtained with this reduced model are also undistinguishable from more complex chemical models for the estimation of the induction time in isobaric reactors for equivalence ratios in the range $10^{-1} - 10$. We have implemented this reduced model to couple the plasma discharge with combustion reactions. As nanosecond spark discharges are able to heat-up the air up to 3000 K close to the tip of the electrodes, and due to the highly exo-energetic reactions involved in the hydrogen-air combustion, the maximum air temperature may be higher than 4000 K in some points. Thermochemical data for the 9 species of the 12-step mechanism that are available between 300 and 6000 K were taken from the NIST-JANAF Thermochemical Tables.

The energy source term due to combustion reactions ω_e is given by:

$$\dot{\omega_\mathrm{e}} = -\sum_k \Delta h^0_{f,k} \dot{\omega_k} \tag{7.3}$$

where $\dot{\omega_k}$ is the mass source term of specie k due to chemical reactions, $\Delta h^0_{f,k}$ is the formation enthalpy of specie k. The temperature can be deduced by computing the specific thermal capacity at constant volume of the mixture $\mathrm{C_{vm}}$ from the mass fractions Y_k and the specific thermal capacities $\mathrm{C}_{\mathrm{v}k}$ of specie k:

$$\mathrm{C_{vm}}(T) = \sum_k \mathrm{Y}_k \mathrm{C}_{\mathrm{v}k}(T) \qquad \frac{\mathrm{d}T}{\mathrm{d}t} = \frac{\dot{\omega_\mathrm{e}}}{\mathrm{C_{vm}}(T)} \tag{7.4}$$

The temperature of the mixture is obtained by solving numerically Equations (7.4) using an iterative procedure.

We have considered the following equations for the reactive multi-species mixture. There are Euler equations with species diffusion and thermal conduction:

$$\begin{cases} \partial_t \rho \mathrm{Y}_k + \vec{\nabla} \cdot (\rho(\vec{u} + \vec{V}_k)\mathrm{Y}_k) = \dot{\omega_k} \\ \partial_t(\rho u_x) + \vec{\nabla} \cdot (\rho u_x \vec{u}) = -\partial_x P \\ \partial_t(\rho u_r) + \vec{\nabla} \cdot (\rho u_r \vec{u}) = -\partial_r P \\ \partial_t(\rho e) + \vec{\nabla} \cdot (\rho h \vec{u}) = \vec{\nabla} \cdot (-\lambda \vec{\nabla} \mathrm{T}) + \dot{\omega_\mathrm{e}} \end{cases} \tag{7.5}$$

$$\text{with :} \qquad \mathrm{e} = \frac{1}{2}\mathrm{V}^2 + \mathrm{u} \qquad \mathrm{u} = \mathrm{C_{vm}T} = \frac{\mathrm{R_m T}}{(\gamma_\mathrm{m} - 1)} \qquad \mathrm{h} = \mathrm{u} + \frac{\mathrm{P}}{\rho}$$

The diffusion velocities V_k can be estimated thanks to the Hirschfelder and Curtiss approximation [*Poinsot and Veynante*, 2005]. Diffusion fluxes for each specie then reduce to a Fick's law with the diffusion coefficient of the specie k in the mixture D_k:

$$\vec{\mathrm{V}}_k \mathrm{X}_k = -\mathrm{D}_k \vec{\nabla} \mathrm{X}_k \quad \mathrm{D}_k = \frac{1 - \mathrm{Y}_k}{\sum_{j \neq k} \mathrm{X}_j / \mathcal{D}_{kj}}$$

where X_k is the mole fraction of specie k. As Fick's law does not preserve mass conservation, usually in codes, the density of a non reactive component is adjusted to preserve the mass conservation [*Poinsot and Veynante*, 2005].

In our case we adjust N_2 density (as N_2 does not participate to combustion reactions) to ensure the mass conservation. This correction has a small influence on the N_2 density since its mass fraction is much more significant than the mass fraction of the highly diffusive species in the mixture.

The thermal conductivity λ of the mixture is computed thanks to the semi-empirical formula:

$$\lambda = \frac{1}{2}\left(\sum_k \mathrm{X}_k \lambda_k + \frac{1}{\sum_k \mathrm{X}_k \lambda_k^{-1}}\right) \tag{7.6}$$

where λ_k is the thermal conductivity of specie k. To compute the diffusion coefficients and the thermal conductivity of the mixture, we use the subroutines of the REGATH program written by Nasser Darabiha at the laboratory EM2C and used in *Candel et al.* [2011]. The diffusion is solved implicitly with the ROCK4 subroutine developed by *Abdulle* [2002]. Chemistry is also solved implicitly with the RADAU5 code [*Hairer and Wanner*, 2010]. The numerical scheme used to solve the Euler equations is the MUSCL scheme described in chapter 4.

7.4 Validation of the H_2-air combustion model

7.4.1 Autoignition of a H_2-air mixture

To validate the thermo-chemistry used in the combustion code, we have simulated the autoignition of a stoichiometric H_2-air mixture at 1200 K at atmospheric pressure as in *Boivin et al.* [2011]. Figure 7.1 shows the evolution of the densities of H_2, O_2, H, O, OH, and H_2O and the corresponding temperature evolution during the autoignition process. Hydrogen and oxygen are consumed leading to the production of a significant amount of H_2O. The autoignition delay is defined as the time when the temperature starts to increase sharply with a peak production of H_2O, H, OH, and atomic oxygen. We found that the autoignition is at 4.5×10^{-5}s, in agreement with the results of *Boivin et al.* [2011]. On Figure 7.1, we note that the final temperature is close to 2800 K. Due to this high temperature, the H_2O formed during the combustion, dissociates and then some H_2 is present in the burnt gases.

We have tested different initial temperatures and equivalence ratios and we have checked that the thermo-chemical model implemented in the code is capable to reproduce the correct auto-ignition delays in all the cases studied.

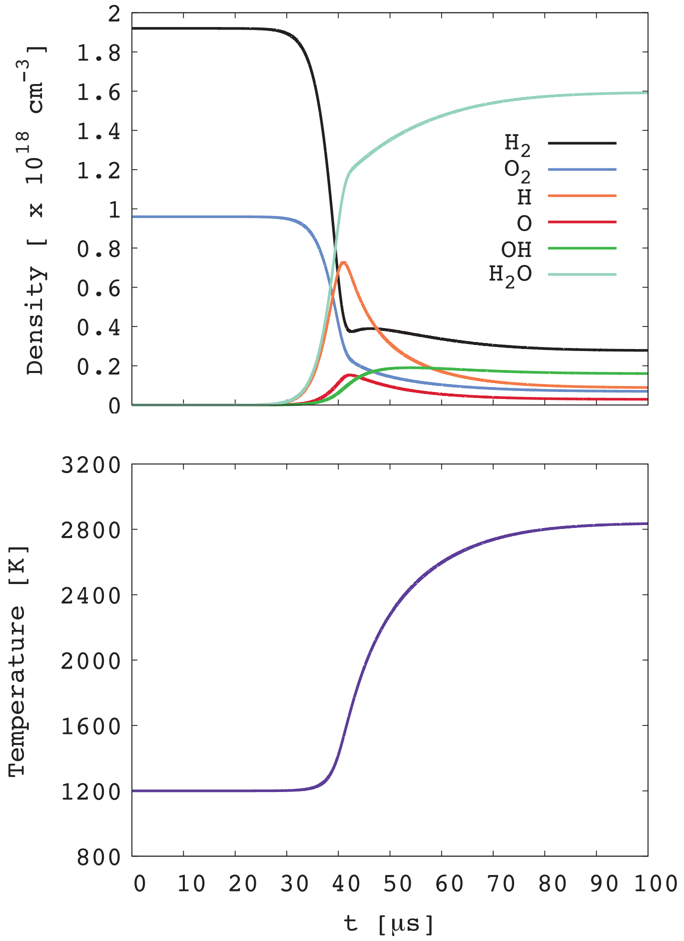

Figure 7.1: *Evolution of species concentrations and of the temperature during the autoignition of a H_2-air mixture in stoichiometric conditions at 1200 K at atmospheric pressure.*

7.4.2 Flame propagation in a H_2-air mixture

The coupling between thermo-chemical processes, the energy released in the combustion and the transport of species in the gas can be validated considering a flame propagation. To be able to predict accurately the flame velocity, a thorough description of the coupling between all the processes involved in the flame is required. It is particularly true for hydrogen-air mixtures as some of the light species like O, H_2 and H may diffuse much faster than the other species and an accurate description of their transport is required. For this reason, the widely used assumption of a Lewis number (ratio between thermal diffusivity and molecular diffusion) equal to unity was not used in our model, since for light species the molecular diffusion may be higher than the thermal diffusivity of the mixture. Another usual simplification is to consider that the pressure is constant during a flame propagation. However, this simplification can not be used in our case since during the ignition phase the compressible flow dynamics may play a significant role.

To study the flame propagation, we have considered a stoichiometric H_2-air mixture at 600 K. This low temperature has been chosen to have a rather long autoignition delay to allow the study of the flame propagation. Figure 7.2 shows the 1D propagation in the radial direction of a cylindrical laminar premixed flame. The flame is ignited by a hot cylindrical channel representing a spark discharge located on the symmetry axis with a temperature of 2000 K and a radius of 250μs. On short timescales, between 0 and 6 μs, we observe that the initial high temperature region generates a shockwave with a sharp front that propagates radially at the speed of sound at 600 K. As the shockwave propagates, its amplitude decreases and becomes negligible. To prevent reflections on the boundaries, the simulation domain has been extended to a very large region of a few meters (not shown on the figure) thanks to a geometric expansion of the mesh. Behind the shockwave, as explained in Chapter 4 a low density channel is formed in the hot region, in which the pressure is constant. Due to the dilatation of the pre-heated region with an initial radius of 250μm, the low density channel is around two times wider with a radius of $\simeq 500\,\mu$m. As explained in Chapter 4, the shockwave takes a significant fraction of the initial energy of the hot region at 2000 K. Then the low density channel has a lower temperature (decrease of about 20%) than the initial hot channel. Then the ignition of the mixture occurs in a low density region (density is $\simeq$ 2.5 times less than the one of the gas mixture at 8 mm from the symmetry axis) with a high temperature of about 1600 K. It can be seen at t=6 μs that the production of H_2O has already started close to the symmetry axis. At t=50 μs, all the oxygen has been consumed in the low-density region and a significant amount of H_2O has been produced. During this phase, a significant amount of energy is released by the combustion in the low-density region and the maximum temperature increases from 1600 K to 2300 K. However, this heating occurs on a timescale of 40 μs which correspond to a slow increase of the temperature, and then no shockwave is generated in this case.

Then, we observe the propagation of a flame front between 50, 300 and 600 μs. The highest temperature in the flame is around 2800 K, and its velocity is around 8.5 m s^{-1}. The velocity for a planar premixed hydrogen-air mixture at 600 K in stoeichiometric conditions is around 7 m s^{-1} [*Gelfand et al.*, 2012] which makes a difference of 17%. In our case, the slightly higher flame velocity calculated may be due to the cylindrical shape of the flame, and the ignition process we have used with an initial hot channel. We also note that the MUSCL scheme used to solve Euler equations may also add some numerical diffusion on long timescales, which may increase a little the speed of the flame (CFL is around 5×10^{-9} s and the total simulation time is 600 μs).

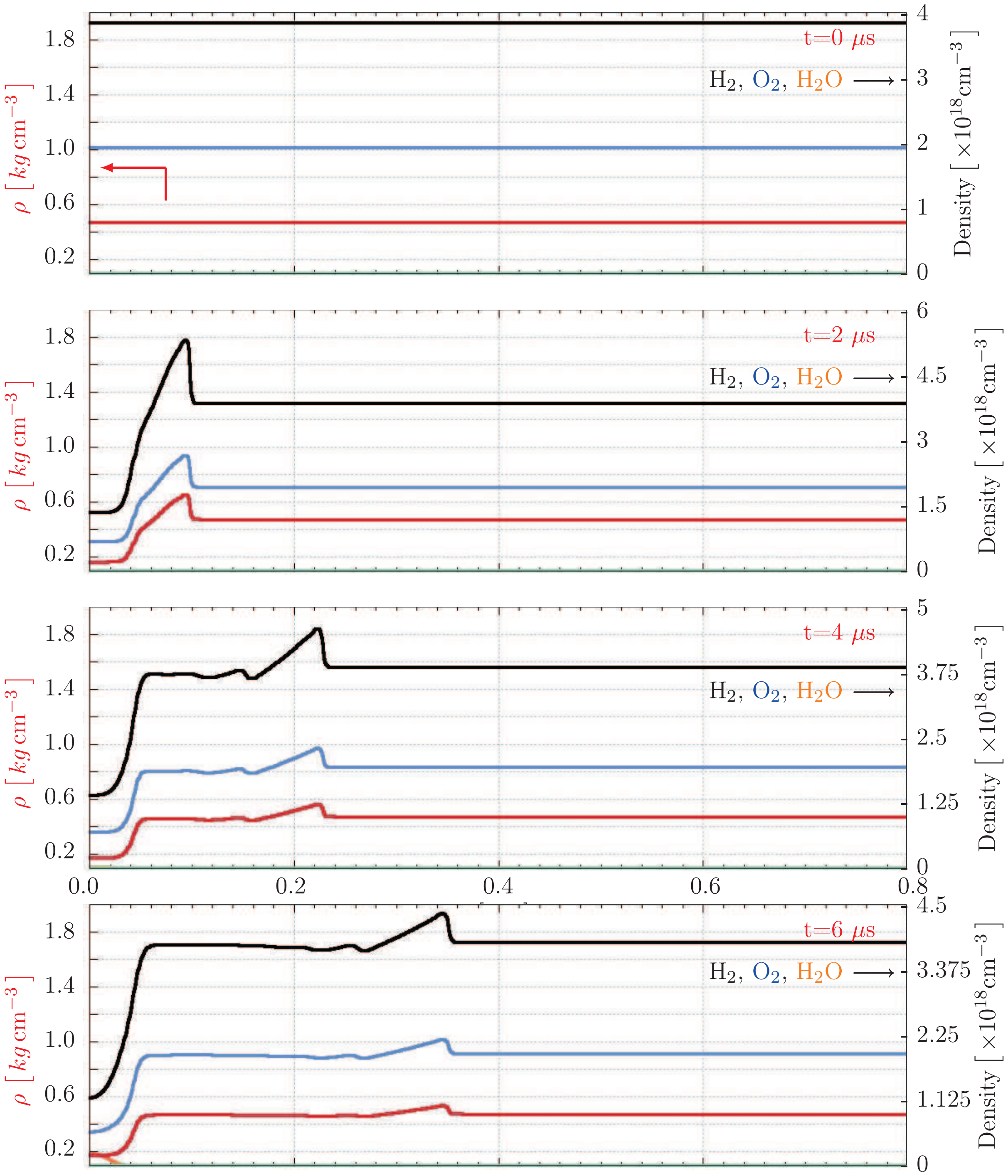
t=0 μs
H2, O2, H2O ⟶
ρ [kg cm−3]
Density [×10^18 cm−3]
1.8
1.4
1.0
0.6
0.2
4
3
2
1
0
t=2 μs
6
4.5
3
1.5
0
t=4 μs
5
3.75
2.5
1.25
0
0.0
0.2
0.4
0.6
0.8
t=6 μs
4.5
3.375
2.25
1.125
0

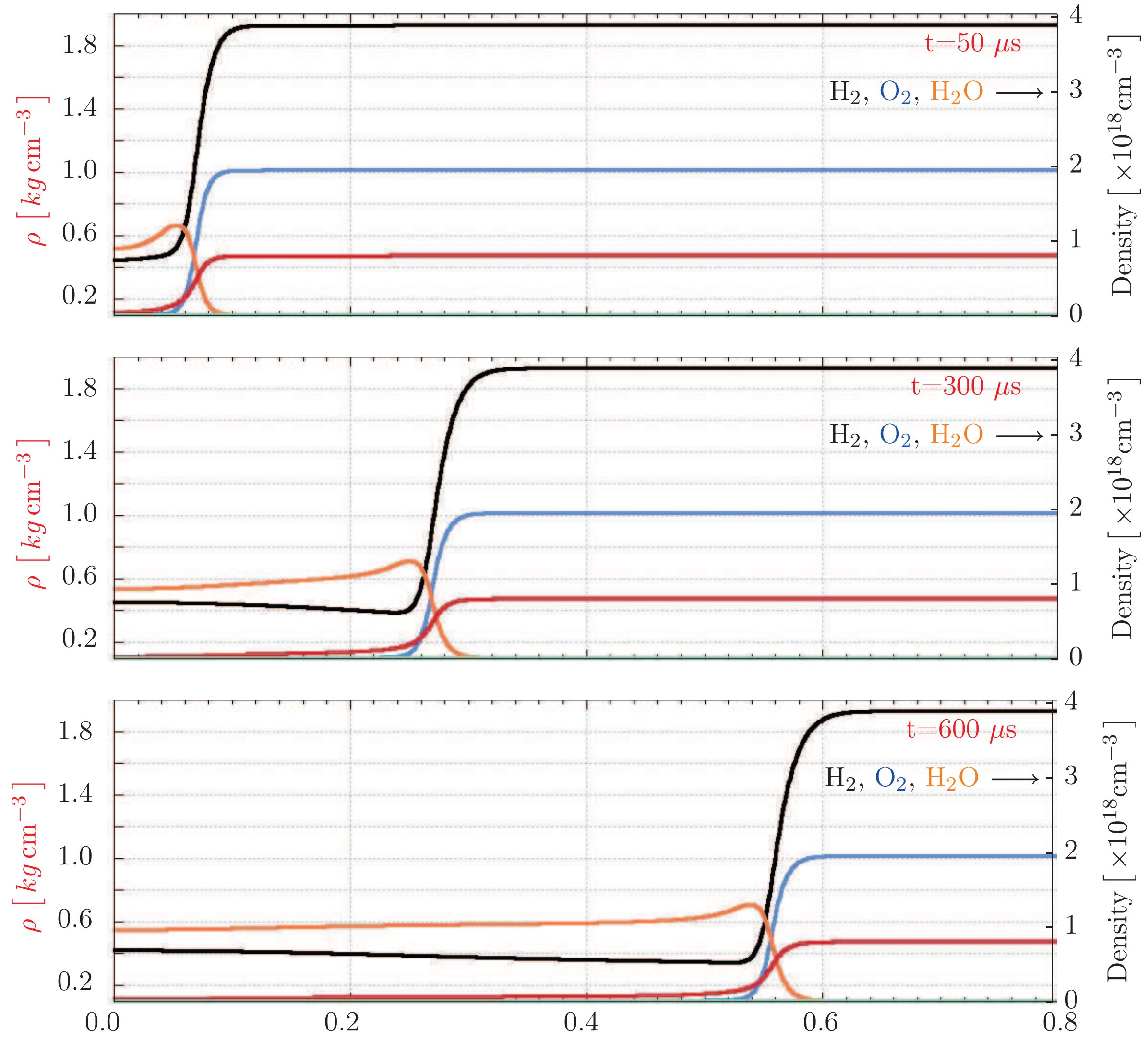

Figure 7.2: *1D Ignition and propagation of a flame in stoechiometric H_2-air mixture at 600 K and atmospheric pressure. The propagation is in the radial direction. Red line: mass density of the gas mixture. Dark line: H_2 density. Blue line: O_2 density. Orange line: H_2O density.*

7.5 Plasma assisted ignition of a lean H_2-air mixture: role of the fast-heating

The temperature increase due to a nanosecond spark discharge in air at atmospheric pressure can be very high and of the order of thousands of degrees. For the reference nanosecond spark discharge case studied in Chapter 4, the temperature at the end of the voltage pulse is around 1900 K in the middle of the inter-electrode gap and 3000 K close to the electrode tips (Figure

4.11). This temperature increase is important for ignition as all reaction rates of combustion reactions are Arrhenius laws with an exponential dependence with temperature. However, it is important to note that in classical spark plug systems for combustion ignition the gas can be heated up to higher temperatures (5000 K) but on much longer timescales (several milliseconds).

Today, the relative importance of the fast-heating for plasma assisted ignition compared to other mechanisms such as the production of active chemical species is still under debate in the scientific community. It is then not clear if the very-fast heating of a nanosecond spark is able to ignite a lean mixture by itself. To test this hypothesis, we consider the ignition of a lean H_2-air mixture with an equivalence ratio $\Phi = 0.3$ at 1000 K and atmospheric pressure. With such a high temperature, the auto-ignition delay is of the order 10^{-4} s, then the discharge has to ignite the mixture on even shorter timescales. As initial condition of the combustion code, we consider the 2D temperature field at the end of the pulse shown on Figure 4.2 at $t = 10$ ns for the reference nanosecond spark discharge at 1000 K and atmospheric pressure. In this case, we neglect the production of active species by the discharge. In the work of *Thiele et al.* [2002] on classical spark ignition, similar numerical simulations have been performed at 300 K with as initial source term a temperature field representative of a classical spark ignition system. These authors have shown that the thermal conduction in the electrodes has a negligible influence on short timescales up to 130 μs. Then in the following, the electrodes are assumed to be adiabatic and the thermal conduction flux at their surface is set to zero.

Figure 7.3 shows the 2D evolution of the H_2O concentration as a function of time. The 2D evolution of the concentration of H_2O allows us to identify clearly the boundary between the fresh and the burnt gas and to follow the flame formation and propagation. At t=1 μs there is no ignition yet but the shockwave formation and propagation have already occurred and the pressure is uniform in the domain. The compressible flow dynamics and the low density channel formation described in Chapter 4 seem then to be decoupled from the combustion dynamics as they occur on slightly shorter timescales. It can be seen that the ignition starts at t=5 μs close to the tip of the electrodes due to the higher initial temperature in these regions. Then the flame propagates very rapidly in the heated channel on the symmetry axis between electrodes. The two flame-fronts impact each other at t=15 μs and at t=20 μs they merge into a cylindrical flame. Then between 20 and 100 μs the flame propagates radially in the fresh gas with a velocity of about 15 m s^{-1} which is close to typical premixed-flame velocities for H_2-air in those conditions [*Gelfand et al.*, 2012]. At t=100 μs, it has been checked that the flame is then able to propagate on distances longer than the inter-electrode gap with a spherical shape, without being influenced any more by the initial conditions. The cylindrical flame kernel structure that propagates radially, its evolution to a more spherical shape and the initial dependence of the ignition with the temperature source term are in good agreement with the experimental and numerical results of *Thiele* *et al.* [2002] for a lower initial temperature of the mixture. However, in their simulations, they observed a more toroidal structure of the flame kernel. Based on their experimental results, it seems that this shape may be obtained when rather stump electrodes are used, but for sharpened electrodes the flame kernel is more oval as in our simulation results. In a future work, it would be interesting to study the influence of the shape of the electrodes on the flame kernel expansion initiated by the fast-heating of a nanosecond spark discharge.

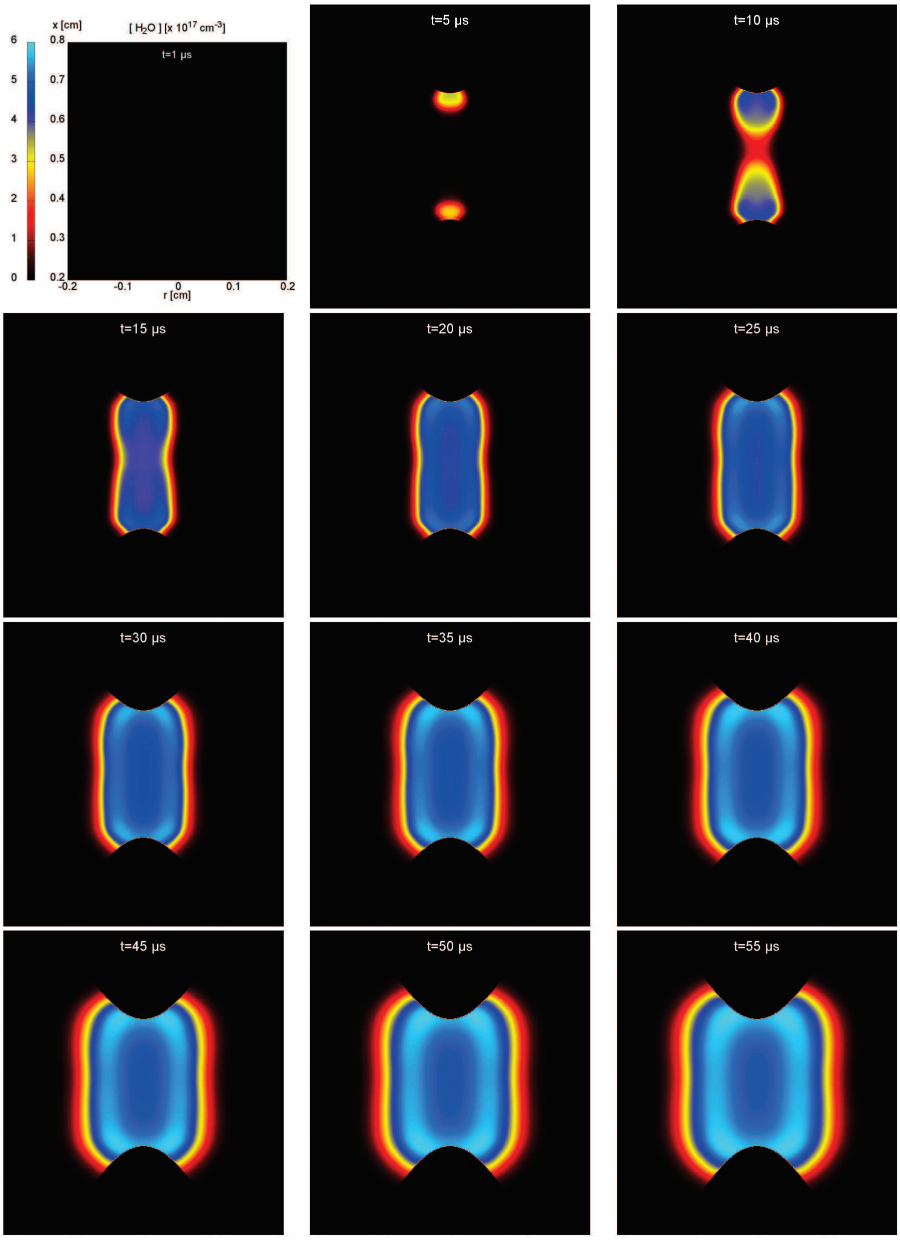
x [cm]
[H$_2$O] [x 10^{17} cm^{-3}]
6
5
4
3
2
1
0
0.8
0.7
0.6
0.5
0.4
0.3
0.2
-0.2
-0.1
0
0.1
0.2
r [cm]
t=1 µs
t=5 µs
t=10 µs
t=15 µs
t=20 µs
t=25 µs
t=30 µs
t=35 µs
t=40 µs
t=45 µs
t=50 µs
t=55 µs

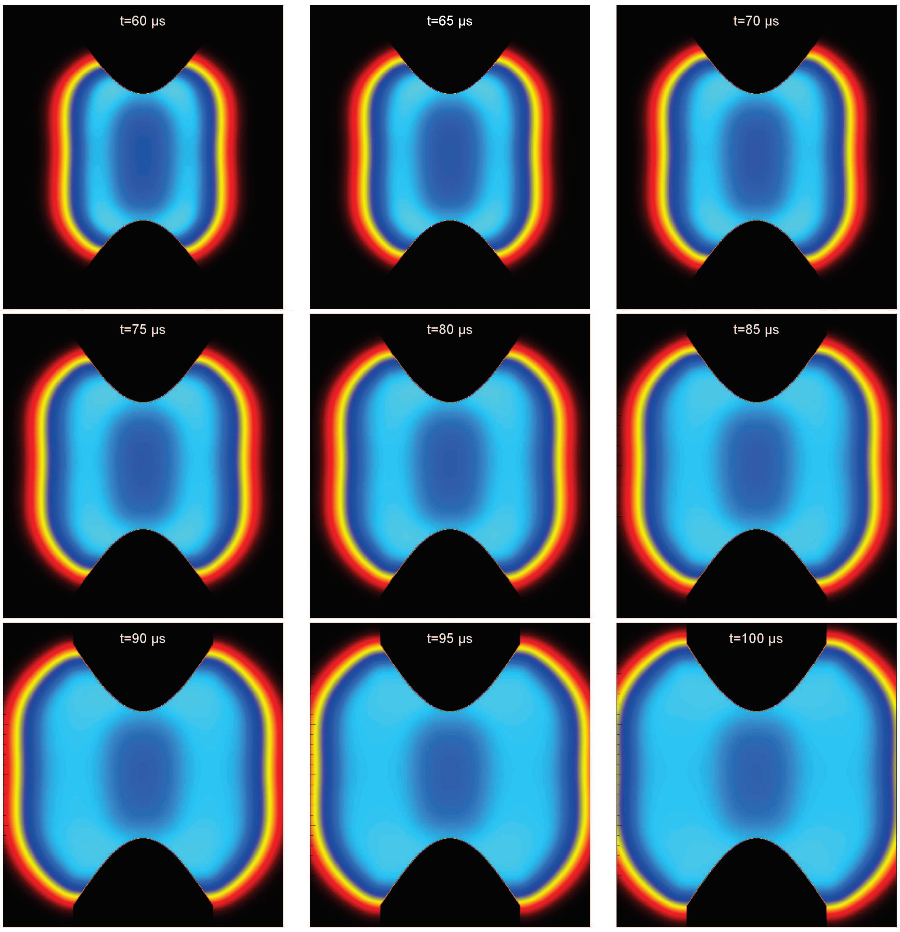

Figure 7.3: *2D distribution of the density of H_2O for a lean H_2-air mixture with an equivalence ratio $\Phi = 0.3$ at 1000 K and atmospheric pressure. Only the fast-heating by the nanosecond spark discharge is taken into account.*

7.6 Plasma assisted ignition of a lean H_2-air mixture: role of the atomic oxygen

The chemical model used in Chapter 4 to predict the fast-heating due to the two-step mechanism allows also to compute the production of atomic oxygen by a nanosecond spark discharge. For the reference nanosecond spark discharge studied in Chapter 4 at 1000 K, the evolution as a function of time of the atomic oxygen concentration in the middle of the inter-electrode-gap is shown on Figure 7.4. The voltage pulse lasts from 0 to 10 ns. It can be seen that most of the atomic oxygen is produced after the pulse due to the dissociative quenching of electronically excited N_2. However, it is interesting to note that almost 10% of the atomic oxygen is produced during the voltage pulse by electron impact dissociation. Dissociation rates through electron impact and electronic excitation rates of nitrogen increase with the reduced electric. Then the dissociation rate is much higher in the head of a streamer than in the plasma channel after connection. However, most of the O atoms are produced during the spark regime due to the much higher electron density in the plasma channel in the spark phase than in the streamer phase. It has been checked that even if the energetic efficiency for O atom production is higher for a corona or a glow regime, the spark regime produces very high concentrations of atomic oxygen due to the much higher energy release. Figure 7.5 shows the 2D distribution of the final atomic oxygen concentration at $t = 20$ ns. The atomic oxygen is mainly concentrated close to the electrode tips where the discharge energy density is higher (see Figure 4.2). The final dissociation level of molecular oxygen is around 30% in the plasma channel in the middle of the inter-electrode gap and around 60% close to the tip of electrodes. These results are in good qualitative agreement with experimental TALIF measurements of atomic oxygen concentrations performed by *Stancu et al.* [2010] in a nanosecond spark discharge very close to the reference discharge we considered in this chapter.

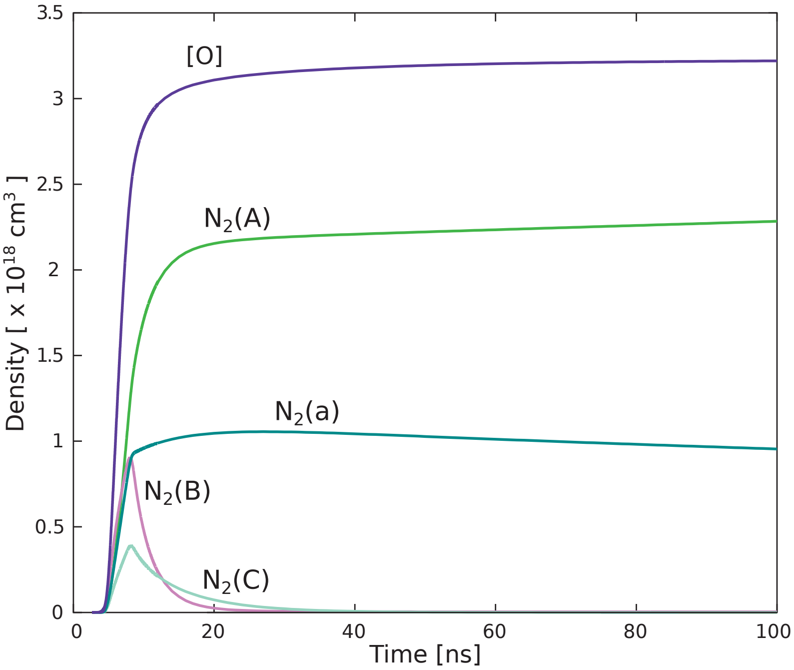

Figure 7.4: *Evolution of atomic oxygen and of the electronically excited levels of N_2 as a function of time during the reference nanosecond spark discharge defined in Chapter 4 at 1000 K in air at atmospheric pressure.*

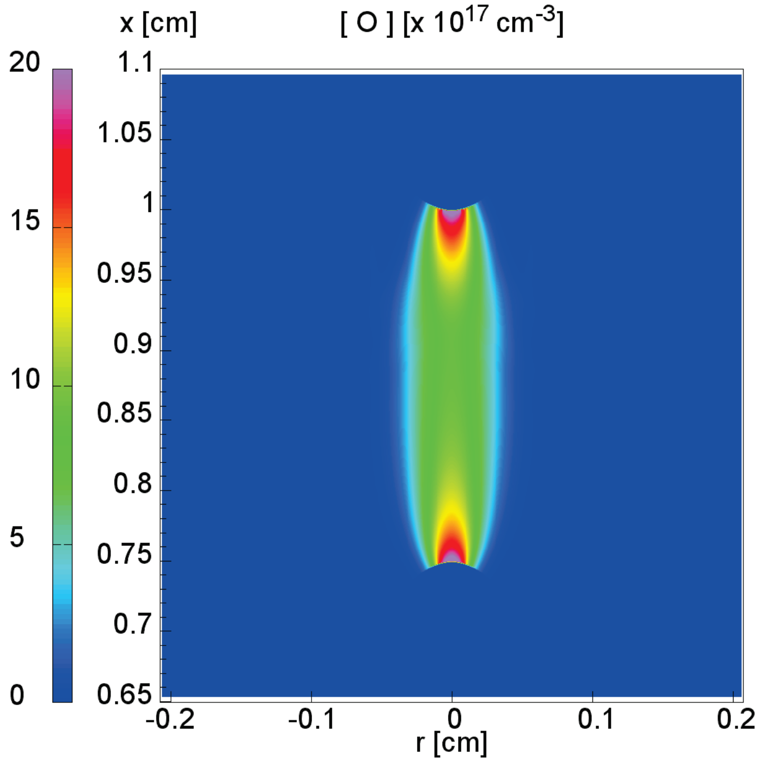

Figure 7.5: *2D distribution of the atomic oxygen concentration at* $t = 20$ *ns for the reference nanosecond spark discharge defined in Chapter 4 at 1000 K in air at atmospheric pressure.*

The high dissociation level of the molecular oxygen is very likely to increase the reactivity of the mixture and to enhance the combustion reactions: As explained by *Bowman et al.* [2010] for lower pressures, the high temperature chain propagation mechanism is determinant for ignition:

$$\left\{ \begin{array}{lll} O + H_2 & \rightarrow H + OH & (R2) \\ H + O_2 & \rightarrow O + OH & (R1) \end{array} \right. \tag{7.7}$$

Then, the atomic oxygen production from the discharge may accelerate significantly reaction (R2) improving the activation and the efficiency of this mechanism. To check the influence of the atomic oxygen produced by the discharge, we performed the same simulation as in the previous Section 7.5 but this time without taking into account the fast heating. Instead, we started the simulation only with the atomic oxygen concentration field of Figure 7.5 as initial condition. The initial condition is then an homogeneous temperature at T=1000 K and a H_2-air mixture with $\Phi = 0.3$ but with highly dissociated oxygen close to the electrodes and in the discharge path.

Figure 7.6 shows the time sequence of the evolution of H_2O concentration between 1 μs and 100 μs. Conversely to the ignition case with fast-heating on Figure 7.3, on Figure 7.6, between 0 and 5 μs there is no shockwave formation since no heating is taken into account and the density in the discharge path remains constant. At t=5 μs, the maximum of the H_2O concentration is much less than for the fast-heating ignition case. However, the O concentration is homogeneously distributed in the all discharge region. We observe that it takes up to 20 μs for the H_2O concentration to reach its maximum value and for the flame to start to propagate. The ignition is then slower during the first 20 μs than for the fast-heating ignition case but it is a more volumetric ignition. This slower initial dynamics seems to correspond to the induction time of the high temperature chain propagation mechanism (Reactions R1 and R2). For the fast heating ignition, the initial dynamics of the flame kernel is linked to the high temperature regions close to the electrodes while in this case the higher atomic oxygen concentrations close to the electrodes barely affect the shape of the kernel. This is probably due to the fact that reaction rates depend exponentially on temperature but only linearly on initial concentrations. From 20 to 100 μs, the flame propagates radially with a spherical shape while the flame kernel is more cylindrical for the fast-heating ignition (Figure 7.3).

To compare both results, we define a criterion to measure the efficiency of the ignition process: we consider the time at which the radius of the flame kernel reaches the value of 2 mm which corresponds to position of the left and right borders on Figures 7.3 and 7.6. It is interesting to note that this time is around 70 μs for the ignition with atomic oxygen and 85 μs for the fast-heating ignition case. The relative importance of fast heating and the atomic oxygen production is then of the same order in this particular case with a slightly higher ignition efficiency for the atomic oxygen. It would be interesting to carry out further studies to compare the relative influence of these two processes in a larger range of conditions and at lower temperatures.

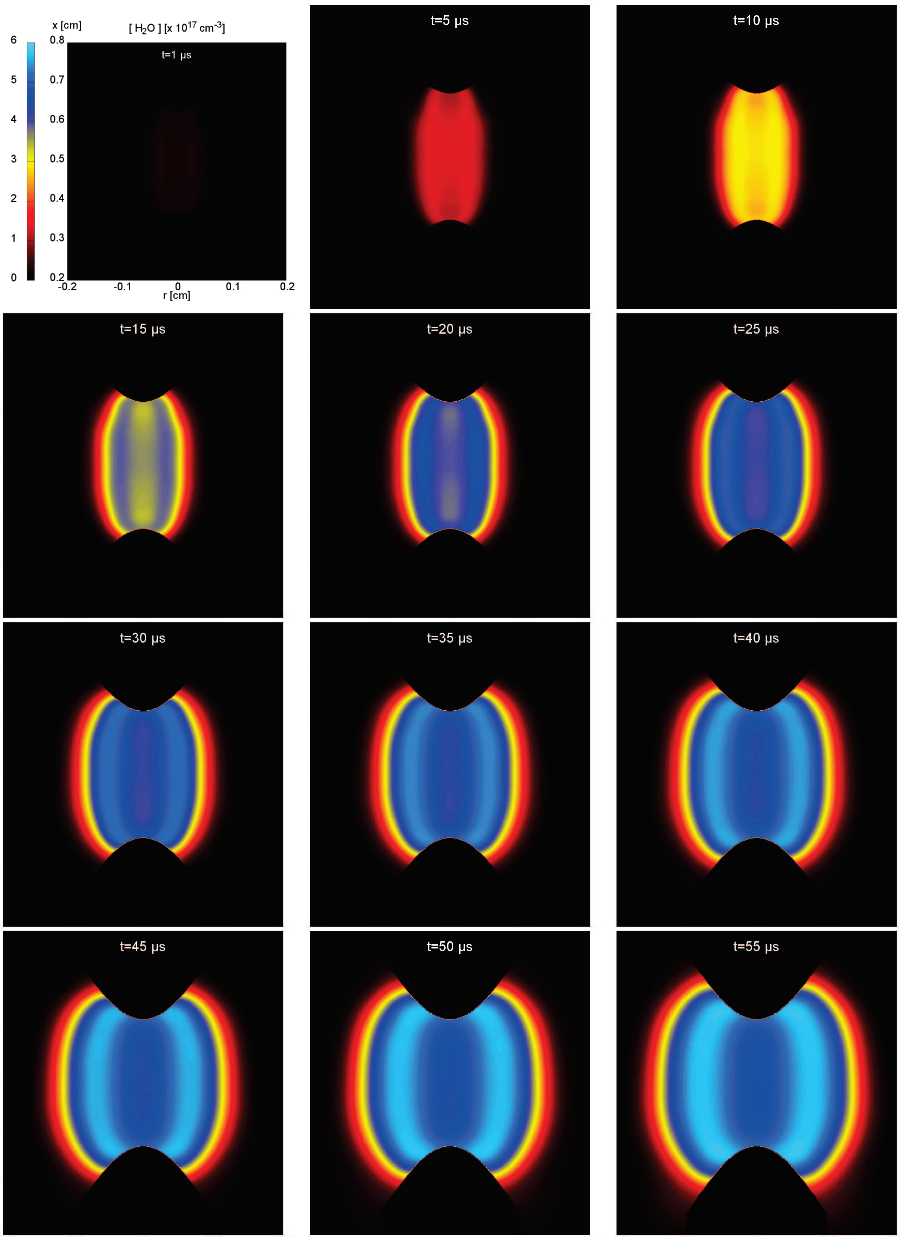
x [cm]
[H₂O] [x 10¹⁷ cm⁻³]
6
5
4
3
2
1
0
0.8
0.7
0.6
0.5
0.4
0.3
0.2
-0.2
-0.1
0
0.1
0.2
r [cm]
t=1 µs
t=5 µs
t=10 µs
t=15 µs
t=20 µs
t=25 µs
t=30 µs
t=35 µs
t=40 µs
t=45 µs
t=50 µs
t=55 µs

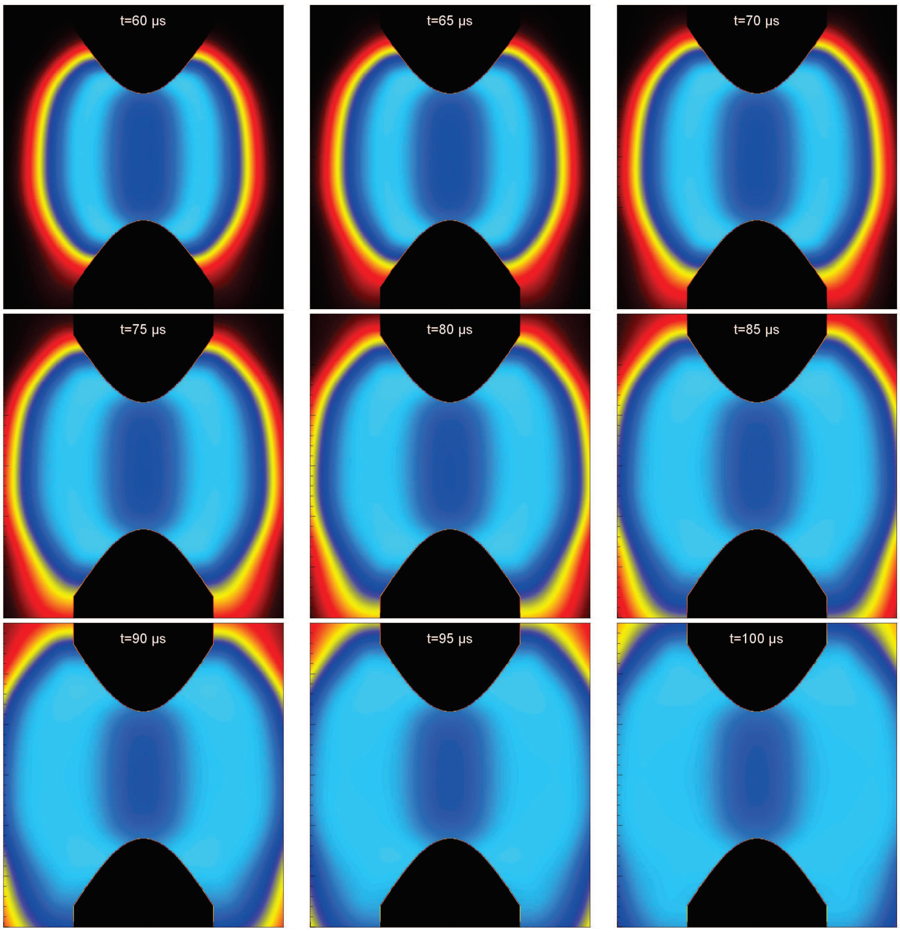

Figure 7.6: *2D distribution of the density of H_2O for a lean H_2-air mixture with an equivalence ratio $\Phi = 0.3$ at 1000 K and atmospheric pressure. Only the O production by the nanosecond spark discharge is taken into account.*

7.7 conclusion

The ignition by a nanosecond spark discharge of a lean H_2-air mixture at 1000 K with an equivalence ratio of $\Phi = 0.3$ has been studied on short timescales ($t \leq 100 \mu s$). Two numerical simulations have been performed : For the first one only the fast-heating of the nanosecond spark discharge has been taken into account. In this case, a flame kernel formation has been observed that ignites close to the tip of the electrodes and finally propagates radially with a cylindrical shape. At the beginning, the flame structure depends strongly on the initial temperature distribution, but as soon as it escapes from the inter-electrode gap it becomes spherical and is able to propagate on long distances. In the second case, we have assumed no heating by the discharge and we have taken into account the atomic oxygen production by the nanosecond spark discharge. In this case, a slower but volumetric ignition is observed in the inter-electrode gap that barely depends on the initial 2D distribution of the atomic oxygen. Then the flame propagates with a more spherical shape than for the fast-heating ignition case. Finally, it appears that both mechanisms are able to ignite the mixture on these short timescales. However, the ignition with the atomic oxygen seems to be slightly more efficient and has a completely different dynamics. It would be interesting in future works to study first the relative importance of both processes at lower temperatures. In a second step, further studies would be of interest on the influence of other parameters as the electrode geometry, the thermal conduction and the equivalence ratio on the combustion ignition by a nanosecond spark discharge.

Conclusion

In this Ph.D. thesis, we have carried out numerical simulations to study nanosecond repetitively pulsed discharges (NRPD) in a point-to-point geometry at atmospheric pressure in air and in H_2-air mixtures.

Experimentally, three discharge regimes have been observed for NRPD in air at atmospheric pressure for the temperature range $T_g = 300$ to 1000 K: corona, glow and spark. To better understand and control the conditions to obtain these regimes, we have carried out a parametric study on the influence of the applied voltage, the gap size, the radius of the electrodes and the air temperature. First, we have considered a discharge occurring during one of the nanosecond voltage pulses, assuming that many discharges have occurred before the studied one. The discharge has been simulated in 2D using a classical fluid model and we have estimated that the density of seed charges in the interelectrode gap at the end of a given interpulse after many voltage pulses is of the order of 10^9 cm^{-3} for $T_g = 300$ to 1000 K. From the simulation results, it seems that one key parameter for the transition between the three discharge regimes at 300 and 1000 K is the ratio between the connection-time (time to have the connection between the positive and the negative discharges initiated at the anode and the cathode point electrode, respectively) and the pulse duration. If this ratio is less than 1, the pulse duration is too short for the discharges to connect and then it corresponds to the corona regime. If this ratio is around 1, the plasma discharge has just the time to fill the interelectrode gap, no heating is observed and then, this corresponds to the glow regime. Finally, if this ratio is larger than 1, the applied voltage is maintained during the conduction phase and the discharge may heat the gas and then the glow-to-spark transition may occur.

It is interesting to note that, for the same geometries, the same pulse durations and applied voltages scaled with the air density, it appears that the heating of the gas is more significant at 300 K than at 1000 K. Then, the glow to spark transition may occur more easily at 300 K than as 1000 K if the pulse duration is slightly longer than the connection-time. This may explain the difficulty to obtain a stable glow discharge at 300 K in experiments. Finally, we have compared experimental and simulated images of the dynamics of a NRP discharge in air at atmospheric pressure and at $T_{\rm g} = 300$ K. The excellent agreement obtained validates the dynamics of formation of the air discharge between two point electrodes at the early stages of its development.

In a second step, we have studied the dynamics of charged species during the interpulse at $T_g = 300$ and 1000 K for repetitive pulses. We have shown that in the frequency range 10-100 kHz, at 300 and 1000 K the highest preionization level at the end of an interpulse is between 10^{10} and $4 \times 10^{11}\,\mathrm{cm}^{-3}$. The preionization level of $10^9\,\mathrm{cm}^{-3}$ used in the first part of this Ph.D. report corresponds to repetition frequencies in the range 1-10 kHz. For frequencies in the range 1-100 kHz, we have observed that the final value of seed charges at the end of the interpulse is independent on charged species densities at the end of the previous voltage pulse. At 300 K, we have shown that the preionization left by previous discharges consists in positive and negative ions. Nevertheless, when photoionization is taken into account, we have observed that the dynamics and the characteristics of the discharge are only weakly dependent on the nature of negative charges (either ions or electrons). Therefore we have shown that the use of a preionization with electrons and positive ions at a density of $10^9\mathrm{cm}^{-3}$ without photoionization is a good compromise between complexity and accuracy to study the discharge characteristics at 300 K. At 1000 K, a significant amount of electrons remains at the end of the interpulse and the role of negative ions on the next discharge dynamics is much less important than at 300 K. However, in the frequency range 10-100 kHz, as the electron density may be as high as $4 \times 10^{11}\,\mathrm{cm}^{-3}$, we have studied how such a high electron density preionization impacts the discharge dynamics. We have shown that the discharge dynamics and the connection-times remain rather close whatever the preionization level considered in the range 10^9-$10^{11}\,\mathrm{cm}^{-3}$.

Then, we have simulated several consecutive nanosecond voltage pulses at $T_g = 1000$ K and at a frequency of 10 kHz. We have observed that in a few voltage pulses, the discharge reaches a 'stable' glow regime also observed in the experiments. The shape of the voltage pulse has been chosen such that the voltage starts to decrease 0.5 ns after the connection of discharges to be in the glow regime. We have also observed that the preionization is after the two first pulses rather high ($\mathrm{n_e} = 10^{10}\,cm^{-3}$) and uniform over a radius of about 2 mm, much larger than the diameter of the positive discharge ignited at the positive point. These results validate the assumption of a uniform preionization of the interelectrode gap used in the first part of the Ph.D. report to study in detail the discharge dynamics during one voltage pulse. Finally, we have taken into account the convection of charged species during the interpulse due to an external air flow. We have found that the external air flow may promote the corona-to-glow transition in a very narrow range of parameters. It would be interesting in future works to study more in detail the influence of the flow on the discharge. In the simulations, we have considered a simple laminar convection with a flow aligned with the discharge axis, neglecting the presence of electrodes. It would be interesting to study the influence of a laminar air flow perpendicular to the discharge axis and also of a turbulent air flow on the NRPD.

We have then studied the spark regime of NRPD in developing a simple model for a nanosecond spark discharge in air at atmospheric pressure. As shown in the experiments, the nanosecond spark discharge may significantly heat the ambient air on short time-scales and induce shockwave propagation. Therefore we have studied the mechanisms of fast heating of the ambient air by the nanosecond spark discharge and we have solved 2D Euler equations to study the compressible gas dynamics induced by this heating. As a reference test case, we have considered a nanosecond spark discharge at 1000 K. For the modelling of the fast heating, as a first step, we have considered that a fixed fraction $\eta_R = 30\%$ of the discharge energy instantaneously heats the neutral gas. Then the value of η_R has been varied as a parameter in the range 15 to 60%, and in all cases, we have observed the formation and propagation of a cylindrical shockwave and its reflection on the electrode tips. The propagation velocity of these shockwaves is in all cases very close to the speed of sound in air at 1000 K, and followed by the formation of a hot channel in the path of the discharge that expands radially on short timescales $t < 1$ μs. These results are in good qualitative agreement with experiments. Finally, we have tested more accurate models for the computation of the fast-heating. They confirm that the fraction of the discharge energy going to fast heating is in the range 20%-30% and that the discharge energy is not deposited uniformly in the air with two hot spots close to electrode tips. Part of this energy deposited in the gas is efficiently dissipated on short time-scales by the shockwaves that are found to be an important energy dissipation process for NRPD.

To be closer to experiments, we have taken into account an external circuit model based on the BNC cable used in experiments to limit the discharge current. With the circuit model used, the applied voltage decreases dynamically when the conductivity of the plasma increases. Therefore, we have been able to simulate several consecutive discharge pulses and to study the transition from multipulse nanosecond glow to spark discharges. In the multipulse nanosecond spark regime, the discharges have to ignite and propagate in the hot, low density channels produced by the fast-heating of the previous discharges. This interaction through heating and gas dynamics tends to decrease the discharge radius pulse after pulse. To further increase the current limitation, we have added a ballast resistance to the circuit and we have shown that for a value of R=10,000 Ω, the heating after each pulse is negligible and then the multipulse nanosecond discharge in this case remains in a 'stable' glow regime.

All the results obtained on the physics of nanosecond pulsed discharges in air, and the numerical tools developed during this Ph.D. thesis have then been used

to address two key questions for NRPD applications.
First, for many applications as biomedical, surface treatment and decontamination, the challenge is to produce a large plasma volume at atmospheric pressure with a low gas temperature and a high chemical reactivity. Thus, we have carried out a detailed parametric study on the conditions to obtain a stable glow regime in air at 300 K and atmospheric pressure. We have shown that this regime could be obtained in large gaps with under-voltage conditions, but with a significant axial electric field to prevent branching and facilitate the propagation of the discharges. We have demonstrated that this can be obtained by using large electrodes or by adding large metallic plane holders behind the tip of the electrodes.

The second application of interest in this work is related to the plasma assisted ignition using NRPD. We have studied on short time-scales ($t \leq 100\mu s$) the ignition by a nanosecond spark discharge of a lean H_2-air mixture at 1000 K and atmospheric pressure with an equivalence ratio of $\Phi = 0.3$. To determine the relative importance for ignition of the fast-heating of the discharge or its chemical reactivity, we have performed two simulations: For the first one only the fast-heating of the nanosecond spark discharge has been taken into account. In the second case, we have assumed no heating by the discharge but we have taken into account the atomic oxygen production by the nanosecond spark. Finally, it appeared that both mechanisms are able to ignite the mixture on these short timescales. However, the ignition with the atomic oxygen seems to be slightly more efficient and has a completely different dynamics. It would be interesting in future works to study first the relative importance of both processes at lower temperatures. In a second step, further studies would be of interest on the influence of other parameters as the electrode geometry, the thermal conduction and the equivalence ratio on the combustion ignition by a nanosecond spark discharge for H_2-air mixtures and also other hydrocarbon-air mixtures.

Appendix A

Appendix

A.1 Magenetic field produced by a nanosecond spark discharge

In this section we compute an estimation of the magnetic-field generated by the current I passing through a plasma channel of radius R, of length G, and oriented in the axial direction. Due to the symmetry revolution of the plasma around axis $\vec{x}$ the magnetic-field is ortho-radial:

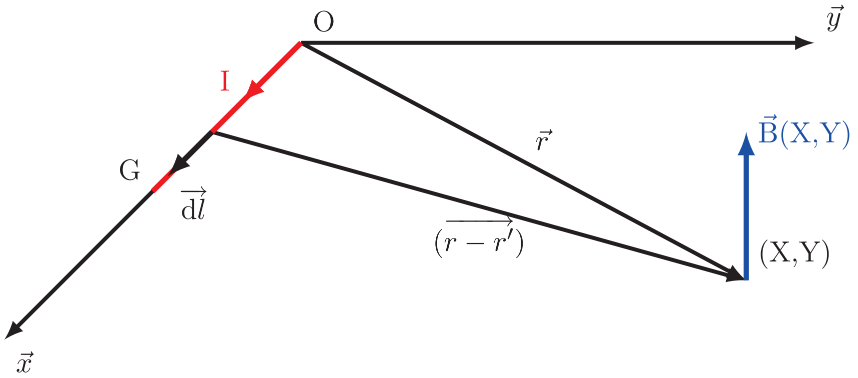

Figure A.1: *Scheme of the distribution of current and the coordinate system. There is a symmetry revolution around $\vec{x}$ axis.*

$$
\begin{aligned}
\vec{\mathrm{B}} &= \frac{\mu_0 I}{4\Pi}\int_0^G \frac{\vec{\mathrm{d}l} \wedge (\overrightarrow{r-r'})}{\parallel \overrightarrow{r-r'} \parallel^3} \\
\mathrm{B}(X,Y) &= \frac{\mu_0 I}{4\Pi}\int_0^G \frac{Y\mathrm{d}x}{\sqrt{Y^2+(x-X)^2}^3} \\
\mathrm{B}(X,Y) &= \frac{\mu_0 IY}{4\Pi}\left[\frac{x-X}{Y^2\sqrt{Y^2+(x-X)^2}}\right]_0^G \\
\mathrm{B}(X,Y) &= \frac{\mu_0 I}{4\Pi Y}\left[\frac{G-X}{\sqrt{Y^2+(G-X)^2}}+\frac{X}{\sqrt{X^2+Y^2}}\right]
\end{aligned}
\tag{A.1}
$$

At the middle of the inter-electrode gap (X=G/2) and for Y=R, where R is the discharge radius one gets:

$$B_{max} = \frac{\mu_0 IG}{4\pi R\sqrt{(\frac{G}{2})^2+R^2}} \tag{A.2}$$

For a conductive current I=40 A, a radius of curvature R= 500 μm, and a gap size G=2.5 mm, the maximum magnetic field is about 0.01 T. The magnetic field of the discharge can also be obtained numerically by applying the Ampère’s circuital law in each cell of the domain:

$$\oint_{\mathrm{C}} \vec{\mathrm{B}}\cdot\vec{\mathrm{d}l} = \mu_0 I_{\mathrm{S}} \qquad \Rightarrow \mathrm{B}(x,r) = \frac{\mu_0 I_{\mathrm{S}}(x,r)}{2\pi r} \tag{A.3}$$

Where $I_{\mathrm{S}}(x,r)$ is the current passing through the surface S enclosed by the closed curve C. In our case:

$$I_{\mathrm{S}}(x,r) = \int_0^r 2\pi r \mathrm{j}_{\mathrm{xc}}(x,r)\mathrm{d}r \tag{A.4}$$

$\mathrm{j}_{\mathrm{xc}}(x,r)$ being the conductive current density in the axial direction. Figure A.2 shows the time evolution every 0.1 ns of the magnetic field during the spark regime for the reference spark discharge of chapter 4.2.1 (p. 73) from t=6.9 ns to t=8.4 ns which corresponds to the end of the pulse (see figure 4.1 76). It can be seen that the maximum magnetic-field obtained is around 0.04 T which is of the same order of magnitude as the value computed analytically.

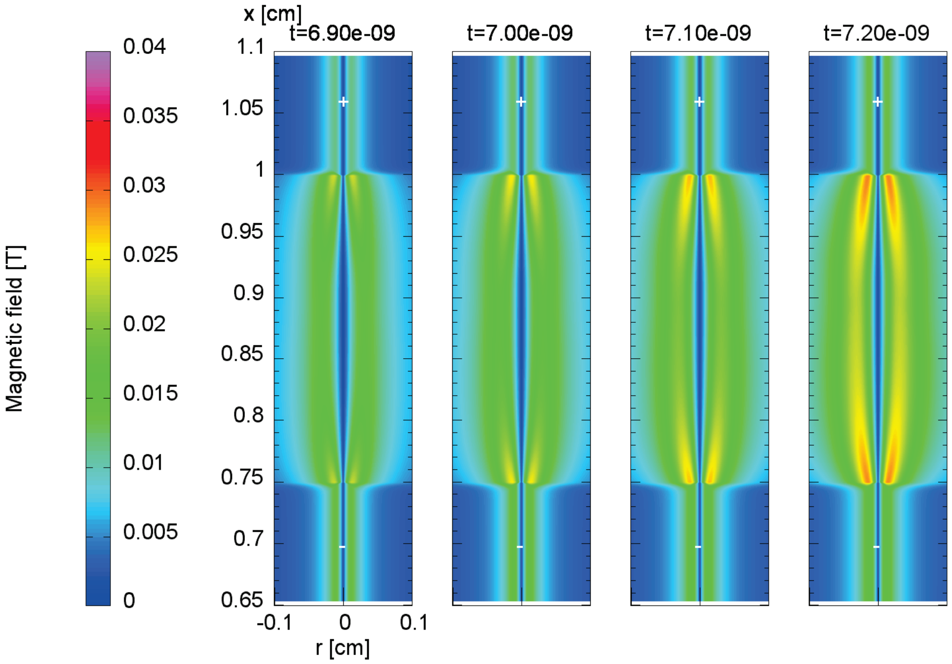
Magnetic field [T]
0.04
0.035
0.03
0.025
0.02
0.015
0.01
0.005
0
x [cm]
1.1
1.05
1
0.95
0.9
0.85
0.8
0.75
0.7
0.65
-0.1
0
0.1
r [cm]
t=6.90e-09
t=7.00e-09
t=7.10e-09
t=7.20e-09

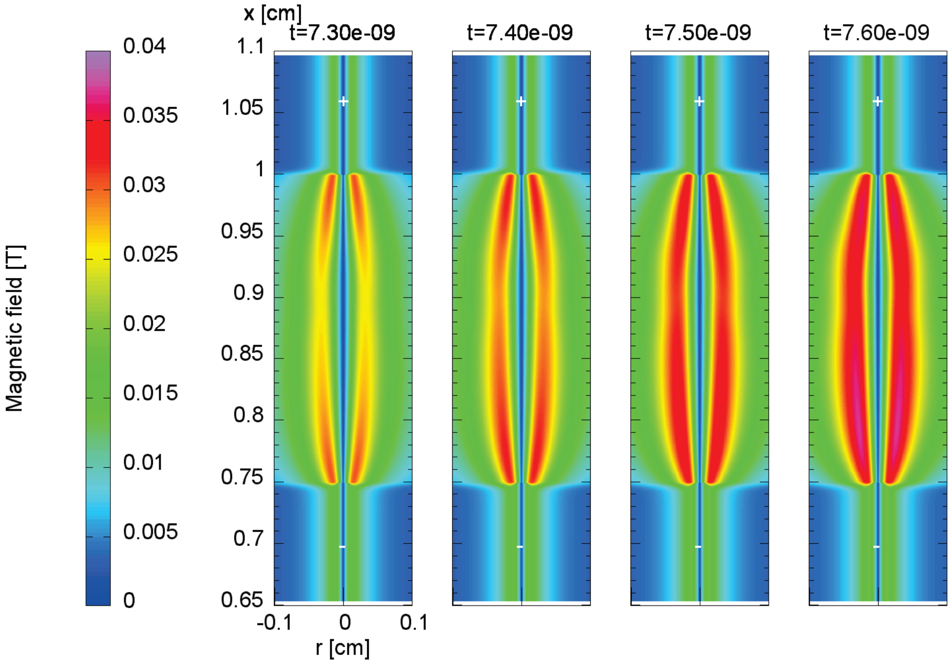
Magnetic field [T]
0.04
0.035
0.03
0.025
0.02
0.015
0.01
0.005
0
x [cm]
1.1
1.05
1
0.95
0.9
0.85
0.8
0.75
0.7
0.65
-0.1
0
0.1
r [cm]
t=7.30e-09
t=7.40e-09
t=7.50e-09
t=7.60e-09

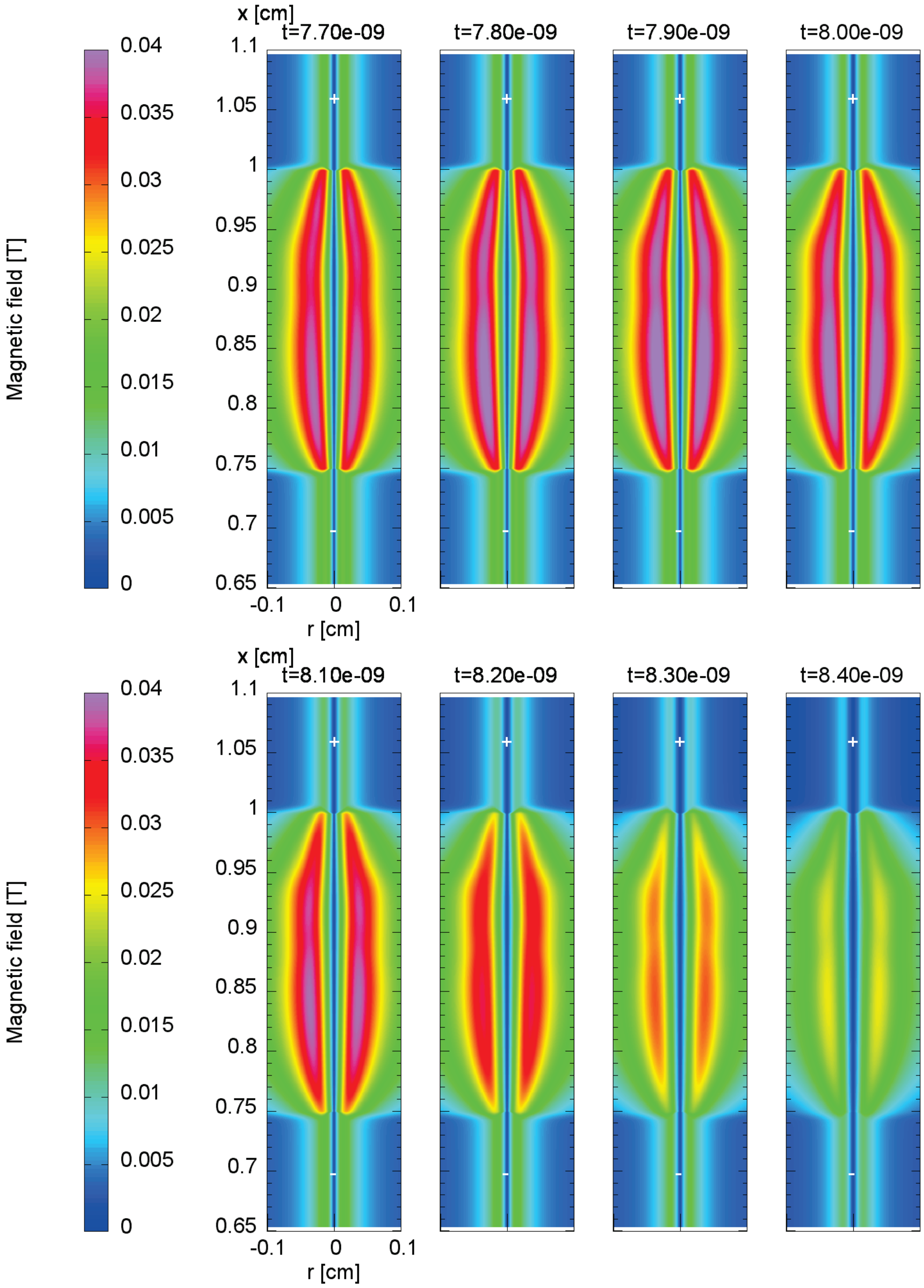

Figure A.2: *2D distribution of the magnetic-field of a nanosecond spark discharge.*

A.2 Estimation of the plasma inductance

The plasma inductance can be estimated by integrating over the volume V of the plasma the electromagnetic energy density e and using equation A.5:

$$\mathrm{e} = \frac{1}{2}\mathcal{L}I^2 \tag{A.5}$$

Where $\mathcal{L}$ is the inductance of the plasma. The electro-magnetic energy density is given by:

$$\mathrm{e} = \iiint_{\mathrm{V}} \left(\frac{1}{2}\epsilon_0 \mathrm{E}^2 + \frac{1}{2\mu_0}\mathrm{B}^2\right) \mathrm{d}V \tag{A.6}$$

The electric-field E is uniform in the conducting channel of a spark discharge:

$$\mathrm{E} = \frac{\mathrm{j}}{\gamma} = \frac{I}{\pi R^2 \gamma} \tag{A.7}$$

Where γ is the plasma conductivity, j the conductive current density, I the conductive current passing through the plasma and R the radius of the plasma channel which is assumed to be a cylinder. The magnetic field can be computed using the Ampère's circuital law:

$$\mathrm{B}(r)2\pi r = \mu_0 \pi r^2 \mathrm{j} \Rightarrow \mathrm{B}(r) = \frac{\mu_0 I r}{2\pi R^2} \tag{A.8}$$

By integrating the electromagnetic energy one gets:

$$\mathrm{e} = \frac{1}{2}\left(\frac{\epsilon_0 G}{\pi \gamma^2 R^2} + \frac{G\mu_0}{8\pi}\right)I^2 \tag{A.9}$$

Where G is the length of the plasma which is the gap size.

$$\Rightarrow \mathcal{L} = \left(\frac{\epsilon_0 G}{\pi \gamma^2 R^2} + \frac{G\mu_0}{8\pi}\right) \tag{A.10}$$

For I=40 A, R=500 μm, E=20 kV/cm, and G=2.5 mm, one finds the inductance $\mathcal{L}$=1.69 10^{-10} H.

A.3 Symmetry effects of the potential on the optical emission

In Chapter 2, Section 2.8, we describe a comparison between experiments and simulations of a point-to-point discharge at 300 K (Figure 2.11). Important is to note that in the experiments, a symmetric potential of +9 kV at the anode and -9 kV at the cathode has been used. In this case, both the positive and the negative discharges are perfectly observed as in the simulation where the potential of +15 kV applied at the anode and 0 V at the cathode is perfectly symmetric due the the Neumann boundary conditions on the boundaries of the domain (x_{min}=0 mm, x_{max}=20 mm, r_{max}=1 mm). This special attention to the symmetry of the applied voltage between the electrodes is necessary to be able to observe the negative discharge at the cathode. When considering a cathode at 0 V, the presence of all the grounded surfaces around the experiment apparatus may influence the potential distribution and the applied electric-field in the inter-electrode gap in a non-symmetric way. For example, experiments may be performed over a grounded laboratory table, with vertical electrodes and the cathode at the bottom. From an electrostatic point of view, it is equivalent to put an infinite grounded plane behind the cathode in the simulation domain. The influence of this asymmetric configuration is shown on figures A.3 and A.4. Figure A.3 shows the potential and the electric-field on the symmetry axis of the electrodes for the symmetric potential case: when no plane is added behind the cathode and when Neumann boundary conditions on the potential are applied on the boundaries. It can be seen clearly that both the electric-field and the potential are symmetric relatively to the middle of the gap and that the maximum electric-field is exactly the same at the tip of each electrodes, located at x=7.5 mm for the cathode and x=12.5 mm for the anode. Figure A.4 shows the potential and the electric-field for the non-symmetric case, when a grounded, infinite plane is placed behind the anode at x=0 cm. In this case, we can clearly see that the fields are no longer symmetric, with an increase of the electric-field at the anode from 200 to 250 kV cm^{-1}, and a decrease at the cathode from 200 to 140 kV cm^{-1}. Because the discharges dynamics and structures are very dependent on the applied electric-field, this modification may have a significant influence on the optical emission of the discharges and on the experimental pictures obtained by fast-camera imaging.

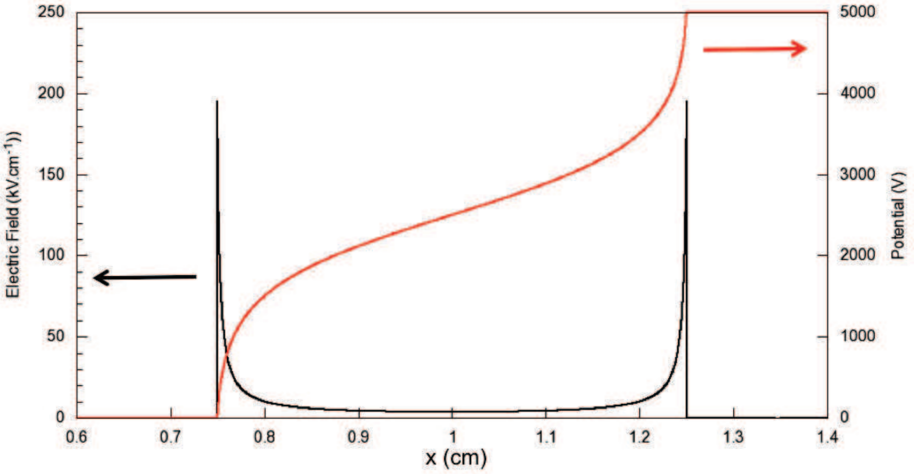

Figure A.3: *Electric field and electric potential on the symmetry axis of a point-to-point electrode configuration. Symmetric boundary conditions are applied: Neumann boundary conditions on the potential are used on all the boundaries at $x_{\rm min}$=0 cm, $x_{\rm max}$=1.8 cm and $r_{\rm max}$=1 cm*

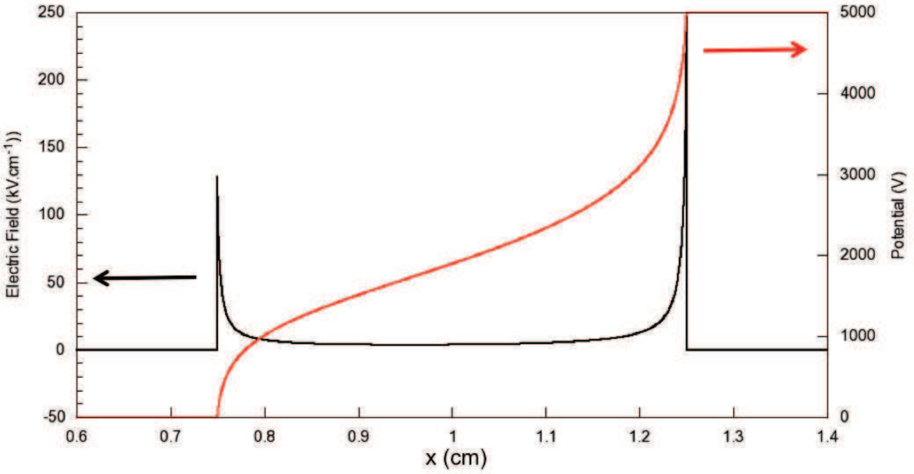

Figure A.4: *Electric field and electric potential on the symmetry axis of a point-to-point electrode configuration. Non symmetric boundary conditions are used in the computation domain: A grounded plane is placed at $x_{\rm min}$=0 cm (not shown), and Neumann boundary conditions on the potential are used on the other boundaries: $x_{\rm max}$=1.8 cm and $r_{\rm max}$=1 cm*

Figure A.5 shows the spatial distribution of the calculated 2P emissions integrated over 2 ns and Abel integrated for a discharge at 1000 K. The applied voltage is 5 kV, the gap is 5 mm and the radius of curvature R_p=100 μm (see Table 2.1 in Chapter 2, Section 2.6). It is interesting to note that the emission is much higher at the anode than at the cathode. When compared to the case at 300 K described in Chapter 2, Section 2.8 (Figure 2.11), the emission of the negative discharge relatively to the positive discharge appears to be lower at 1000 K than at 300 K. This is probably one of the reasons why the negative discharges at 1000 K are not observed experimentally in *Pai et al.* [2009] during the corona and the glow regime, because it is much less intense than the positive discharge. Figure A.6 shows the same simulation results for the non-symmetric case, with a grounded plane behind the cathode at x=0 cm. It can be observed that the emission of the positive discharge close to the anode is much higher than in the symmetric-case, and it has a wider radial expansion. This is coherent with the higher laplacian electric-field close the anode in the non-symmetric case (Figure A.4). On the other hand, the intensity of the negative discharge and the cathode region is even lower in this case than in the symmetric case. Then, the relative intensity of the negative discharge to the intensity of the positive discharge is considerably reduced when a non-symmetric potential is applied with a grounded plane behind the cathode. This may explain why a symmetric potential with a negative voltage applied at the cathode is important to be able to observe experimentally the negative discharge [*Tholin et al.*, 2011].

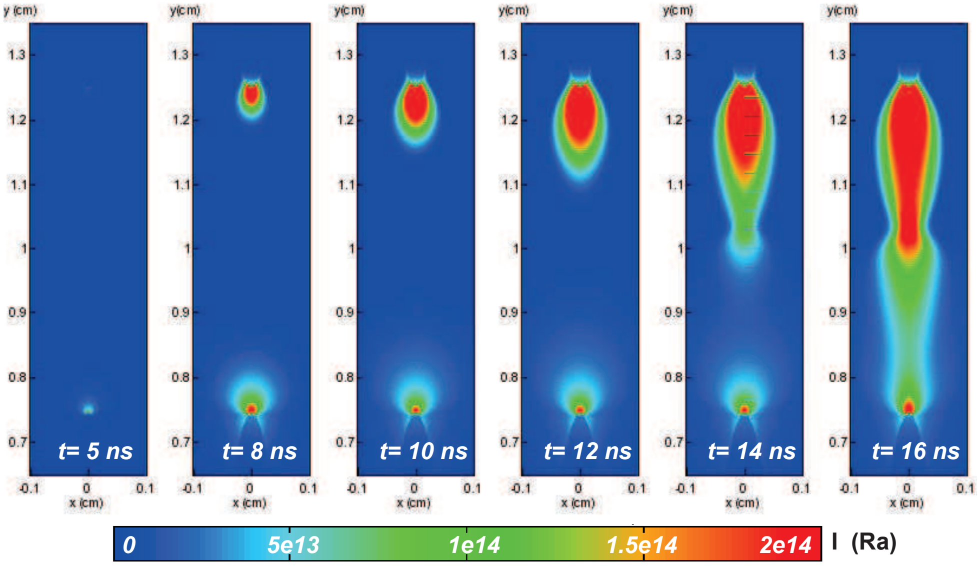

Figure A.5: *Nanosecond pulsed discharge at 1000 K with an applied voltage of 5 kV, a gap of 5 mm and* R_p=*100* μ*m. Spatial distribution of calculated line-of-sight 2P emission time integrated over 2 ns. A linear intensity scale is used. Symmetric boundary conditions are used in the computation domain: Neumann boundary conditions on the potential are used on all the boundaries at* $x_{\min}$=*0 cm,* $x_{\max}$=*1.8 cm and* $r_{\max}$=*1 cm.*

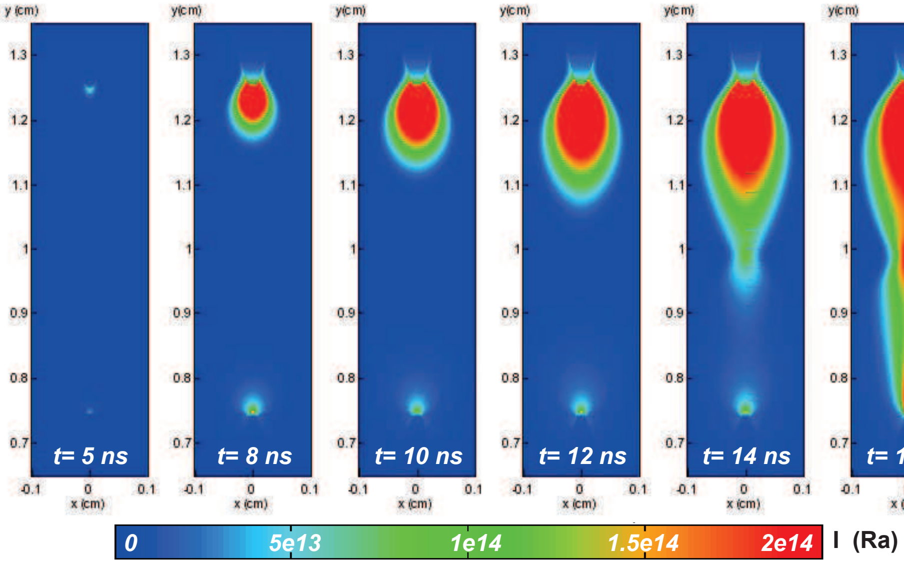

Figure A.6: *Nanosecond pulsed discharge at 1000 K with an applied voltage of 5 kV, a gap of 5 mm and* $R_{\rm p}$*=100 μm. Spatial distributions of calculated line-of-sight 2P emission time integrated over 2 ns. A linear intensity scale is used. Non symmetric boundary conditions are used in the computational domain: A grounded plane is placed at* $x_{\rm min}$*=0 cm (not shown), and Neumann boundary conditions on the potential are used on the other boundaries:* $x_{\rm max}$*=1.8 cm and* $r_{\rm max}$*=1 cm*

A.4 Model for the spark regime of NRPDs

The 2D distribution of the discharge is assumed to remain constant during the spark phase, which is verified in all the explicit simulations that has been performed. Moreover, no transport phenomena such as ambipolar diffusion or thermal expansion is likely to modify the discharge structure on these timscales because the nanosecond spark lasts only a few nanoseconds.

Keeping same the structure of the electric-field $\vec{\rm E}$ means that its direction remains constant during the spark phase but its amplitude may change due to the time-varying applied voltage. When the voltage changes by a given ratio, the electric-field $\vec{\rm E}$ has to evolve by the same ratio everywhere in order to maintain the same structure. This assumption means that during the voltage decrease the $\vec{\rm x}$ and $\vec{\rm r}$ components of the electric-field, $\rm E_x$ and $\rm E_r$, are scaled to the voltage amplitude (Equation (A.11)).

$$\begin{aligned} {\rm E_x}^{-1}\partial_{\rm t}{\rm E_x} &= {\rm U}^{-1}\partial_{\rm t}{\rm U} \\ {\rm E_r}^{-1}\partial_{\rm t}{\rm E_r} &= {\rm U}^{-1}\partial_{\rm t}{\rm U} \end{aligned} \tag{A.11}$$

It can be verified that Equation (A.11) ensures that the total electric-field is also scaled to the applied voltage U:

$$\begin{aligned}
|\vec{E}|^2 &= {E_x}^2 + {E_r}^2 \\
\partial_t|\vec{E}|^2 &= \partial_t {E_x}^2 + \partial_t {E_r}^2 \\
|\vec{E}|\partial_t|\vec{E}| &= E_x\partial_t E_x + E_r\partial_t E_r \\
|\vec{E}|\partial_t|\vec{E}| &= {E_x}^2 U^{-1}\partial_t U + {E_r}^2 U^{-1}\partial_t U \\
|\vec{E}|^{-1}\partial_t|\vec{E}| &= U^{-1}\partial_t U
\end{aligned} \tag{A.12}$$

Taking the time derivative of Gauss's law and using the Schwarz theorem, it can be shown that under this hypothesis the volumetric space charge ρ has to be scaled to the applied voltage:

$$\begin{aligned}
&\vec{\nabla}\cdot\vec{E} = \tfrac{\rho}{\epsilon_0} \\
&\partial_x E_x + r^{-1}\partial_r E_r = \tfrac{\rho}{\epsilon_0} \\
&\partial_x\partial_t E_x + r^{-1}\partial_r\partial_t E_r = \tfrac{1}{\epsilon_0}\partial_t\rho
\end{aligned} \tag{A.13}$$

Replacing the time derivatives thanks to Equation (A.11) one gets:

$$\begin{aligned}
&\partial_x(E_x U^{-1}\partial_t U) + r^{-1}\partial_r(E_r U^{-1}\partial_t U) = \tfrac{1}{\epsilon_0}\partial_t\rho \\
&U^{-1}\partial_t U(\partial_x E_x + r^{-1}\partial_r E_r)
\end{aligned} \tag{A.14}$$

$$\rho^{-1}\partial_t\rho = U^{-1}\partial_t U \tag{A.15}$$

The space charge evolution is then forced by the applied voltage evolution to ensure Equation (A.11). As a consequence, the fluxes of the charged species are imposed by the current conservation equation (Equation (A.16))

$$\partial_t\rho + \vec{\nabla}\cdot\vec{j_c} = 0 \tag{A.16}$$

Where $\vec{j_c}$ is the conductive current density vector. If we neglect the conductive current due to diffusion fluxes we have $\vec{j_c} = \gamma\vec{E}$, with γ the plasma conductivity. Then Equation (A.16) is equivalent to Equation (A.17):

$$\partial_t\rho - \vec{\nabla}\cdot(\gamma\vec{\nabla}V) = 0 \tag{A.17}$$

In most 2D arc models, the time derivative of the space charge is set to zero, because the plasma is assumed to be neutral, and Equation (A.17) reduces to a Laplace equation on the potential that can be solved.

In our case, the space charge variation is forced by adding a source term of electrons in each cell that ensures Equation (A.15).

Bibliography

Abdulle, A., Fourth order Chebyshev methods with recurrence relation, *SIAM Journal on Scientific Computing*, *23*(6), 2041–2054, 2002. *(p. 162)*

Adamovich, I. V., W. R. Lempert, M. Nishihara, J. W. Rich, and Y. G. Utkin, Repetitively pulsed nonequilibrium plasmas for magnetohydrodynamic flow control and plasma-assisted combustion, *Journal of Propulsion and Power*, *24*(6), 1198–1215, 2008. *(p. 79)*

Aleksandrov, N. L., Mechanism of ultra-fast heating in a non-equilibrium weakly ionized air discharge plasma in high electric fields, *Journal of Physics D: Applied Physics*, *43*, 255,201, 2010. *(p. 81, 106, 114, 121)*

Benilov, M. S., and G. V. Naidis, Modelling of low-current discharges in atmospheric-pressure air taking account of non-equilibrium effects, *Journal of Physics D: Applied Physics*, *36*(15), 1834–1841, 2003. *(p. 46)*

Berezhetskaya, N., S. Gritsinin, V. Kopev, I. Kossyi, N. Popov, and V. Silakov, Microwave discharge as a method for igniting combustion in gas mixtures, *43rd AIAA aerospace sciences meeting and exhibit*, pp. AIAA–2005–2991, 2005. *(p. 158)*

Bityurin, V. A., A. N. Bocharov, and N. A. Popov, Numerical simulation of an electric discharge in supersonic flow, *Fluid Dynamics*, *43*(4), 642–653, 2008. *(p. 80)*

Boeuf, J. P., Y. Lagmich, T. Unfer, T. Callegari, and L. C. Pitchford, Electrohydrodynamic force in dielectric barrier discharge plasma actuators, *Journal of Physics D: Applied Physics*, *40*(3), 652–662, 2007. *(p. 79)*

Boivin, P., C. Jiménez, A. L. Sánchez, and F. A. Williams, An explicit reduced mechanism for H_2 air combustion, *Proceedings of the Combustion Institute*, *33*(1), 517–523, 2011. *(p. 160, 162)*

Bonaventura, Z., A. Bourdon, S. Celestin, and V. P. Pasko, Electric field determination in streamer discharges in air at atmospheric pressure, *Plasma Sources Science and Technology*, *20*(3), 035,012, 2011. *(p. 18)*

Bourdon, A., V. P. Pasko, N. Y. Liu, S. Célestin, P. Ségur, and E. Marode, Efficient models for photoionization produced by non-thermal gas discharges in air based on radiative transfer and the Helmholtz equations, *Plasma Sources Science and Technology*, *16*(3), 656–678, 2007. *(p. 16)*

Bourdon, A., Z. Bonaventura, and S. Celestin, Influence of the pre-ionization background and simulation of the optical emission of a streamer discharge in preheated air at atmospheric pressure between two point electrodes, *Plasma Sources Science and Technology*, *19*(3), 034,012, 2010. *(p. 11, 21, 22, 27)*

Bowman, S., I. Choi, K. Takashima, I. V. Adamovich, and W. Lempert, Kinetics of low-temperature hydrogen oxidation and ignition by repetitively pulsed nonequilibrium plasmas, *48th AIAA aerospace sciences meeting including the new horizons forum and aerospace exposition*, 2010. *(p. 172)*

Brandenburg, R., V. A. Maiorov, Y. B. Golubovskii, H.-E. Wagner, J. Behnke, and J. F. Behnke, Diffuse barrier discharges in nitrogen with small admixtures of oxygen: discharge mechanism and transition to the filamentary regime, *Journal of Physics D: Applied Physics*, *38*(13), 2187–2197, 2005. *(p. 117)*

Candel, S., T. Schmitt, and N. Darabiha, Progress in transcritical combustion: Experimentation, modeling and simulation, *23rd ICDERS*, 2011. *(p. 162)*

Celestin, S., Study of the dynamics of streamers in air at atmospheric pressure, Ph.D. thesis, Ecole Centrale Paris (ECP), 2008. *(p. 3, 8)*

Celestin, S., Z. Bonaventura, B. Zeghondy, A. Bourdon, and P. Ségur, The use of the ghost fluid method for Poisson’s equation to simulate streamer propagation in point-to-plane and point-to-point geometries, *Journal of Physics D: Applied Physics*, *42*(6), 065,203, 2009. *(p. 9, 11, 21, 22)*

Cerkanowicz, A. E., *Radiation Augmented Combustion*, Defense Technical Information Center, 1979. *(p. 158)*

Demmel, J. W., S. C. Eisenstat, J. R. Gilbert, X. S. Li, and J. W. H. Liu, A supernodal approach to sparse partial pivoting, *SIAM Journal on Matrix Analysis and Applications*, *20*(3), 720–755, 1999. *(p. 9)*

Demore, W. B., S. P. Sander, C. J. Howard, A. R. Ravishankara, D. M. Golden, C. E. Kolb, R. F. Hampson, M. J. Kurylo, and M. J. Molina, Chemical kinetics and photochemical data for use in stratospheric Modeling, *JPL Publication*, (12), 1997. *(p. 158)*

Doroshenko,V.M., Kudryavtsev, N., and V. Smetanin, Equilibrium of internal degrees of freedom of molecules and atoms in hypersonic flight in the upper atmosphere, *High Temperature*, *29*(5), 1013–1027, 1991. *(p. 115)*

Ferziger, J., and M. Peric, *Computational Methods for Fluid Dynamics*, 3 ed., 2002. *(p. 9)*

Fridman, A., A. Chirokov, and A. Gutsol, Non-thermal atmospheric pressure discharges, *J. Phys. D: Appl. Phys.*, *38*(2), R1–R24, 2005. *(p. 1)*

Gelfand, B. E., M. V. Silnikov, S. P. Medvedev, and S. V. Khomik, *Thermo-Gas Dynamics of Hydrogen Combustion and Explosion*, 2012. *(p. 164, 167)*

Hadjadj, A., and A. Kudryavtsev, Computation and flow visualization in high-speed aerodynamics, *Journal of Turbulence*, *6*, 37–41, 2005. *(p. 98, 99)*

Hagelaar, G. J. M., and L. C. Pitchford, Solving the Boltzmann equation to obtain electron transport coefficients and rate coefficients for fluid models, *Plasma Sources Science and Technology*, *14*(4), 722–733, 2005. *(p. 11, 12, 13, 14, 15, 54, 114)*

Hairer, E., and G. Wanner, *Solving Ordinary Differential Equations II*, *Springer Series in Computational Mathematics*, vol. 14, Springer Berlin Heidelberg, Berlin, Heidelberg, 2010. *(p. 49, 162)*

Ivanov, I., I. Kryukov, D. Orlov, and I. Znamenskaya, Investigations of shock wave interaction with nanosecond surface discharge, *Experiments in Fluids*, *48*(4), 607–613, 2009. *(p. 79)*

Jarrige, J., personal communication, 2011. *(p. 145, 151)*

Kamm, J. R., Evaluation of the Sedov-von Neumann-Taylor Blast Wave Solution, *Applied Physics*, 2000. *(p. 87, 88)*

Kossyi, I. A., A. Y. Kostinsky, A. A. Matveyev, and V. P. Silakov, Kinetic scheme of the non-equilibrium discharge in nitrogen-oxygen mixtures, *Plasma Sources Science and Technology*, *1*(3), 207–220, 1992. *(p. 46, 47, 48, 117)*

Kozlov, K. V., H.-E. Wagner, R. Brandenburg, and P. Michel, Spatio-temporally resolved spectroscopic diagnostics of the barrier discharge in air at atmospheric pressure, *Journal of Physics D: Applied Physics*, *34*(21), 2001. *(p. 18)*

Kulikovsky, A. A., A more accurate scharfetter-gummel algorithm of electron transport for semiconductor and gas discharge simulation, *Journal of Computational Physics*, *119*, 149–155, 1995. *(p. 8)*

Kulikovsky, A. A., Positive streamer between parallel plate electrodes in atmospheric pressure air, *Journal of Physics D: Applied Physics*, *30*, 441–50, 1997. *(p. 8)*

Kulikovsky, A. A., Three-dimensional simulation of a positive streamer in air near curved anode, *Physics letters A*, *9601*(August), 1998. *(p. 26, 40)*

Laroussi, M., M. G. Kong, G. Morfill, and W. Stolz, *Plasma medicine, Applications of low temperature gas plasmas in medicine biology*, 2012. *(p. 1)*

Li, S., WENO schemes for cylindrical and spherical geometry, *Elsevier Science*, (1), 1–14, 2003. *(p. 84, 86)*

Liu, N., and V. P. Pasko, Effects of photoionization on propagation and branching of positive and negative streamers in sprites, *Journal of Geophysical Research*, *109*(A4), 1–18, 2004. *(p. 16, 17, 18, 19, 117)*

Liu, N., and V. P. Pasko, Effects of photoionization on similarity properties of streamers at various pressures in air, *Journal of Physics D: Applied Physics*, *39*(2), 327–334, 2006. *(p. 17, 26, 36)*

Liu, N., S. Celestin, A. Bourdon, V. P. Pasko, P. Segur, and E. Marode, Application of photoionization models based on radiative transfer and the Helmholtz equations to studies of streamers in weak electric fields, *Applied Physics Letters*, *91*(21), 211,501, 2007. *(p. 16)*

Lu, X., M. Laroussi, and V. Puech, On atmospheric-pressure non-equilibrium plasma jets and plasma bullets, *Plasma Sources Science and Technology*, *21*, 034,005, 2012. *(p. 1)*

Maly, R., *Spark ignition: its physics and effect on the internal combustion engine*, 91–148 pp., Plenum Press, New York, 1984. *(p. 158)*

Massines, F., P. Segur, N. Gherardi, C. Khamphan, and A. Ricard, Physics and chemistry in a glow dielectric barrier discharge at atmospheric pressure: diagnostics and modelling, *Surface and Coatings Technology*, *8*(14), 174–175, 2003. *(p. 1)*

Millikan, R. C., and D. R. White, Systematics of vibrational relaxation, *Journal of Chemical Physics*, *39*(12), 3209–3213, 1963. *(p. 115)*

Mintoussov, E. I., S. J. Pendleton, F. G. Gerbault, N. A. Popov, and S. M. Starikovskaia, Fast gas heating in nitrogen-oxygen discharge plasma: II. Energy exchange in the afterglow of a volume nanosecond discharge at moderate pressures, *Journal of Physics D: Applied Physics*, *44*(28), 285,202, 2011. *(p. 81)*

Mnatsakanyan, A., and G. Naidis, Charged particle production and loss processes in nitrogen-oxygen plasmas, *Reviews of Plasma Chemistry*, *1*, 259–292, 1991. *(p. 46)*

Mnatsakanyan, A. K., and G. V. Naidis, The vibrational energy balance in a discharge in air, *High Temperature*, *23*(4), 506–513, 1985. *(p. 115)*

Morrow, R., and J. J. Lowke, Streamer propagation in air, *Journal of Physics D: Applied Physics*, *30*, 614–627, 1997. *(p. 11, 12, 13, 14, 15)*

Munafo, A., Personal communication, 2011. *(p. 84)*

Naidis, G., Simulation of streamer-to-spark transition in short non-uniform air gaps, *Journal of Physics D: Applied Physics*, pp. 2649–2654, 1999. *(p. 48)*

Naidis, G. V., Simulation of spark discharges in high-pressure air sustained by repetitive high-voltage nanosecond pulses, *Journal of Physics D: Applied Physics*, *41*(23), 234,017, 2008. *(p. 74, 80)*

Nijdam, S., G. Wormeester, and E. M. V. Veldhuizen, Probing background ionization : Positive streamers with varying pulse repetition rate and with a radioactive admixture, *Journal of Physics D: Applied Physics*, p. 455201, 2011. *(p. 55)*

Nikipelov, A., I. B. Popov, and S. Pancheshnyi, Localized and distributed behavior of nanosecond pulse-periodic discharge in air, *proceedings of the 30th ICPIG*, pp. 28–31, 2011. *(p. 130)*

Nishihara, M., N. Jiang, J. W. Rich, W. R. Lempert, I. V. Adamovich, and S. Gogineni, Low-temperature supersonic boundary layer control using repetitively pulsed magnetohydrodynamic forcing, *Physics of Fluids*, *17*(10), 106,102, 2005. *(p. 79)*

Nishihara, M., K. Takashima, J. W. Rich, and I. V. Adamovich, Mach 5 bow shock control by a nanosecond pulse surface dielectric barrier discharge, *Physics of Fluids*, *23*(6), 066,101, 2011. *(p. 79)*

Packan, D., Repetitive nanosecond glow discharge in atmospheric pressure air, Ph.D. thesis, Stanford University, 2003. *(p. 127)*

Pai, D. Z., Nanosecond repetitively pulsed plasmas in preheated air at atmospheric pressure, Ph.D. thesis, Ecole Centrale Paris (ECP), 2008. *(p. 2, 45, 62, 63, 70, 124)*

Pai, D. Z., G. D. Stancu, D. A. Lacoste, and C. O. Laux, Nanosecond repetitively pulsed discharges in air at atmospheric pressure: the glow regime, *Plasma Sources Science and Technology*, *18*(4), 045,030, 2009. *(p. 27, 41, 188)*

Pai, D. Z., D. A. Lacoste, and C. O. Laux, Transitions between corona, glow, and spark regimes of nanosecond repetitively pulsed discharges in air at atmospheric pressure, *Journal of Applied Physics*, *107*(9), 093,303, 2010a. *(p. 3, 21, 22, 27, 30, 35, 36, 43, 145, 151, 152)*

Pai, D. Z., D. A. Lacoste, and C. O. Laux, Nanosecond repetitively pulsed discharges in air at atmospheric pressure: the spark regime, *Plasma Sources Science and Technology*, *19*(6), 065,015, 2010b. *(p. 2, 3)*

Pancheshnyi, S., Role of electronegative gas admixtures in streamer start, propagation and branching phenomena, *Plasma Sources Science and Technology*, *14*(4), 645–653, 2005. *(p. 47, 63)*

Pancheshnyi, S. V., S. M. Starikovskaia, and A. Y. Starikovskii, Collisional deactivation of $N_2(C^3\Pi_u$, v=0, 1, 2, 3) states by N_2 , O_2 , H_2 and H_2O molecules, *Chemical Physics*, *262*, 2000. *(p. 117)*

Pasko, V. P., U. S. Inan, T. F. Bell, and Y. N. Taranenko, Sprites produced by quasi-electrostatic heating and ionization in the lower ionosphere, *Journal of Geophysical Research*, *102*(A3), 4529–4561, 1997. *(p. 18)*

Pilla, G., D. Galley, D. A. Lacoste, F. Lacas, D. Veynante, and C. O. Laux, Stabilization of a turbulent premixed flame using a nanosecond repetitively pulsed plasma, *IEEE Trans. Plasma Sci.*, *34*(6), 2471–2477, 2006. *(p. 1)*

Piper, L. G., Energy transfer studies on $N_2(X^1\Sigma_g$,v) and $N_2(B^3\Pi_g)$, *The Journal of Chemical Physics*, *97*(1), 270, 1992. *(p. 116, 117)*

Poinsot, T., and D. Veynante, *Theoretical And Numerical Combustion*, 2nd ed., 2005. *(p. 161)*

Popov, N. A., Investigation of the mechanism for rapid heating of nitrogen and air in gas discharges, *Plasma Physics Report*, *27*(10), 886–896, 2001. *(p. 115, 116, 117, 121)*

Popov, N. A., The effect of nonequilibrium excitation on the ignition of hydrogen-oxygen mixtures, *High Temperature*, *45*(2), 261–279, 2007. *(p. 158, 159)*

Popov, N. A., Evolution of the negative ion composition in the afterglow of a streamer discharge in air, *Plasma Physics Reports*, *36*(9), 812–818, 2010. *(p. 46, 56)*

Popov, N. A., Fast gas heating in a nitrogen-oxygen discharge plasma: I. Kinetic mechanism, *Journal of Physics D: Applied Physics*, *44*(28), 285,201, 2011a. *(p. 81, 114)*

Popov, N. A., Kinetic processes initiated by a nanosecond high-current discharge in hot air, *Plasma Physics Reports*, *37*(9), 807–815, 2011b. *(p. 74, 81)*

Quirk, J. J., A contribution to the great Riemann solver debate, *International Journal of Numerical Methods in Fluids*, *18*, 555–574, 1994. *(p. 99)*

Raizer, Y. P., *Gas Discharge Physics*, 1991. *(p. 145)*

Ramshaw, J. D., and C. H. Chang, Ambipolar diffusion in two-temperature multicomponent plasmas, *Plasma Chemistry and Plasma Processing*, *13*(3), 489–498, 1993. *(p. 51)*

Riousset, J. A., V. P. Pasko, and A. Bourdon, Air density dependent model for analysis of air heating associated with streamers , leaders , and transient luminous events, *Journal of Geophysical Research*, 2010. *(p. 48, 114, 115)*

Rusterholtz, D. L., Nanosecond repetitively pulsed discharges in atmospheric pressure air, Ph.D. thesis, Ecole Centrale Paris (ECP), 2012. *(p. 2, 3, 67)*

Rusterholtz, D. L., D. Z. Pai, G. D. Stancu, D. A. Lacoste, and C. O. Laux, Ultrafast heating in nanosecond discharges in atmospheric pressure air, *50th AIAA Aerospace Sciences Meeting including the New Horizons Forum and Aerospace Exposition*, (January), AIAA–2012–0509, 2012. *(p. 62, 75, 80, 81, 106, 116, 118, 124, 133)*

Shu, C., Essentially Non-Oscillatory and Weighted Essentially Non-Oscillatory Schemes for Hyperbolic Conservation Laws, *ICASE Report*, (97-65), 1997. *(p. 86)*

Smirnov, V. V., O. M. Stelmakh, V. I. Fabelinsky, D. N. Kozlov, A. M. Starik, and N. S. Titova, On the influence of electronically excited oxygen molecules on combustion of hydrogeneoxygen mixture, *Journal of Physics D: Applied Physics*, *41*(192001), 2008. *(p. 159)*

Stancu, G. D., F. Kaddouri, D. A. Lacoste, and C. O. Laux, Atmospheric pressure plasma diagnostics by OES, CRDS and TALIF, *Journal of Physics D: Applied Physics*, *43*(12), 124,002, 2010. *(p. 171)*

Starikovskii, A. Y., A. A. Nikipelov, M. M. Nudnova, and D. V. Roupassov, SDBD plasma actuator with nanosecond pulse-periodic discharge, *Plasma Sources Science and Technology*, *18*(3), 034,015, 2009. *(p. 79, 80)*

Starikovskiy, A., and N. Aleksandrov, Plasma-assisted ignition and combustion, *Progress in Energy and Combustion Science*, *39*(1), 61–110, 2013. *(p. 1, 3, 159)*

Starikovskiy, A., N. Aleksandrov, and A. Rakitin, Plasma-assisted ignition and deflagration-to-detonation transition., *Philosophical transactions. Series A, Mathematical, physical, and engineering sciences*, *370*(1960), 740–73, 2012. *(p. 158)*

Tanaka, Y., Prediction of dielectric properties of N_2/O_2 mixtures in the temperature range of 300 - 3500 K, *Journal of Physics D: Applied Physics*, *37*, 851–859, 2004. *(p. 11, 13, 14)*

Tardiveau, P., E. Marode, A. Agneray, and M. Cheaib, Pressure effects on the development of an electric discharge in non-uniform fields, *Journal of Physics D: Applied Physics*, pp. 1690–1696, 2001. *(p. 40)*

Taylor, R. L., Energy transfer processes in the stratosphere, *Canadian Journal of Chemistry*, *52*, 1436–1451, 1974. *(p. 115)*

Thiele, M., J. Warnatz, A. Dreizler, S. Lindenmaier, U. Maas, A. Grant, and P. Ewart, Spark Ignited hydrogen/air mixtures : Two dimensional detailed modeling and laser based diagnostics, *Combustion and Flame*, *87*, 74–87, 2002. *(p. 167)*

Tholin, F., and A. Bourdon, Influence of temperature on the glow regime of a discharge in air at atmospheric pressure between two point electrodes, *Journal of Physics D: Applied Physics*, *44*(38), 385,203, doi:10.1088/0022-3727/44/38/385203, 2011. *(p. 21)*

Tholin, F., D. L. Rusterholtz, D. A. Lacoste, D. Z. Pai, S. Celestin, J. Jarrige, G. D. Stancu, A. Bourdon, and C. O. Laux, Images of a nanosecond repetitively pulsed glow discharge between two point electrodes in air at 300K and at atmospheric pressure, *IEEE Transactions on Plasma Science*, *39*(11), 2254–2255, 2011. *(p. 21, 188)*

Toro, E. F., *Riemann Solvers and Numerical Methods for Fluid Dynamics*, third ed., 2009. *(p. 84, 85)*

Vitello, P. A., B. M. Penetrante, and J. N. Bardsley, Simulation of negative-streamer dynamics in nitrogen, *Physical Review E*, *49*(6), 1994. *(p. 9)*

Wormeester, G., S. Pancheshnyi, A. Luque, S. Nijdam, and U. Ebert, Probing photoionization: simulations of positive streamers in varying $N_2 : O_2$ mixtures, *Journal of Physics D: Applied Physics*, *43*(50), 505,201, 2010. *(p. 49)*

Wu, L., A. A. Fridman, and A. Y. Starikovskiy, Kinetics of plasma assisted combustion at low reduced electric fields., *48th AIAA aerospace sciences meeting including the new horizons forum and aerospace exposition*, pp. AIAA–2010–1593, 2010. *(p. 159)*

Xu, D. A., D. A. Lacoste, D. L. Rusterholtz, P.-Q. Elias, G. D. Stancu, and C. O. Laux, Experimental study of the hydrodynamic expansion following a nanosecond repetitively pulsed discharge in air, *Applied Physics Letters*, *99*(12), 121,502, 2011. *(p. 80, 98, 107)*

Xu, D. A., D. A. Lacoste, D. L. Rusterholtz, and C. O. Laux, Investigation of the hydrodynamic expansion following a nanosecond repetitively pulsed discharge in air, *50th AIAA Aerospace Sciences Meeting including the New Horizons Forum and Aerospace Exposition*, (January), AIAA–2012–0508, 2012. *(p. 73, 79, 101, 121)*

Zheleznyak, M. B., A. K. Mnatsakanyan, and S. V. Sizykh, photoionization of nitrogen and oxygen mixtures by radiation from a gas discharge, *High Temperature*, *20*, 357, 1982. *(p. 16, 17)*

Zuzeek, Y., S. Bowman, I. Choi, I. Adamovich, and W. Lempert, Pure rotational CARS studies of thermal energy release and ignition in nanosecond repetitively pulsed hydrogen-air plasmas, *Proceedings of the Combustion Institute*, *33*(2), 3225–3232, 2011. *(p. 116, 159)*